Studying the structure of vertebrate kinetochore using a high-resolution microscopy approach

Giulia Vargiu

A thesis presented for the degree of Doctor of Philosophy

University of Edinburgh

September 2015

Declaration

I hereby declare that this thesis was composed entirely by myself and that the work here contained is my own, except where contributions of others are clearly stated in the text. This work has not been submitted for any other degree or professional qualification.

Giulia Vargiu
Edinburgh
August 2015

Acknowledgments

The first acknowledgment goes to the Darwin Trust of Edinburgh for the three-year funding they awarded me with. Without this support none of this would have ever happened.

I would like to thank my supervisor, Bill Earnshaw, for giving me the opportunity of working in your lab, and for the encouragement you gave me. I learnt so much and had the opportunity to attend really good conferences and courses and this was because of your support. I am not going to thank you for the Monday meetings at 9:30 am though.

I would like to say 'thank you' to all the Earnshaw Lab members, present and past, starting with:

Dan, Diana (Papi), Oscar (ma non ci credo!!!) and Mar (loca!) you are colleagues and (will be!) friends and this PhD would not have been such a good experience without you guys!!

Also Laura, Alisa, Melpi, Nuno, Jan, Helena, Paola, Florence, Kumiko, Hiromi, Emma…. I most luckily came to you, at some point, asking really absurd questions or having terrible doubts about things…well 'thank you' for sharing your knowledge/time with me. You all certainly contributed with your inputs to the nice science contained in this thesis.

Thank you, thank you, thank you to all the thesis readers: Dan, Oscar, Alisa e Alba. I cannot tell how much you helped me and how grateful I am for this!!!

Thank you Alisa for always having delicious food and for being willing to share it with me! Maybe not much of choice as your desk is adjacent to mine, and maybe you were just being very polite but anyway it is nice!

Vorrei esprimere un enorme GRAZIE alla mia famiglia!!! Grazie mamma e papà per avermi sempre supportata ed incoraggiata a perseguire tutti i traguardi che

mi ero prefissata! So che la lontananza è stata dura ma speriamo che il futuro riservi delle nuove possibilità più vicino a casa. Grazie agli amici di sempre: Simona, Arianna, Simone, Valentino, Riccardo, Marina, Valeria, Luca, Francesco, Massi e Ramona. Tornare a casa e trovarvi, fa parte del tornare a casa, rappresentate ormai una'estensione della parola famiglia. Adesso con i piccoletti è ancora più bello tornare! Anche a Daniele, a cui piace viaggiare in tutto il mondo ma non è mai venuto in Scozia in quasi 5 anni!!!

Thank you to the 'italian' crew in Edinburgh, which now is actually almost exstinguished. Dianina e Manuela I don't even know how many time I had dinner in your place! Thank you for taking care of me when I felt lonely! Adriana for being such a good person/friend despite the distance these days!

The last 'thank you' but not the least, goes to the dearest person is now in my life. I certainly was not expecting my life to change so much during my PhD and even so I met you and now I can't even remember how it was before! Thank you for being the best friend, the best partner, best chef in the house, a super-good scientist, and the most patient person on the planet. The support you gave me is beyond my ability to describe things… Daniel, I love you. I wish we will always be happy together as we are now.

Lay Summary

Cells are the core components of all living organisms. To allow growth and development, cells must divide and pass on their genetic information (DNA) to daughter cells. For this to be achieved the entire genome is duplicated and packaged into compact units known as chromosomes.

During cell division, the chromosomes become attached to string-like protein complexes, the microtubules of the spindle. Microtubules are capable of exerting minute forces with the aim of pulling the duplicated chromosomes into opposite directions. Unfortunately it is not possible for microtubules to interact with chromosomes directly, but instead, they attach to a structure on the front of chromosomes known as the kinetochore. In this regard, the kinetochore acts much like the handle of a handbag. Unlike one handle of a handbag however, the kinetochore is composed of more than 100 different parts (proteins) in all, and it has an essential role during cell division. As an example, if microtubule attachment to chromosomes is too weak, or indeed too strong, this can lead to abnormal cell division, a condition often associated with cancer. The kinetochore therefore acts as a regulator for the proper attachment of microtubules to chromosomes.

How all of these kinetochore proteins work to perform this complex function is still poorly understood, therefore the focus of my PhD was to study a selection of the components that make-up the kinetochore, to better understand how these proteins both individually and collectively function to achieve a solid attachment site for microtubules.

A key aim of this research was to study the region of the kinetochore that engages with the underlying DNA. Very little is known about the ultra-structure of this particular compartment and how, if it all, its architecture confers functional relevance. To achieve my aims I used an elegant microscopy technique that allowed the DNA associated with the kinetochore to be unfolded, and accurately measured, both with and without the presence of some of the key kinetochore components.

Using this method of microscopy, combined with complex statistical analyses, I acquired data that has allowed a more detailed ultra-structural model of the kinetochore to be proposed.

Abstract

The kinetochore is a highly complex proteinaceous structure located at the primary constriction of mitotic chromosomes. Here, it performs an essential role in accurate chromosome segregation. Recently, much interest has been directed towards the Constitutive Centromere Associated Network (CCAN) components, as they participate in the formation of a scaffold involved in kinetochore assembly. It is therefore important to fully understand their role, and their distribution, at the kinetochore. Although many kinetochore proteins have already been identified, it is still unclear how centromeric chromatin folds to form the structure of the inner kinetochore. This is an interesting yet still open field of study, where the literature reports are still quite divided. In this study we take advantage of the high homologous recombination efficiency in DT40 B-lymphoma chicken cell lines, allowing the generation of conditional knockouts and deletion cell lines of several centromere proteins, subsequently engineered to stably express GFP:CENP-A. In the parental cell line the unfolding properties of the centromeric region were investigated by using TEEN buffer. Using fluorescence microscopy we were able to measure the length of many unfolded centromeric chromatin fibres, from both interphase and mitotic samples, based on the signal of GFP:CENP-A. A multi-peak analysis revealed the presence of discrete populations of fibres, recognised as peaks, in both interphase and mitotic samples. Compared with interphase, mitotic centromeres showed a greater level of compaction. Next, mutants for CCAN components, blocked in mitosis, were subjected to centromere chromatin unfolding. Results revealed that mitotic kinetochores depleted of CENP-C and CENP-S behaved similarly to the parental interphase samples, suggesting a role of those proteins in maintaining kinetochore structure. In contrast, CENP-O, CENP-H and CENP-I depletion did not seem to weaken the structure of the kinetochore. Additionally, we tested a hypothesis revealed by the multi-peak analyses, that chromatin layers exist in the inner kinetochore. Our data, when combined with published electron microscopy and crystallography measurements of centromere/kinetochore components, allowed us to assemble a robust and mathematically viable model that supports a

boustrophedon organisation of the kinetochore chromatin. Finally, characterization studies of the novel kinetochore protein CENP-Z were performed. An involvement of CENP-Z in controlling the levels of di-methylation on lysine 4 of histone H3 was shown. This work represents an advance in our understanding of kinetochore structure in vertebrates.

Table of Contents

List of Figures

List of tables

Abbreviations

aa	amino acid
ACA	anti-centromere antibodies
AFM	atomic force microscopy
APC/C	anaphase promoting complex/cyclosome
bp	base pair(s)
BSA	bovine serum albumin
CATD	CENP-A targeting domain
CCAN	constitutive centromere associated network
C. elegans	*Caenorhabditis elegans*
CENP	centromere protein
ConA	concanavalineA
C-terminus	carboxyl-terminus
Δ	delta, deletion cell lines
DAPI	4', 6-diamidino-2-phenylindole
dd	double-distilled
DNA	deoxyribonucleic acid
D. melanogaster	*Drosophila melanogaster*
E. coli	*Escherichia coli*
EGFP	enhanced green fluorescent protein
EM	electron microscopy

FBS	foetal bovine serum
FRET	Forster resonance energy transfer
Gg	*Gallus gallus*
IP	immunoprecipitation
IPTG	isopropyl β-D-thiogalactopyranoside
kDa	kilodalton
KMN	KNL1-Mis12-Ndc80
KO	conditional knockout
KT	kinetochore
LacO	lac operator
mass-spectrometry	mass-spectrometry
MNase	micrococcal nuclease
MTs	microtubules
N-terminus	amino-terminus
PALM	Photo-activation localization microscopy
PFA	paraformaldehyde
RNAi	RNA interference
S. cerevisiae	*Saccharomyces cerevisiae*
S. pombe	*Schizosaccharomyces pombe*
SDS-PAGE	sodium dodecyl sulphate-polyacrylamide gel electrophoresis
TIRF	total internal reflection fluorescence
X. laevis	*Xenopus laevis*

1 Chapter 1: Introduction

1.1 Cell cycle

To guarantee faithful transfer of their genetic information to the progeny, cells must complete a series of highly coordinated processes including: cell growth, DNA duplication, equal distribution of duplicated chromosomes and cell division. These events, in almost all eukaryotes, are divided into distinct phases: Gap-phase 1 (G1), synthesis (S), Gap-phase 2 (G2) and Mitosis (M). G1, S and G2 phases constitute the interphase (Norbury and Nurse, 1992), which is the longest portion of the cell cycle, where a cell increases in size (G1), generates a copy of its own DNA (S) and duplicates cell organelles (G2). Interphase is followed by mitosis. During mitosis duplicated DNA becomes organised into chromosomes that will be then equally segregated into two daughter cells. Cells can also enter into Gap-phase 0 (G0) when they stop proliferating. Typically, only senescent or differentiated cells enter G0. Senescent cells are not able to re-enter the cell cycle, whereas differentiated cells could start to proliferate again in response to the appropriate physiological signalling **(Figure 1.1)**.

For the cell cycle to be executed successfully, each phase of the cell cycle has to be completed before the next one can begin. There are control checkpoints present in both interphase and mitosis **(Figure 1.1)**. Cells delay cell cycle progression until the checkpoint conditions are satisfied. During interphase, a checkpoint for DNA damage and a checkpoint for unduplicated DNA are responsible for impairing cells carrying errors in their genome, from continuing cell division, until these errors are corrected (Painter and Young, 1980; Weinert and Hartwell, 1988). During mitosis, the spindle assembly checkpoint (SAC) ensures that all the chromosomes are properly attached to the microtubules of the mitotic spindle before entering anaphase, the mitotic phase in which chromosomes segregation into two daughter cells is initiated (Rieder et al., 1995; Sluder, 1979; Sluder and Begg, 1983).

Importantly, the cell cycle can only proceed in one direction. This is achieved by a tight regulation. Cyclin-dependent kinases (CDKs) are serine/threonine dual specificity kinases and some of them are key regulators of cell cycle progression

(Baldin et al., 1993; Nakayama et al., 2001; Pines, 1999). CDKs are enzymatically active only when they are associated with their regulatory subunits, cyclins. This allows the phosphorylation of a subset of substrates and pushes the cell cycle forward (Evans et al., 1983; Hadwiger et al., 1989; Lohka et al., 1988; Nash et al., 1988). A caveat for CDK activity is constituted by the levels of cyclins in the cells that are tightly regulated by ubiquitin mediated proteolysis, as CDKs are, in contrast, constitutively expressed (Glotzer et al., 1991; Hershko et al., 1991). Therefore, different cyclins regulate distinct stages of the cell cycle: cyclin D is present in G1; cyclin E in S phase; cyclin A in S, G2 and M phases and cyclin B in M phase.

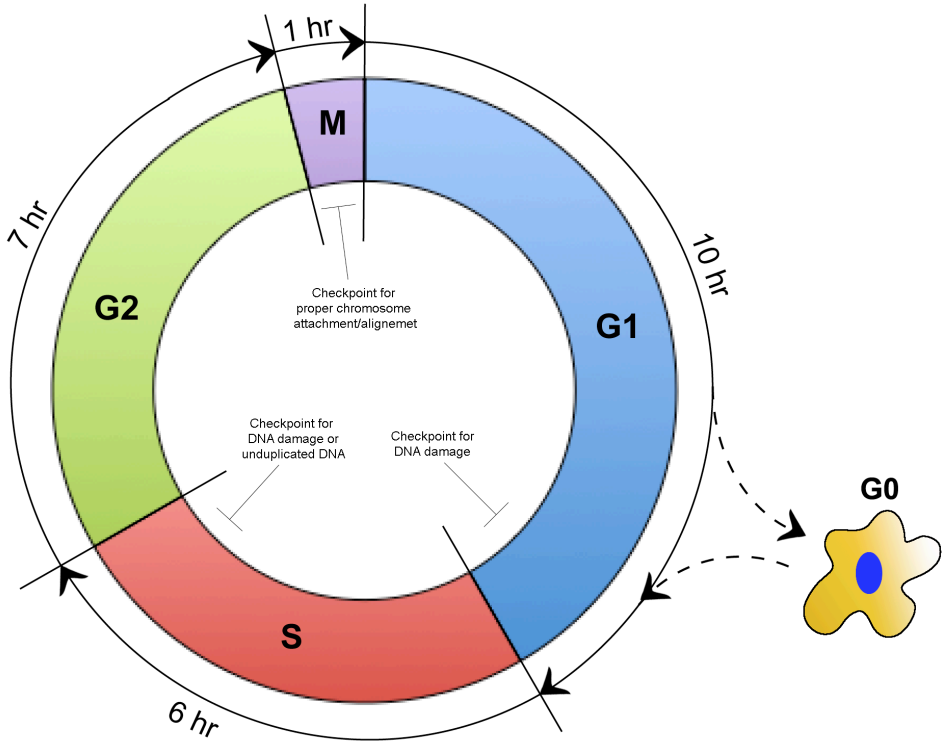

Figure 1.1. Cell cycle in eukaryotic cells. A diagram representing the phases of the cell cycle, highlighted by different colours. The uni-directionality of the cell cycle is indicated by the arrows and the length of each phase in commonly used human, tissue-cultured, cells is specified. Checkpoints for monitoring and regulating cell cycle progression are shown.

1.2 Stages of mitosis

Mitosis is the shortest phase of the cell cycle, only one hour in most human cells, and indeed finely regulated to allow the generation of two genetically identical daughter cells. Mitosis is composed of five stages: prophase, prometaphase, metaphase, anaphase and telophase/cytokinesis **(Figure 1.2)**.

1.2.1 Prophase

In prophase, the nuclear envelope and nucleoli start to disassemble and chromatin condensation begins. At this point, duplicated DNA is organised into X-shaped chromosomes (Koshland and Strunnikov, 1996) due to the activity of the Condensin II complex (Hirano, 2005). Each chromosome is composed of a pair of sister chromatids, one chromatid per daughter cell **(Figure 1.2)**. Sister chromatids are held together by the cohesin complex (Nasmyth et al., 2000) present along chromosome arms and at the primary constriction. Previously duplicated centrosomes migrate to the opposite sides of the nucleus and increase their microtubule nucleation activity, re-organizing the cytoskeleton into radial arrays of short tubulin filaments (asters) (Ault and Rieder, 1994).

1.2.2 Prometaphase

Prometaphase starts with nuclear envelope breakdown (NEB). Chromosomes are now in contact with cytosolic environment where the Condensin I complex is present. The interaction between the two condensin complexes completes chromosome condensation (Hirano, 2005). Dynamic spindle microtubules emanate from the centrosomes and start capturing chromosomes. The attachment of microtubules to chromosomes occurs at a specialized structure called the kinetochore (Cheeseman and Desai, 2008; Maiato et al., 2004). Usually, one sister chromatid is captured while the other is still unattached, a configuration known as mono-orientation. At this stage, microtubules are highly unstable, undergoing cycles of polymerization and depolymerization and syntelic attachments (both sister chromatids are attached by microtubules emanating from the same spindle pole) or

merotelic attachments (one sister chromatid is attached to microtubules coming from opposite poles) can occur and need to be corrected to proceed to the next stage of mitosis (Cimini and Degrassi, 2005; Tanaka, 2013). Microtubules stabilise when the plus end engages with the kinetochore, forming end-on attachments. At the same time, interpolar microtubules extending from opposite poles interact with each other in an anti-parallel fashion to promote the formation of a bipolar spindle (Mastronarde et al., 1993). When all the chromosomes are bi-oriented (sister kinetochores are attached by microtubules coming from opposed spindle poles), the balance of tension on both sides of the mitotic spindle causes the chromosomes to align on a plate, equidistant from spindle poles; this is called metaphase plate **(Figure 1.2)**.

1.2.3 Metaphase

At this point, all chromosomes are bi-oriented and aligned on the metaphase plate. This satisfies the spindle assembly checkpoint (SAC) that regulates the transition between metaphase and anaphase onset (Rieder and Khodjakov, 1997). When checkpoint signalling stops, cell division cycle protein 20 (Cdc20) activates the anaphase promoting complex/cyclosome (APC/C), an E3 ubiquitin ligase, allowing it to mark for degradation its targets, securin and the cyclins (Peters, 2002). Securin is a protein that normally binds the protease separase, keeping the enzyme inactive. When the proteasome degrades securin, separase passes to its active state and cleaves cohesin, allowing sister chromatid segregation to occur (Nasmyth et al., 2000).

1.2.4 Anaphase

Pulling forces generated by the depolymerization of microtubules facilitate chromatid migration towards the spindle poles **(Figure 1.2)** (Scholey et al., 2003). Interpolar microtubule interactions contribute to an elongation of the mitotic spindle to further separate chromosomes in preparation of telophase and nuclear envelope reformation. When the chromatid clusters are sufficiently separate, the spindle midzone forms, which consists of arrays of anti-parallel microtubules. The position of the midzone determines the position of the future cleavage plane, the portion of

the cell where the division of the cytoplasm of the two daughter cells will start (Field et al., 1999).

1.2.5 Telophase/Cytokinesis

Key events in telophase are the reformation of the nuclear envelope and the onset of DNA decondensation. More anti-parallel microtubules concentrate at the midzone and a cortical furrow starts to ingress. During cytokinesis, the progressive ingression of the furrow is mediated by actin that forms the contractile ring (Salmon, 1989). In its final stages, only a bridge of membranes, containing microtubules, is left between the two daughter cells, this is called the midbody (Salmon and Wolniak, 1990) **(Figure 1.2)**. Final abscission (Carlton et al., 2012) and creation of two identical daughter cells is hence achieved.

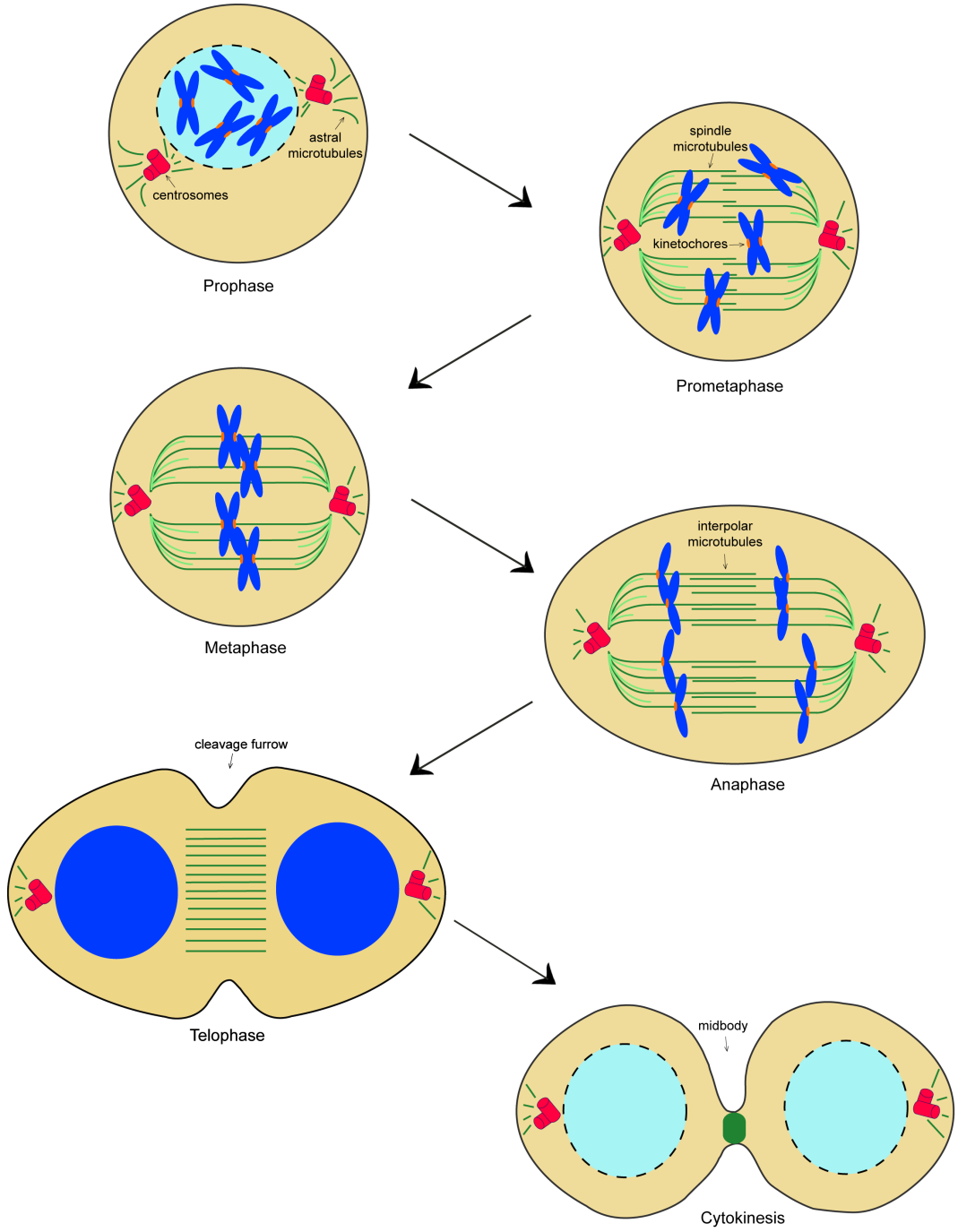

Figure 1.2. Diagram representing the stages of mitosis. Changes in cell morphology are represented as follows: DNA compaction (light blue – decondensed; dark blue – compact); microtubules (green) and centrosomes (red). A dashed line around nuclei represents nuclear envelope breakdown (NEB) and nuclear envelope reassembly. Orange dots on both sides of chromosomes indicate kinetochores.

1.3 The kinetochore

Faithful mitosis could not be achieved, in eukaryotes, without a functional kinetochore. The kinetochore is a multi-subunit protein complex positioned on the external surface of chromosomes at the primary constriction site, with the exception of holocentric chromosomes. Approximately 100 different proteins compose the kinetochore, which work in cohort to finely coordinate essential functions (Cheeseman and Desai, 2008), such as (i) supplying an anchor point for microtubule binding, (ii) correcting erroneous KT-MT attachments and (iii) monitoring that chromatid segregation occurs only when bi-orientation in achieved. Since a large part of this Ph.D. research is dedicated to better understanding the role of kinetochore components in the maintenance of kinetochore structural integrity, this will now be discussed in greater detail.

1.3.1 Kinetochore ultrastructure

The kinetochore was first observed by electron microscopy during the late sixties (Brinkley and Stubblefield, 1966). Later it was shown to be a plate-like structure found on chromosomes only during mitosis (Brenner et al., 1981). The kinetochore plate, in vertebrates, was visualised as a trilaminar structure composed of two electron dense regions, separated by an electron translucent area **(Figure 1.3 A)** (Maiato et al., 2006). In these studies, the inner plate includes the centromeric chromatin together with several protein complexes, that function to stabilize the kinetochore foundations. Typically, the outer kinetochore plate in vertebrates is 30-40 nm thick with a diameter of 500 nm. Electron microscopy shows that microtubules are terminating at this site of the kinetochore, where an adequate scaffold for microtubule binding is provided **(Figure 1.3 A right panel and B)**. The fibrous corona, also indicated as corona filaments (Rieder, 1982), progressively become visible irradiating from the outer kinetochore plate as the number of microtubules attached to the kinetochore decreases, as shown following nocodazole treatment (Cassimeris et al., 1990) **(Figure 1.3 A left panel)**. By contributing to poleward kinetochore movements, corona filaments could provide a stable anchor point for microtubule attachment at the kinetochore (Rieder and Alexander, 1990).

Figure 1.3. Kinetochore architecture in vertebrates. A. Schematic of a condensed chromosome flanked by EM pictures of specific structures on both sides. The left panel shows a section of kinetochore imaged using transmission electron microscopy where Ptk1 cells were treated with nocodazole for 20 minutes before fixation. The fibrous corona appears irradiating from the kinetochore (arrowheads) (Cassimeris et al., 1990). In the panel on the right an electron tomography slice of a human kinetochore displays the presence of an outer plate, in contact with the microtubules of the spindle, and a separate inner plate that lies on condensed, centromeric chromatin. Scale bar, 100 nm. Adapted from (Cheeseman and Desai, 2008). **B.** A schematic representation of kinetochore components at centromere chromatin, inner and outer kinetochore plates. The main functions of these groups of proteins are also indicated. Centromere proteins classified as CENP are illustrated as single letters (i.e. 'N' stands for CENP-N); A and H3 indicate nucleosomes containing CENP-A or H3 respectively; CPC, chromosome passenger complex; MCAK, mitotic centromere-associated kinesin; Mis12, Missegregation 12 complex; Ndc80, nuclear division cycle 80 complex; KNL1, kinetochore null protein 1; ZWINT, ZW10-interacting protein; Ska, spindle and kinetochore associated complex. Adapted from (Maiato et al., 2004). **C.** Enlargement of the area of the schematic in panel B highlighted by a black square, showing the interaction between CENP-C and the LEEGLG amino acid sequence present at the C-terminus of CENP-A.

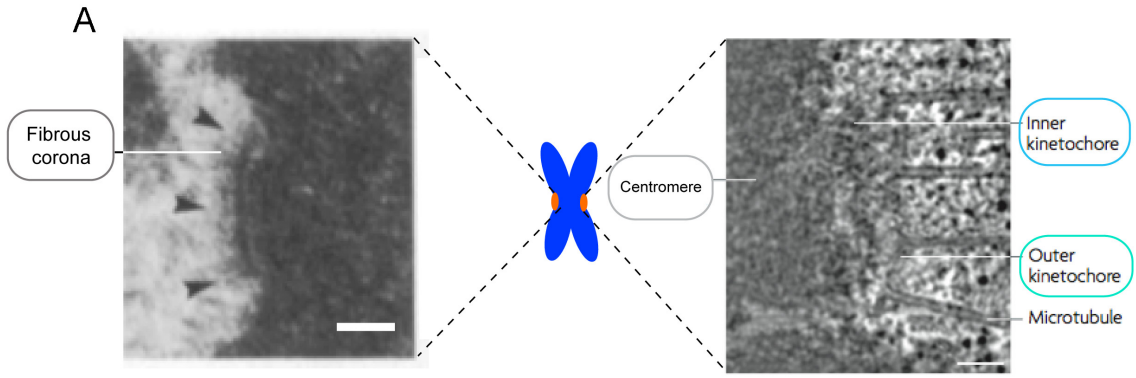
A
Fibrous corona
Centromere
Inner kinetochore
Outer kinetochore
Microtubule

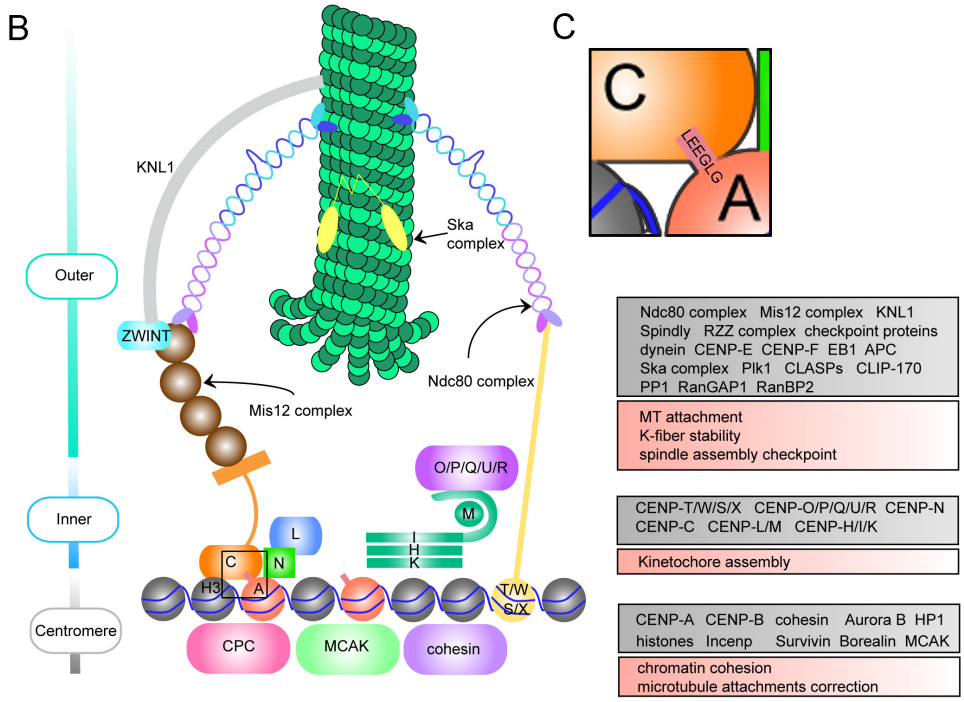
B
KNL1
Ska complex
Outer
ZWINT
Mis12 complex
Ndc80 complex
O/P/Q/U/R
M
L
I
H
K
C
N
H3
A
T/W
S/X
Inner
Centromere
CPC
MCAK
cohesin
C
LEEGLG
A
Ndc80 complex Mis12 complex KNL1
Spindly RZZ complex checkpoint proteins
dynein CENP-E CENP-F EB1 APC
Ska complex Plk1 CLASPs CLIP-170
PP1 RanGAP1 RanBP2
MT attachment
K-fiber stability
spindle assembly checkpoint
CENP-T/W/S/X CENP-O/P/Q/U/R CENP-N
CENP-C CENP-L/M CENP-H/I/K
Kinetochore assembly
CENP-A CENP-B cohesin Aurora B HP1
histones Incenp Survivin Borealin MCAK
chromatin cohesion
microtubule attachments correction

This is the 'classical' structure of the kinetochore in vertebrates (Rieder, 1982), however, extending the study of kinetochore structure to different organisms and by adopting different fixation procedure (i.e. high pressure freezing in place of aldehyde fixatives) of the sample for electron microscopy introduced some inconsistencies. Already in 1998, by using high-pressure freezing, the outer plate appeared as a fibrous mat (McEwen et al., 1998). Recently, by combining high-pressure freezing with 3D electron tomography (4-5 nm resolution), flared protofilaments were shown to extend from the microtubule plus end and slender fibrils constitute an element of continuity between the protofilaments and the kinetochore. These structures were apparently conserved in phylogenetically distant organisms (McIntosh et al., 2013). Therefore, the current view pictures the outer kinetochore more as fibrous net rather than a stack of plates (Dong et al., 2007; McIntosh et al., 2013).

Despite the essential role during mitosis played by kinetochores, their structure remains still poorly understood. With regards to better characterize kinetochore structure, en elegant combination of biochemistry with electron microscopy gave an insight on the simplest kinetochore structure, in *S. cerevisiae* (Gonen et al., 2012*)*. In this study kinetochore particles were purified performing flag purification (Dsn1-flag) and imaged attached to microtubules after taxol treatment. Large kinetochore particles (126 nm in length) were found to interact with microtubules via their globular domains with additional rod-like structures (predicted Ndc80 complex) extending in a parallel manner along the microtubule and occasionally through a ring-like structure (predicted Dam1/Ska complex) orthogonally oriented with respect to the microtubules. When bound to microtubule tips, the ring-like structure was always present however kinetochore particles measured an additional 50 nm in length. This study provided a first insight of kinetochore dimensions and structure exploiting the high resolution obtained using EM and also it was demonstrated that the core hub of the kinetochore is connected through a flexible linker to his globular domains.

1.3.2 Centromere and kinetochore inner layer

In human chromosomes, the primary constriction site is also the locus of the centromere. The centromere is the region of DNA where determinants for kinetochore assembly are present. For this reason, the specification of the position of the centromere is relevant for the outcome of cell division. However, despite its importance in eukaryotes, the structure and complexity of the centromere varies between different organisms and is poorly understood (Cleveland et al., 2003).

Three types of centromere have been described: point, holocentric and regional (Pluta et al., 1995).

In *S. cerevisiae* centromere function is genetically determined by 125 bp of DNA sequence, also referred as point centromere **(Figure 1.4 A)**. This is sufficient to ensure the binding of one microtubule to the centromere (McAinsh et al., 2003; Westermann et al., 2007). It consists of, a single nucleosome (Clarke and Carbon, 1980; Clarke and Carbon, 1985) composed of three distinct centromere DNA elements (CDEs): both CDE I and CDE III present a conserved sequence able to specify for centromere function as a single mutation in these regions can abolish it. CDE II varies in sequence when comparing different budding yeast chromosomes, however the length (76-84 bp) and AT composition (90%) remains unchanged. Importantly, CDE II region interacts with Cse4/CENP-A (Stoler et al., 1995).

Organisms like *C. elegans* have holocentric centromeres, which extends along the entire length of the chromosomes **(Figure 1.4 B)**. Similarly, the kinetochore here forms a single long plate where HCP-3/CENP-A nucleosomes are intercalated with H3-containing nucleosomes. Multiple microtubule attachment occurs in holocentric kinetochores (Maddox et al., 2004).

Regional centromeres are considered to be predominant in eukaryotes (fission yeasts, plants, flies and vertebrates) and are constituted of α-satellite DNA, spanning from hundreds of kilobases to megabases (Sullivan et al., 2001; Willard, 1985). In humans, α-satellite DNA is organized in higher order repeats (HOR) where a tandem of core monomers, 171 bp long, are flanked, on each side, by other monomers which share only 50% sequence identity, although the same monomer when repeated

present 90% of sequence identity **(Figure 1.4 C)** (Waye and Willard, 1989; Willard, 1990).

Regional centromeres are specified not only by the DNA sequence, but also by epigenetic factors (Allshire and Karpen, 2008). Three lines of evidence support this hypothesis. First, the sequence of the centromere is not evolutionarily conserved, not only across chromosomes of different organisms, but also between chromosomes in the same species (Henikoff et al., 2001). Second, centromere sequence is not sufficient to determine centromere function, as observed in some dicentric chromosomes, where one of the centromeres is inactivated without undergoing sequence rearrangements (Earnshaw and Migeon, 1985; Sullivan and Willard, 1998). Lastly, centromeres have been observed moving to a different locus, not containing a-satellite repeats, called a neocentromere (Amor et al., 2004; Saffery et al., 2000). Thus, if centromere identity relies on epigenetic factors, then kinetochore assembly localisation is also determined by the epigenetic landscape.

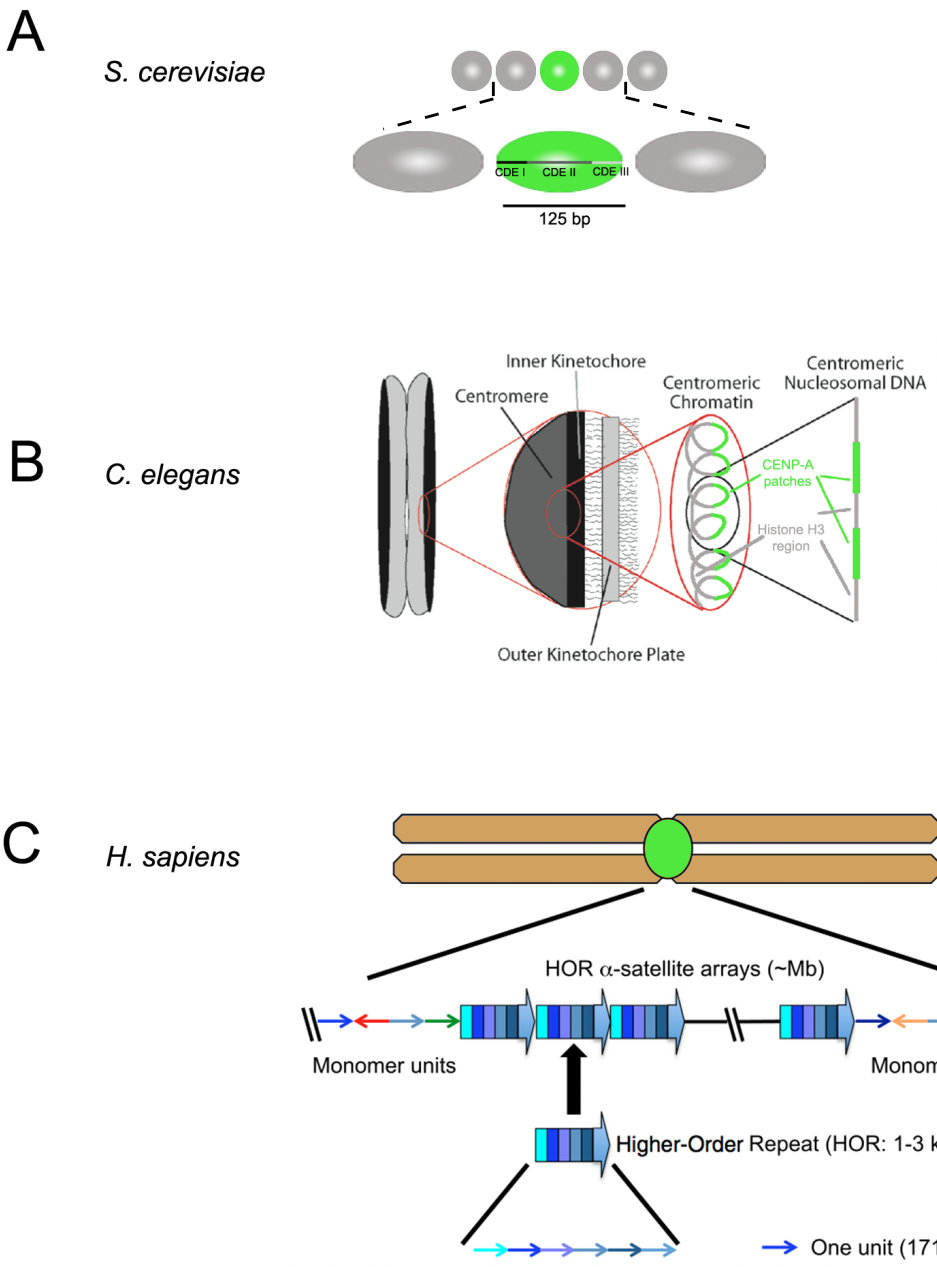

Figure 1.4. Schematic centromere representation in different model organisms. A. In *S. cerevisiae* the centromere is composed of one nucleosome able to bind Cse4/CENP-A. Centromere DNA sequence spreads for 125 bp and contains three constitutive elements: CDE I, CDE II and CDE III. Adapted from (Allshire and Karpen, 2008). **B.** *C. elegans* carries holocentric centromeres. These extends for the whole length of chromosomes and therefore HCP-3/CENP-A is intercalated with histone H3-containing nucleosomes. Adapted from (Maddox et al., 2004). **C.** Human centromeres are characterised by the presence of α-satellite DNA that is organised into higher order repeats (HOR). Each HOR is composed of different monomers (171 bp in length), which share only 50% of sequence identity. Adapted from (Fukagawa and Earnshaw, 2014).

1.3.2.1 CENP-A, a centromere unifier and a core kinetochore component

Despite the lack of DNA sequence conservation, eukaryotic centromeres all assemble CENP-A. Most fundamentally, centromere chromatin is defined by the presence of CENP-A (Earnshaw and Rothfield, 1985), the centromere specific histone variant of H3 (Palmer et al., 1991), present in centromere nucleosomes (Palmer et al., 1987). CENP-A, together with CENP-B and CENP-C, were the first centromere proteins identified, found localising to the primary constriction of human chromosomes using serum obtained from patients affected by scleroderma CREST (Earnshaw and Rothfield, 1985). Following this discovery, an entire new subset of centromere proteins have been identified and studied (Amano et al., 2009; Foltz et al., 2006; Izuta et al., 2006; Nishihashi et al., 2002; Okada et al., 2006; Perpelescu and Fukagawa, 2011). CENP-A homologs have also been identified in other species: Cse4p in *S. cerevisiae* (Meluh et al., 1998), Cnp1 in *S. pombe* (Takahashi et al., 2000), HCP3 in *C. elegans* (Buchwitz et al., 1999) and CID in *D. melanogaster* (Henikoff et al., 2000). At present, the only known group of eukaryotes that do not assemble CENP-A nucleosomes at centromeres is the Trypanosomatid. CENP-A overexpression studies in *D. melanogaster* showed that CENP-A can be ectopically loaded into chromosome arms and generate functional kinetochores (Heun et al., 2006). However, in human cells, tethering CENP-A to ectopic sites is not sufficient to generate functional *de novo* kinetochores (Van Hooser et al., 2001), which suggests that additional factors are required (Gascoigne et al., 2011). Nonetheless, depletion studies performed in *C. elegans* (Oegema et al., 2001), mouse (Howman et al., 2000), chicken (Regnier et al., 2005) and human (Goshima et al., 2003) indicated an essential role of CENP-A in proper chromosome congression at the metaphase plate, and segregation in anaphase. In addition, *in vitro* studies showed that, once in contact with *X. laevis* egg extracts, CENP-A chromatin arrays are able to recruit several kinetochore components (Guse et al., 2011).

These observations support a primary role of CENP-A as centromere identifier and kinetochore pillar. Due to the relevance of CENP-A, the question arose

about how cells control the location of CENP-A deposition, avoiding its spreading onto the chromosome arms.

1.3.2.2 Spatial and temporal deposition of CENP-A

The amount of CENP-A at the centromere is diluted after every cycle of DNA replication (Jansen et al., 2007; Kim et al., 2003; Shelby et al., 2000; Sullivan and Karpen, 2001), therefore the loading of new CENP-A is an essential process for the maintenance of a functional centromere. The only exception found is in *S. cerevisiae* where all old CENP-A molecules are substituted for new ones during S-phase (Pearson et al., 2004).

Despite the fact that CENP-A mRNA levels peak during G2 (Shelby et al., 1997), it has been shown that, in human cells, CENP-A incorporation into newly replicated DNA occurs in early G1 (Jansen et al., 2007; Maddox et al., 2007). The process of CENP-A deposition can be divided into several steps: priming, incorporation and maturation.

Initially, the Mis18 complex, which consists of Mis18α, Mis18β and Mis18 binding protein (Mis18BP1 or KNL2) (Fujita et al., 2007; Hayashi et al., 2004; Maddox et al., 2007), prime the centromeric chromatin for CENP-A loading. The Mis18 complex localises to centromeres in late mitosis, just before the loading of new CENP-A occurs. This could explain why a direct interaction between CENP-A and Mis18 complex has not been observed. However, it has been shown that the Mis18 complex physically binds to the Mis16/RbAp48/46 complex. RbAp46 is a member of histone acetyl-transferase complexes (HATs). The combination of the Mis18 and the Mis16/RbAp48/46 complexes affect acetylation levels at the centromere (Fujita et al., 2007). Additionally, depletion of any single component of the Mis18 complex ablates loading of newly synthesized CENP-A, leading to mitotic defects (Fujita et al., 2007). Therefore, increasing levels of acetylation at the centromere turn the chromatin into a ‘permissive’ state for CENP-A assembly.

Next, newly synthesized CENP-A must be assembled onto centromere chromatin. This is the task performed by the Holliday junction-recognition protein (HJURP), which works as a CENP-A specific chaperone (Dunleavy et al., 2009;

Foltz et al., 2009). HJURP only localizes at centromeres during a short window of time, extending from late telophase to early G1 (3 hours in human cells) (Dunleavy et al., 2009; Foltz et al., 2009), in parallel with CENP-A deposition (Jansen et al., 2007). HJURP is able to recognize CENP-A, in combination with H4, through a highly conserved N-terminal region in CENP-A sequence called CENP-A targeting domain (CATD) (Foltz et al., 2009). Depletion of HJURP in human cells severely limits the loading of CENP-A, with the appearance of segregation defects and micronuclei only after several rounds of mitosis (Dunleavy et al., 2009; Foltz et al., 2009), suggesting that in normal circumstances an excess of CENP-A is present at centromeres, however, a minimal amount of CENP-A is critical for the execution of centromere functions.

Remodeling and spacing factor (RSF) complex, composed by Rsf-1 and Snf2h, is involved in the stabilization of new CENP-A at centromeres. The complex co-IPs with CENP-A and it can transiently accumulate at centromeres in the middle of G1 where it recruits new CENP-A. Additionally, Rsf-1 depleted cells showed reduced levels of CENP-A signal at centromeres (Perpelescu et al., 2009).

More recently, it has been shown that Plk1 activity is required for proper centromere localization of Mis18 complex and HJURP (McKinley and Cheeseman, 2014) and that CDK1 and CDK2 inhibit the loading of CENP-A during phases S, G2 and M of the cell cycle (Silva et al., 2012). Thus, spatio temporal regulation of CENP-A deposition is essential for centromere maintenance and function.

The mechanisms described here referred to studies performed in human cells or metazoans, however, with some mechanical differences in chromatin licensing and CENP-A chaperones are found across eukaryotes.

Also found at the inner kinetochore is the chromosomal passenger complex (CPC), present only in the early stages of mitosis. Here, the CPC is responsible for the correction of erroneous attachments of microtubules onto kinetochores. This will be discussed in more detail in a later section.

Although CENP-A specifies where the kinetochore is going to be established, kinetochore functions are exerted by several other proteins, such as members of the CCAN and the KMN network.

1.3.3 Bridging inner and outer kinetochore: CCAN

In 2006, a number of new centromere proteins were discovered (Foltz et al., 2006; Izuta et al., 2006; Okada et al., 2006). The entire subset of new centromere proteins has been termed, constitutive centromere associated network (CCAN). These proteins are mostly located at the inner kinetochore and contribute to the stabilization of the outer kinetochore components, conferring stability for microtubule binding.

Three different laboratories published the discovery of CCAN components in the same year. Foltz and colleagues (Foltz et al., 2006) expressed tagged versions of CENP-A or H3 in HeLa cells and performed IP and affinity purification experiments of the tagged histones. This led to the identification of CENP-M, CENP-N and CENP-T by mass-spectrometry. Later, these three proteins were individually overexpressed, followed by double affinity purification step (TAP-tag purification followed by incubation with S-protein beads), further identifying CENP-I/K/L/O/P/Q/S. In this work, CENP-A proximal nucleosome associated complex (NAC, CENP-C/H/N/M/U/T) or CENP-A-nucleosome distal (CAD, CENP-I/L/O/P/Q/R/S) proteins were identified. Other researchers (Izuta et al., 2006) developed a method to identify interaction partners of CENP-A or H3 by using specific monoclonal antibodies (Ando et al., 2002) using interphase nuclei isolated from HeLa cells. To preserve its native structure, isolated DNA mixed with proteins was not sonicated or cross-linked with formaldehyde, as in conventional ChIP protocols, but treated with micrococcal nuclease followed by salt treatment (0.3 M NaCl). This procedure was called Native Chromatin IP (NChIP). DNA digestion led to isolation of the components of the Interphase Centromere Complex (ICEN). Ultimately, the expression of tagged CENP-H and CENP-I in chicken DT40 cells and of CENP-H, CENP-O and CENP-P in HeLa cells prompted the identification of CENP-H/I/K/L/M/N/O/P/Q/R/U as centromere proteins by performing immuno-precipitation and mass-spectrometry (Okada et al., 2006). This list was later expanded when CENP-W (Hori et al., 2008a) and CENP-X (Amano et al., 2009) were also identified.

At present 16 components have been classified as members of the CCAN **(Figure 1.3 B)**, and divided into sub-groups on the basis of reciprocal dependencies (McAinsh and Meraldi, 2011; Perpelescu and Fukagawa, 2011). These studies have provided an almost exhaustive parts list of the CCAN, however the mechanism by which a functional kinetochore is assembled from these parts (CCAN components) is yet to be fully elucidated. In addition, as the initial studies pointed out, there are a number of CCAN components that can directly interact with chromatin and others that do not. These will be now discussed.

1.3.3.1 Chromatin interface

The CCAN, placed in between the centromere chromatin and the outer kinetochore protein complexes, mediates the interaction between these two compartments. In order to do so, some CCAN members have shown to bind to chromatin. Currently three connection points have been found between chromatin and CCAN. These involve CENP-N, CENP-C and CENP-T.

In vitro experiments showed that CENP-N binds directly to CENP-A, but not to H3 containing nucleosomes (Carroll et al., 2009). This was shown by incubating ^{35}S-labelled centromere proteins with reconstituted nucleosomes containing or lacking CENP-A and by looking at the shift of nucleosome migration on an agarose gel. In addition, CENP-N could interact with a mutant H3 containing the CENP-A targeting domain (CATD), H3^{CATD}. This highlighted and confirmed the importance of the CATD domain to CENP-A functions (Black et al., 2004; Black et al., 2007). Furthermore, it was found that upon CENP-A overexpression, CENP-N co-localized to the chromosome arm, supporting previous evidences for CENP-A binding (Gascoigne et al., 2011). Despite its dependence on CENP-A, CENP-N was observed to be recruited at CENP-A free chromatin sites (lacO arrays) where N-terminus fragment of CENP-T or CENP-C lacI fusion proteins were tethered (Gascoigne et al., 2011), suggesting that not only interaction with CENP-A but also contacts with other CENPs can contribute to CENP-N localization. More recently, it has been shown that CENP-N levels at kinetochores are higher during S and G2 phases compared to M and G1 phases (Fang et al., 2015; Hellwig et al., 2011) as a consequence of the exposure to an Arg80/Gly81 loop on CENP-A (Fang et al., 2015) that recruits

CENP-N in a cell cycle-regulated manner. Following these observations, a possible role of CENP-N in centromere chromatin replication has been hypothesised.

CENP-C, recognised as part of the inner kinetochore (Saitoh et al., 1992), is involved in the binding of both DNA (with its C-terminus) (Yang et al., 1996) and Mis12 complex (with its N-terminus), placed in the outer kinetochore (Przewloka et al., 2011; Screpanti et al., 2011). Similarly to CENP-N, the ability of CENP-C to bind CENP-A nucleosomes was tested by incubation *in vitro*, prior to running a gel and observing a shift in CENP-A nucleosomes migration (Carroll et al., 2010). A motif at the C-terminus of CENP-A, 'LEEGLG', located outside of the CATD domain, was found to be sufficient to promote CENP-C binding to H3 **(Figure 1.3 C)**. In contrast, studies in chicken DT40 cells revealed an interaction by immunoprecipitation of CENP-C with H3 mononucleosomes, but not with CENP-A (Hori et al., 2008a), although super-resolution images of stretched centromere fibers in DT40 cells showed co-localization of CENP-A and CENP-C (Ribeiro et al., 2010). However, one evidence supporting a dependency of CENP-C on CENP-A in chicken cells derives from the observation of a decrease in the levels of CENP-C following CENP-A depletion (Hori et al., 2008a). Additionally, structural studies on Mif2p, the CENP-C homologue in *S. cerevisiae*, revealed the presence of a dimerization domain at the C-terminus of the protein (Cohen et al., 2008). Mutantions designed to disrupt the dimer formation impaired mutants growth at 37°C, suggesting a role of the CENP-C dimer for kinetochore function *in vivo*. Importantly CENP-C, besides making connections with inner kinetochore chromatin, organises, together with other CCAN, a platform for the outer kinetochore as it has been shown that ectopic expression of CENP-C can recruit the Mis12 complex (Gascoigne et al., 2011).

CENP-T contains a long, unstructured N-terminal tail and a histone-fold domain (HFD) at the C-terminus. The HFD is required for CENP-T DNA binding activity (Hori et al., 2008a). CENP-T was found to bind preferentially with H3 containing nucleosomes, rather than CENP-A. However, reduced levels of CENP-T were found in cells depleted of CENP-A (Hori et al., 2008a). In addition, the HFD also allows CENP-T to combine with CENP-W (a 100 amino acid protein, a majority

of which also comprises a HFD (Hori et al., 2008a; Nishino et al., 2012), forming a heterodimer. Following its isolation (Foltz et al., 2006), CENP-S was identified as putative binding/interacting partner of CENP-X and CENP-T by mass-spectrometry (Amano et al., 2009). Later, it was confirmed by *in vitro* experiments that chicken CENP T/W and S/X sub-complexes form a heterotetramer able to super-coil the DNA in a nucleosome-like fashion (Nishino et al., 2012). However, unlike canonical nucleosomes, which must have 147 bp of DNA wrapped around them, the CENP-T/W/S/X heterotetramer was able to protect only 100 bp of chromatin from micrococcal nuclease digestion. Furthermore, CENP-T/W/S/X complex purified from chicken cells induces positive supercoiling of the DNA, in contrast to the negative supercoiling imposed by canonical nucleosomes (Takeuchi et al., 2014). This activity is only found in the complete T/W/S/X complex, as T/W and S/X sub-complexes alone do not induce positive supercoiling in chromatin. Interestingly, the positive supercoiling thus obtained has been proposed to be a characteristic signature of centromere chromatin, which would contribute to the recruitment of other CCAN components specifically to the centromere. This hypothesis has been supported by FRET experiments in human cells, where the observation of the loading at the centromere of CENP-T/W/S/X complex from mid-S phase up until G2, preceding CENP-A loading (in early G1), and also at DNA damaged sites, suggested a role for the complex in turning the chromatin into a 'kinetochore-competent' state (Dornblut et al., 2014). Despite the T/W and S/X sub-complexes co-operating together in DNA binding, their contribution to the overall kinetochore assembly process must be separate since deletion of CENP-T/W is lethal in chicken DT40 cells (Hori et al., 2008a), whereas depletion of CENP-S/X is not, although it has been reported to affects outer kinetochore plate length (Amano et al., 2009).

CENP-T/W/S/X complex also has a primary role in connecting inner kinetochore chromatin with outer kinetochore protein complexes. Indeed, the N-terminal tail of CENP-T has been shown to directly interact with the Ndc80 complex (Gascoigne et al., 2011; Hori et al., 2008a; Nishino et al., 2013; Schleiffer et al., 2012). Also, the CENP-T N-terminal tail is phosphorylated in a cell cycle dependent manner by CDK1 kinase, which could be a mechanism for ensuring a time-regulated

formation of a functional kinetochore (Gascoigne and Cheeseman, 2013; Gascoigne et al., 2011).

If CENP-C and CENP-T confer their essential role in kinetochore function due to the simultaneous interaction with centromere chromatin and outer kinetochore components at the same time, it is relevant that CENP-N, the only one of the three interacting directly with CENP-A, does not extend far from CENP-A chromatin. However, more components of the CCAN are positioned more distal than CENP-A chromatin, overlooking at outer kinetochore components, whose role/function has been less studied.

1.3.3.2 Trapped in the middle: extended CCAN

The CENP-H/I/K/M complex centromere localization is dependent on CENP-A, CENP-T/W (Hori et al., 2008a) and in humans, also CENP-C (Gascoigne et al., 2011). This complex has been reported to influence CENP-A chromatin and plus tips of microtubules. CENP-H and CENP-I have been reported to affect the recruitment of newly synthesized CENP-A to the centromere (Hori et al., 2013; Okada et al., 2006). Although one study found that CENP-H did not directly bind to CENP-A (Hori et al., 2008a), recent work, using super-resolution microscopy revealed that the two components localize close to each other on centromere fibers (Ribeiro et al., 2010) and in human neocentromeres (Alonso et al., 2007). Importantly, the overexpression of CENP-H has been linked to an increase in chromosomal instability (CIN) and has been found in several primary tumours (Liao et al., 2009; Shigeishi et al., 2006). CENP-K plays a role in Hec1/Ndc80 localization, where depletion of both CENP-K and KNL1 drastically impairs Hec1/Ndc80 kinetochore localization (Cheeseman et al., 2008). Depletion of CENP-I can trigger severe mitotic defects as this protein is known to interact with outer kinetochore protein components such as CENP-F and Mad1/2 (Liu et al., 2003). It has been recently shown that CENP-H and CENP-I can modulate microtubule dynamics during chromosome congression onto the metaphase plate, by accumulating at the kinetochore in favour of microtubule polymerisation (Amaro et al., 2010). If the CENP-H/I/K complex can affect microtubule dynamics this would explain the phenotypes of mitotic block and defective chromosome congression upon depletion of these proteins. In support of

this evidence, a new mechanism for spindle checkpoint maintenance during prometaphase was found. CENP-I was shown to be involved in preventing Mad1 and the RZZ complex from dissociating from kinetochores that have not been properly attached by spindle microtubules. This action would complement Aurora B activity, which induces Mad1 and RZZ complex association, which is particularly important in the absence of Aurora B activity (Matson and Stukenberg, 2014). Recently, CENP-M was found to be cross-linked with CENP-I, and its depletion associated with chromosome alignment defects. CENP-M has also been shown to be an inactive GTPase, related to the Rab1 family; it is required for proper CENP-I localization and interaction with outer kinetochore proteins. Surprisingly, depletion of CENP-M decreased the levels of CENP-T/W and Ndc80 (Basilico et al., 2014).

CENP-L/M were initially classified as a small sub-complex, however new evidence supports CENP-M as part of the CENP-H/I/K sub-complex. Despite this, CENP-L was shown to relate to CENP-M in some aspects as follows. CENP-L/M were initially co-purified with the H/I/K sub-complex and the centromere localization was shown to be interdependent among these centromere proteins (Okada et al., 2006). Depletion of CENP-L/M in HeLa cells, by RNAi, caused a decrease in the amount of CENP-H/I at kinetochores (Foltz et al., 2006; Izuta et al., 2006). Specifically with CENP-L, RNAi studies showed that its depletion is connected with the increase of monopolar spindles in mitotic cells (McClelland et al., 2007), and *in vitro* studies demonstrated an interaction between CENP-L and the N-terminus of CENP-N (Carroll et al., 2009).

Some research suggests that the CENP-O/P/R/Q/U sub-complex functions downstream of the sub-complexes previously described (Takeuchi and Fukagawa, 2012). Although depletion of any of these components does not affect cell viability in DT40 cells, mitotic phenotypes can arise following chromosome segregation in a depletion background (Hori et al., 2008b; Izuta et al., 2006; Okada et al., 2006). Its role becomes essential in DT40 cells for spindle recovery following impairment of spindle dynamics, such as after nocodazole treatment (Hori et al., 2008b). Using a fluorescent three-hybrid assay (F3H), it has been shown that CENP-O/P/R/Q/U can interact with one another at an ectopic site on the chromosomes (Eskat et al., 2012).

Fluorescence resonance energy transfer (FRET) data also confirmed the proximity of the subunits to one another in the kinetochore. In addition, fluorescence cross-correlation spectroscopy (FCCS) measurements demonstrated that the complex does not pre-assemble in the nucleoplasm (Eskat et al., 2012). In addition, CENP-O has been reported to be present at centromeres in S-phase, similarly to CENP-N and CENP-T/W. Its protein levels at the prekinetochore/kinetochore progressively decrease during mitosis (Eskat et al., 2012; McAinsh et al., 2006). Moreover, recent studies showed a connection between members of this sub-complex and the mechanism driving chromosome congression: CENP-U would recruit Polo-like kinase 1 (Plk1) to the kinetochore through a phosphorylation step and Plk1/CENP-U/CENP-Q form a ternary complex, and only in this conformation CENP-Q is phosphorylated by Plk1 in human cells (Kang et al., 2011). In addition, a Plk1 independent mechanism has been shown where CENP-Q is essential for the recruitment of motor-protein CENP-E at kinetochores, contributing to chromosome segregation (Bancroft et al., 2015).

The most recently characterised kinetochore proteins were identified by SILAC mass-spectrometry analysis of chromosomes isolated from DT40 cells (Ohta et al., 2010). Out of the entire DT40 chromosome-proteome, 13 novel kinetochore proteins were identified that, in agreement with the established nomenclature, have been named with letters Y and Z and numbers from 27 to 36 (i.e. CENP-Y or CENP-27). These proteins are still mostly uncharacterised, although a recent study described an essential role for CENP-32 in the maintenance of centrosome/spindle pole association (Ohta et al., 2015).

1.3.4 Outer kinetochore: KMN network and SAC

The KMN is a conserved network of proteins, across eukaryotes, which functions as a microtubule binding site and as a platform for the recruitment of SAC components. The acronym KMN stands for the initials of the components of the network: kinetochore null protein 1 (KNL1), missegregation 12 (Mis12) and nuclear division cycle 80 (Ndc80) complexes. These protein complexes are bound to the kinetochore in mitosis where they play an essential role in the formation of end-on

attachments. The assembly of a defective KMN has been shown to result in problems in chromosome segregation errors (Cheeseman and Desai, 2008).

1.3.4.1 KMN network components

The Ndc80 complex is a heterotetramer composed of: Ndc80 (also known as Hec1 in human) and nuclear filamentous 2 (Nuf2), organized into one heterodimer, and spindle pole component 24 (Spc24) and 25 (Spc25) forming a second heterodimer. Each heterodimer consists of a long coiled-coil region, with two globular domains at one end (one per protein). Spc24/25 heterodimer has globular heads located at the C-terminus, whereas in Ndc80/Nuf2 heterodimer they are located at the N-terminus of the proteins. The heterodimers interact via the extremities of their coiled-coils, and the overall complex forms a dumb-bell shaped structure with a total length of ~ 60 nm (Ciferri et al., 2005; Ciferri et al., 2008; Wei et al., 2005) **(Figure 1.3 B)**. The C-terminal globular heads of Spc24/25 are important for the recruitment of the complex at the kinetochore as they interact with Mis12 (Petrovic et al., 2010) and with the CCAN via CENP-T (Bock et al., 2012; Gascoigne et al., 2011; Hori et al., 2013; Nishino et al., 2013; Schleiffer et al., 2012). The N-terminal globular heads of Ndc80/Nuf2 fold into a calponin homology (CH) domain, required for binding to microtubules (Cheeseman et al., 2006; Ciferri et al., 2008; Wei et al., 2007). Structural studies of $Ndc80^{bonsai}$ (a shorter version of Ndc80, lacking the coiled-coil region) in combination with tubulin dimers, clarified that microtubules interact with a site contained in the CH domain of Ndc80, called the 'toe' (Alushin et al., 2010). The toe includes positively charged residues that recognise a negatively charged region at the interface between α and β tubulin, named the 'toe print'. It has been proposed that the presence of this site might act as a sensor, limiting the binding of Ndc80 to straight microtubule protofilaments rather than to curled ones. In addition, Ndc80 forms electrostatic interactions between its positively charged N-terminus and the E-hooks (acidic carboxy-terminal tails) present on each tubulin monomer (Alushin et al., 2010; Ciferri et al., 2008; Wei et al., 2007). This contributes to the co-operative binding of Ndc80 to microtubules, which is mediated by Ndc80 N-terminal tail. When the 'toe print', recognised by Ndc80, is displaced due to microtubule depolymerisation, Ndc80 shifts preferentially

towards the microtubule minus end (biased diffusion) for the maintenance of a stable attachment (Alushin et al., 2010).

The human Mis12 complex consists of Nnf1, Mis12, Dsn1 and Nsl1. These subunits form a rod-like structure (Petrovic et al., 2010; Wan et al., 2009) **(Figure 1.3 B)**. The yeast Mis12 complex homologue (Mtw1/MIND) was shown to have a similar structure as the human, and an interaction was observed with the Spc24/25 subunit of the Ndc80 complex (Hornung et al., 2011; Maskell et al., 2010). In vertebrates, cross-linking studies revealed that the C-terminus tail of Nsl1 interacts with both the Ndc80 and KNL1 complexes, even though these two complexes do not interact with one another (Petrovic et al., 2010).

KNL1, first identified in *C. elegans* (Desai et al., 2003), forms a heterodimer with ZW10-interacting protein 1 (ZWINT1) in humans (Petrovic et al., 2010). KNL1 depletion demonstrated that it is required for proper chromosome alignment at the metaphase plate, and showed that its loss can lead to cell death in chicken DT40 cells (Cheeseman and Desai, 2008). More observations in *C. elegans* and *D. melonogaster* demonstrated that KNL1 is required for the localization of Ndc80 at kinetochores (Desai et al., 2003; Przewloka et al., 2007). However in humans, this pathway is also influenced by CENP-H/I/K (Cheeseman et al., 2008; Liu et al., 2003).

1.3.4.2 KMN is a platform for both microtubule attachments and SAC activity

The spindle assembly checkpoint (SAC) includes a group of proteins, conserved across eukaryotes, which tightly regulate the process of chromatid segregation, delaying anaphase entry until all the chromosomes are bioriented, in order to avoid missegregation events. The SAC is activated by unattached kinetochores. This is due to the inactivation of cell division cycle 20 (Cdc20) that normally activates the APC/C. In order to do so, Cdc20 is sequestered by the mitotic checkpoint complex (MCC), composed of mitotic arrest deficient 2 (Mad2), budding uninhibited by benomyl 3 (Bub3) and Bub1-related (BubR1) proteins (Sudakin et al., 2001). APC/C, once active, triggers the proteolytic degradation of Cyclin B and securin, allowing anaphase to start. For this reason, modulating the activity of

APC/C is crucial for the achievement of a correct ploidy in the daughter cells (Foley and Kapoor, 2013).

Unattached kinetochores recruit high levels of monopolar spindle protein 1 (Mps1) kinase (Hewitt et al., 2010; Kwiatkowski et al., 2010; Maciejowski et al., 2010; Santaguida et al., 2010). Recently, a new model has been proposed for SAC activation **(Figure 1.5)**. In this model it was suggested that Mps1 phosphorylates KNL1 at its MELT (M[D/E][I/L/V/M][S/T]) repeats (London et al., 2012; Shepperd et al., 2012; Yamagishi et al., 2012), recruiting Bub1 and Bub3 to kinetochores (Kiyomitsu et al., 2007). Moreover, in addition to ZWINT1, within which KNL1 is in complex, other members of the RZZ complex such as Rod, Zwilch and ZW10 are targeted to KNL1; however it is unclear whether their binding depend on the Mps1 phosphorylation of KNL1 (Hewitt et al., 2010; Maciejowski et al., 2010; Santaguida et al., 2010). The kinetochore localization of Mad1 and Mad2 heterodimers is dependent on the RZZ (Kops et al., 2005). Mad2 has been proposed to exist in two conformations: 'open' and 'closed' **(Figure 1.5)**. When Mad2, through its association with Mad1, is recruited to the kinetochore, it is in a closed conformation. Closed-Mad2 can bind Cdc20 preventing its interaction and activation of the APC/C. In addition to the pool of Mad2 bound to the kinetochore, there is also a pool of free cytosolic open-Mad2. Open-Mad2 cannot bind Cdc20 (Luo et al., 2000; Luo et al., 2002; Luo et al., 2004). Closed-Mad2 at the kinetochore is able to interact with open-Mad2 and induce a conformational change in its structure to revert it into a closed Mad2, which is now able to interact with Cdc20 and sequester it into the MCC complex, until the 'anaphase-waiting signal' is switched off (all the kinetochores are attached to microtubules and chromosomes are bioriented) (De Antoni et al., 2005; Luo and Yu, 2008; Mapelli et al., 2007; Mapelli and Musacchio, 2007).

In this context, the Aurora B dependent mechanism of biorientation silences the SAC. Aurora B kinase, a member of the CPC complex, by phosphorylating its targets is responsible for the correction of erroneous attachments of microtubules onto kinetochores (Carmena et al., 2012). As previously mentioned, the CPC complex localizes at centromeres in early mitosis. The CPC complex is composed of four subunits: Incenp, Survivin, Borealin/Dasra and Aurora B. Incenp, Survivin and

Borealin all contribute to the centromere localization of the complex (Carmena et al., 2012). Aurora B kinase can phosphorylate, in addition to other substrates, the Ndc80 complex (Cheeseman et al., 2006; DeLuca et al., 2006) and MCAK, a microtubule depolymerazing kinesin (Andrews et al., 2004; Lan et al., 2004; Ohi et al., 2004), causing a destabilization of microtubule attachments. More recently, a mechanism coupling the phosphorylation activity of Aurora B kinase with tension generated by bipolar attachments was proposed in both yeast and human cells (Liu et al., 2009; Tanaka et al., 2002). The tension generated at the centromere, as a result of correct microtubule attachments, increases the distance of kinetochore proteins from Aurora B kinase, which, in this configuration is unable to phosphorylate these targets (Tanaka, 2013). In contrast, when erroneous or none attachments are present at kinetochores, kinetochore proteins are now located in close proximity with the kinase, which can now phosphorylate them. During anaphase the CPC migrates to the spindle midzone where it remains until completion of cytokinesis. At the midzone CPC promotes an accurate cell abscission (Carmena et al., 2012; Earnshaw and Cooke, 1991; Jeyaprakash et al., 2007; Yamagishi et al., 2010). Specifically, it has been reported that Borealin interacts with the ESCRT-III, the complex that mediates the end of cytokinesis (Capalbo et al., 2012; Carlton et al., 2012).

How stable kinetochore-MT attachments are maintained is still not fully understood. Growing evidence suggests that this could be the role of the spindle and kinetochore associated (Ska) complex. The composition of this complex with Ska1, Ska2 and Ska3 (Rama1) has been deeply studied (Abad et al., 2014; Daum et al., 2009; Gaitanos et al., 2009; Hanisch et al., 2006; Jeyaprakash et al., 2012; Raaijmakers et al., 2009; Theis et al., 2009; Welburn et al., 2009). A functional homolog in yeast has been also identified, known as Dam1 complex, and it is composed by ten subunits assembled in the shape of a ring that surrounds microtubules (Gaitanos et al., 2009; Hanisch et al., 2006; Schmidt et al., 2012; Welburn et al., 2009). This conformation differs from the structure of the metazoan Ska complex, recently elucidated by crystallography (W shaped) (Jeyaprakash et al., 2012) (Figure 1.3 B). *In vitro* experiments showed that both Ska and Dam complexes are able to bind to dynamic microtubules (Abad et al., 2014; Asbury et al., 2006; Grishchuk et al., 2008; Welburn et al., 2009; Westermann et al., 2006). In addition, it

has been shown that the association of the Cdt1 and Dis1 proteins, with the loop domain (loop that interrupts the coiled-coil region) of Ndc80, stabilise the interactions between the kinetochore and microtubules (Hsu and Toda, 2011; Varma et al., 2012).

The SAC signal is removed by the recruitment of protein phosphatase PP1 to the kinetochore via a PP1 binding motif in KNL1 (Pinsky et al., 2009; Vanoosthuyse and Hardwick, 2009) and also through dynein/dynactin stripping of Mad1 from the kinetochore in the direction of the spindle poles (Howell et al., 2001).

Recent evidence has highlighted a possible role of KNL1 in activating Aurora B kinase, coupling the SAC with KT-MTs attachment error-correction (Caldas et al., 2013). According to this model, the N-terminal region of KNL1 is sufficient for protein kinase Bub1 recruitment at the kinetochore, triggering the phosphorylation of histone H2A and thereby contributing to Aurora B localization at the centromere (Yamagishi et al., 2010). To support this, measurements of Bub1 activity with Aurora B activity seemed to correlate, and levels in such activities were dropping upon KNL1 silencing.

In summary, the kinetochore in eukaryotes is an essential structure required for microtubule attachment, and therefore viable cell division. This structure has been visualized in numerous ways since its first observation in 1966 by transmission electron microscopy (TEM) (Brinkley and Stubblefield, 1966). Attempts have also been made using scanning electron microscopy (SEM) (Harrison et al., 1985) and atomic force microscopy (AFM) (Pietrasanta et al., 1999), however these modes of microscopy either do not have the resolving power necessary (SEM) or they are too technically challenging (AFM). At present the most frequent mode of microscopy used to visualize the kinetochore is light microscopy, exploiting the properties of fluorescent probes or GFP-fusion proteins.

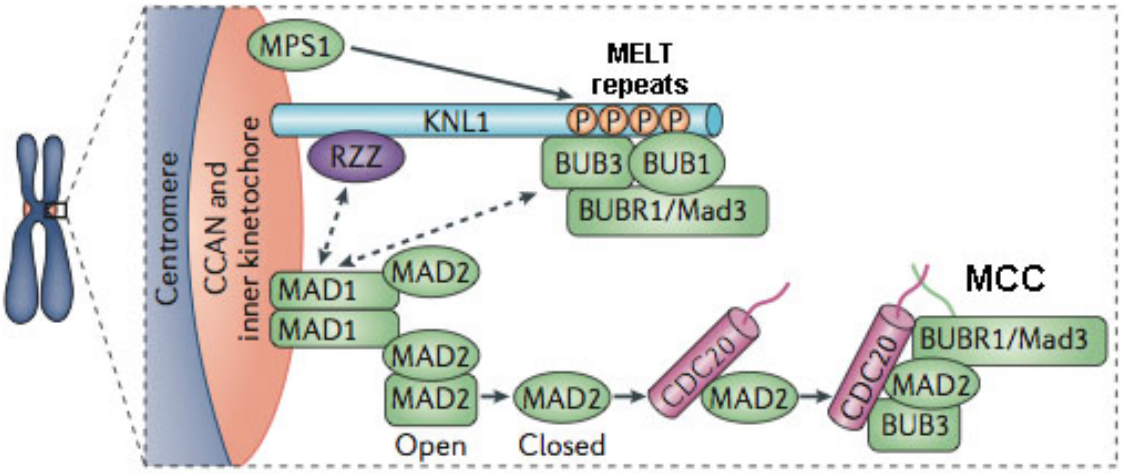

Figure 1.5. Spindle assembly checkpoint and the 'anaphase-wait' signal. MPS1 kinase phosphorylates KNL1 at the MELT repeats at no microtubule bound kinetochores. This phosphorylation event triggers the recruitment of RZZ complex and Bub3, Bub1 and BubR1 to the kinetochore. The recruitment of the latter group of proteins is linked to the kinetochore localization of Mad1/Mad2 heterodimer. The heterodimer is composed of closed Mad2, which is able to interact with free open Mad2 and catalyse its transition to the closed conformation. Closed Mad2 binds Cdc20, Bub3 and BubR1 subsequently sequester them in the mitotic checkpoint complex (MCC). Adapted from (Foley and Kapoor, 2013).

1.4 Contemporary methods for imaging the structure of the inner kinetochore

Although the protein composition of the kinetochore has been deeply studied, much less is known about the spatial arrangements of these components and their interactions with the chromatin, an event that allows the kinetochore to perform its crucial roles. Methods currently used to tackle this question are conventional fluorescence microscopy (Blower et al., 2002; Bodor et al., 2014; Coffman et al., 2011; Haase et al., 2013; Joglekar et al., 2009; Joglekar et al., 2008; Joglekar et al., 2006; Lawrimore et al., 2011; Sullivan and Karpen, 2004; Suzuki et al., 2014; Wan et al., 2009) and super-resolution microscopy (Ribeiro et al., 2010). As the work presented in this thesis is based on fluorescence microscopy methods, I will discuss recent advances in the understanding of kinetochore structure achieved using fluorescence microscopy techniques.

1.4.1 Conventional wide field fluorescence microscopy: centromere protein copy number and localization

Conventional light microscopy enables the visualization of proteins of interest within cells with relatively routine sample preparation, compared with other microscopy methods (i.e. electron microscopy). The use of this technique increased exponentially after the generation of the first fluorescent proteins (Lippincott-Schwartz and Patterson, 2003; Tsien, 1998).

The earliest studies looking at protein copy number were performed starting in *S. cerevisiae*, where the aim was to calculate protein copy number at kinetochores based on fluorescence intensities. It was found that, when comparing the copy of kinetochore proteins, from *S. pombe* and in *C. albicans*, the amount of CENP-A nucleosomes does not positively correlate with centromere chromatin length, however it does positively correlate with the number of microtubules bound per kinetochore (Joglekar et al., 2008; Joglekar et al., 2006). However, these quantifications are still contentious as changing reference standard parameters determined a different estimation of kinetochore protein copy number (Coffman et al., 2011; Lawrimore et al., 2011).

Concomitantly, studies in *S. cerevisiae* and human cells developed similar methods to measure distances between fluorescence centroids of kinetochore proteins using a two-colour fluorescent labelling approach in the presence of tension (metaphase plate), (Joglekar et al., 2009; Wan et al., 2009). These studies showed a comparable distribution of proteins within the kinetochore in both organisms **(Figure 1.6)**. Adopting two-colour fluorescent labelling and centroid distance measurements, allowed quantification of distances for SAC proteins as well as CCAN components with an accuracy of few tens of nanometers in human cells (Suzuki et al., 2014; Varma et al., 2013).

Studies have also been focused on mapping the localization of core kinetochore components or histone modifications onto centromere chromatin with the aim of better characterising the inner kinetochore structure. To compare the fluorescence pattern of specific histone modifications relative to CENP-A on metaphase chromosomes **(Figure 1.7 A)** or on stretched chromatin fibers **(Figure 1.7 B)** (Blower et al., 2002; Sullivan and Karpen, 2004) studies were performed in *D. melanogaster* and human centromeres, where a distinct separation between Cid/CENP-A and H3K4me2 containing nucleosomes was observed. These results were formalized into a model, known as 'amphipathic model', for centromere chromatin architecture.

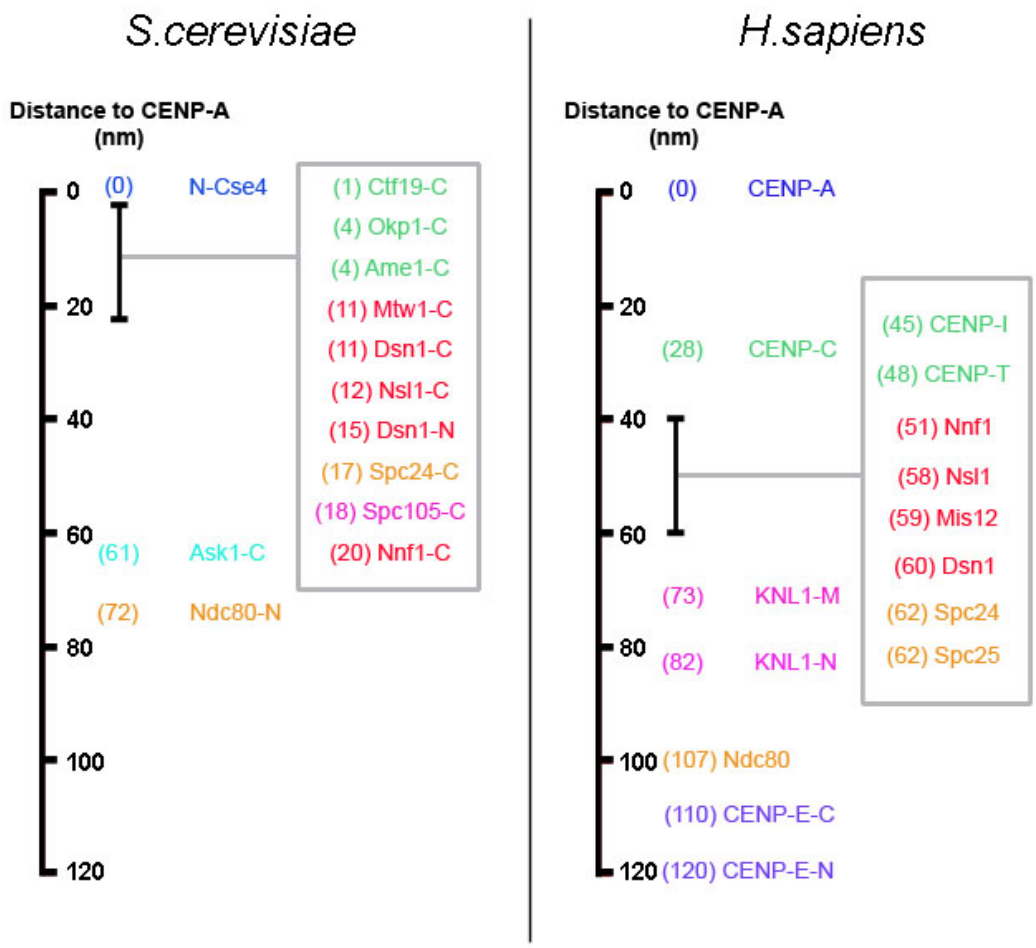

Figure 1.6. Distances measured between CENP-A and other kinetochore components in both *S. cerevisiae* and human kinetochores. Schematic summarising the distances, expressed in nm, measured between each CENP and CENP-A in human (Wan et al., 2009) and budding yeast (Joglekar et al., 2009) kinetochores under tension. The following budding yeast proteins are homologs of: (Cse4) CENP-A, (Ctf19) CENP-P, (Okp1) CENP-Q, (Ame1) CENP-U, (Mtw1) Mis12, (Spc105) KNL1. Ask1 is a component of the Dam1 complex in yeast. CENP proteins are coloured in green, with the exception of CENP-A (blue), Ndc80 complex in orange, KNL1 in pink and Mis12 complex in red. When protein localization is measured from the N-terminus, C-terminus or middle region, letters N, C or M are indicated.

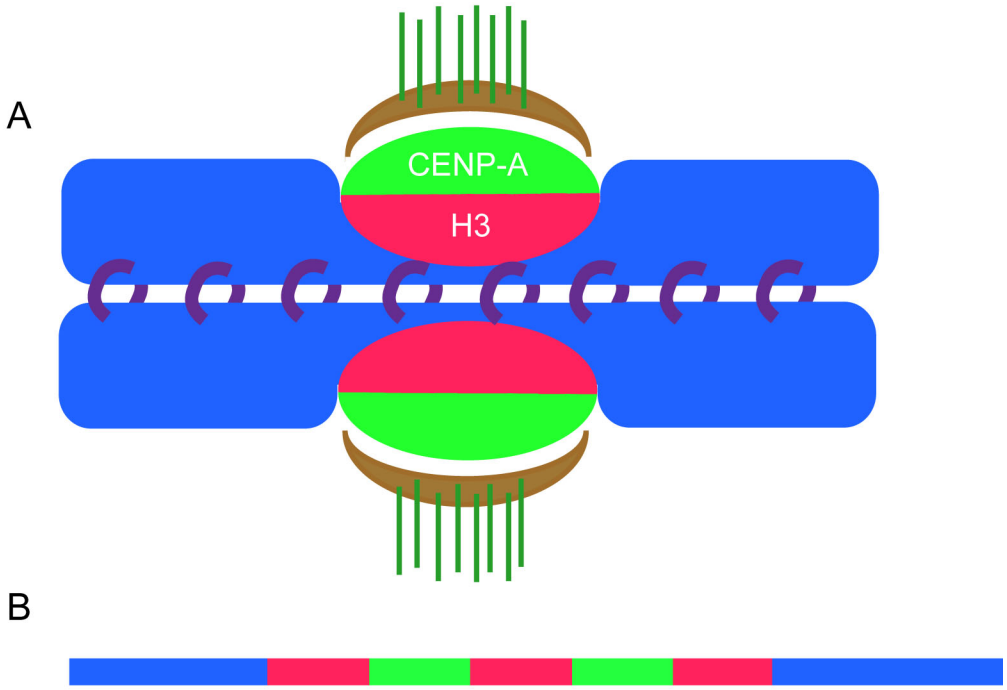

Figure 1.7. Amphipathic model for centromere chromatin assembly. A. Configuration of chromatin at centromeres in intact chromosomes. Chromatin containing CENP-A (light green) is found on the external surface of the centromere, facing the outer kinetochore plate (brown) where microtubules are bound (dark green); whereas H3K4me2 nucleosomes are restricted to the inner centromere region and have no contact with kinetochore proteins. Cohesin complex is represented in purple. **B.** Pattern of CENP-A and H3 containing chromatin observed in fibers, that supports this model.

1.4.2 Super-Resolution Microscopy: the new frontier of light microscopy

Conventional fluorescence microscopy has a resolution limit dictated by the diffraction limit of light (250 nm) (Abbe, 1873). This means that any light-emitting object smaller than 250 nm will be visualised as a blurry spot, impairing the observation of fine structural details. Similarly, two light-emitting objects in close proximity (i.e. distance <250 nm) will be seen as one when observed by conventional microscopy. This effect is due to what is better known as 'point spread function' (PSF), which describes how an imaginary light-emitting object, with the shape of a point, is represented in an image. The PSF is a common parameter used to indicate the resolution achieved by an optical system, like a microscope. The range of sizes of macro-molecules generally spans from tens to a few hundred nm, therefore the observation of most sub-cellular compartments, smaller than the Abbe limit (250 nm), is highly limitated by conventional microscopy.

During the last 20 years improved novel microscopy methods have been developed, allowing imaging with greater resolution (between 30-100 nm) (Betzig et al., 2006; Dickson et al., 1997; Hell and Wichmann, 1994). Collectively, these techniques are known as 'super-resolution' (SR) imaging (Gustafsson, 2000; Huang et al., 2009; Lippincott-Schwartz and Patterson, 2009; Schermelleh et al., 2010). A brief description of the most commonly used SR techniques is presented here, including: structured illumination microscopy (SIM) and stimulated emission depletion (STED), which both rely on characteristic illumination systems and single molecule localization techniques such as stochastic optical reconstruction microscopy (STORM) and photo-activation localization microscopy (PALM) **(Figure 1.8 A)**.

'Structured illumination microscopy' (SIM) is based on a characteristic sample illumination where the light passes through a movable optical grating, which can be oriented in different directions, projecting light patterns onto the sample (Gustafsson, 2000; Heintzmann and Cremer, 1999). This is also referred to as non-uniform wide-field illumination **(Figure 1.8 B)**. The application of coarser shading patterns to finer cellular structures produces a set of moiré fringes in the light

emitted. Multiple raw images are acquired of every vertical section. The complete set of images is then computationally processed to identify the size of the grating, its periodicity and direction, determining an increase in resolution in x and y. By superimposing raw images where moiré fringes are present, in different areas of the samples, an image can be reconstructed that has lateral resolution that is twice that of wide-field microscopy. With the development of three-dimensional SIM (3D-SIM), the potential resolution achieved along the z axis doubled **(Figure 1.8 A**, 350 nm versus ~ 700 nm**)**. This is achieved by modulation of the light excitation in the z axis using three-beam interference (Gustafsson et al., 2008; Schermelleh et al., 2008). One particular benefit is that standard staining techniques of cell samples can be combined with SIM and 3D-SIM acquisition enabling the visualization of multiple structures at the same time, and the study of their reciprocal localization.

'Stimulated emission depletion' (STED) (Dyba and Hell, 2002; Dyba et al., 2003; Hell and Wichmann, 1994; Klar et al., 2000) typically uses a combination of two laser beams for scanning the sample, that are shone on the sample in sequence, not at the same time **(Figure 1.8 B)**. The first beam excites the fluorophores present in the sample. Illumination by the second laser is delayed, and this is referred to as the STED laser. This has a longer wavelength (less energy) and has the shape of a doughnut, illuminating the fluorophores positioned off the center of the emitting object. This causes all the fluorophores surrounding the centre of the PSF to return back to ground state (de-excitation). The centre of the emitting object is protected from the effects of the STED laser by a phase plate through which the laser light is unable to pass. Therefore, the STED reduces the size of the PSF beyond the diffraction limit. Doing so, the resolution that can be achieved in x and y is approximately 60 nm **(Figure 1.8 A)**. The main limitation of this technique is related to the restricted combination of probes available per experiment. It is important to avoid any excitation in the wave-length of the depletion beam, as this would not allow the de-excitation of the signal. Commonly used combinations of secondary antibodies are: Alexa 488 and Alexa 555 or Alexa 488 and Alexa 568 (Schermelleh et al., 2008).

Single molecule localization techniques rely on the light-emitting properties of the fluorescent molecules used and they are based on the assumption that many photons contribute to the appearance of the PSF of an object. The photons are emitted from the same object, therefore the PSF can be described by a gaussian function, where a gaussian fitting can determine the centroid from which the fluorescence departs. Despite this rather simple formulation, several difficulties have been encountered in order to separate single photons. Approaches based on colour emission (Bornfleth et al., 1998) and fluorescence life-time (Heilemann et al., 2002) have been attempted without achieving acceptable results. However, much better results were achieved when tests to separate photons in time were performed (Lidke et al., 2005). This advanced technology was named 'pointillism', after the famous painting technique, and is based on the usage of photoactivatable or photoswitchable dyes. By reducing the number of molecules emitting in a specific region of the specimen, at a given time, the probability of signals overlapping is greatly reduced (Betzig et al., 2006; Hess et al., 2006; Rust et al., 2006). The two best known technologies that arose from pointillism are the 'stochastic optical reconstruction microscopy' (STORM) (Rust et al., 2006) and 'photo-activation localization microscopy' (PALM) (Betzig et al., 2006) **(Figure 1.8 B)**. The difference between PALM and STORM classically lies in the type of probe used. PALM exploits the advantages of genetically encoded proteins fused to a photoactivatable tag, whereas STORM takes advantage of antibodies labelled with reporter dyes that can be activated or inactivated in turn, or just spontaneously switch between bright and dark states. However, the two approaches can be combined, generating for example, a two colour acquisition system where one protein candidate is tagged with a photoactivatable protein and the second one is labelled with a metastable secondary antibody. This is a conjugated secondary antibody where the fluorophore, supplied with enzymes, is able to catalyse the change between dark and bright states and appropriate energy (in the form of laser wave length) spontaneously blink (Ribeiro et al., 2010). For both PALM and STORM, images are acquired by modulating laser wave-lengths through a shutter, activating only a small subset of molecules in the specimen at a time. Next, prior to the acquisition of the signal of another group of molecules, the signals are turned off by irradiation with a different laser wave-length

or simply due to oscillations to a dark state. The process is repeated, acquiring several hundreds of frames per structure of interest (Sengupta et al., 2012). High resolution images are obtained by reconstructing the entire set of molecule positions related to one focal plane, by applying a gaussian fitting and incorporating them into a density map. The resolution obtained is dependent on the accuracy of the localization of each fluorescent molecule, labelling density and the biological structure itself. Results are generally more reliable when a long and thin object is analysed rather then a globular and dense one.

Each mode of microscopy carries its own pros and cons. For example the preparation of samples for 3D-SIM is relatively simple and follows standard protocols for indirect immunofluorescence, however one limitation is the small improvement in resolution compared with other super-resolution microscopy techniques. In contrast, PALM/STORM allow a resolution of ~ 30 nm to be achieved, however, for these methods, preparation of samples is more complex and restricted by the chemical properties of the probes. Accurate single molecule localization achieved by PALM has been employed in one attempt to study centromere chromatin structure (Ribeiro et al., 2010).

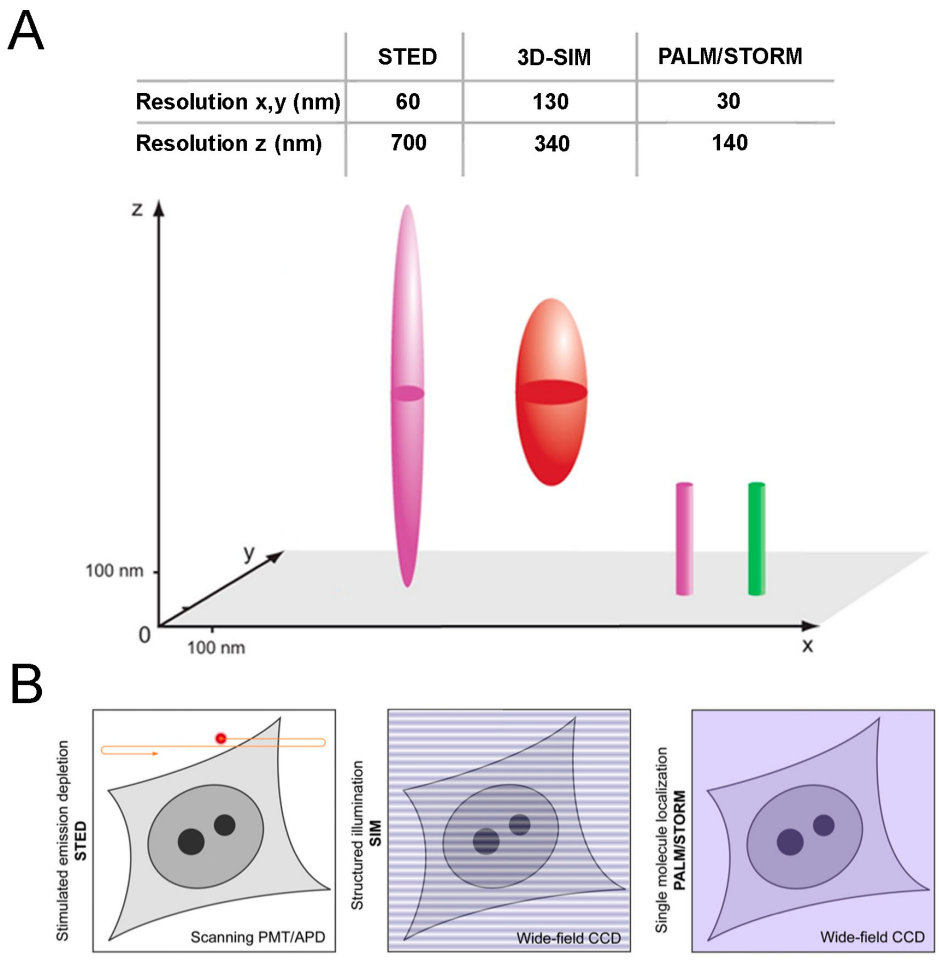

Figure 1.8. Overview of super-resolution imaging methods applied in cell biology. A. Diagram representing size and shape of 'point spread function' (PSF) in STED, 3D-SIM and PALM/STORM. On the top of the diagram, values indicating the resolution achieved in x,y and z using each method are shown. **B.** Schematic illustration of sample illumination and signal detector used for each technique. In STED, an excitation laser scans the specimen followed by a 'doughnut' shaped STED, which takes back to ground level the excitation of peripheral molecules, overall reducing the PSF. A photomultiplier tube (PMT) or avalanche photodiodes (APD) detectors are used. In the case of SIM and 3D-SIM, conventional wide-field illumination is coupled to grating filtering of the light, creating a moiree fringe shadowing effect. After acquiring images where the grating was rotate of different degrees, the super-resolution image of the sample is generated by a mathematical reconstruction of dark and bright areas. Here, charge-coupled devices (CCD) are used for signal detection. PALM/STORM uses wide-field illumination and charge-coupled devices (CCD) for signal detection. Adapted from (Schermelleh et al., 2010).

1.4.2.1 Use of PALM/STORM microscopy as a tool to analyse kinetochore structure

Recently, single-molecule fluorescence techniques have been applied to the study of inner kinetochore chromatin structure and composition in chicken cells (Ribeiro et al., 2010). Here, CENP-A molecules were tagged with the protein Dronpa (Ando et al., 2004; Habuchi et al., 2005), which is activated (bright) or inactivated (dark) depending on the wave-length of the irradiating laser beam (488 and 405 nm respectively). To map the position of histone modifications relative to CENP-A, Alexa Fluor 647 secondary labelled antibody was used in presence of a 'switching buffer' that contains enzymes able to catalyse the change between dark and bright states at an appropriate wave length (633 nm) (see section **2.7**). This approach allowed the visualization of H3 nucleosomes in CENP-A chromatin fibers **(Figure 1.9 A)**. Results showed that H3 nucleosomes had the same pattern of distribution as CENP-T on centromere fibers, relative to CENP-A **(Figure 1.9 B)**. This suggested that a revision of the previous amphipathic model was required as it predicted a confinement of H3 to the inner side of the centrochromatin, which is incompatible with the pattern of distribution of CENP-T (Sullivan and Karpen, 2004). Therefore, the 'boustrophedon' model was proposed. This described the centromere as composed of a stack of layers of chromatin, where in each layer chromatin is folded in a sinusoidal pattern **(Figure 1.9 C)**. In this conformation, both CENP-A and H3 are present at the interface with inner kinetochore components and interact with CCAN members. In this study, the resolution achieved to determine single molecule position was approximately 37 nm.

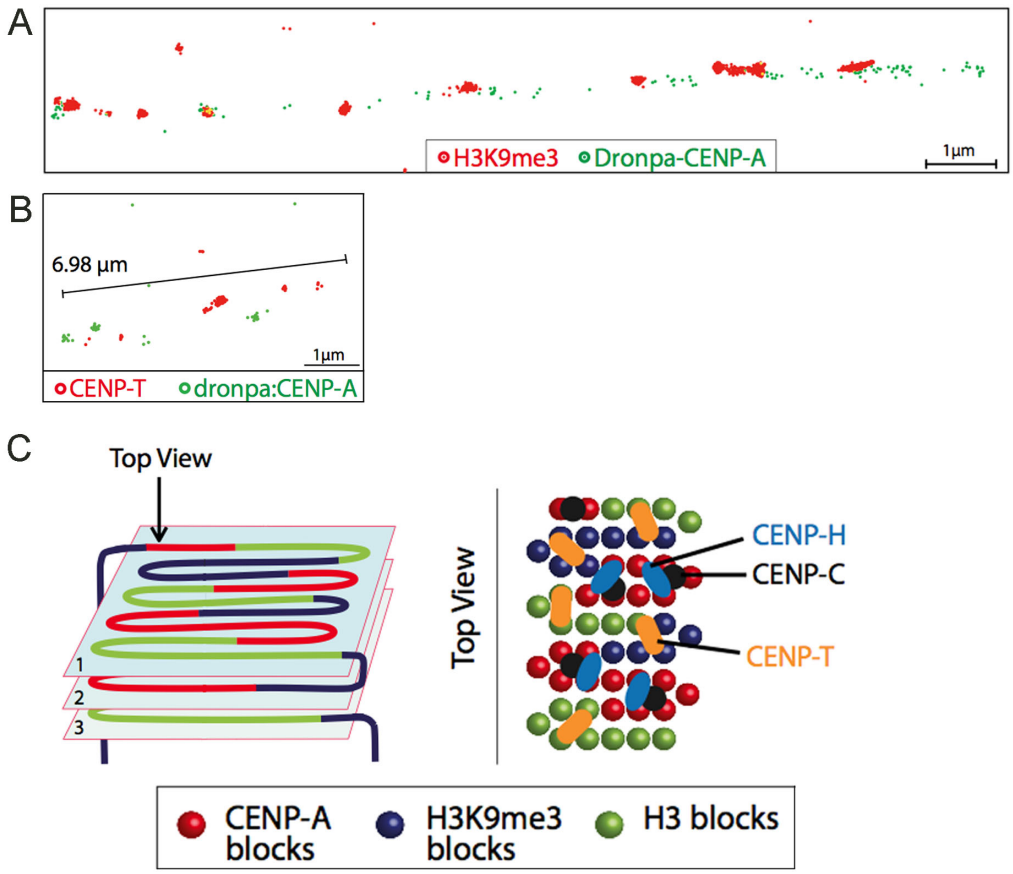

Figure 1.9. Super-resolution analysis of chicken kinetochore architecture by PALM. A. and **B.** Single molecule signals of Dronpa:CENP-A (green) and Alexa Fluor 647 labelled secondary antibody (red) were acquired. Areas of signal co-localization are false coloured in yellow. Scale bar, 1 µm. **A.** Representative stretched centromere fiber showing localization of CENP-A (green) and histone H3 tri-methylated on lysine 9 (red) (modification observed surrounding CENP-A chromatin (Sullivan and Karpen, 2004)). **B.** Representative stretched centromere fiber, showing localization of CENP-A (green) and CENP-T (red). **C.** Schematic representing the predicted boustrophedon model for inner kinetochore organization. DNA, including both CENP-A and H3 nucleosomes, is composed of a stack of layers, where chromatin folds into sinusoidal curves. On the external surface (top view) both CANP-A and H3 interact with CCAN components to direct and stabilise the kinetochore.

1.5 Aim of the project and experimental approach

The purpose of this research is to establish a more comprehensive understanding of the hierarchies of kinetochore assembly and to further characterize the structure of the vertebrate kinetochore, uncovering novel relationships between different components. At present, the field is divided between support of one of two best established models: the amphipathic model or the boustrophedon model. With this study I hope to provide evidence supporting one of these two models.

To achieve this aim different approaches will be used:

1) as this research will be focussed on the architecture of centromeric chromatin, methods for observing and measuring changes in its biophysical properties will need to be optimised. These include testing diverse sample preparations, procedures and microscopy methods, in order to identify the most suitable conditions to accomplish my aim;

2) cell cycle related changes will be interrogated by measuring the stretching of centromeric chromatin of interphase and mitotic cells *in vitro*. For this, parental DT40 cell lines stably expressing GFP:CENP-A will be generated. Using conventional wide field fluorescence microscopy, stretched centromere fibers will be observed using GFP:CENP-A, before being measured and analysed using multi-peak algorithms to identify sub-populations of fibers;

3) to better understand the role of individual CCAN members in stabilising the architecture of the centromeric chromatin, I will analyse stretched centromere fibers prepared from a range of cell lines depleted for salient proteins. Therefore, a selection of DT40 conditional knockout (KO) and deletion (Δ) cell lines will be engineered to stably express GFP:CENP-A. Similarly with aim (2), the length of unfolded GFP:CENP-A centromere fibers will be measured in the different cell lines. This will allow me to identify which CCAN components are required for the stable folding and rigid ultra-structure of the kinetochore in mitosis;

4) the effects of the depletion of CCAN proteins required for the maintenance of kinetochore ultra-structure will also be analysed on stretched centromere fibers using super-resolution microscopy. The level of co-localization between Dronpa:CENP-A and CENP-R will be analysed by PALM following CENP depletion, as a tool to observe fine changes in distribution;

5) finally, with the goal of identifying an additional contributor to kinetochore structure, maintenance or function, the novel kinetochore protein CENP-Z will be characterised.

If successful, this study will provide novel insights into kinetochore assembly, folding and overall stability, by addressing a series of previously unanswered questions.

2 Chapter 2: Materials and Methods

2.1 Buffers and solutions

Unless otherwise stated, buffers and solutions were prepared by dissolving chemicals, purchased from Sigma-Aldrich, in ddH_2O.

Table 2.1 - General solutions and buffers

Name	Composition
Electrophoresis buffer SDS (Severn Biotech)	25 mM Tris pH 8.8; 192 mM glycine; 0.1% SDS
Transfer buffer	25 mM Tris-HCl pH 8.8; 192 mM glycine; 20% methanol
3X sample buffer (3XSB)	50 mM Tris-HCl pH 6.8; 15% sucrose; 2 mM EDTA; 3% SDS; 0.5% Bromo Phenol Blue
1X sample buffer (1XSB)	300 μl 3X SB; 510 μl ddH_2O; 90 μl Beta-mercaptoEtOH
PBS	0.01 M phosphate buffer; 137 mM NaCl; 2.7 mM KCl; pH 7.4
PBS-Tw (Tween-20, BioRad)	PBS; 0.1% or 0.05% Tween-20
PBS-Triton (TritonX-100, BioRad)	PBS; 0.03% 0.3% TritonX-100
Luria-Bertani (LB)	1% tryptone; 0.5% yeast extract; 10 mM NaCl; pH 7.4
Ponceau Red	0.5% Ponceau Red; 1% Acetic acid
Ponceau destaining	3% Acetic acid
4X Lower gel buffer	1.5 M Tris-HCl pH 8; 0.4% SDS
4X Upper gel buffer	0.5 M Tris-HCl pH 6.8; 0.4% SDS
TEEN 10X	10 mM Triethanolamine:HCl pH 8; 10 mM NaCl; 5mM EDTA
Doxycycline (BD Biosciences)	1 mg/ml in ddH_2O and filtered with 0.2 μm pore size filter
Nocodazole	1 mg/ml in DMSO

2.2 Molecular biology

2.2.1 Preparation of competent cells

TOP10 bacteria were streaked out on LB plates, in sterile conditions, to obtain single colonies two days in advance. 10 ml of LB was inoculated in the evening with a single colony. The next morning the culture was diluted 1:200 with fresh LB, supplemented with 20 mM $MgSO_4$, and incubated in a shaker at 37°C for 3-4 hours or until OD600 reaches 0.48. The culture was transferred to 50 ml falcon tubes and cooled on ice for 10 minutes. Next, cells were centrifuged at 3500 rpm for 7 minutes at 4°C in a pre-chilled rotor. Supernatant was discarded and the pellets resuspended in 20 ml of cold TfbI buffer **(Table 2.2)**. Following a 5 minute incubation on ice, the bacteria was collected by centrifugation at 3000 rpm for 10 minutes at 4°C. Supernatant was discarded and the pellets gently resuspended in 2 ml of cold TfbII **(Table 2.2)**. Cell suspension was incubated on ice for 15 minutes after which cells were promptly aliquoted and either used directly or stored at -80°C for future use.

Table 2.2 – Buffer used for competent cells preparation

Name	Composition
TbfI	30 mM KOAc; 100 mM $RbCl_2$; 10 mM $CaCl_2$; 50 mM $MnCl_2$; 15% v/v Glycerol; pH 5.8 using acetic acid (filter sterilize, store at +4°C)
TbfII	10 mM MOPS; 75 mM $CaCl_2$; 10 mM $RbCl_2$; 15% v/v Glycerol; pH 6.5 using KOH (filter sterilize, store at +4°C)

2.2.2 Transformation of competent *E. coli*

Ligated DNA constructs were amplified by transformation into competent *E. coli* TOP10 cells. 1 μg of DNA was added to 100 μl of *E. coli* TOP10 cells and incubated on ice for 30 minutes. Bacteria were heat-shocked at 42°C for 42 seconds and then transferred into ice for two minutes. Next, the transformed bacteria were diluted in 900 μl of LB broth and incubated for 1 hour at 37°C in an orbital shaker. Cells were then centrifuged at 7000 rpm for 2 minutes and most of the supernatant was discarded. Transformed bacteria were resuspended in the remaining 100 μl

before seeding onto LB agar plates, supplemented with the appropriate antibiotic (kanamycin or ampicillin, both 50 μg/ml), and then left to grow overnight in an incubator at 37°C. The following morning, single colonies were picked using 10 μl sterile pipette tips and suspended in LB (supplemented with 50 μg/ml of the appropriate antibiotic). Cultures were incubated overnight in an orbital shaker at 37°C. Bacterial stocks were prepared by mixing 750 μl of culture with 250 μl of autoclaved, 100% glycerol, and stored at -80°C.

2.2.3 Recovery of DNA from bacterial culture

Purification of the DNA was performed using a HiSpeed Midi-prep kit (Qiagen). 100 ml of LB cultured broth was centrifuged at 3500 rpm for 15 minutes at 4°C. The supernatant was discarded and pellet resuspended in 4 ml of Buffer P1. Next 4 ml of Buffer P2 was added to this mixture. Bacterial cells were mixed in this lysis solution by inverting 4-6 times and incubated for 5 minutes at room temperature. Next, 4ml of pre-chilled Buffer P3 was added and mixed by inverting 4-6 times. The lysate was poured into a QIAfilter Cartridge and left to incubate for 10 minutes. During this time, one HiSpeed Midi Tip was equilibrated by the addition of 4 ml of Buffer QBT; the column was allowed to empty by gravity flow. By inserting a plunger into the QIAfilter Cartridge clear cell lysate was filtered into the equilibrated HiSpeed Midi Tip. Lysate was allowed to enter the resin by gravity flow. 2 washes of 10 ml of Buffer QC were applied, followed by DNA elution with 5 ml of Buffer QF. Obtained DNA was precipitated by adding 3.5 ml of isopropanol, mixed and incubated for 5 minutes at room temperature. DNA was next transferred to a QIAprecipitator module where it was washed with 2 ml of ethanol and dried by forcing air through the QIAprecipitator module. Finally, the DNA was eluted using 1 ml of TE Buffer.

2.2.4 Sequencing reactions

To check the sequence of the generated vectors BigDye® Direct Cycle Sequencing Kit was used. The reaction volume was 10 μl containing: 2 μl BigDye

solution, 200 ng DNA, 1 μl sequencing primer 1.6 μM, ddH_2O to adjust the volume. The thermal cycler programme used for sequencing was as follows: initial denaturation - 2 minutes at 96°C; followed by 25 cycles of: 30 seconds denaturation at 96°C, 15 seconds annealing at 50°C and 4 minutes extension at 60°C. Samples were analysed by the GenePool Sequencing Facility (The University of Edinburgh) and the chromatograms examined with the free software ApE (A Plasmid Editor).

2.2.5 Constructs used in this thesis

The GFP:GgCENP-A (Gg: Gallus gallus) construct was obtained by cloning GgCENP-A into the pEGFPC1 vector (Clontech) with the addition of a 17 amino acid linker (Ribeiro et al., 2009).

The Dronpa:GgCENP-A construct was obtained by swapping the GFP of the construct described above, with cDNA coding for Dronpa. This construct was a kind gift from Dr Jennifer Lippincott-Schwartz.

Human cDNA of CENP-Z (isoform b) was recombined, using the Gateway system into a pDEST3.2NGFP by Dr Laura Wood, and subsequently ligated into a TetR-EYFP vector (Bergmann et al., 2011) to perform tethering studies.

2.3 Biochemistry

2.3.1 Standard protein sample preparation

For all experiments the number of cells/ml was calculated and an equal number of cells across the samples was collected in falcon tubes and centrifuged at 1300 x g for 5 minutes. Cells were washed once in ice-cold 1X PBS before lysis in 1X SB **(Table 2.1)** supplemented with protease inhibitors (cOmplete EDTA-free, Roche). Lysates were sonicated to shear genomic DNA and then boiled for 5 minutes at 95°C before storage at -80°C.

2.3.2 Preparation of nuclei protein extracts

For all experiments, an equal number of cells across the samples were collected in falcon tubes and centrifuged at 1300 x g for 5 minutes. Cells were washed twice in ice-cold 1X PBS. The PBS was removed and cells were resuspended in cold hypotonic buffer (10 mM Hepes pH 7.5; 2 mM $MgCl_2$; 25 mM KCl; protease inhibitors; 1 mM DTT; 1 mM PMSF). 0.5% NP-40 was added to the cell suspension and mixed gently. Cell lysate was centrifuged at 1500 rpm for 7 minutes at 4°C. Carefully the supernatant was discarded and the pellet, which contains nuclei, was resuspended in buffer N (10 mM Hepes pH 7.5; 2 mM $MgCl_2$; 25 mM KCl; 250 mM Sucrose; protease inhibitors; 1 mM DTT; 1 mM PMSF). Nuclei were pelleted at 1500 rpm for 10 minutes at 4°C. Supernatant was discarded and pelleted nuclei resuspended in an appropriate volume of 1X sample buffer.

2.3.3 SDS-PAGE

Denaturing protein gel electrophoresis was carried out using the Tris-glycine buffer system previously described (Laemmli et al., 1978). Polyacrylamide gels were prepared from a 30% (v/v) acrylamide/bisacrylamide mixture (Severn Biotech). Gels were assembled in a vertical electrophoresis apparatus (BioRad). A 4X resolving gel solution containing 1.5 M Tris-HCl pH 8.8 was poured at the bottom of the apparatus. A 4X stacking gel solution containing 0.5 M Tris-HCl pH 6.8 was placed on top of the resolving gel. Samples were loaded on the gels and run for 90 minutes at 100 V. Next, the proteins were transferred to a nitrocellulose membrane (Amersham GE) at 250 mA constant for 2 hours or 30 mA constant overnight. Both electrophoresis and protein transfer were performed in a BioRad apparatus according to the manufacturer instructions and suitable buffers (Table 2.1).

2.3.4 Immunoblotting

Membranes were washed abundantly in ddH_2O and incubated in Ponceau Red **(Table 2.1)** to check for protein transfer. Following Ponceau destaining **(Table 2.1)**, membranes were blocked with 3% low fat milk in 0.05% PBS-Tween for 1 hour at room temperature on a rocking shaker. Blocking solution was removed and membranes incubated with primary antibody solution in 1% low fat milk in 0.05%

PBS-Tw for 2 hours at room temperature or overnight at 4°C on a rocking shaker. Conditions and specifications of the primary antibodies used for membrane immunoblotting in this thesis are indicated in **Table 2.3**. Membranes were washed three times in 0.05% PBS-Tw for five minutes on a rocking shaker. Solutions of the appropriate secondary antibodies were prepared in 1% low fat milk in 0.05% PBS-Tw. Conditions and specifications of the secondary antibodies used for membrane immunoblotting in this thesis are indicated in **Table 2.3**. Next, membranes were incubated 45 minutes at room temperature on a rocking shaker. Following generous washes with 0.05% PBS-Tw and lastly with 1X PBS only were applied to the membranes for 5 minutes each on a rocking shaker. Labelled proteins were detected using the Li-Cor Odyssey system.

2.3.5 Affinity purification of CENP-Z protein fragments for antigen production

Purification of human CENP-Z fragments from *E. coli* cells was done in collaboration with Dr Maria Alba Abad, who performed the initial cloning (pEC-K-GST-3C-CENPZ 79-153, pEC-K-His-3C-CENPZ 347-580) and supervised during initial steps of protein expression and purification.

2.3.5.1 GST 79-153 human CENP-Z

The expression of glutathione *S*-transferase (GST) tagged 79-153 human CENP-Z fragment was induced with IPTG (350 mM) in a 6 L culture of *E. coli* BL21 Gold competent cells overnight at 18°C. The next morning, cells were pelleted and resuspended in 100 ml of a lysis buffer containing 20 mM Tris pH 8, 400 mM NaCl, 2 mM dithiothreitol (DTT). Protease inhibitors (cOmplete EDTA-free, Roche), DNase (10 μg/ml, DN25, Sigma) and PMSF (1 mM) were added to the cell lysate. From here onwards everything was performed at +4°C or on ice. Next, sample was sonicated for 10 minutes (60% Amp pulse, 1 ON, 1 OFF). The lysate was clarified by spinning down at 22000 rpm for 50 minutes at (JLA rotor 25.50, Beckman ultracentrifuge). Both pellet and supernatant were kept and 1 μl of each sample was diluted in sample buffer and later loaded onto a polyacrylamide gel.

Table 2.3 - List of antibodies used in western blots

Antibody	Species	Source	Dilution	Comments
Primaries				
GFP	Rabbit	Life Technologies	1:1000	Overnight, +4°C
GgCENP-A	Rabbit	Fukagawa*	1:1000	Overnight, +4°C
GgCENP-I	Rabbit	Fukagawa*	1:500	Overnight, +4°C
GgCENP-H	Rabbit	Fukagawa*	1:500	Overnight, +4°C
GgCENP-O	Rabbit	Fukagawa*	1:500	Overnight, +4°C
GgCENP-S	Rabbit	Fukagawa*	1:500	Overnight, +4°C
α–tubulin (B512)	Mouse	Sigma	1:5000	1 hour, room temp
Abmart anti CENP-Z antibodies	Mouse	Abmart	1:200	2 hours, room temp
Rabbits pre-immune sera	Rabbit	Scottish National Blood Transfusion Service	1:100	2 hours, room temp
Secondaries				
IRDye 680 (red)	Donkey anti-Rabbit	Licor Biosciences	1:10,000	1 hour, room temp
IRDye 800 (green)	Donkey anti-Mouse		1:10,000	1 hour, room temp

*Tatsuo Fukagawa, National Institute of Genetics, Japan

During the centrifugation time, 15 ml of glutathione sepharose (GSH) beads (GE Healthcare), kept at +4°C, were washed twice in ddH_2O and equilibrated with 35 ml of lysis buffer. For each wash described, form here onwards, beads were resuspended in the indicated buffer and centrifuged. The supernatant was incubated with GSH beads for 3 hours. To remove proteins that could unspecifically bind to the GSH resin, beads were washed first with 350 ml of lysis buffer, next with 200 ml of high salt buffer (20 mM Tris pH 8, 1 M NaCl, 50 mM KCl, 10 mM MgCl, 2 mM ATP and 2 mM DTT) and lastly with cleavage buffer (20 mM Tris pH 8, 200 mM NaCl and 2 mM DTT). Cleavage was performed with the addition of protease 3C (1 mg/ml) in the cleavage buffer overnight. The next day, elutions from the beads were collected through centrifugation cycles into cleavage buffer. Elutions were next checked for protein concentration. A polyacrylamide gel, where samples obtained during the purification were run, is shown in Figure 5.4 C. The elutions containing the purified protein were pooled together and the sample was concentrated by using cellulose concentrators (Amicon concentrators 3 kDa, Millipore). The eluted and concentrated was aliquoted, snap-frozen and kept at -80°C.

2.3.5.2 His 347-580 human CENP-Z

The expression of poly-histidine (His) tagged 347-580 human CENP-Z fragment was induced with IPTG (350 mM) in a 3 L culture of *E. coli* BL21 Gold competent cells overnight at 18°C. The next morning, cells were pelleted and resuspended in 100 ml of a lysis buffer containing 20 mM Tris pH 8, 500 mM NaCl, 35 mM Imidazole and 2 mM β-mercaptoethanol. Protease inhibitors (cOmplete EDTA-free, Roche), DNase (10 μg/ml, DN25, Sigma) and PMSF (1 mM) were added to the cell lysate. From here onwards everything was performed at +4°C or on ice. Next, sample was sonicated for 10 minutes (60% Amp pulse, 1 ON, 1 OFF). The lysate was clarified by spining down at 22000 rpm for 50 minutes (JLA rotor 25.50, Beckman ultracentrifuge). Pellet and supernatant were kept and 1 μl of each sample was diluted in sample buffer and later loaded onto a polyacrylamide gel. A single 5 ml Ni-NTA HisTrap column (GE Healthcare) was washed with 50 ml of ddH_2O. The supernatant was loaded onto the pre-equilibrated column (flow speed 1 ml/minute). Flow-through was collected and 1 μl was diluted in sample buffer and later loaded

onto a polyacrylamide gel. The column was next washed with 350 ml of lysis buffer, followed by 250 ml wash of a high salt buffer (20 mM Tris pH 8, 1M NaCl, 50 mM KCl, 10 mM MgCl, 2 mM ATP, 35 mM Imidazole and 2 mM β-mercaptoethanol). Finally, His tagged protein elution was obtained by a 50 ml wash with elution buffer containing 20 mM Tris pH 8, 200 mM NaCl, 400 mM Imidazole and 2 mM β-mercaptoethanol. 10 elutions of 5 ml each were collected and checked for protein concentration. A polyacrylamide gel, where samples obtained during the purification were run, is shown in Figure 5.4 D. The elutions containing the purified protein were pooled together. Cleavage was performed overnight with the addition of protease 3C (1 mg/ml) to the elutions and dialysis (Spectra por 6-8 kDa cut-off) against 20 mM Tris pH 8, 500 mM NaCl, 2 mM DTT. The next morning, the sample was concentrated by using cellulose concentrators (Amicon concentrators 10 kDa, Millipore). The concentrated protein was aliquoted, snap-frozen and kept at -80°C.

2.3.6 Antigen preparation for antibody production

800 μg of purified 79-153 and 347-580 human CENP-Z fragments were loaded onto two 15% polyacrylamide gels. After the run, the gels were stained with Aqueous Blue Comassie (0.1% Comassie Brilliant Blue in 1X running buffer without SDS) for 2 hours at room temperature. Gels were de-stained using ddH_2O to allow the visualization of the bands. Images of the gels at this stage are shown in **Figure 5.4 E and F**. The bands excised using scalpels and frozen at -80°C overnight in a 50 ml falcon tube. This step is essential for the de-hydration of the bands. The next morning, a bucket was filled with dry ice and a pestle and mortar were left to cool down. Gel bands were processed one by one. After taking one band out of the -80°C freezer it was easily scraped off the falcon tube from frozen and it was possible to avoid frozen water. The band was placed in the mortar and liquid nitrogen was poured and left to evaporate. This step was repeated two times more. The band was ground to fine powder by using a pestle **(Figure 2.1 B)**. Liquid nitrogen was applied during the grinding to maintain the sample cold **(Figure 2.1 A)**. When the powder was fine enough to pass through a 25 G needle (needle size used for animal immunization) then the material was resuspended in 800 μl of sterile D-PBS (Gibco)

aliquoted into 400 µl for the first injection and two busters of 200 µl each. This procedure was performed for both the antigens. Aliquots were snap frozen, kept at -80°C and delivered at the Scottish National Blood Transfusion Service (Pentlands Science Park, Penicuik).

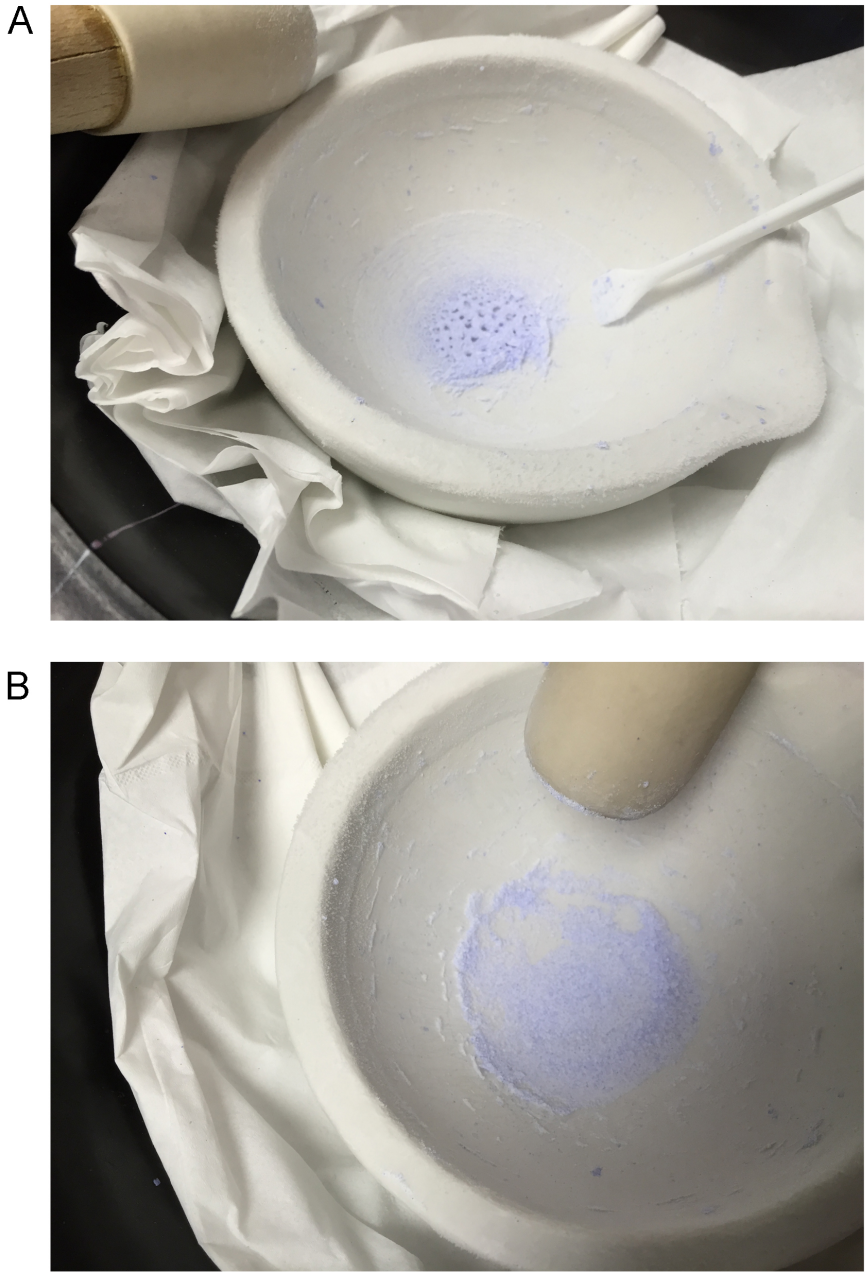

Figure 2.1. Antigen preparation for rabbit immunisation. A. Grounded gel band after boiling in liquid nitrogen. **B.** Gel band ground to a fine powder.

2.4 Cell Culture

2.4.1 Cell lines used and growth conditions

HeLa Kyoto cells were grown in Dulbecco's modified essential media (DMEM, Gibco) supplemented with 10% foetal bovine serum (FBS; Biosera) and 1% Penicillin/Streptomycin (Gibco) at 37°C in 5% CO_2. For experiments that required enrichment in mitotic cells, nocodazole was added in the media (100 ng/ml) overnight.

HeLa 3-8 cells were grown in DMEM (Gibco) supplemented with 10% foetal bovine serum (FBS; Biosera) and 1% Penicillin/Streptomycin (Gibco) at 37°C in 5% CO_2. Cells were grown in constant geneticin selection (400 μg/ml) to enrich for cells containing an integrated TetO array at a chromosome arm.

1C7 cells were grown in DMEM (Gibco) supplemented with 10% foetal bovine serum (FBS; Biosera) and 1% Penicillin/Streptomycin (Gibco) at 37°C in 5% CO_2. Cells were grown in constant blasticidine selection (4 μg/ml) to maintain in culture only cells containing the Human Artificial Chromosome (HAC).

Chicken DT40 cell lines were grown in RPMI 1640 (Gibco) supplemented with 10% foetal bovine serum (FBS; Biosera), 1% chicken serum (Gibco) and 1% Penicillin/Streptomycin (Gibco) at 39°C in 5% CO_2. To deplete proteins, conditional knockout cell lines were treated with doxycycline (BD Biosciences) (500 ng/ml), added directly to the culture media (CENP-C KO and CENP-H KO, 36 hours treatment; CENP-I KO, 24 hours treatment). A high enrichment in mitotic cells (>90 %) was obtained after 12-13 hours of nocodazole treatment (500 ng/ml).

2.4.2 Transient transfection in human cell lines

HeLa Kyoto/HeLa 3-8/1C7 cells were seeded in 12-well dishes on coverslips and grown up to 50% confluency. On the day of the transfection 50 μl of Optimem (Gibco) were mixed by vortex with 1.5 μl of GeneJuice® (Novagen) transfection reagent in a 1.5 ml tube. The mixture was incubated for five minutes at room temperature. Next, 0.5 μg of DNA was added and gently mixed by pipetting. The

DNA mix was incubated for 15 minutes at room temperature. Next, the transfection mix was added to the cells in a drop wise manner. Typically, cells were fixed after 24 or 48 hours. Reagents and DNA amount were scaled up or down depending on the total surface of the culture dish.

2.4.3 RNA interference in human cells

HeLa Kyoto were seeded in 12-well dishes on coverslips and grown up to 50% confluency. On the day of the transfection siRNA oligos **(Table 2.4)** were diluted at concentration of 50 nM in Jet Prime buffer (Polyplus trasfection$_{TM}$) in one 1.5 ml tube and vortexed for 10 seconds. 6 μl of Jet Prime reagent was added to the mixture, vortexed for 10 seconds, spun down and incubated for 10 minutes at room temperature. At the end of the incubation time the transfection mix was supplied to the cells in a drop wise manner. Typically, cells were fixed after 48 hours. Reagents and siRNA amount were scaled up or down depending on the total surface of the culture dish.

Table 2.4 – RNAi oligos target DNA sequences

Name	Target DNA sequence 5'-3'
CENP-Z oligo 0	GCTTCCTGTCTCCTGGGTCGT
CENP-Z oligo 1	CAGGTTAGAAGACATACAGAA
CENP-Z oligo 2	GACGTCTTGAGTGAAGATGAA
CENP-Z oligo 3	CAGGTCGGGCTTCCCACCTCA
CENP-Z oligo 4	CACCATCTACAAGTGTCCTTA

2.4.4 Generation of chicken DT40 stable cell lines

Parental (Clone 18), knockout (KO) and deletion cell lines (Δ) stably expressing GFP:CENP-A or Dronpa:CENP-A were obtained by electroporation of the DNA construct (see section **2.2.5**). Between 1 and 2 x 10^7 cells/ml were collected by centrifugation and washed twice in cold Optimem (Gibco). After the last wash,

cells were re-suspended in 1 ml of cold Optimem. Half of the cell suspension was placed in one cuvette compatible with the Gene Pulser Xcell Electroporation System (BioRad). Between 10 and 12 μg of DNA was added to the same cuvette and incubated on ice for 5-10 min both before and after the electric pulse (300 V, 950 μF). Finally, the electroporated cells were seeded and left growing in completed media (without antibiotics selection) overnight. The following day, cells were diluted and aliquoted in 4 x 96-well plates containing media supplemented with antibiotics to select for successfully stably transfected cells. Antibiotic selection of stable cells usually takes 7-14 days.

Table 2.5. DT40 cell lines generated.

Cell line	Parental cell line*	cDNA stably expressed	Antibiotic resistance
CENP-C KO Dronpa:CENP-A	CENP-C KO	Dronpa:CENP-A	Geneticin (1.5 mg/ml)
CENP-S Δ Dronpa:CENP-A	CENP-S Δ	Dronpa:CENP-A	Geneticin (1.5 mg/ml)
CENP-S Δ GFP:CENP-A	CENP-S Δ	GFP:CENP-A	Geneticin (1.5 mg/ml)
Clone 18 GFP:CENP-A	Clone 18	GFP:CENP-A	Geneticin (1.5 mg/ml)
CENP-I KO GFP:CENP-A	CENP-I KO	GFP:CENP-A	Hygromycin (2.5 mg/ml)
CENP-O Δ GFP:CENP-A	CENP-O Δ	GFP:CENP-A	Hygromycin (2.5 mg/ml)

*Parental cell lines are a kind gift from Tatsuo Fukagawa

Potential stable clones positive for GFP or Dronpa were screened using a flow cytometer **(Figure 2.2)**. For CENP-I KO GFP:CENP-A and CENP-O Δ GFP:CENP-A, as only few clones grew following antibiotic selection, screening for the presence of GFP:CENP-A (green) was performed by fluorescence microscopy. For images of the chosen clones please refer to **Figure 4.9**.

Figure 2.2. Flow cytometer profiles of GFP:CENP-A or Dronpa:CENP-A generated cell lines. Clones obtained after antibiotics selection were screened for the presence of green fluorescence using a flow cytometer. Final clones were chosen by gating the alive cells (using forward scatter (FSC) and side scatter (SSC)) and measuring the amount of green fluorescence (FLH-1 channel) only in the gated region. **A.** A parental cell lines (Clone 18) and one GFP positive cell line are shown for direct comparison with the selected clones. **B.** A parental cell line (Clone 18) and one Dronpa positive cell line are shown for direct comparison with the selected clones.

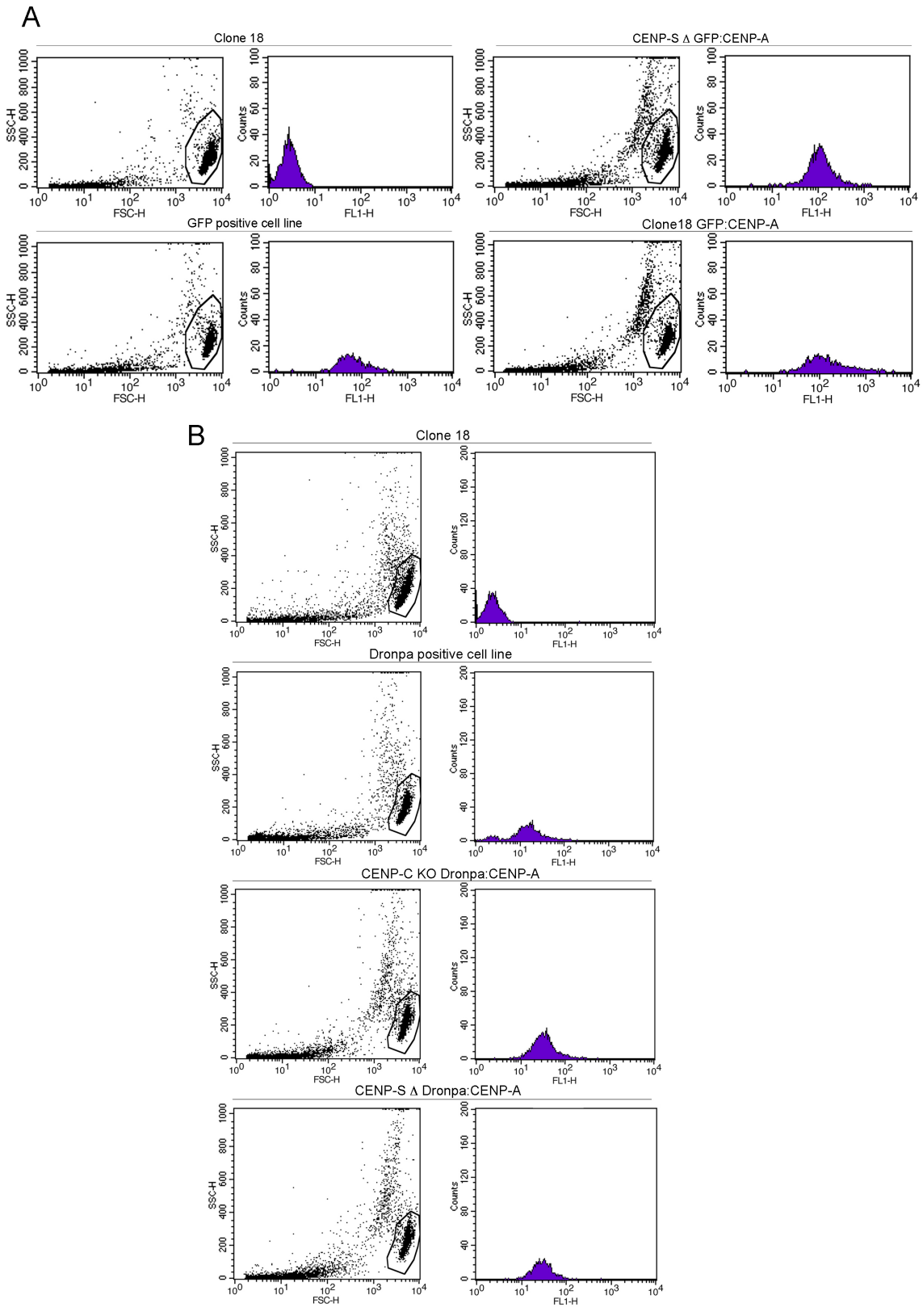
A
Clone 18
CENP-S Δ GFP:CENP-A
GFP positive cell line
Clone18 GFP:CENP-A
B
Clone 18
Dronpa positive cell line
CENP-C KO Dronpa:CENP-A
CENP-S Δ Dronpa:CENP-A
SSC-H
FSC-H
Counts
FL1-H

2.4.5 Cell vital counts using Trypan Blue

DT40 cells were maintained at a concentration of 20 X 10^4 cells/ml at every dilution time. For cell counts experiments, 1 part of Trypan Blue was mixed with 1 part of cell suspension at room temperature. Trypan Blue is a colorant able to penetrate the cell membrane of dead cells while living cells would remain transparent. 10 μl of cell suspension were used to count living cells using a haemocytometer.

2.5 Fixation procedures for microscopy

In order to perform any fluorescence microscopy experiment, DT40 cells were seeded onto Concanavaline A (Calbiochem) (ConA) coated coverslips and left to adhere for two to three hours at 39°C prior to fixation. HeLa and 1C7 cells were seeded onto uncoated coverslips and allowed to grow for one day prior to fixation. ConA coated coverslips were obtained by dipping coverslips into 0.5 mg/ml ConA solution, washed with ddH_2O and allowed to dry underneath UV light.

2.5.1 Paraformaldehyde fixation

Cell media was discarded and coverslips were washed with pre-warmed 1X PBS. Next, cells were fixed with pre-warmed 4% PFA (16% Formaldehyde (w/v) methanol-free, Thermo Fisher Scientific) diluted in 1X PBS for 10 minutes. Afterwards, coverslips were abundantly washed in 1X PBS to remove any trace of paraformaldehyde. Permeabilization was carried out by applying 0.3% TritonX-100 (BioRad) diluted in 1X PBS for 5 minutes. Cells were abundantly washed in 1X PBS prior to blocking.

2.5.2 Methanol fixation

Cell media was discarded and coverslips were washed with pre-warmed 1X PBS. Next, cells were fixed and permeabilized using glacial methanol (VWR) for 10

minutes at -20°C. Before proceeding with the blocking step, coverslips were abundantly washed in 1X PBS.

2.5.3 Preparation of chromatin fibers in DT40 cells using TEEN buffer

Cells were seeded onto ConA coated coverslips and left to adhere for two to three hours at 39°C. Next, the media was discarded and cells washed with warm D-PBS without calcium and magnesium (Gibco). To obtain chromatin fibers, hypotonic TEEN solution **(Table 2.1)** was used to swell the cells. Additionally, because of the presence of EDTA, cations are sequestered causing repulsive forces amongst the negative charges present on the DNA and triggering the release of the DNA into thin chromatin fibers. To uniformly stretch fibers in one direction coverslips were maintained in a vertical position in coplin jars for 30 minutes at RT. Coverslips were then quickly dried by placing 3MM filter paper at the bottom edge of each coverslip before being immersed into 4% PFA (16% Formaldehyde (w/v) methanol-free, Thermo Fisher Scientific) diluted in TEEN solution for 10 minutes at room temperature. Coverslips were washed several times in D-PBS. Finally, DNA was stained with Hoechst (2 μg/ml) for 5 minutes at room temperature in the dark. Coverslips were mounted onto slides using Vectashield (Vector) mounting media and sealed with nail varnish. Imaging was performed using a 100X NA 1.4 Plan Apochromat lens, achieving a pixel size of 63 nm. The objective was mounted on a DeltaVision microscope (Applied Precision).

2.5.4 Preparation of chromatin fibers in 1C7 cells

1C7 cells blocked in mitosis following colcemid treatment (KaryoMAX®, Gibco, 100 ng/ml), were detached by mitotic shake off and washed in 1X PBS. The cell pellet was washed in 1X PBS and resuspended at the concentration of 10 X 10^4 cells/ml in 75 mM KCl for 10 minutes at 37°C. 100 μl of cell suspension was used per cytofunnel. Cytofunnels were placed into a Shandon CytoSpin 3 (Thermo Scientific) and mitotic cells were centrifuged directly onto poly-lysine coated slides (POLYSINE^{TM} glass slides, VWR). The centrifugation was performed at 500 rpm

for 10 minutes at room temperature. Slides were successively immersed into a chromatin lysis buffer (2.5 mM Tri-HCl pH 7.4; 0.5 M NaCl; 1% TritonX-100; 0.4 M Urea) for 15 minutes. The slides were then immersed in 4% PFA (16% Formaldehyde (w/v) methanol-free, Thermo Fisher Scientific) diluted in 1X PBS for 10 minutes. Samples were abundantly washed in 1X PBS and permeabilized in 0.1% TritonX-100 in 1X PBS for 7 minutes. Samples were washed at least three times in 1X PBS, and 3% BSA (30% BSA solution, Sigma) diluted in 1X PBS was used as blocking solution. The protocol was completed as a standard indirect immunofluorescence. All incubations in this protocol were performed at room temperature. See section **2.6.2** for TetR-EYFP purified protein *in-situ* labelling.

2.5.5 Chromosome spreads in 1C7

1C7 cells blocked in mitosis following colcemid treatment (KaryoMAX®, Gibco, 100 ng/ml), were detached by mitotic shake off and washed in 1X PBS. The cell pellet was washed in 1X PBS and resuspended at the concentration of 10 X 10^4 cells/ml in 75 mM KCl for 10 minutes at 37°C. 100 µl of cell suspension was used per cytofunnel. Cytofunnels were placed into a Shandon CytoSpin 3 (Thermo Scientific) and mitotic cells were centrifuged directly onto poly-lysine coated slides (POLYSINE^{TM} glass slides, VWR). The centrifugation was performed at 1800 rpm for 10 minutes at room temperature. Slides were successively immersed into a KCM buffer (10 mM Tris-HCl pH 8; 120 mM KCl; 20 mM NaCl; 0.5 mM EDTA; 0.1% v/v TritonX-100) for 10 minutes. Slides were next blocked in 3% BSA diluted in KCM for 30 minutes at 4°C. Next, slides were incubated with primary antibodies diluted in 1% BSA in KCM for 1 hour at 4°C. Slides were washed twice in KCM buffer. Next, slides were incubated with secondary antibodies diluted in 1% BSA in KCM for 1 hour at 4°C. Slides were washed twice in KCM buffer. Afterwards, slides were washed abundantly in 1X PBS and incubated with TetR-EYFP purified protein (**2.6.2**). After this, samples were fixed in 4% PFA (16% Formaldehyde (w/v) methanol-free, Thermo Fisher Scientific) diluted in KCM for 10 minutes and then DNA stained with Hoechst. Coverslips were mounted on top of slides using Vectashield mounting media (Vector) and sealed with nail vanish.

2.6 Indirect immunofluorescence

2.6.1 Standard procedure for indirect immunofluorescence

After fixation, cells were blocked in 3% BSA (30% BSA solution, Sigma) diluted in 1X PBS. Cells were then incubated for one hour at 37°C with the appropriate primary antibodies, diluted in 1% BSA (30% BSA solution, Sigma) and PBS. Primary antibodies used in this thesis are listed in **Table 2.6** where details about the source, host species and dilution used are given. Coverslips were then washed three times with 0.1% PBS-Tw for 5 minutes per wash. Next, coverslips were incubated with secondary antibodies diluted in 1% BSA (30% BSA solution, Sigma) in PBS, for 1 hour at room temperature, unless otherwise stated. A list of the secondary antibodies used in this thesis is provided in **Table 2.6**. Next, coverslips were washed three times with 0.1% PBS-Tw for 5 minutes per wash, followed by another three washes with 1X PBS, 5 minutes per wash. Coverslips were mounted on top of slides using Vectashield mounting media containing DAPI (Vector) and sealed with nail vanish.

2.6.2 Protocol for TetR *in situ* labelling

Incubation with purified TetR-EYFP was performed following secondary antibodies incubations. Samples were abundantly washed with 1X PBS in order to completely remove the Tween used in previous washes. TetR-EYFP was used at 1:100 and diluted in 1% BSA (30% BSA solution, Sigma) in PBS. Incubation lasted 1 hour at room temperature and was followed by 1X PBS 5 minutes washes. Coverslips were mounted on top of slides using Vectashield mounting media containing DAPI (Vector) and sealed with nail vanish.

Table 2.6 - List of antibodies used in indirect immunofluorescence

Antibody	Species	Source	Dilution	Comments
Primaries				
GgCENP-T	Rabbit	Fukagawa*	1:1000	1 hour, room temp
GgCENP-R	Rabbit	Fukagawa*	1:100	1 hour, room temp
GgCENP-O	Rabbit	Fukagawa*	1:100	1 hour, room temp
GgCENP-S	Rabbit	Fukagawa*	1:100	1 hour, room temp
α–tubulin (B512)	Mouse	Sigma	1:1000	1 hour, room temp
RNA polII $Ser2^{p}$	Mouse	AbCam	1:1000	1 hour, room temp
H4K20me (15F11)	Mouse	Kimura**	1:300	1 hour, room temp
HsCENP-A (A1)	Mouse	Masumoto***	1:500	1 hour, room temp
HsCENP-C (554)	Rabbit	Earnshaw lab	1:500	1 hour, room temp
ACA	Human	Earnshaw lab	1:200	1 hour, room temp
H3K4me2	Rabbit	Upstate	1:200	2 hours, room temp
H3K9me3	Rabbit	Upstate	1:250	1 hour, room temp
Secondaries				
Alexa Fluor 594	Donkey anti-Rabbit	Jackson ImmunoResearch Laboratories	1:1000	45 minutes, at room temperature
Alexa Fluor 647	Donkey anti-Mouse		1:250	
Alexa Fluor 488	Donkey anti-Mouse		1:500	
Alexa Fluor 647	Donkey anti-Human		1:200	

*Tatsuo Fukagawa, National Institute of Genetics, Japan

**Hiroshi Kimura, Osaka University, Japan

***Hiroshi Masumoto, Kazusa DNA Research Institute, Japan

2.7 Super-resolution microscopy with single-molecule sensitivity: sample preparation and imaging

DT40 cells stably expressing Dronpa:CENP-A were seeded onto ConA coated coverslips, thickness n° 1.5 (VWR), and processed to obtain chromatin fibers as previously described (**2.5.3**). After fixation, samples were blocked in 3% BSA (30% BSA solution, Sigma) diluted in 1X PBS. Primary antibodies were diluted in 1% BSA (30% BSA solution, Sigma) in PBS and used at the concentrations indicated in **Table 2.6**. Washes between primary and secondary antibodies were performed with 0.1% PBS-Tw as described (**2.6.1**). Primary antibodies were detected using Alexa Fluor 647 conjugated secondary antibody, used at a dilution of 1:20,000 and incubated for 1 hour at room temperature. Three washes with 0.1% PBS-Tw, of five minutes each, were performed. Following the immuno-staining, coverslips were inserted into imaging chambers (Grace Bio Labs) containing 'switching buffer': 0.5 mg/ml glycose oxidase, 40 μg/ml catalase, 10% w/v glucose (Fisher Scientific), in D-PBS pH 7.4 (Heilemann et al., 2008). The switching buffer allows blinking of Alexa Fluor 647 conjugated secondary antibody when exposed to a far-red wave length laser (633 nm) and, in addition, it reduces photo-bleaching of the sample. The presence of the switching buffer does not affect the blinking properties of protein Dronpa that passes from a bright state into a dark state as a consequence of irradiation with lasers of different wave length (405 nm and 488 nm respectively).

The imaging chambers used are designed to fit a specially adapted, anti-drift, microscope stage. The samples were analysed using a 60X TIRF oil-immersed objective (Nikon), NA 1.49, achieving a pixel size of 74 nm. The objective was mounted on a Nikon Eclipse TE2000 inverted microscope. Movies were captured using an Andor Luca S electron-multiplying CCD camera. 500 frames were collected for each sample and saved as .sif files. The acquisition of green and red signals were separated and therefore two .sif files were generated for each fiber. In order to correct for photo-chromatic shift aberrations multi-fluorescent Tetra Speck microspheres (Invitrogen) were used and imaged in one single frame at 488 and 633 nm wave lengths.

2.8 Bio-informatics and data analyses

2.8.1 CENP-Z protein sequence analysis

Human CENP-Z (ZNF276) protein sequence was found in NCBI (gene ID: 92822) and in Uniprot (Q8N554). This sequence was next imported into Jalview (Waterhouse et al., 2009). In addition, sequences of MmCENP-Z, GgCENP-Z and XlCENP-Z were also imported and conserved residues highlighted in different shades of blue **(Figure 5.1 A)**.

Human CENP-Z protein secondary structure was obtained using Psi-pred (Jones, 1999), a platform for secondary structure prediction. Here, CENP-Z sequence was submitted and results were received within a few hours **(Figure 5.1 B)**.

Human CENP-Z protein domain in-depth analysis was performed using PHYRE2 protein folding recognition server (Kelley et al., 2015). CENP-Z protein sequence was imported into PHYRE2 server and here different domains recognised in the sequence were identified and their folding predicted. In addition, a comparison of known structures, with similar folding, was performed and results indicated the percentage of identity between CENP-Z sequence and the known protein and the percentage of confidence for the prediction **(**see section **5.2.1** and **Figure 5.1 B)**.

2.8.2 PALM data analysis

Sif files (.sif), each containing 500 frames of data per sample, were imported into Igor Pro (WaveMetrics). The software provides the user with an interface where it is possible to make adjustments for the standard deviation of the point spread function (PSF) of the objects imaged and to adjust the GLRT-based (generalized likelihood ratio test) sensitivity, allowing the user to visualize which particles are detected in the specimen (yellow circles) **(Figure 2.3 A)**. At this point, the analysis was launched and particle positions identified. The results of particle position identification can be visualised as a 2D scatter plot where a coloured coded percentage of the number of fluorescent signals, detected in a particular position, is shown **(Figure 2.3 B)**. Positions of the detected signals are organised as a set of coordinates in X and Y. This set of coordinates can be accessed in Igor Pro and

copied and pasted into a GraphPad Prism (GraphPad Software, Inc) spread sheet. Here coordinates are plotted into a graph and corrected for the photo-chromatic shift aberrations measured between green and red channel using multi-fluorescent Tetra Speck microspheres (Invitrogen), by subtracting a delta distance. A representative graph produced in GraphPad is shown in **Figure 2.4 A**, left panel.

For this analysis it is essential to minimise, if not eliminate, all sample drifting, as this would impair the accuracy of localization measurements within the specimen. Therefore, the acquisition system used was tested for sample drifting by measuring signals of multi-fluorescent Tetra Speck microspheres in unperturbed or perturbed conditions **(Figure 2.4 B)**. Unperturbed conditions are the standard conditions for data acquisition used for this type of experiment. Perturbed conditions were obtained by gently tapping on the microscope stage during the acquisition. If the sample moves during data acquisition (perturbed stage) a smear of colour is observed in the 2D scatter plot indicating a shift in the position of the same molecule **(Figure 2.4 B)**. In contrast, acquiring signals following the standard procedure (unperturbed stage) did not show drifting of the Tetra Speck beads. It can be seen from a representative 2D scatter plot derived from a cellular sample **(Figure 2.4 A**, right panel**)** that measurements performed according to standard conditions are accurate, as no drifting in the samples was detected.

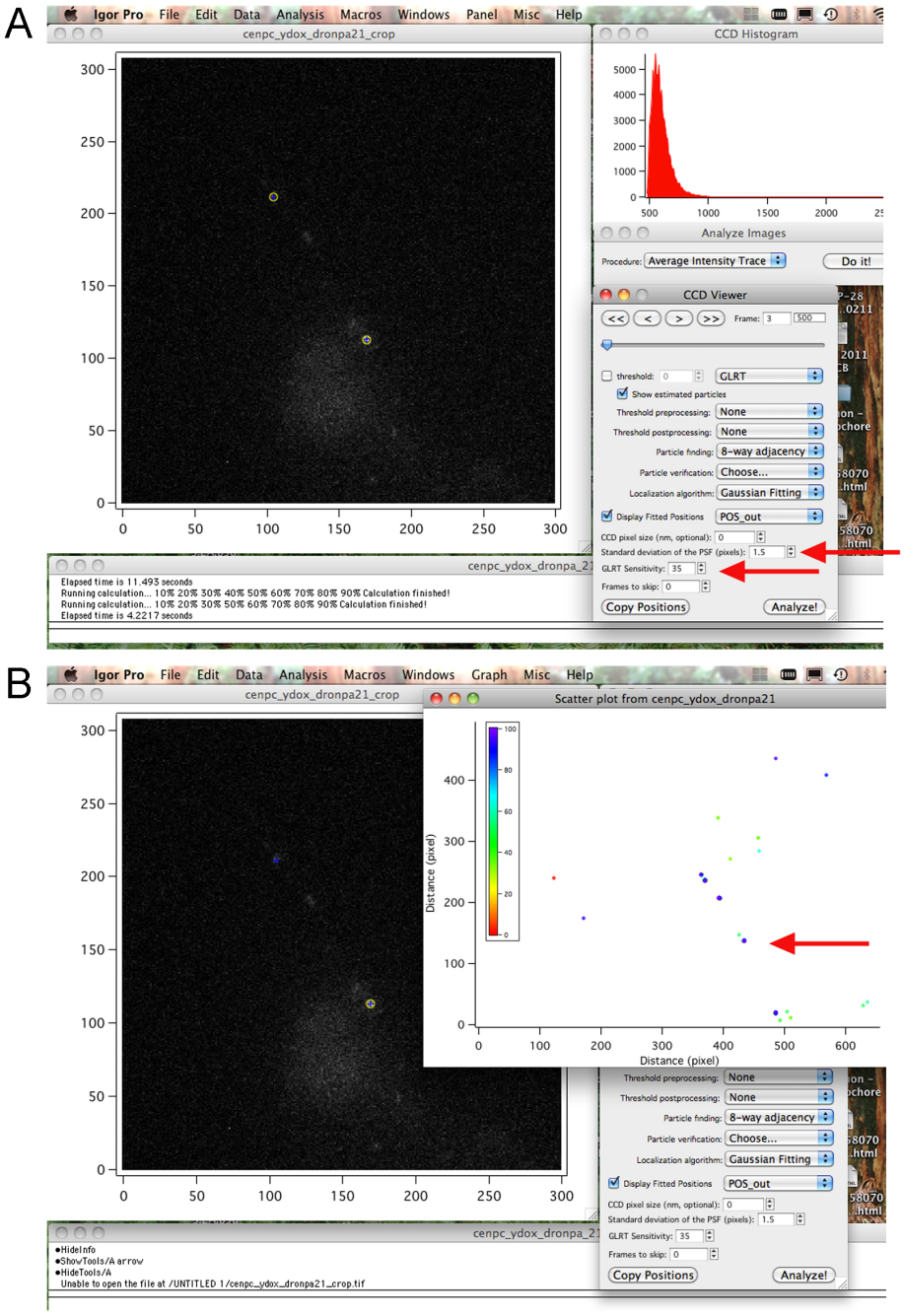

Figure 2.3. Analysis of PALM data using Igor Pro. Screen-shots of the Igor Pro workflow during analysis of PALM data. **A.** Red arrows indicate the parameters (standard deviation of the PSF; GLRT sensitivity) adjusted during the analysis. In accordance with these settings yellow circles are present around signals identified in the frame shown. **B.** The positions of the signals were mapped onto a 2D scatter plot (red arrow). In addition, a heat-map gradient showing the presence of re-occurring signals is also shown.

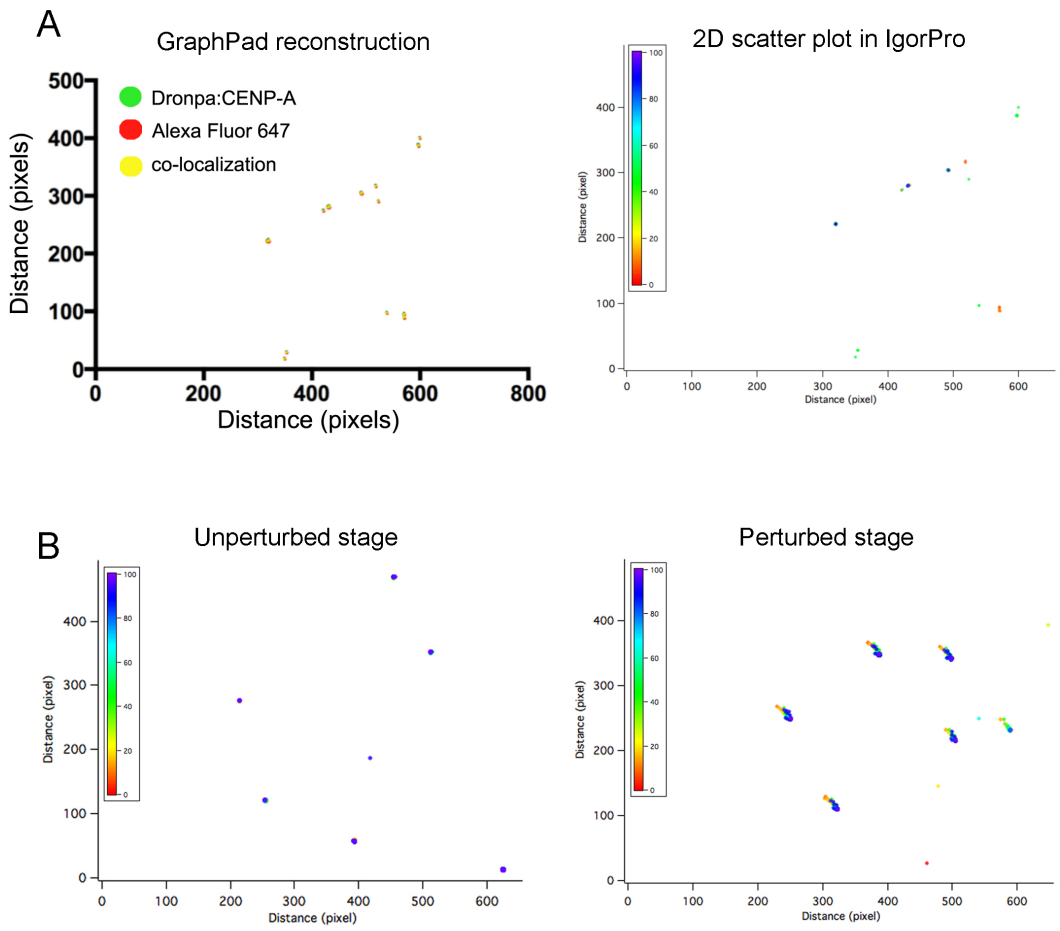

Figure 2.4. Assessing for molecule drifting in the PALM acquisition set-up used. A. Left panel: a chromatin fiber where the reconstructed positions of Dronpa:CENP-A and Alexa Fluor 647 conjugated secondary antibody directed against CENP-R are shown. In the right panel, the same biological sample is visualized after performing particle localization analysis in IgorPro as a 2D scatter plot, showing absence of fluorescent particles drifting. **B.** Tetra Speck spheres signals acquired in unperturbed or perturbed conditions. **A** and **B** the size of one pixel is 74 nm.

2.8.3 Igor Pro and multi-peak analysis of stretched centromere fibers data-sets

Fiber unfolding measurements were imported into Igor Pro **(Figure 2.5, 1)** where the data were divided into an appropriate number of histogram bins (see sections **4.2.2** and **4.2.4**). The multi-peak fitting 2 package was used for peak identification. Here, the software allows the user to adjust parameters such as noise level, smooth fraction and minimal fraction in order to identify the peaks **(Figure 2.5, 2)**. All parameters within specific ranges were kept constant across all samples: noise level 0.00005-0.06; smooth fraction 0.05-2.5; minimal fraction 0.035-0.5. At this point the software predicts whether the peaks identified are Gaussian, Lorentzian or Voigt. Once the peaks have been identified, the multi-peak fitting **(Figure 2.5, 3)** and results were summarized into a table containing information about peak location, area, type and amplitude **(Figure 2.5, 4)**. Also, a line of best fit is shown in the graphs containing data represented as histograms. Parameters such as chi-squired value and residuals were also returned in order to assess the reliability of the analysis. A detailed discussion of such parameters will be presented in the discussion of Chapter 4.

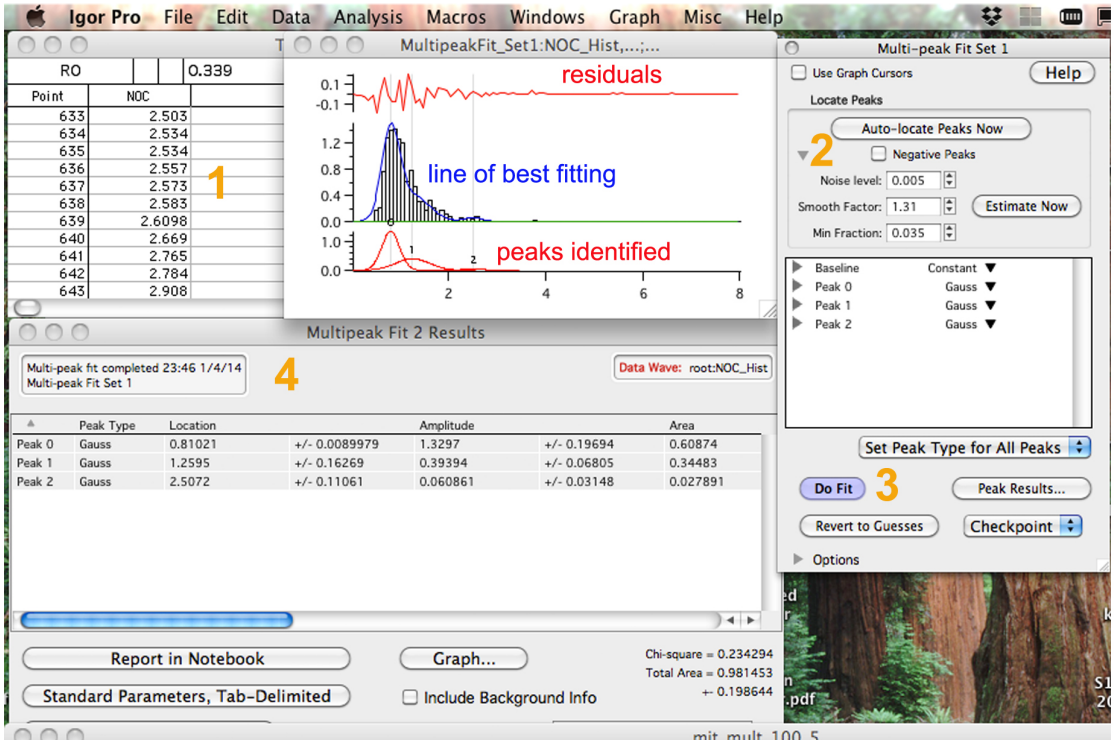

Figure 2.5. Performing multi-peak analysis using Igor Pro. Representative screen-shot image of Igor Pro while performing multi-peak analysis. Data is copied into a spread sheet (1) and divided into an appropriate number of histogram bins. Next, multi-peak fitting 2 package is opened and parameters adjusted for peak identification (2). By pressing on the 'Do Fit' button (3) the fitting runs and results are organised into a table (4).

2.9 Electron microscopy

Electron microscopy of chicken DNA fibers unfolded using TEEN buffer was performed in collaboration with Dr Daniel Booth.

2.9.1 Sample preparation

DT40 cells expressing GFP:CENPA were seeded onto poly-l-lysine coated gridded dishes (MatTeK), and left to adhere for 30 minutes. Fibers were prepared as described in **2.5.3** up until the point of fixation.

2.9.2 CLEM processing

Fibers were fixed for 1 hour with 3% glutaraldehyde and 0.5% paraformaldehyde in 0.2 M cacodylate buffer containing 5 μg/mL Hoechst. Cells were washed with 1X PBS (3 washes of 5 minutes) and the last PBS wash was left on. Unfolded fibers were identified using a wide field fluorescence DeltaVision microscope (Applied Precision) where GFP tagged CENP-A highlighted centromeres on DNA fibers visualized by Hoechst staining. Transmitted light was used to map cell positions via etched coordinates. The reference images allowed for the correlative re-identification of cells of interest by electron microscopy. DeltaVision acquisition was followed by treatment with tannic acid (0.1% in water) for 20 minutes, followed by osmication (1% osmium tetroxide in PBS) for 1 hour. Samples were then washed with PBS (3 washes of 5 minutes), ddH2O (2 washes of 20 minutes) and 30% ethanol (1 wash of 10 minutes) before the incubation in uranyl acetate (0.5% in 30% ethanol) for 1 hour. Next, cells were dehydrated using a graded series of ethanol washes followed by 2 washes of 10 minutes with 100% ethanol. Following dehydration, cells were infiltrated with ethonal:resin mixtures (2:1 and 1:1) for 20 minutes each. Finally, cells were embedded in 100% resin (TAAB), with a gelatin capsule of resin covering the cells of interest, before curing at 60 °C for 3 days. Polymerised resin blocks were sectioned and post stained as routine. Samples were viewed using a Phillips CM120 BioTwin transmission electron microscope (FEI) and micrographs acquired using a Gatan Orius CCD camera (Gatan).

3 Chapter 3: DNA unfolding: a high resolution tool to resolve protein localization onto chromatin

3.1 Introduction

Since 1839, it has been possible to visualize and study individual cells by microscopy (Schwann, 2013). With advances in technology, not only cells but also subcellular components have been detected and therefore further studied (Verdaasdonk et al., 2014). One obstacle that cell biology and imaging technologies are trying to overcome is how to assess whether two proteins truly co-localize. To overcome this, three issues need to be addressed: 1) diffraction limit of the optics in use; 2) resolving complex structures (i.e. compact globular structures); 3) development of a computational system for data analysis (i.e. choice of suitable software).

The purpose of this Ph.D. project was to study the ultrastructure of the kinetochore, taking advantage of the most suitable microscopy procedures. Before this could be achieved the best method for data acquisition, given the time and equipment available, needed to be explored. Therefore two diverse approaches have been attempted: conventional wide-field light microscopy and super-resolution light microscopy.

Conventional light microscopy exploits the properties of fluorescent molecules, where a typical standardized wide-field system can achieve a maximum resolution of ~ 250 nm; therefore any structures or distances smaller than 250 nm cannot be accurately measured. More recently, new microscopy techniques have been developed which are grouped into the category of "super-resolution" microscopy (Flors and Earnshaw, 2011; Schermelleh et al., 2010). Here the illumination coupled with improved, genetically engineered, fluorescent molecules, reduces the resolution limit from 250 nm to 100 or 30 nm in x and y, depending on the specific technique used (Betzig et al., 2006; Dickson et al., 1997; Hell and Wichmann, 1994). Unfortunately, a caveat with such high resolution equipment is that these systems are often not suitable for high throughput screenings as the

acquisition time can be long and thus acquisition of an appropriate N number for statistical purposes is extremely time consuming.

The focus of this study is to analyse centromere chromatin, wrapped into the kinetochore, which has a compact structure. Therefore, both high resolution imaging and large sample size for statistical analyses were essential. An indirect solution would be to modify the centromere chromatin structure in order to increase its dimensions so that even conventional microscopy would be useful on such samples. One way to do this is to extend the chromatin into what are known as DNA fibers.

In this chapter developing protocols for fiber stretching preparation, on both human and chicken cells, will be presented. The development of such protocols was essential for carrying out further studies on the kinetochore ultrastructure. The second part of this chapter describes both internal and external collaborations where I applied my optimised protocols to answer biological questions, whilst also becaming proficient at localizing proteins or histone modifications on stretched kinetochore chromatin fibers. Here, I used conventional wide-field microscopy or Photo-Activation Localization Microscopy, PALM. The technical experience gained by performing these techniques was essential for addressing my core research questions in later chapters.

3.2 Results

3.2.1 Optimizating the preparation of stretched centromere DNA fibers

Independently from the microscopy method used, the generation of stretched chromatin fibers was an important prerequisite for my project to achieve the maximal resolution possible (Weier, 2001). Therefore protocols for the preparation of chromatin fibers were optimised in cell types commonly used in the laboratory.

DT40 cells are a commonly used cell line in many laboratories. DT40 cells are a chicken B-lymphoma cell line that shows several advantages, such as high homologous recombination efficiency and rapid doubling time (9-10 hours). DT40 cells also have a highly stable karyotype (Takata et al., 1998).

As a preliminary test, control DT40 cells (clone 18) stably expressing GFP:CENP-A (**2.4.4**) were used for a quick identification of the centromere region. To test that GFP:CENP-A localised to centromeres, cells left to adhere on conA coated coverslips, were fixed in 4% PFA and DNA counterstained with DAPI. Representative images were acquired showing that GFP:CENP-A localised, as expected, in focused GFP spots on centromeres in mitotic chromosomes, and showed the typical centromere localization in interphase **(Figure 3.1 A)**. Next, my aim was to perform high-resolution studies by stretching kinetochore fibers. To stretch chromatin in DT40 cells TEEN buffer was used (10 mM Triethanolamine:HCl pH 8.0, 10 mM NaCl, 5 mM EDTA) as previously described (Earnshaw and Laemmli, 1983; Hudson et al., 2003). TEEN buffer contains EDTA that functions as a divalent cation chelator and has a low salt concentration, creating a hypotonic environment. Osmotic pressure together with the excess of negative charges triggers cell lysis and ultimately causes the chromatin to unfold **(Figure 3.1 B)**. This protocol was tested in samples as follows: cells were left to adhere to conA coated coverslips for two hours, before one wash in PBS 1X. Next, coverslips were dipped vertically into TEEN buffer for 30 minutes and then fixed in 4% PFA diluted in TEEN **(Figure 3.1 C**, method **2.5.3)**; DNA was counterstained with Hoechst diluted in ddH_2O at room temperature. The protocol was tested and successfully reproduced in DT40 cells

stably expressing GFP:CENP-A. Representative fibers with stretched centromeres obtained with this protocol are shown in **Figure 3.1 D**.

Figure 3.1. Optimisation of TEEN buffer protocol for chromatin stretching in DT40 cells. A. Representative images of DT40 cells stably expressing GFP:CENP-A used to test and optimise the protocol. Interphase (top) and mitosis (bottom) are shown. After fixation, DNA was counterstained with DAPI (blue). Centromere regions were identified by the localization pattern observed for the GFP signal (green). Scale bar, 5 μm. **B.** Schematic summarising the mechanism of action of TEEN buffer. The low salt concentration of the buffer generates an osmotic movement of solvent from outside to inside the cells causing cell lysis; in addition, EDTA is an efficient cation chelator, sequestering positive charges from the surroundings. As a consequence, negative charges present on the DNA repel each other and DNA stretches in an unconfined environment. **C.** Diagram of the experimental protocol used as described in **2.5.3**. **D.** Examples of fibers obtained performing the protocol illustrated in C. 60% confluent DT40 cells stably expressing GFP:CENP-A attached to conA coated coverslips were fixed and dipped vertically into TEEN buffer for 30 minutes. DNA was counterstained with Hoechst (blue). Centromere regions were identified looking at the fluorescence of GFP (green). Scale bar, 5 μm. 2X enlargement, scale bar, 5 μm. In the inset, an unfolded centromere (green) is shown at higher magnification.

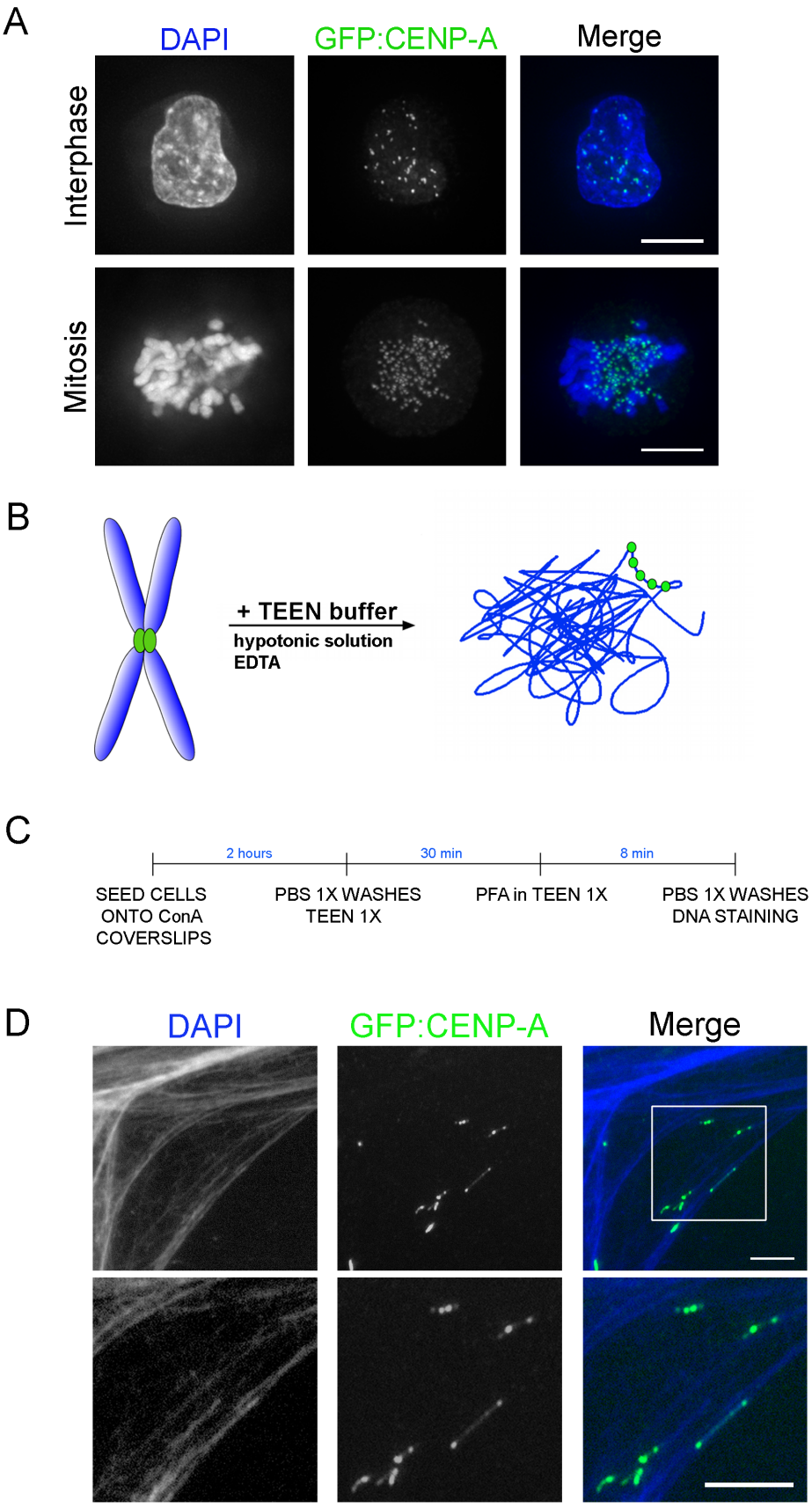
A
DAPI
GFP:CENP-A
Merge
Interphase
Mitosis
B
+ TEEN buffer
hypotonic solution
EDTA
C
2 hours
30 min
8 min
SEED CELLS ONTO ConA COVERSLIPS
PBS 1X WASHES TEEN 1X
PFA in TEEN 1X
PBS 1X WASHES DNA STAINING
D
DAPI
GFP:CENP-A
Merge

3.2.2 A comparison of intact cells versus chromatin fibers

Having selected a model system compatible with stretching of chromatin, the next aim was to examine to what extent the sample preparation could affect the level of resolution achieved during data acquisition, particularly on a compact structure such as the chromatin inside a kinetochore. This step was essential in order to decide how to proceed in further experiments.

DT40 cells stably expressing GFP:CENP-A were used for this test. Cells were either fixed for standard microscopy (**2.5.1**) or processed for fiber preparation (**2.5.3**). To assess whether it was possible to obtain enough resolution after stretching DNA fibers, samples were probed with anti histone H3 tri-methylated (me3) on lysine 9 (K9) (H3K9me3). Nucleosome octamers, in addition to H2A, H2B and H4, also contain either H3 or CENP-A, the centromere variant of H3, but not both (Luger et al., 1997; Richmond et al., 1984; Warburton et al., 1997). Therefore H3 and CENP-A should never directly co-localise. After image acquisition using a conventional wide-field light microscopy system (DeltaVision RT, Applied Precision). ImageJ software (National Institutes of Health, Bethesda, MD) was used to perform line-scan analysis of the signals of GFP:CENP-A and H3K9me3. In the case of intact cells, H3K9me3 and GFP:CENP-A showed a clear co-localization, as underlined by the line-scan plots, where the majority of the peak of CENP-A (blue curve) overlapped with the peak of H3K9me3 (green curve) **(Figure 3.2 A)**. This was observed in both interphase and mitotic samples. In addition, H3K9me3 signal was present on centromeres but, as expected, was also extended to pericentromeric chromatin **(Figure 3.2 A**, enlarged IF insets**)**. In contrast, on stretched chromatin fibers H3K9me3 peaks of fluorescence intensities rarely overlap with the peaks of fluorescence intensities of GFP:CENP-A. When CENP-A showed a peak, there was a corresponding decrease in the histone mark and vice versa **(Figure 3.2 B)**. This demonstrates the presence of H3 in between CENP-A nucleosomes. This result was in agreement with previously published data where the authors showed this typical alternated pattern between CENP-A and H3K9me3 after centromere stretching (Jin et al., 2008; Ribeiro et al., 2010; Yan et al., 2005).

Figure 3.2. Chromatin fibers provide a more accurate system to assess co-localization in comparison with intact cells. A. Representative images of mitotic and interphase DT40 cells stably expressing GFP:CENP-A. Confluent coverslips were fixed and samples were probed with anti H3K9me3 antibody. Signals were detected using Alexa Fluor 594 conjugated secondary antibody (red). DNA was counterstained with DAPI (blue). Centromere regions were identified looking at the fluorescence of GFP (green). Scale bar, 5 μm. 3X enlargement panels are shown. Line-scan plots for interphase and mitosis are shown. **B**. Representative images of two stretched fibers from DT40 cells stably expressing GFP:CENP-A. 60 % confluent coverslips were processed for fiber preparation using TEEN buffer (**2.5.3**). Samples were stained as specified in A. and DNA counterstained with Hoechst. Scale bar, 5 μm. Line-scan plots for Fiber 1 and 2 are shown. Thin yellow lines were drawn beside unfolded centromeres whose fluorescence was measured in the line-scans using ImageJ software. On the x axis of the plot is represented distance expressed in pixels whilst on the y is a measurement of fluorescence intensity. CENP-A and H3K9me3 fluorescence peaks are traced by a blue and a green curve respectively. Intact cells showed overlap between CENP-A and H3K9me3 signals in both interphase and mitosis, whereas stretched centromere fibers revealed an alternate pattern of either CENP-A or H3K9me3 signals.

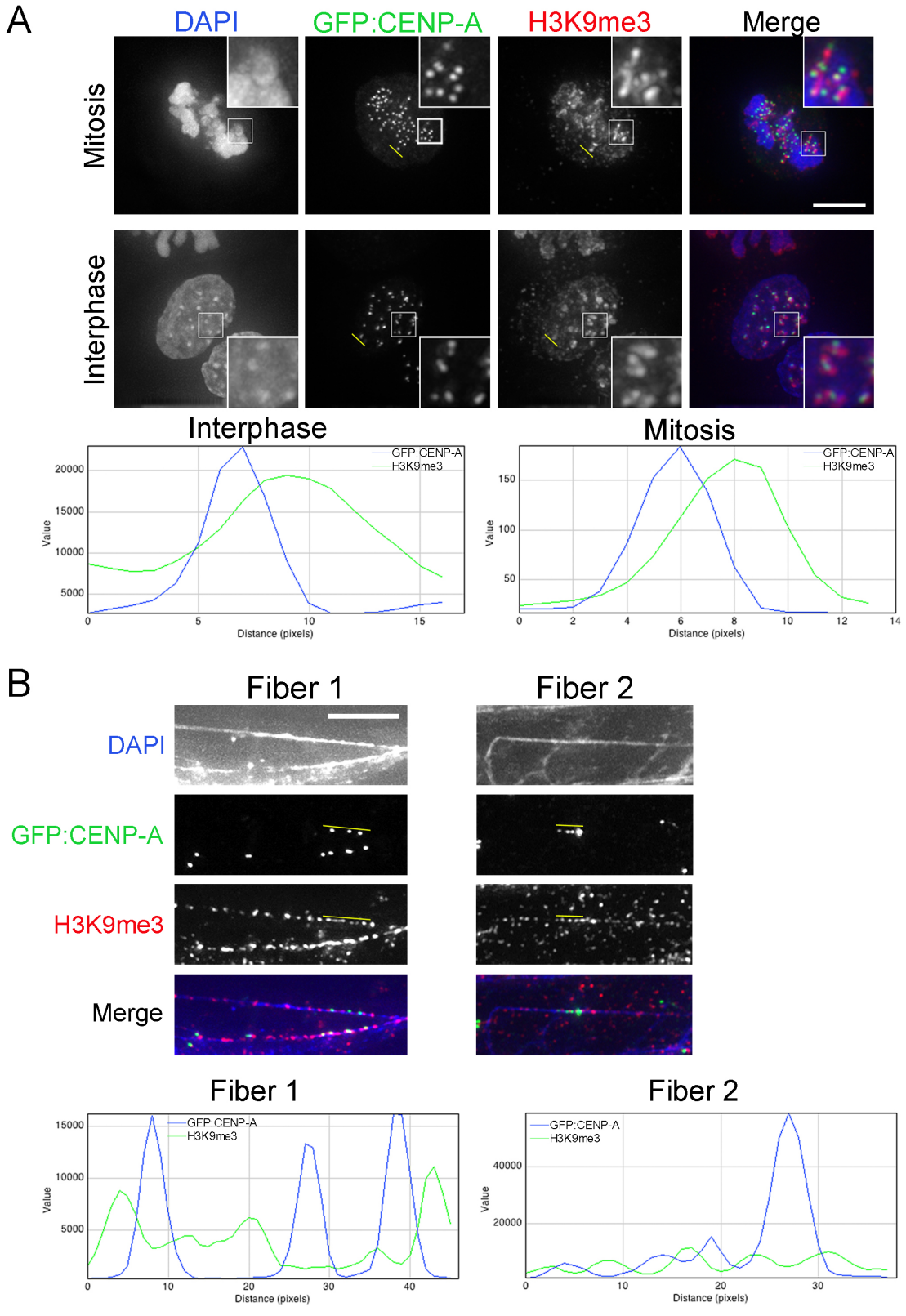
A
DAPI
GFP:CENP-A
H3K9me3
Merge
Mitosis
Interphase
Interphase
Mitosis
GFP:CENP-A
H3K9me3
Value
Distance (pixels)
B
Fiber 1
Fiber 2
DAPI
GFP:CENP-A
H3K9me3
Merge
Fiber 1
Fiber 2
GFP:CENP-A
H3K9me3
Value
Distance (pixels)

To study the ultra-structure of the kinetochore in human cells, it was next considered whether TEEN buffer protocol for chromatin stretching would work in HeLa cells. HeLa is a common human cell line derived from a cervical cancer biopsy and is routinely used in research laboratory practises. As HeLa cells are cancerous, they do not differentiate, their doubling time is approximately 24 hours and their transfection efficiency is high compared with other cell lines.

HeLa cells were left to adhere onto coverslips for 24 hours before proceeding with the fiber stretching protocol. Cells were then washed with PBS 1X. Next, TEEN buffer treatment was performed for up to one hour, followed by fixation with 4% PFA diluted in TEEN buffer **(Figure 3.3 A)**. A panel of different conditions was tested **(Figure 3.3 B)**. Chromatin stretching was performed with TEEN buffer either alone or in the presence of non-ionic detergents, dissolved in TEEN buffer, at the concentration of 0.1 % v/v **(Figure 3.3 B)**. No chromatin stretching was observed in HeLa cells after treatment with TEEN buffer alone **(Figure 3.3 C1)**. Therefore, the same protocol was repeated with TEEN buffer supplemented with the detergents in **Figure 3.3 B**. Results showed no reproducible high quality stretched chromatin when TEEN was added with 0.1% v/v of TritonX-100 or Octyl-β-D-maltopyranoside **(Figure 3.3 C2 and C3)**. In contrast, treatment with 0.1% v/v Decyl-β-D-maltopyranoside in TEEN buffer showed successful chromatin stretching in HeLa cells **(Figure 3.3 C4)**. However, although using this method stretched chromatin fibers were generated, the quality of the stretching was poor compared with the results obtained previously in DT40 cells, and the samples showed a high degree of heterogeneity regarding the levels of chromatin stretching.

In conclusion, an analysis of protein co-localization was performed on both intact cells and stretched chromatin fibers using a light wide-field system. Results confirmed that centromere chromatin fibers provided a better resolution for centromere measurement compared to intact cells. Unfortunately, the same gentle method for chromatin stretching was not as efficient in human cells, where despite the addition of detergents to TEEN buffer, a lower level of chromatin stretching was observed.

Figure 3.3. Attempts to develop a method to stretch chromatin in human cells. A. Diagram representing the experimental protocol designed. **B**. Table listing different TEEN and detergents combinations tested to obtain stretched chromatin fibers in human cells, number coded as in panel C. Each detergent was added to TEEN buffer at the concentration of 0.1% v/v. **C.** Representative images of cells treated with the correspondent buffer as described in panel B. DNA was counterstained with DAPI (blue). Scale bar, 5 μm. None of the detergents tested, diluted in TEEN, allowed the reproducible generation of high quality DNA fibers.

A

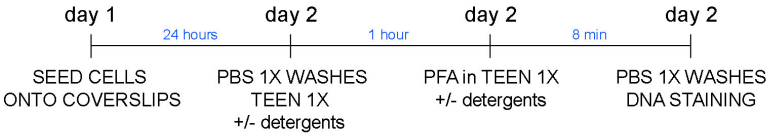

B

SAMPLE n	UNFOLDING BUFFER COMPOSITION
1	TEEN 1X
2	TEEN 1X + 0.1% TritonX-100
3	TEEN 1X + 0.1% Octyl-B-D-maltopyranoside
4	TEEN 1X + 0.1% Decyl-B-D-maltopyranoside

C

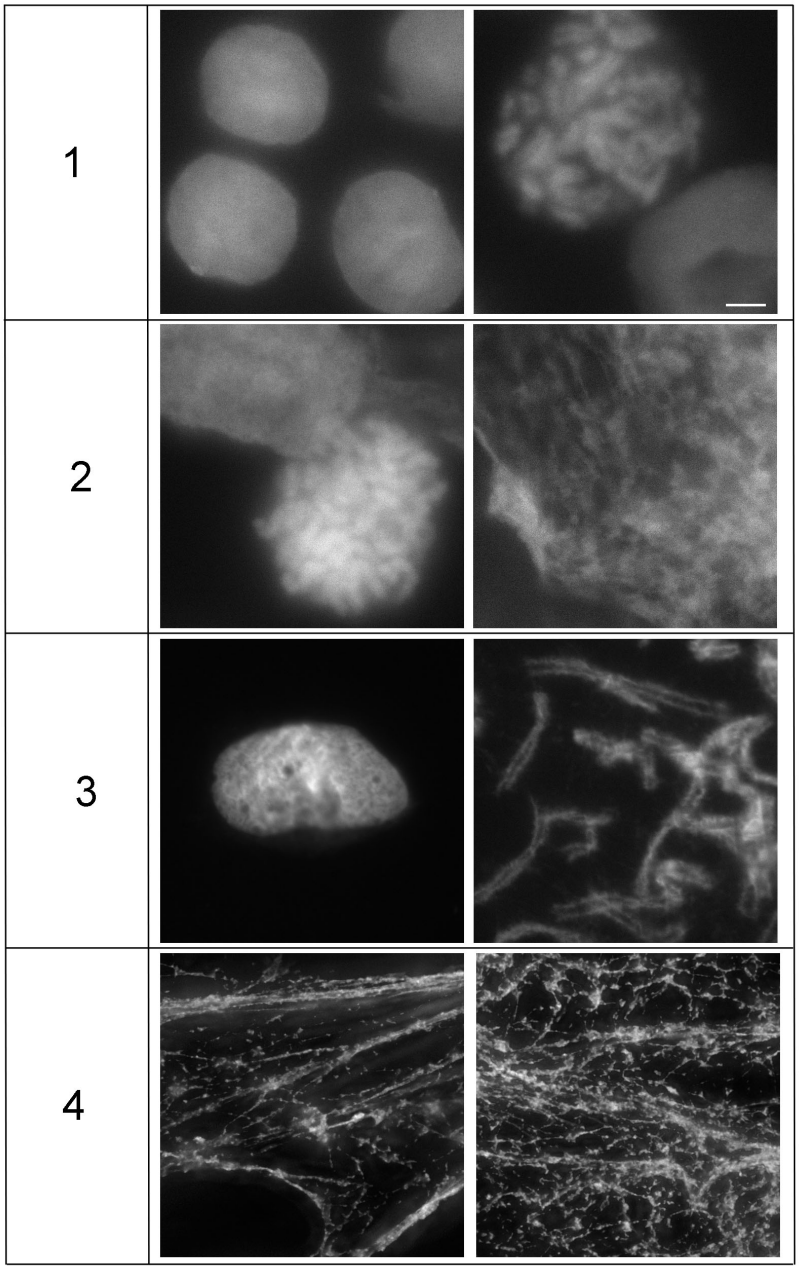

3.2.3 Immunofluorescence on stretched chromatin fibers allowed the visualization of elongating RNA polymerase II at kinetochore

This section describes a collaboration with Dr Oscar Molina Campoy. The data collected has been included as part of a main text figure in a manuscript currently under review at the JCB (Molina et al., 2015). The project aims to study the effects of the removal of H3K4me2 from kinetochore chromatin on the maintenance of a functional centromere that allows a faithful chromosome segregation. To do so, a Human Artificial Chromosome, the alphoid^{tetO} HAC system, previously used in our laboratory, has been further exploited (Bergmann et al., 2012; Bergmann et al., 2011; Cardinale et al., 2009; Nakano et al., 2008). In this system, a synthetic array of cloned α-satellite monomers containing alternating tetracycline operators (TetO) and CENP-B boxes were introduced into HT1080 cells (Kouprina et al., 2012; Nakano et al., 2008) to generate the alphoid^{tetO} HAC. 1C7 is a hybrid cell line derived from the fusion of the original HT1080 cell line that carried the alphoid^{tetO} HAC, with HeLa cells. Resultant 1C7 cells were still carrying the HAC and in addition, they were growing faster and were more efficiently transfected (Cardinale et al., 2009) compared to the original HT1080 cells. TetR-EYFP fusion proteins were transfected into 1C7 cells where they were specifically tethered to the TetO sequence present in the alphoid^{tetO} HAC. This system allows us to tether different chromatin modifiers to the alphoid^{tetO} HAC for studying the epigenetic landscape of the centromere. Importantly, the alphoid^{tetO} HAC is visualised as a fluorescent spot (from the EYFP) in transfected interphase nuclei.

Some authors had reported the presence of RNApolIIS2^{P} on centromeres in metaphase spreads (Chan et al., 2012) and, more recently, on stretched centromere chromatin fibers (Quenet and Dalal, 2014). Although these studies demonstrated the presence of RNApolIIS2^{P} at centromeres, no evidence of RNApolIIS2^{P} at the kinetochore domain, where CENP-A is present, was reported. My role in this project was to study whether the active elongating RNA polymerase II, which is phosphorylated at the serine 2 of its CTD tail (RNApolIIS2^{P}) (Komarnitsky et al.,

2000; Morris et al., 2005), is specifically present at the kinetochore domain of the centromere.

The development of a method to obtain better stretching of chromatin fibers in human cells was required in order to perform high resolution co-localization studies. A successful protocol to obtain stretched chromatin fibers in mitotic human cells was performed as follows (**2.5.4**). Mitotic 1C7 cells were harvested through mitotic shake-off following metaphase arrest with colcemid (100 ng/ml for 3 hours). Next, samples were incubated for 10 minutes with 75 mM KCl buffer at 37°C causing hypotonic swelling, and then cytospun onto polylysine coated slides. Finally, slides were immersed into a lysis buffer **(Figure 3.4 A)**, whose composition is indicated in section **2.5.4**. A representative image of stretched chromatin fibers, generated with this protocol is shown in **Figure 3.4 B**. Next, immunofluorescence staining for both CENP-C, as a kinetochore reference, and RNApolIIS2^{P} was performed as described in **2.5.1** and **2.6.1**. With this protocol, stretched mitotic kinetochore fibers were obtained, shown by DAPI staining **(Figure 3.4 C)**. Fiber images were acquired with a fluorescence microscope, deconvolved and processed for fluorescence intensity line-scan analysis using ImageJ software. Fluorescence intensities of CENP-C and RNApolIIS2^{P} were detected along DNA fibers, recognised by DAPI staining, and plotted together as shown in the representative plot in **Figure 3.4 C**. Results demonstrated an average frequency of co-localization between CENP-C and RNApolIIS2^{P} of 66.73%, whereas the remaining 33.27% of RNApolIIS2^{P} signal was found extended in the regions flanking the kinetochore **(Figure 3.4 C**; n=10**)**.

After testing the presence of the elongating RNA polymerase in native kinetochores we wanted to test whether RNApolIIS2^{P} was also present on the alphoid^{tetO} HAC kinetochore. In order to do so, it was not enough to perform a normal transfection followed by fiber protocol, as the presence of detergent in the lysis buffer washed away the tethered TetR-EYFP (data not shown). Therefore, an alternative solution for detecting the HAC was found. In a joint effort with Dr Jeyaprakash Arulanandam's laboratory TetR-EYFP protein was expressed in *E.coli* BL21 Gold competent cells and purified by affinity chromatography using a Ni-NTA

column (GE Healthcare). To test the *in vitro* binding efficiency of the purified TetR-EYFP, chromosome spreads were prepared **2.5.5**. TetR-EYFP was added to chromosome spread samples, diluted in a blocking solution without Tween20 or any detergent (**2.6.2**). The alphoid^{tetO} HAC was successfully detected by the presence of EYFP as illustrated in **Figure 3.4 D** (arrow). Next, chromatin fibers were stretched and incubated with the TetR-EYFP purified protein, ensuring that no detergent was added to any washing solution. Results showed that performing such protocol allowed the binding between TetR and TetO to be preserved also on chromatin fibers **(Figure 3.4 E)**. Having optimised conditions for alphoid^{tetO} HAC detection onto stretched chromatin fibers, an experiment to look at the kinetochore domain of the alphoid^{tetO} HAC was designed. Mitotic fibers were prepared and probed with anti CENP-C and anti RNApolIIS2^{P} antibodies. Afterwards, following secondary antibody labelling, an *in-situ* tethering of the TetR-EYFP was performed, thereby allowing the detection of the alphoid^{tetO} HAC on kinetochore fibers. Results showed co-localization of RNApolIIS2^{P} and CENP-C on the alphoid^{tetO} HAC (TetR-EYFP signal) in 60% of the fibers analysed **(Figure 3.4 F**; n=32, three independent experiments**)**.

In summary, a new and more efficient protocol for stretching chromatin fibers in human cells was successfully optimised. This protocol overcame the limitation of stretching chromatin fibers observed with the former protocol (section 3.2.2). Results demonstrated that the RNApolIIS2^{P} was present on the alphoid^{tetO} HAC in a similar frequency in which RNApolIIS2^{P} was detected in endogenous metaphase chromosomes (~ 60%). This finding lead to further experiments performed by Dr Molina in order to analyse the role of RNApolIIS2^{P} on maintaining active kinetochores. This was made possible by a new method for *in-situ* tethering using purified TetR-EYFP (Molina et al., 2015).

Figure 3.4. Kinetochore chromatin fiber analysis: visualization of the RNA polymerase II Ser2^{P}. **A**. Diagram illustrating the experimental procedure for fiber generation in human cells. **B**. Representative image of chromatin fibers obtained with the protocol described in A. DNA was counterstained with DAPI. Scale bar, 5 μm. **C**. Co-localization analysis of CENP-C and RNA polymerase II Ser2^{p} (elongating polymerase). Representative image of colcemid arrested 1C7 cells processed for chromatin fibers as described in 2.5.4. Samples were probed with anti CENP-C and anti RNApolIISer2^{P} antibodies. Signals were detected using Alexa Fluor 488 (green) and 594 (red) conjugated secondary antibodies. DNA was counterstained with DAPI. Scale bar, 5 μm. The plot, produced in ImageJ, was based on line-scans of pixel fluorescence intensity analysis of the above fiber. On the x axis of the plot is represented the distance expressed in μm whilst on the y is a measurement of fluorescence intensity. CENP-C fluorescence intensity overlaps with the intensity of RNApolII Ser2^{p} in 66.73% of the fibers analysed, whereas in 33.27% of the fibers analysed RNApolIISer2^{P} signal extended into regions flanking the kinetochore (n=10). **D**. Chromosome spread showing alphoid^{tetO} HAC detection by using bacterial purified TetR-EYFP (green). DNA was counterstained with DAPI. Scale bar, 5 μm. Enlargement scale bar, 2.5 μm. **E**. Representative images of alphoid^{tetO} HAC fibers obtained using *in-situ* tethering of TetR-EYFP purified protein as described in 2.6.2. **F**. Analysis of the presence of the RNA polymerase II Ser2^{p} (elongating polymerase) at the alphoid^{tetO} HAC. Representative images of presence (green) or absence (red) of co-localization between the signals of RNApolII Ser2^{p} and CENP-C are shown. Colcemid arrested 1C7 cells were processed for chromatin fibers as described in 2.5.4. Samples were probed with anti CENP-C and RNApolIIS2^{P} antibodies. Signals were detected using Alexa Fluor 647 (far red, pseudo coloured as blue) and 594 (red) conjugated secondary antibodies. The kinetochore region of the alphoid^{tetO} HAC was identified by the fluorescence of TetR-EYFP (green). DNA was counterstained with DAPI. Scale bar, 5 μm. The numbers of counted fibers and relative percentages are shown in the brackets (n=32). 60% of the fibers analysed showed an overlap of the signals of CENP-C and RNApolIIS2^{P} at the alphoid^{tetO} HAC.

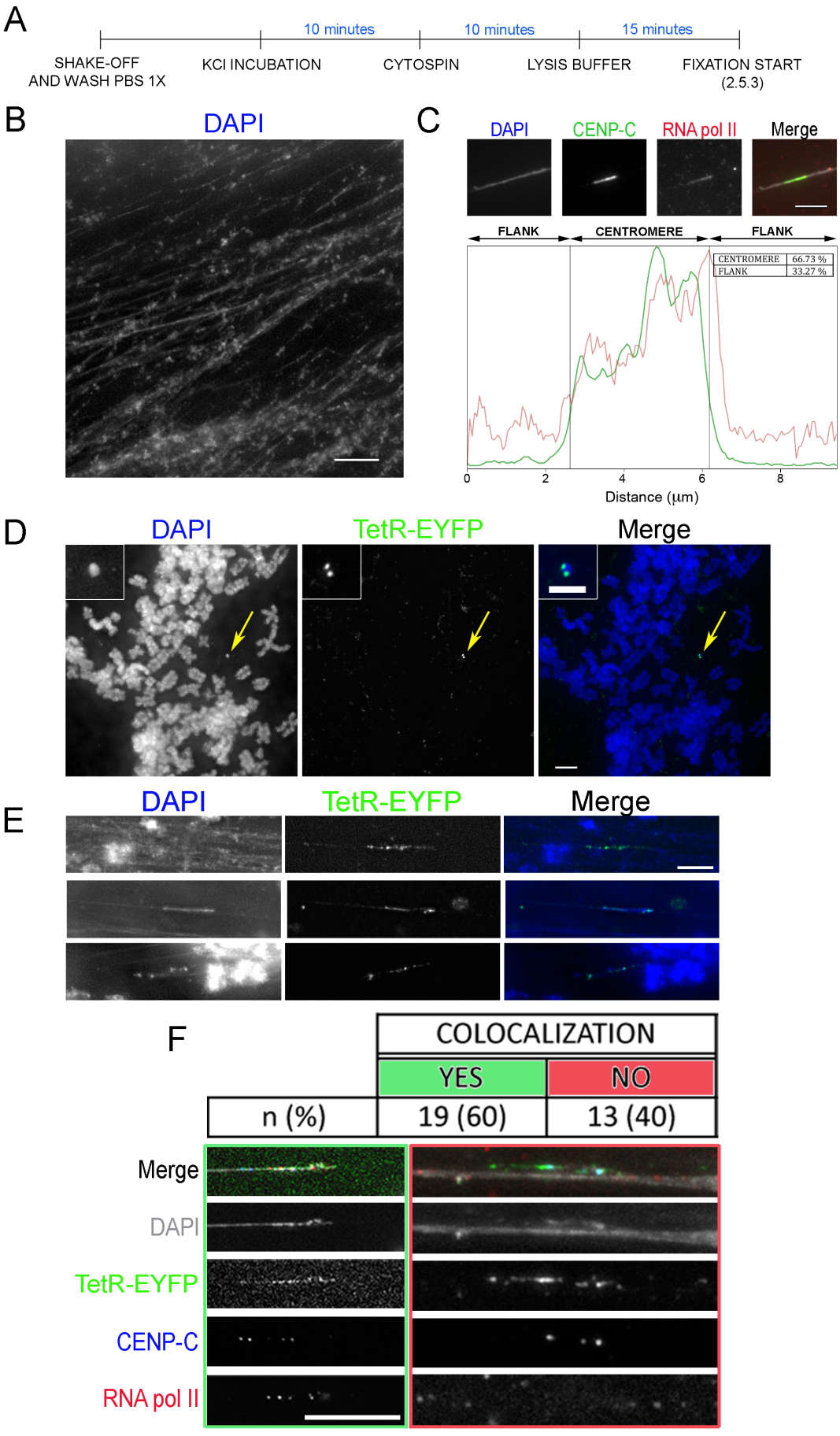
A
10 minutes
10 minutes
15 minutes
SHAKE-OFF AND WASH PBS 1X
KCl INCUBATION
CYTOSPIN
LYSIS BUFFER
FIXATION START (2.5.3)
B
DAPI
C
DAPI
CENP-C
RNA pol II
Merge
FLANK
CENTROMERE
FLANK
CENTROMERE 66.73 %
FLANK 33.27 %
0
2
4
6
8
Distance (µm)
D
DAPI
TetR-EYFP
Merge
E
DAPI
TetR-EYFP
Merge
F
COLOCALIZATION
YES
NO
n (%)
19 (60)
13 (40)
Merge
DAPI
TetR-EYFP
CENP-C
RNA pol II

3.2.4 Microscopy localization study of H4K20me1: novel centromere signature

The epigenetic nature of the centromere is widely recognised and accepted (Karpen and Allshire, 1997; Shang et al., 2013). As DNA sequence is not a unique definer of the centromere, greater importance is currently attributed to the presence of CENP-A and modification signature of the other core histones (Ruthenburg et al., 2007). Although several studies have been focused on the identification of these modifications at centromeres, it is still unclear which are the minimum epigenetic requirements to generate and maintain a functional centromere.

The histone H4 N-terminus tail modifications were early identified in 1969 (DeLange et al., 1969). On lysine 20 of histone H4, three methylation states are possible: mono-, di- and tri-methylation (Kouzarides, 2007). Methyltransferase enzymes are responsible for controlling the methylation levels on H4K20 in a cell cycle dependent manner (Oda et al., 2009). Some of these enzymes have been shown to be involved in gene expression during early stages of development in Drosophila and mice and their loss causes lethality (Karachentsev et al., 2005; Oda et al., 2009). Beyond gene expression, the H4K20me1 mark is also involved in replication control (Beck et al., 2012; Tardat et al., 2010), whilst H4K20me2/3 take part in DNA double strand break (DSB) repair (Fradet-Turcotte et al., 2013; Pei et al., 2011; Tang et al., 2013).

Preliminary ChIP-seq data by Hori and colleagues identified an enrichment of H4K20me1 at the centromere of chromosome Z in chicken DT40 cells. My task in the project was to visualize H4K20me1 centromere localization by immunofluorescence in order to confirm the H4K20me1 localization using an alternative technique. My results confirmed the centromere localization of H4K20me1 and they were included into a paper recently published in Dev. Cell (Hori et al., 2014).

Initially, the localization of H4K20me1 was tested in DT40 intact cells. DT40 cells engineered to stably express GFP:CENP-A (**2.4.4**) were used in order to easily identify centromere regions. DT40 cells were left to adhere onto conA coated coverslips and fixed in 4% PFA. Samples were incubated with anti H4K20me1 and

anti CENP-T antibodies and the distribution of the H4 modification was observed in every mitotic stage **(Figure 3.5)**. The mono-methylation appeared ubiquitous in the chromatin; the presence of a lower signal on compact chromosomes compared to interphase nuclei might be due to a problem of antigen accessibility of the antibody when the chromosomes are highly condensed. However, at the resolution achieved on intact cells, the predicted accumulation of H4K20me1 at centromeres could not be detected. Therefore, H4K20me1 localization was further tested on stretched chromatin fibers obtained using TEEN buffer (**2.5.3**; **3.2.1**). 60% confluent coverslips were treated with TEEN buffer and subsequently fixed using 4% PFA. Antibody incubation conditions were kept identical to the previous experiment. Examples of isolated centromere chromatin fibers are shown where an accumulation of H4K20me1 appeared evident **(Figure 3.6 A)**. To quantify the level of co-localization of GFP:CENP-A and H4K20me1, the overlap of signal was measured using ImageJ; the same quantitation performed between the signals of CENP-A and CENP-T was used as an internal control of the experiment, as CENP-A and CENP-T normally showed high degree of co-localization on chromatin fibers **(Figure 3.6 B**, n=5**)**. As expected, CENP-T largely co-localized with CENP-A (92.2%). Although less than the control, a majority of H4K20me1 co-localized with CENP-A (63.2%). To test for a relationship between fiber length and the level of co-localization of H4K20me1 signal with the centromere, data was integrated as a 2D plot **(Figure 3.6 C)**. Five fibers of different length that displayed H4K20me1 staining at the centromere were included in the analysis visualized as five columns (dashed lines). No correlation between fiber length and percentage of co-localization between CENP-A and H4K20me1 was observed (p=0.083; Spearman's test).

To provide further support to this novel data, co-localization was also tested using Photo-Activation Localization Microscopy, PALM. PALM is a super-resolution microscopy technique based on single molecule sensitivity, which exploits the properties of blinking or photo-switchable fluorescent molecules. For this purpose, Dronpa in place of GFP was used to tag CENP-A and Alexa Fluor 647

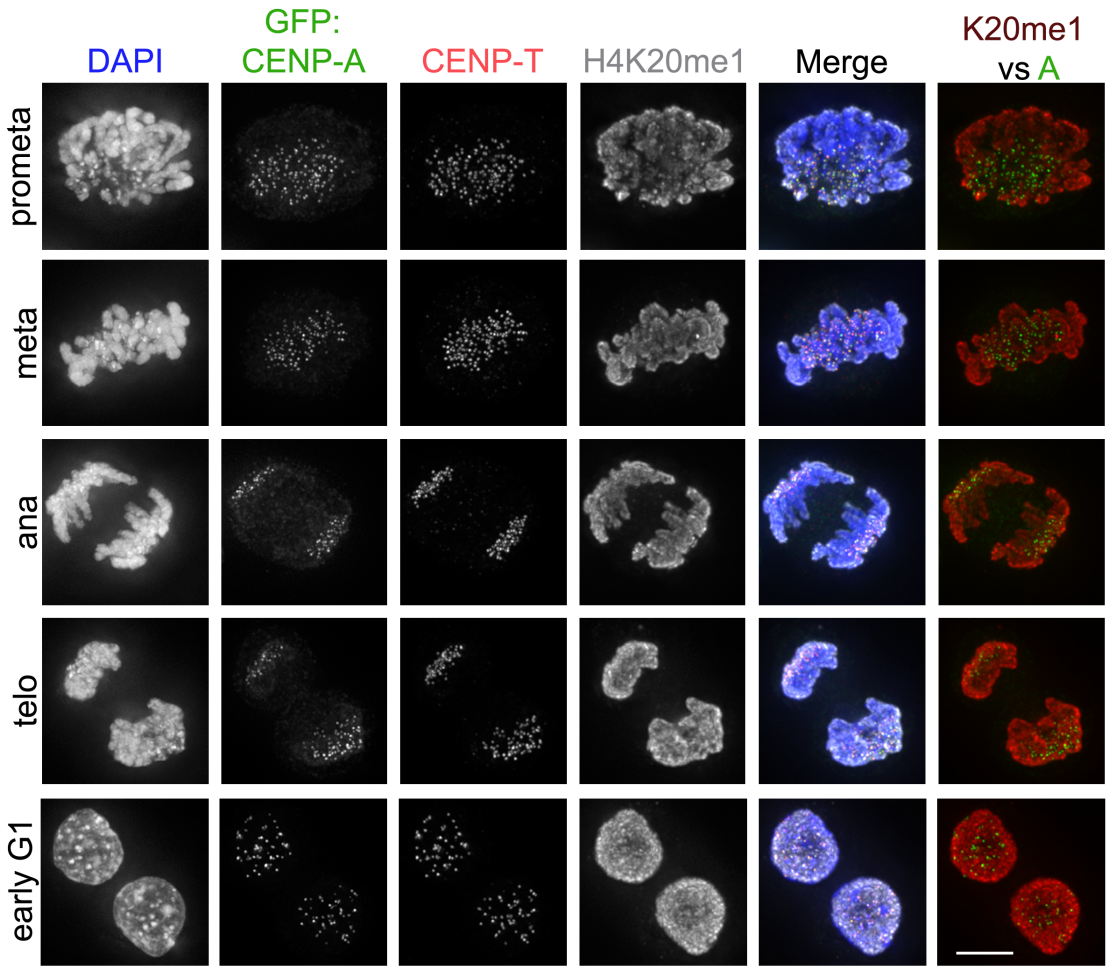

Figure 3.5. H4K20me1 characterization by immunofluorescence in intact chicken cells. Representative immunofluorescence images of DT40 cells stably expressing GFP:CENP-A. Confluent coverslips were fixed and probed with anti CENP-T and anti H4K20me1 antibodies. Signals were detected by using Alexa 594 (red) and 647 (far red, pseudo coloured in grey) conjugated secondary antibodies. The centromere region was identified by the fluorescence of GFP (green). Scale bar, 5 μm. H4K20me1 signal was visible in every stage of mitosis. However, on intact cells, no preferential accumulation of H4K20me1 at centromeres could be detected.

Figure 3.6. Analysis of H4K20me1 positioning on stretched centromeres in chicken cells. A. Representative images of DT40 cells stably expressing GFP:CENP-A processed for generating chromatin fibers (**2.5.3**). Samples were probed with anti-CENP-T and anti-H4K20me1 antibodies. Signals were detected using Alexa Fluor 594 (red) and 647 (far red, pseudo coloured as grey) conjugated secondary antibodies. The centromere region was identified by the fluorescence of GFP (green). DNA was counterstained with Hoechst. Scale bar, 5 μm. Higher levels of H4K20me1 were observed at CENP-A stretched chromatin in comparison with flanking regions. **B**. Graph showing the percentage of co-localization of CENP-A on CENP-T and of CENP-A on H4K20me1 (n=5). To perform this analysis the coloc2 plugin of ImageJ/Fiji was used. CENP-A largely co-localized with CENP-T (92.2%); in addition, the majority of H4K20me1 signal co-localized with CENP-A (63.2%). **C**. 2D plot representing centromere fiber length (x axis, μm) versus signal co-localization (y axis, %). Data from five fibers is shown as five columns defined by dashed lines. In each column specific percentages of co-localization are shown accordingly to the legend. No correlation was observed between H4K20me1 centromere occupancy and stretched centromere fiber length (p=0.083; Spearman's test).

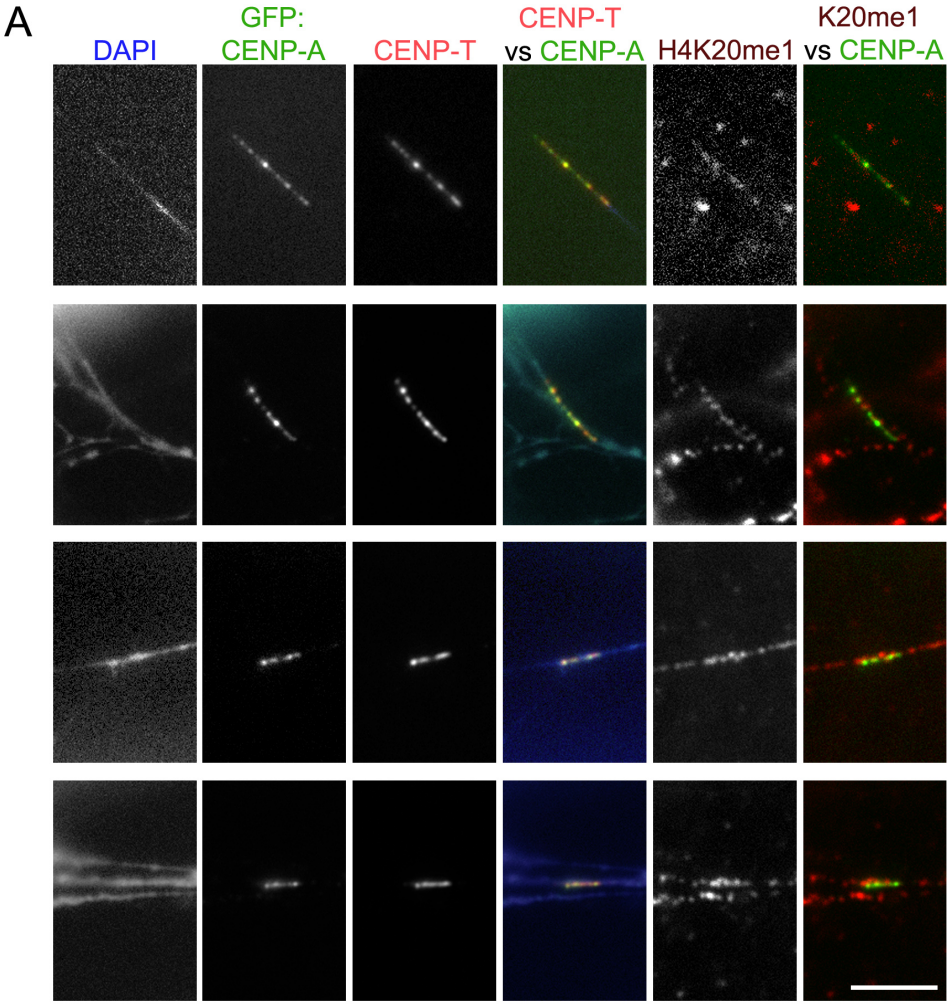
A
DAPI
GFP: CENP-A
CENP-T
CENP-T vs CENP-A
H4K20me1
K20me1 vs CENP-A

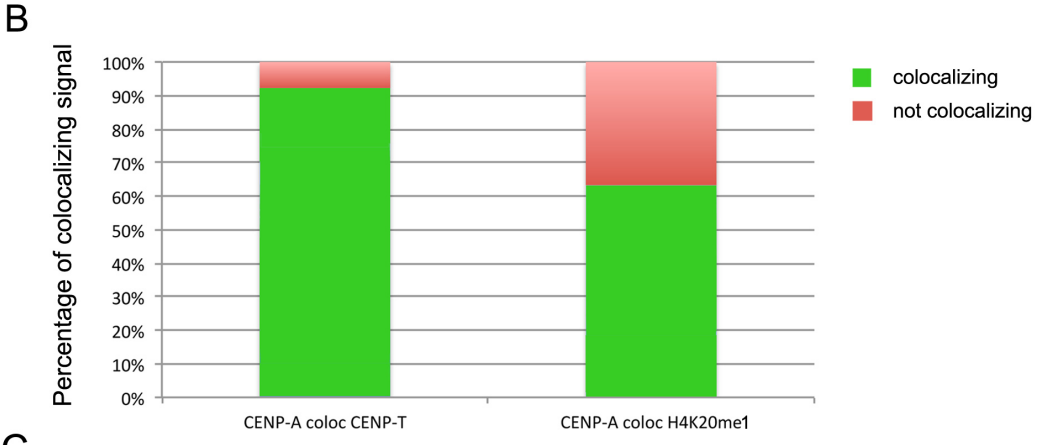
B
Percentage of colocalizing signal
100%
90%
80%
70%
60%
50%
40%
30%
20%
10%
0%
CENP-A coloc CENP-T
CENP-A coloc H4K20me1
colocalizing
not colocalizing

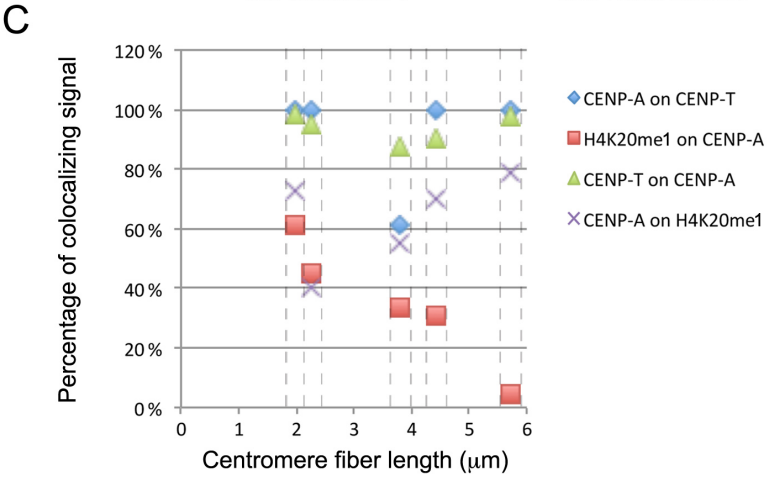
C
Percentage of colocalizing signal
120 %
100 %
80 %
60 %
40 %
20 %
0 %
0
1
2
3
4
5
6
Centromere fiber length (μm)
CENP-A on CENP-T
H4K20me1 on CENP-A
CENP-T on CENP-A
CENP-A on H4K20me1

conjugated secondary antibody was used to detect H4K20me1. Dronpa can 'blink' between bright and dark states when excited at 405 and 488 nm respectively. Alexa Fluor 647 switches between metastable bright and dark states after 633 nm irradiation in presence of a switching buffer that can catalyse the blinking. Previously generated cells expressing Dronpa:CENP-A (Ribeiro et al., 2010) were seeded on conA coated coverslips (n°1.5 thickness), this was important for sample visualization and acquisition as this thickness is optimal for the TIRF objective mounted on our PALM set-up. Samples were processed for chromatin fiber generation using TEEN buffer **(2.5.3**, **Figure 3.7)**. After treatment with TEEN buffer and fixation in 4% PFA, samples were probed with anti H4K20me1 antibody. Coverslips were next sealed into wet chambers where fibers were left incubating in switching buffer. On the day of the acquisition, lasers were manually aligned and put into TIRF. At the end of each session, signals from multi-fluorescent microspheres were acquired in order to correct for chromatic shift. The acquired movies were processed in Igor Pro 6.2 software for particle recognition. In Igor Pro, particles were assigned with coordinates that were subsequently entered in GraphPad Prism (GraphPad Software, Inc.). Here, each coordinate point was corrected for the photo-chromatic shift and graphic representations of particle localization were generated. Fiber images acquired by PALM are shown in **Figure 3.7**. This qualitative data supported my previous findings **(Figure 3.6)** as co-localization between H4K20me1 and Dronpa:CENP-A was observed **(**yellow regions, **Figure 3.7**).

Collectively, these results confirmed the presence of mono-methylation of lysine 20 on histone H4 at CENP-A chromatin in DT40 cells.

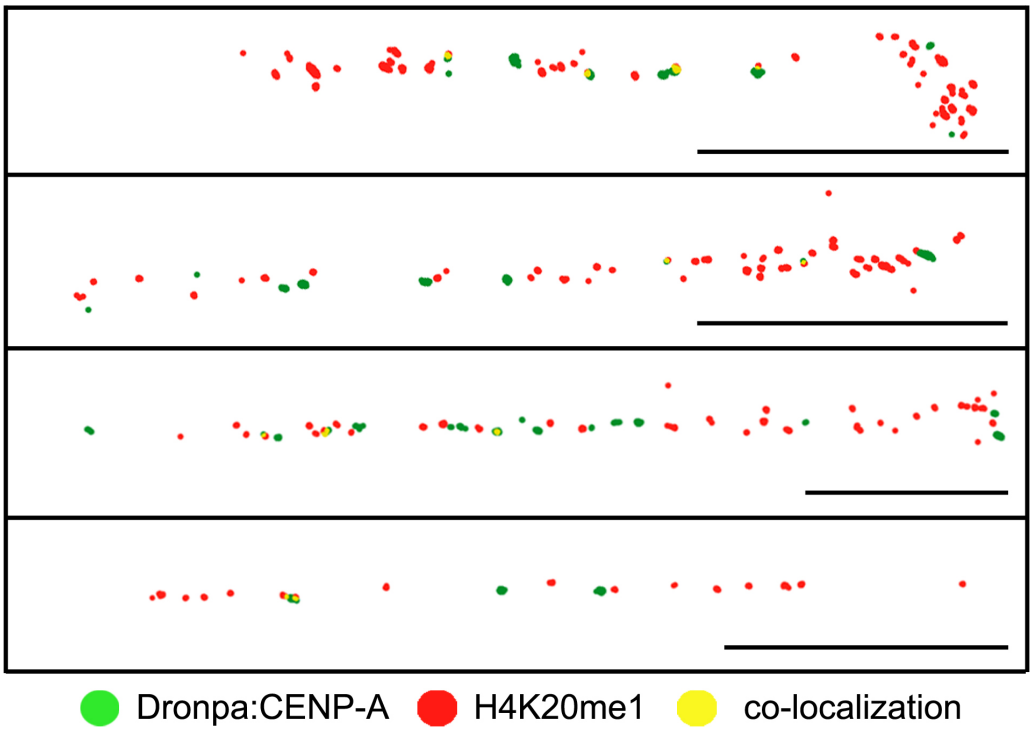

Figure 3.7. PALM localization analysis of H4K20me1 on stretched chicken centromeres. Reconstructed images of DT40 centromere fibers. DT40 cells expressing Dronpa:CENP-A were seeded onto n° 1.5 thickness conA coated coverslips and left to adhere. Sample were next processed for chromatin stretching using TEEN buffer, fixed and probed with anti H4K20me1 antibody. The signal was detected using Alexa Fluor 647 conjugated secondary antibody. Coverslips were sealed into a wet chamber where the fibers were dipped into a switching buffer. This catalysed molecule blinking during laser irradiation. For each fiber, 500 frames were acquired in both channels and the movies were later processed through Igor Pro for particle recognition and coordinate assignment. Coordinates were imported in GraphPad where correction for photo-chromatic shift was applied and a graph generated. Green dots corresponded to Dronpa:CENP-A positions whilst the red ones to H4K20me1 positions along a chromatin fiber. Regions of co-localization were represented as false-coloured in yellow. Scale bar, 7.4 μm.

3.2.5 Confirmation of single, not multiple, fiber generation

It has been considered that fibers generated and measured using protocols established during this chapter, may not be individual fibers, but rather, numerous fibers on top of one another. To confirm this is not the case CLEM analysis of stretched fibers was performed. DT40 cells expressing GFP:CENP-A were seeded into CLEM dishes (**2.9**) and fibers were prepared as in **2.5.3**. Typical fibers were then identified using a light microscope **(Figure 3.8 A)** before processing for EM (**2.9**). The correlative EM analysis showed that individual fibers could be observed **(Figure 3.8 A)**. Remarkably, the thickness of these fibers correlated closely with the expected diameter of DNA-containing nucleosomes as measured by a pixel density line-scan analysis **(**mean thickness of 13 nm, **Figure 3.8 B)**.

Figure 3.8. Correlative light electron microscopy (CLEM) confirms that chromatin fibers are well unfolded and present as individual fibers. A. Fluorescence microscopy images of unfolded chromatin fibers, expressing GFP:CENPA and counterstained with Hoechst. Using CLEM, the same region of interest (white box in the DAPI micrograph) was revisited by transmission electron microscopy (TEM). **B.** Fibers identified by TEM were assayed by line scan and pixel density analysis. Multiple line scans were taken crossing regions of unfolded DNA fibers (see representative line scan in **A.** TEM-right) and pixel density measurements (quantification of white pixels) plotted on a line graph. Profile is an average of 6 different line scans (with standard deviation). Vertical red lines mark the predicted region occupied by the DNA fiber, equating to a diameter of 13 nm. Scale bar in A, 50 nm.

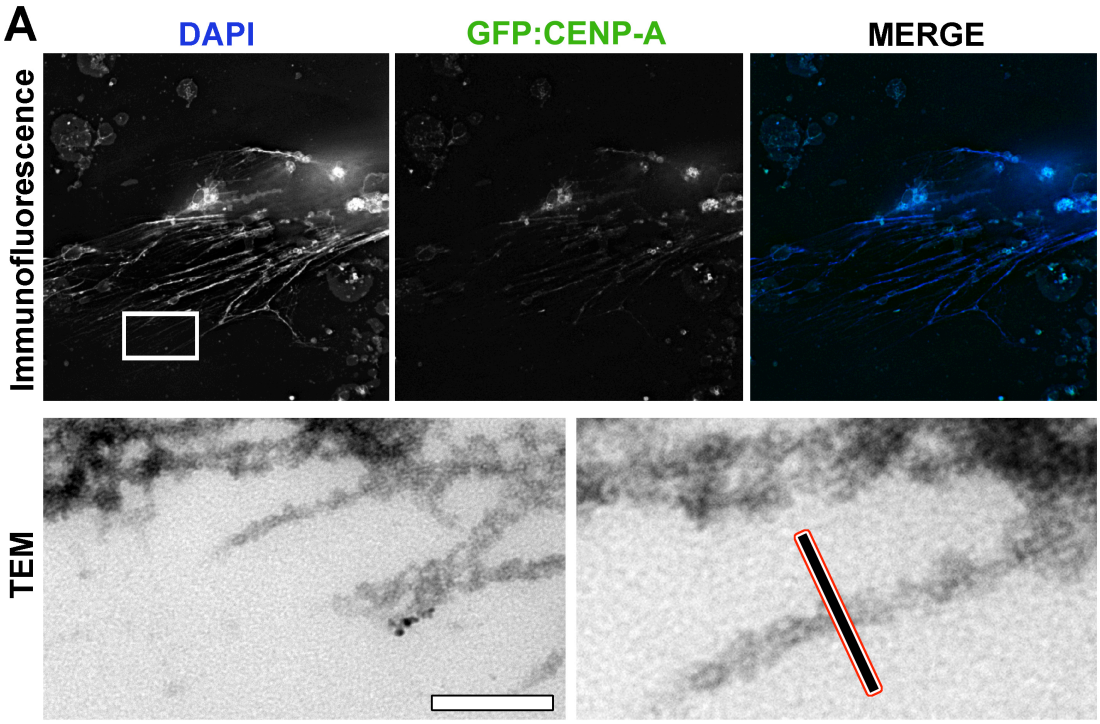
A
DAPI
GFP:CENP-A
MERGE
Immunofluorescence
TEM

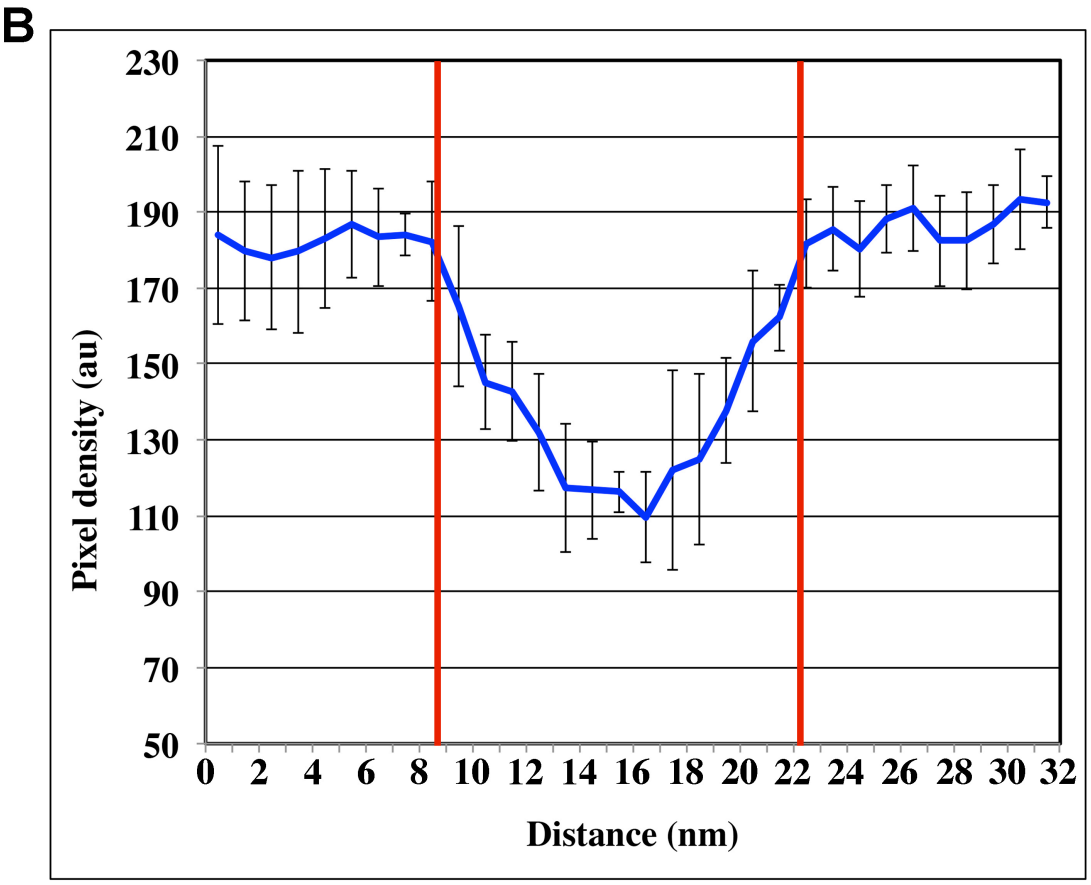
B
Pixel density (au)
230
210
190
170
150
130
110
90
70
50
0 2 4 6 8 10 12 14 16 18 20 22 24 26 28 30 32
Distance (nm)

3.3 Discussion and conclusion

The purpose of the experiments described in this chapter was to gain experience in generating high quality DNA fibers in both human and chicken cells. Both model organisms are useful for different biological questions. I have also presented results from two different projects whose progress was dependent on the development of such methods.

Firstly, I was able to reproduce the TEEN buffer protocol, previously established in the lab (Hudson et al., 2003) in order to obtain fibers in chicken cells **(Figure 3.1)**. The same method however was not successful in human cells. Different adjustments were tested to disperse chromatin in fibers in human cells. The addition of non-ionic detergents such as TritonX-100, Octyl-β-D-maltopyranoside and Decyl-β-D-maltopyranoside to TEEN buffer produced a range of effects **(Figure 3.3)**. Both TritonX-100 and Octyl-β-D-maltopyranoside did not seem to dramatically alter DNA compaction, whereas treatment with Decyl-β-D-maltopyranoside induced chromatin fibers formation, but not at a highly reproducible standard **(Figure 3.3 C)**. The difference observed in the effects of TEEN buffer between chicken and human cells could be explained by the lipid composition of the nuclear membrane. Despite the shared presence of phosphatidylcholine and phosphatidylinositol, chicken erythrocyte nuclear membrane presents more abundant phosphatidylethanolamine and sphingomyelin, whilst in human cells, the membrane also contains traces of phosphatidylserine, cardiolipin and cholesterol (Kleinig et al., 1971; van Meer and de Kroon, 2011). DT40, as previously described, are not erythrocyte cells, however a similar membrane composition could still be possible and offer an explanation for the results obtained with TEEN buffer. Those molecules could supply additional strength to human membranes resulting in tolerance to TEEN buffer. Indeed this difference in lipid composition could also explain why chicken cells cannot be transfected using standard lipid based transfection reagents but instead require electroporation.

As the final goal of this doctorate was to study the centromere chromatin, wrapped up into the kinetochore, it was important from the initial stages of work, to establish a suitable protocol that would allow me to observe samples, in the best

possible conditions. With the aim of testing which was the most suitable sample preparation, H3K9me3 localization compared to CENP-A was analysed in both intact cells and chromatin fibers **(Figure 3.2)**. Line-scan analysis on the images acquired from intact cells revealed that CENP-A and H3K9me3 were both present at kinetochores, where the peaks of the two signals were shifted apart of few pixels (2 pixels = 126 nm) **(Figure 3.2 A)**. In contrast, the analysis of centromere fibers showed that signals of CENP-A and H3K9me3 had an alternating pattern in which a peak of CENP-A corresponded a lower level of H3 and viceversa (Figure 3.2 B). This result is in agreement with previous mapping of H3K9me3 onto centromere fibers (Blower et al., 2002; Ribeiro et al., 2010; Sullivan and Karpen, 2004) and validated the use of centromere fibers for future kinetochore chromatin studies.

With the aim of obtaining fibers in human cells, we decided to use a protocol recently published where the dispersion of chromatin in the sample was enhanced by the use of cytospin, followed by incubation into a lysis buffer (Quenet and Dalal, 2014) **(Figure 3.4 A)**. It was found that RNApolIIS2^{P} was present on 60% of stretched kinetochores analysed, as highlighted by CENP-C signal **(Figure 3.4 C)**. This result was also confirmed on the kinetochore of alphoid^{tetO} HAC **(Figure 3.4 F)**. These results constituted an important contribution to a manuscript currently under review in JCB (Molina et al., 2015). This is also the first time that a purified DNA-binding protein from bacteria has been used for *in-situ* labelling in immunofluorescence experiments. I was responsible for the protocol optimisation in intact cells, chromosome spreads and fibers **(Figure 3.4)**.

CENP-A is the fundamental constituent of the centromere. The work of Hori and colleagues (Hori et al., 2014) represents an exciting step forward in understanding how epigenetic factors might regulate kinetochore assembly. The authors found that the H4K20me1 was co-IPing with CENP-A nucleosomes in both chicken and human cells. In addition they observed the presence of the mark by ChIP-seq in non-repetitive centromeres or neocentromeres comparing prior and after their establishment (CENP-A deposition). My role in this project was to establish a protocol in DT40 cells for imaging the H4K20me1 mark on chromatin fibers, and testing for co-localization of CENP-A and H4K20me1. CENP-T was used as a

standard for high level of co-localization with CENP-A. Using conventional light microscopy it was possible to visualize the H4 modification at centromeres of DT40 cells stably expressing GFP:CENP-A **(Figure 3.6 A)**. A plugin of ImageJ/Fiji, called coloc2, was used in order to quantify the extent of co-localization between CENP-A and H4K20me1 **(Figure 3.6 B)**. The analysis showed that CENP-A and H4K20me1 shared slightly over 60% of their positions on chromatin fibers and also that this percentage is not affected by fiber length (Figure 3.6 C). As I was interested in quantifying the amount of H4K20me1 at the centromere the data was plotted as CENP-A on H4K20me1 **(Figure 3.6 B)**; this is because H4K20me1 is also present outside the centromere therefore if the data was charted as H4K20me1 on CENP-A, then the amount of shared positions would be lower, as CENP-A is not detected outside centromeres by microscopy **(Figure 3.6 C**, red squares**)**. In the cases of CENP-A and CENP-T this shift is less pronounced since CENP-A and CENP-T are both exclusively kinetochore proteins. Qualitative PALM data supported the wide-field experiments, confirming the presence of H4K20me1 on CENP-A nucleosomes. My data together with other results presented in that paper, led to the conclusion that H4K20me1 appears on chromatin where the loading of CENP-A has just occurred and represents a mature chromatin that is able to recruit CENP-T and therefore build a functional kinetochore to ensure correct chromosome segregation at the next mitosis (Hori et al., 2014).

Finally, it was possible to show that the protocols for fiber preparation, optimised in this chapter, allow the generation of highly unfolded, individual chromatin fibers.

The experience and data collected in this chapter has permitted a robust protocol to be established allowing the reproducible generation of high quality DNA fibers in chicken cells. This method was next adopted in efforts to tackle the main research area of this study about kinetochore ultrastructure.

4 Chapter 4: Ultrastructure analysis of the *Gallus gallus* kinetochore

4.1 Introduction

The kinetochore is a multi-subunit protein complex located on the outer surface of each centromere whose main function is to bridge DNA, packed into chromosomes, with attached microtubules, thus playing an essential role in chromosome segregation during mitosis (Cheeseman and Desai, 2008; Joglekar et al., 2010; Khodjakov et al., 1997). The assembly of a non fully functional kinetochore complex can result in aneuploidy (Cleveland et al., 2003).

CENP-A, CENP-B and CENP-C are probably the best studied CENPs, however, over the last decade 16 other centromere proteins have been identified, and further classified as members of the constitutive centromere associated network, CCAN (Foltz et al., 2006; Izuta et al., 2006; Okada et al., 2006). Although it is still unclear how some CCAN components interact between one another it is thought that their location between the inner and outer kinetochore (*i.e.* KMN network) supplies a scaffold for microtubule plus tips on the centromere (Gascoigne et al., 2011; Hori et al., 2008a). CENPs can be broadly classified into several functional sub-groups: CENP-C; CENP-T/W/S/X; CENP-H/I/K/M; CENP-L/N and CENP-P/O/R/Q/U (McAinsh and Meraldi, 2011; Perpelescu and Fukagawa, 2011; Takeuchi and Fukagawa, 2012). Each sub-group occupies a specific region within the kinetochore, however, the exact mechanism of how these proteins function is still ambiguous. Collectively, all of these protein complexes contribute to the organization of centromere chromatin, which composes the kinetochore. At present, the ultra-structural organization of centromere chromatin during mitosis remains unclear, despite the research interest that this topic attracts. Currently, two specific questions remain unanswered: i) how does the chromatin fold into the centromere and ii) what are the differences in its folding between mitosis and interphase.

One hypothesis is that the organization of the chromatin within the centromere resembles a cylinder composed of spirals or loops, where CENP-A

containing nucleosomes are positioned facing the outer kinetochore, whilst H3 chromatin is oriented towards the inner chromatin region in an amphipathic configuration (Sullivan and Karpen, 2004). A more recent study predicts a model, supported by super-resolution microscopy data, suggesting that centromere chromatin is folded back and forth into a boustrophedon and assembled in stacks, where H3 was visualized facing not only the inner kinetochore but also the outer kinetochore, as H3 shared a pattern of localization with CENP-T (Ribeiro et al., 2010). The hypothesis of H3 nucleosomes being widely distributed throughout kinetochore chromatin was contrasting with previous observations (Blower et al., 2002; Sullivan and Karpen, 2004).

In this study we focused on the understanding of the re-organization of centromere chromatin between interphase and mitosis. I generated chromatin fibers from DT40 parental cells and several CENP depleted cell lines. By applying rigorous statistical analysis of fiber measurements from both interphase and mitotic cells, a repetitive module within the kinetochore chromatin was discovered that supports a structure like the boustrophedon, composed by layers. My results suggest that there are five layers of chromatin in interphase, in contrast to only three in mitotic samples. It was also possible to estimate the amount of chromatin present in each layer and therefore predict the amount of chromatin present in a chicken kinetochore. The total length of DNA in each layer was estimated to be 0.5 μm. To further test kinetochore structure, conditional knockout and deletion cell lines of centromere proteins were analysed. These results revealed that CENP-C and CENP-S separately contribute in the maintenance of the structure of the kinetochore, whilst loss of CENP-I did not seem to affect kinetochore assembly. CENP-H and CENP-O depletion did not disrupt kinetochore structure although it did significantly affect centromere chromatin stretching.

4.2 Results

4.2.1 Mitotic kinetochores unfold only half as much as interphase pre-kinetochores

To study the structure of the kinetochore, chromatin fibers were generated from cells stably expressing GFP:CENP-A and the length of the GFP region was measured. A fully mature kinetochore is a structure that exists only during mitosis but the majority of CCAN kinetochore components are also present in interphase. Fibers from both interphase and mitosis samples were prepared, measured and the results of the measurements were compared and statistically analysed.

Firstly, the generation of a stable GFP:CENP-A expressing cell line was required. Clone 18 cells are commonly used as a control or wild-type cell line in chicken DT40; from now onwards, I will refer to them as the parental cell line as other cell lines used in this study derive from this cell progenitor. Parental DT40 cells were electroporated with a GFP:CENP-A expressing vector and plated with geneticin as a selective agent for one week (**2.4.4**). Growing colonies were amplified and screened for GFP expression by flow cytometer (FL1-H profiles for green fluorescence shown in **2.4.4**) and further characterised by immunofluorescence. Western analysis confirmed that the final clone selected was stably expressing GFP:CENP-A at a level that did not affect the expression of endogenous CENP-A, when compared to parental DT40 cells **(Figure 4.1 A)**. Next, GFP:CENP-A expressing cells were processed for immunofluorescence and co-stained with CENP-T antibody, showing that the protein expressed localized correctly at the centromere, at every stage of mitosis and in interphase **(Figure 4.1 B)**. This level of overexpression of CENP-A did not cause mis-localization of GFP:CENP-A onto chromosome arms, as shown by the co-localization of GFP signal with CENP-T on chromatin fibers **(Figure 4.1 C)**. Next, chromatin fibers in chicken cells were obtained using TEEN buffer **(Figure 3.1)**. Fibers were generated from optimally confluent cultures (60%) of both asynchronous and nocodazole arrested cells,

Figure 4.1. Characterization of DT40 cells stably expressing GFP:CENP-A. A. Immunoblot of whole cell lysate prepared from parental DT40 cells and DT40 cells stably expressing GFP:CENP-A; the aim was to check for the expression levels of GFP:CENP-A and endogenous CENP-A. In each lane 3.5 X 10^5 cells were loaded. The membrane was probed with primary antibodies raised against tubulin, GFP and GgCENP-A. Signals were acquired using IRDye® 680 and 800 conjugated secondary antibodies. The Li-Cor Odyssey system was used for signal acquisition. **B.** Indirect immunofluorescence analysis of DT40 cells expressing GFP:CENP-A was performed. Fixed cells were probed with anti GgCENP-T antibody. The signal was detected using Alexa Fluor 594 conjugated secondary antibody (red). DNA was counterstained with DAPI (blue). The localization of the construct was checked in all mitotic stages and in interphase, as specified. Scale bar, 5 μm. **C.** Representative image of DT40 cells stably expressing GFP:CENP-A where CENP-A signal co-localizes with CENP-T on a stretched fiber. Coverslips with cells were processed for fiber preparation using TEEN buffer (2.5.3). Fixed samples were probed with anti GgCENP-T antibody. The signal was detected using Alexa Fluor 594 conjugated secondary antibody (red). Centromere chromatin was identified by the GFP signal (green). DNA was counterstained with Hoechst. Scale bar, 5 μm.

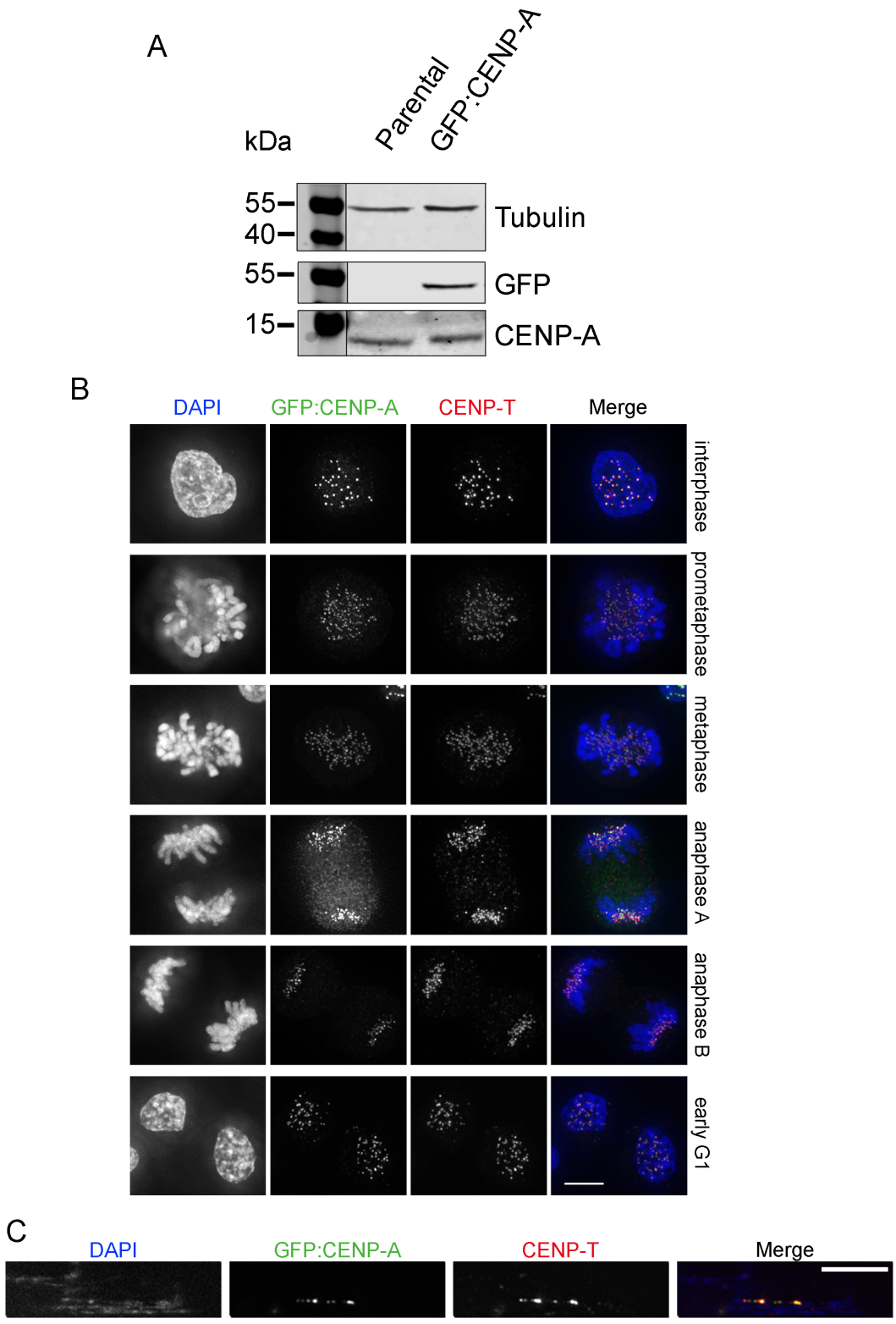
A
Parental
GFP:CENP-A
kDa
55
40
Tubulin
55
GFP
15
CENP-A
B
DAPI
GFP:CENP-A
CENP-T
Merge
interphase
prometaphase
metaphase
anaphase A
anaphase B
early G1
C
DAPI
GFP:CENP-A
CENP-T
Merge

these were fixed in parallel and DNA was stained with Hoechst to allow fiber visualization. Images of fibers were acquired using a DeltaVision RT microscope (Applied Precision). Centromere fibers were identified by the presence of the GFP signal marking CENP-A chromatin **(Figure 4.2 A)**. The lengths of the fibers were measured in microns (μm) using ImageJ and the "segmented line" tool. Clearly distinguishable and non-overlapping fibers in the field of view were used for the data acquisition in order to avoid artefacts deriving from overlapping fibers. All data concerning asynchronous cells will be referred to, from here onwards, as interphase data since ~ 95% of DT40 cell cultures are in interphase at any given time.

The mean centromere unfolding in interphase (1.97 μm +/- 1.27) was greater than the mean centromere unfolding found in mitosis (1.09 μm +/- 0.65) **(**box and whisker plots in **Figure 4.2 B)**. The difference in unfolding between the two samples was statistically significant ($p<0.0001$; Mann-Whitney U test). This difference between the two samples was due to the presence of a higher number of short length fibers in mitosis compared to longer length fibers observed in interphase. This was more apparent when the data was represented as frequency histograms **(Figure 4.2 C)**. The frequency histograms, with a bin width of 1 μm, showed the distribution of the data within a range of lengths between 1 and 10 μm. Hence, if the box and whisker plots showed the mean difference in the overall stretching of interphase and mitotic fibers, the frequency histograms highlighted instead the presence of accumulation points. The histograms showed different patterns of distribution for the two samples.

To confirm that TEEN buffer was allowing genuine unfolding of the centromeres, one would predict that the level of GFP fluorescence should decrease proportionally to the increasing of fiber length. Simultaneous measurements of GFP:CENP-A fluorescence intensity and fiber length were performed on 25 randomly picked fibers for both interphase and mitosis samples. Data obtained was represented in a 2D scatter plot where on the x axis fiber length was represented versus GFP fluorescence intensity on the y axis **(Figure 4.3)**.

Figure 4.2. Unfolding of centromere chromatin in interphase versus mitotic samples. A. 60% confluent coverslips with DT40 cells stably expressing GFP:CENP-A were processed for chromatin stretching (2.5.3). DNA was counterstained with Hoechst. The centromere region was identified by the fluorescence of GFP:CENP-A (green). Scale bar, 1 μm. **B.** Box and whisker plots showing the median fiber length (black line in the boxes) for both interphase and mitotic data sets. The size of the box defines the interquartile range, whilst the whiskers indicate the 10^{th} and the 90^{th} percentile. Asterisks highlight statistically significant differences in fiber length between interphase and mitosis ($p< 0.0001$; Mann-Whitney U test) where n=655. **C.** Frequency histograms containing stretched fiber length data for interphase (blue bars) and mitotic (red bars) samples. The data was allotted into ten 1 μm bin width histograms. Centromere length is expressed in μm on the x axis. Frequency percentages for each bin were calculated and represented on the y axis.

A

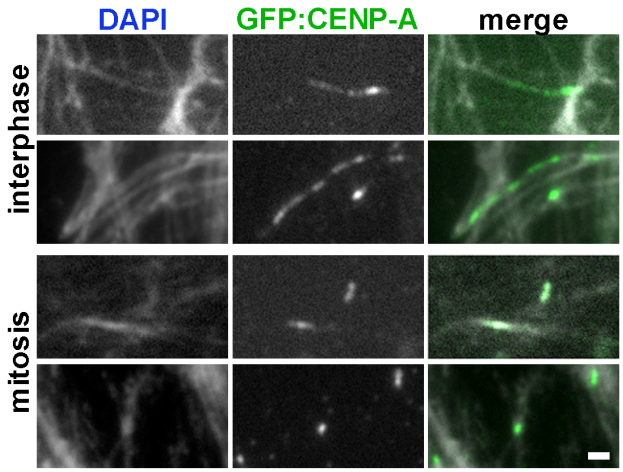
DAPI
GFP:CENP-A
merge
interphase
mitosis

B

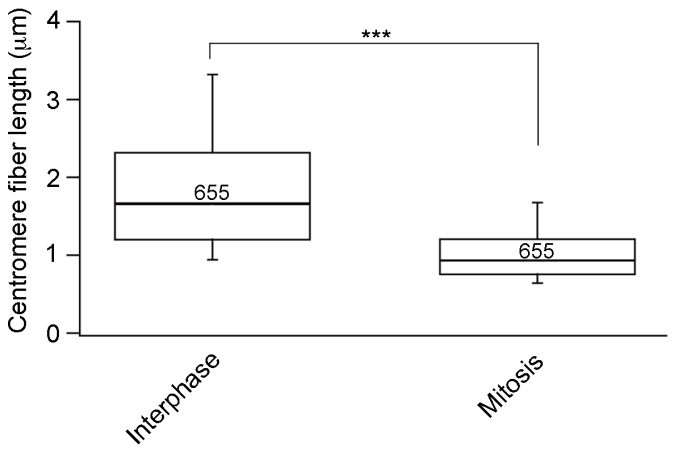
Centromere fiber length (μm)
0
1
2
3
4
***
655
655
Interphase
Mitosis

C

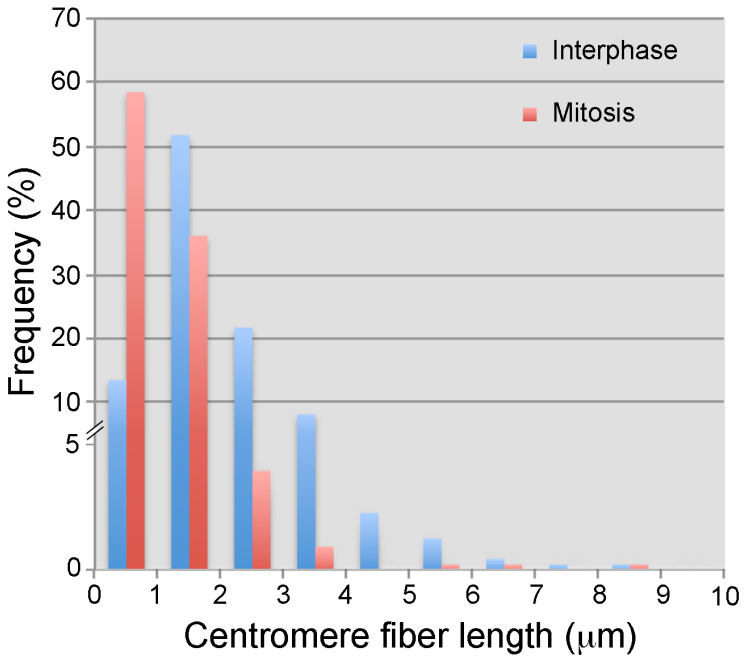
Frequency (%)
70
60
50
40
30
20
10
5
0
Interphase
Mitosis
0
1
2
3
4
5
6
7
8
9
10
Centromere fiber length (μm)

The slope of the line of best fit confirmed that greater unfolding directly correlates with the decrease in fluorescence intensity. Overall, this analysis of the data demonstrated that GFP fluorescence intensity decreased with the increase of the fiber length as expected from the quantification of single fibers.

These results showed that the interphase pre-kinetochore has the potential to unfold to twice the length of its mitotic counterpart (1.97 μm +/-1.27 versus 1.09 μm +/- 0.65), or, an alternative way to interpret this would be that the mitotic kinetochore is twice as compact as that of an interphase. These results support the common literature (Cheeseman and Desai, 2008; Maiato et al., 2004) since one of the key roles of a kinetochore, during mitosis, is to act as a platform for microtubule attachments and the propagation of pushing/pulling forces.

Following the observation that the data-sets displayed different patterns of distribution, it was considered whether a more rigorous statistical analysis would reveal some novel insights.

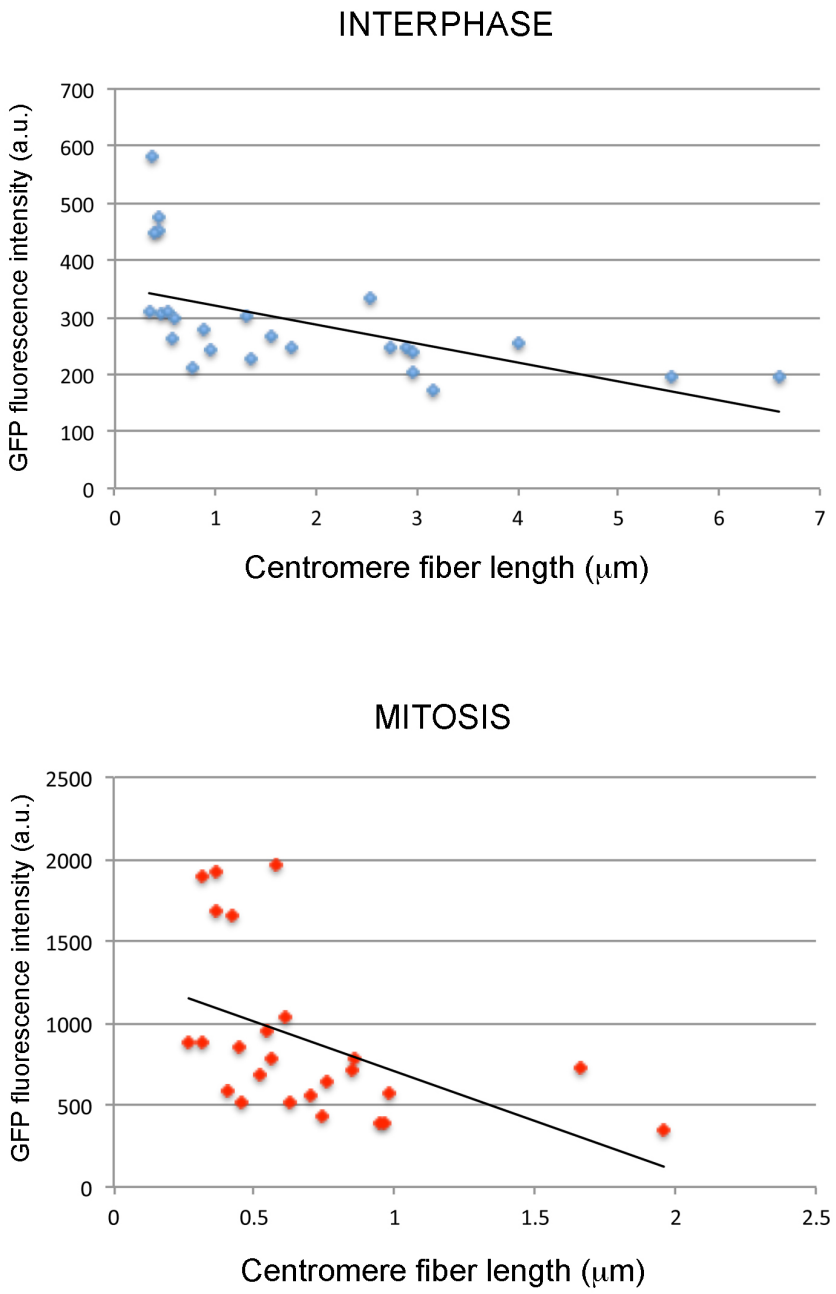

Figure 4.3. Correlation between GFP:CENP-A fiber length and GFP fluorescence intensity. 2D scatter plots representing fiber length measurements versus GFP fluorescence intensity values in 25 fibers, randomly chosen, for both interphase (blue) and mitosis (red). In addition, for both samples, the best fitting line was also calculated together with R squared value. The scatter plots show that longer fibers had weaker GFP fluorescent signals.

4.2.2 Kinetochore unfolding: a new approach to study the organization of the kinetochore chromatin

Due to the large sample size (655 measured fibers) for both interphase and mitosis samples, it was possible to increase the resolution of the data by plotting it into frequency histograms with smaller bin widths. To identify the most appropriate bin width for this sample size, several plots with a range of bins and bin width were attempted. Therefore, from the initial 10 bins (1 μm bin width) data were divided into 50 (200 nm), 60 (166 nm), 80 (125 nm) or 100 (100 nm) bins **(Figure 4.4 A)**. Strikingly, segmenting the data into 100 bin frequency histograms appeared to reveal the presence of distinct populations of fibers within the two data-sets visualized as distinguishable peaks **(Figure 4.4 A**, 100 bins**)**. The difference between both data-sets was most apparent when overlaid onto the same graph **(Figure 4.4 B)**. In mitosis (red bars) a majority of the fibers were short. Therefore the histogram bars were all present on the left end of the graph. In contrast, interphase fibers (blue bars) were rarely observed. A majority of the fibers were found between 1 and 2 μm. The remaining data consisted of a low number of very long fibers **(Figure 4.4 B)**.

In order to test more directly whether or not there were indeed subpopulations of fibers within the data-sets, a multi-peak analysis was performed. 100 bin histograms were chosen as the optimal number of bins applicable to this sample size. A higher number of bins caused saturation of the resolution potential and excessive breaks in the histogram continuity. This was shown when the data was allotted in 250 and 500 bins **(Figure 4.5 A** and **B)**. Multi-peak analysis was performed using the multi-peak fitting package 2.0 in Igor Pro 6.2 software (WaveMetrics) (2.8.2). Interestingly, the algorithm recognised five and three distinct peaks in fibers from interphase and mitosis respectively **(Figure 4.6 A** and **B**, red curves**)**, suggesting the presence of a subpopulations of unfolded centromeres. In addition, it was possible to

Figure 4.4. Increasing the number of bins improves the resolution of the data. A. Two columns of frequency histograms are represented containing fiber length data from interphase (left column, blue bars) and mitotic samples (right column, red bars). Columns show a progressive revealing of substructure of the histograms. This was obtained by adjusting the number of bins and bin width (bin width indicated in brackets): 50 bins (200 nm), 60 bins (166 nm), 80 bins (125 nm) and 100 bins (100 nm). On the x axis centromere length is expressed in μm, while on the y axis frequency of fibers allotted in each bin is represented expressed in percentages. The scale on the y axis has been kept different for interphase and mitosis to allow a better visualization of the peaks in the two data sets. **B.** Frequency histograms containing both data sets allotted into 100 bins (100 nm) were merged together into one graph with the same scale on the y axis. At the optimal bin width of 100 nm putative subpopulations of fibers are observed in both data-sets.

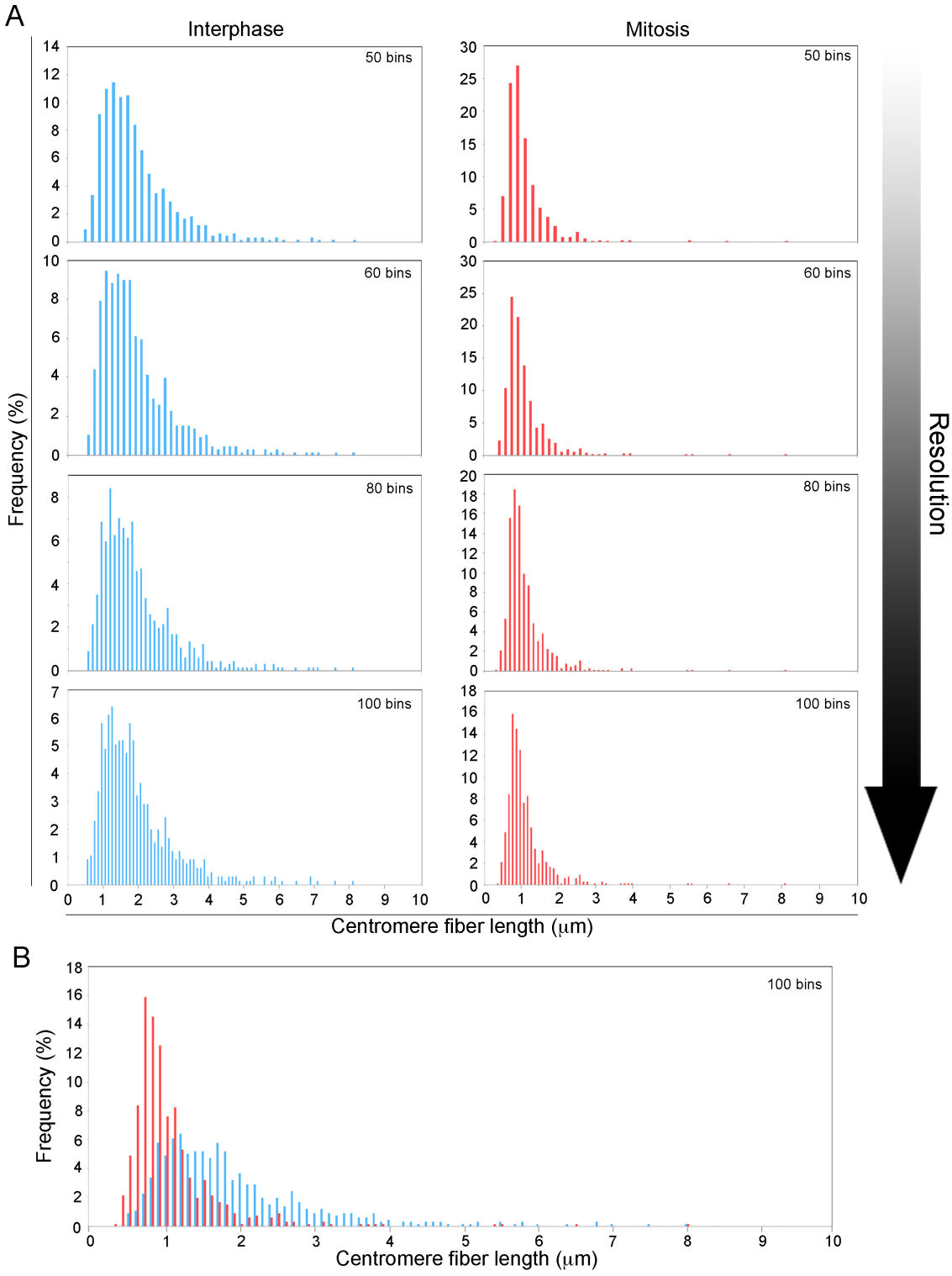
A
Interphase
Mitosis
50 bins
60 bins
80 bins
100 bins
Frequency (%)
Centromere fiber length (μm)
Resolution
B
100 bins
Frequency (%)
Centromere fiber length (μm)

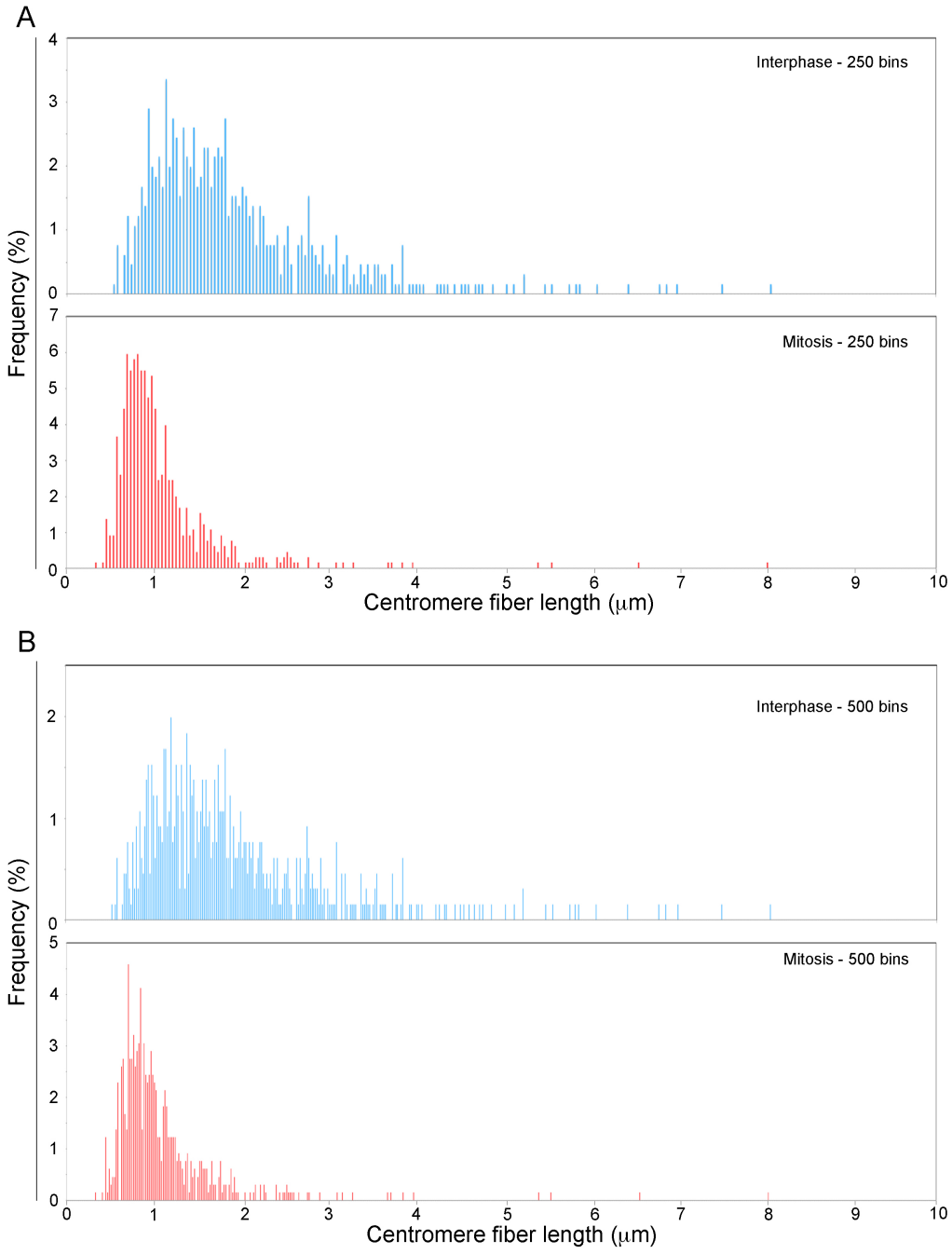

Figure 4.5. The maximum number of bins in which is possible to divide the data is limited by the sample size (n number). For both interphase and mitotis data sets the fiber length measurements were allotted in 250 and 500 bins with bin width of 40 and 20 nm respectively, on the x axis. On the y axis the height of the histograms showed the frequency in which each range of length was represented in the population of fibers. Dividing the data sets in a number of bins greater than 100 with an n number of 655 fibers measured caused the disappearance of clear peaks, which were observed at 100 bins.

visualize the best fitting curve **(Figure 4.6 A** and **B**, blue line**)**. The quality of the fit was measured by the presence of small residuals and the chi-square value **(Figure 4.7)**. Using, Igor Pro software it was also possible to identify the exact localization of each peak in a space scale expressed in μm. The distance between two adjacent peaks was measured and the mean of all the intervals present calculated for the two samples. Intervals of 0.615, 0.464, 0.506 and 0.725 μm were found between peaks from interphase. Remarkably these reflect four approximally equal steps of unfolding (mean = 0.577 μm). In mitosis, intervals were 0.449 and 1.248 μm with a mean of 0.424 μm, where the value 1.248 was counted three times (as a multiple of 0.5 μm) **(Figure 4.6 C)**.

These distances have provisionally been interpreted as steps of unfolding of constituent repetitive units of kinetochore chromatin. These could potentially help estimate the amount of chromatin present on average in each chromatin layer that composes the kinetochore. The mean between the interphase and mitotic step of unfolding (0.577 and 0.424 μm) was calculated equal to 0.5 μm.

Next, both the position and area of each peak were registered and compared, to test whether any of the subpopulations of fibers were common to both data-sets. From the listed values for peak areas **(Figure 4.8)** it was possible to identify two common populations of fibers, across the samples, which were located at ~ 1 μm and at 2.7 μm **(Figure 4.8**, peaks 1 and 4 interphase; peaks 2 and 3 mitosis**)**. When comparing just these peaks the amount of fibers present in mitosis was lower than the one in interphase; this was in agreement with the presence of a greater peak in mitosis at 0.8 μm **(Figure 4.8**, peaks 1 mitosis**)**. In contrast, in interphase two intermediate and one final peak were identified that were undetectable in mitosis **(Figure 4.8**, peaks 2, 3 and 5**)**. Peak-associated colours indicate how the fiber populations distributed in the transition between interphase and mitosis.

These results suggest the existence of a repetitive module underlying the kinetochore structure detectable in both interphase and mitosis. This module is constituted by multiple 500 nm lengths of chromatin. The amount of chromatin present at the kinetochore throughout interphase and mitosis apparently remains constant however the packaging of the layers changes, with increased constraints

during mitosis. If the kinetochore is indeed composed of stacked layers, the nature of the connections between different layers still remained unclear. Following these findings, we next decided to use our newly applied statistical approach to identify which CCAN components are, or are not, relevant for the maintenance of ordered 500 nm arrays of layers. For this, I performed fiber analysis on numerous conditional knockout and deletion cell lines.

Figure 4.6. The centromere is composed of multiple dynamic chromatin layers. Unfolded fiber data from interphase and mitosis samples was plotted as frequency histograms and analysed with a multi-peak fitting algorithm using Igor Pro software (**2.8.3**). In panels **A** and **B** are probability density histograms. The y and x axes show frequency and centromere fiber length (μm) respectively. The data sets are divided in 100 bins with a resolution of 100 nm per bin. Putative populations of fiber lengths within the two data sets were highlighted by discrete peaks (red curves). The best fitting curve is shown (blue line) for both samples. **C**. Schematic representing the location of the peaks (μm) and the length of the intervals between two adjacent peaks (μm). The average step of unfolding was calculated as a mean of these numbers where 1.248 μm was interpreted as 3X of the 0.5 μm step.

A

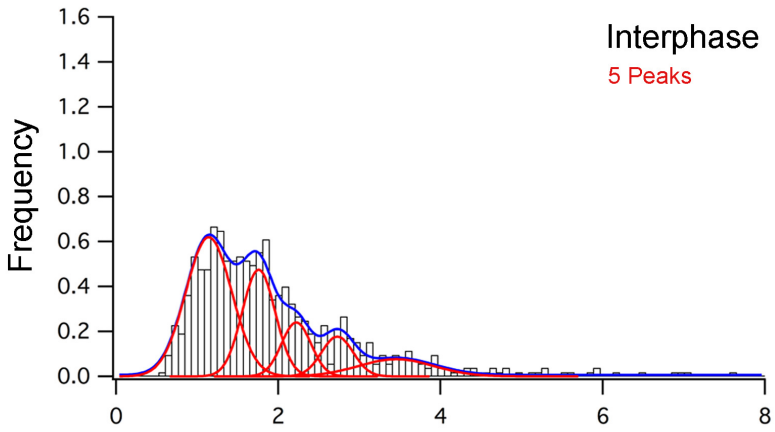

B

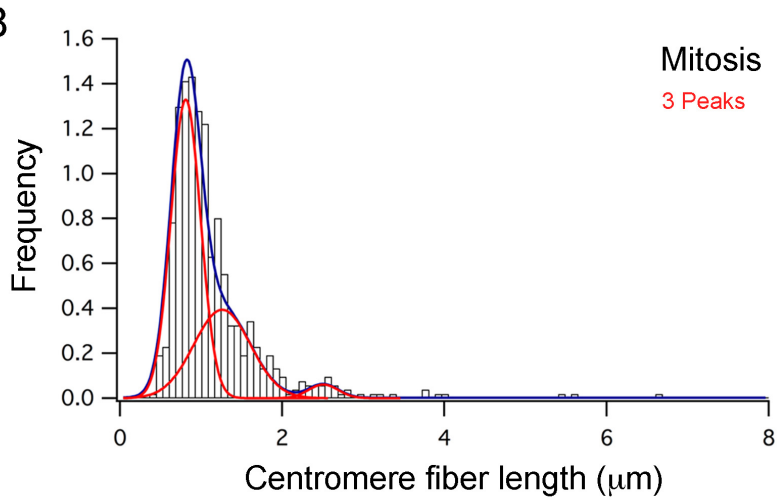

C

	Peaks	1	2	3	4	5
Interphase	Sub-populations of fibers (μm)	1.142	1.757	2.221	2.727	3.452
	Intervals (μm)	0.615	0.464	0.506	0.725	
Mitosis	Sub-populations of fibers (μm)	0.81	1.259	2.507	X	X
	Intervals (μm)	0.449	1.248			

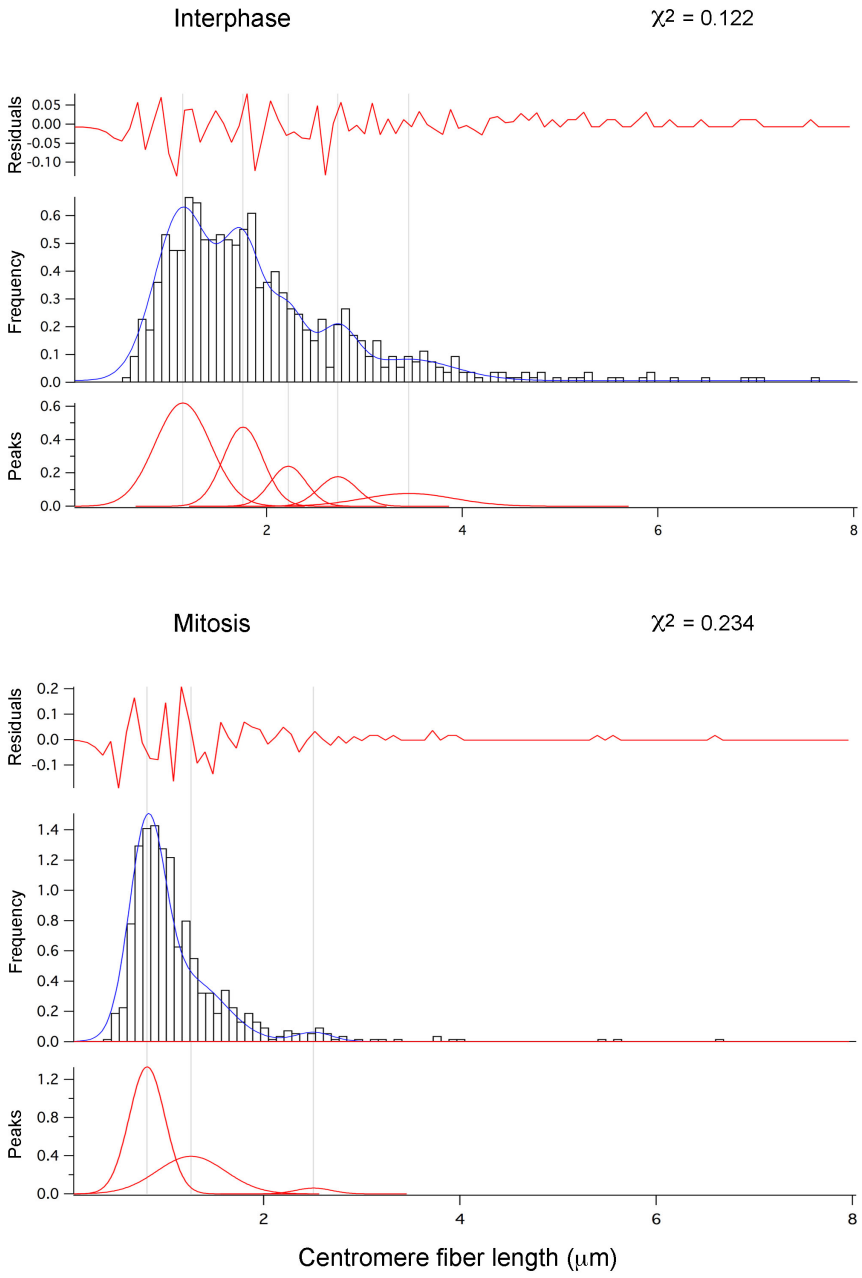

Figure 4.7. Evaluation of the quality of fit of the multi-peak analysis carried out with Igor Pro. A complete series of graphs obtained during a multi-peak fitting of the input data for the two data-sets is shown. Similarly to the previous graphs, on the y axis were plotted frequencies whilst on the x axis was the fiber length (μm). For each sample, the upper diagram highlighted the amount of residuals. The larger the residuals, the worse is the fitting function. In addition the software calculated a chi-square value, which could be employed to calculate the p value together with the degrees of freedom (DF, DF = 100 – 1 = 99). In the middle diagrams the best fitting curve is shown (blue line). In the bottom diagrams individual peaks identified during the analysis were illustrated (red curves).

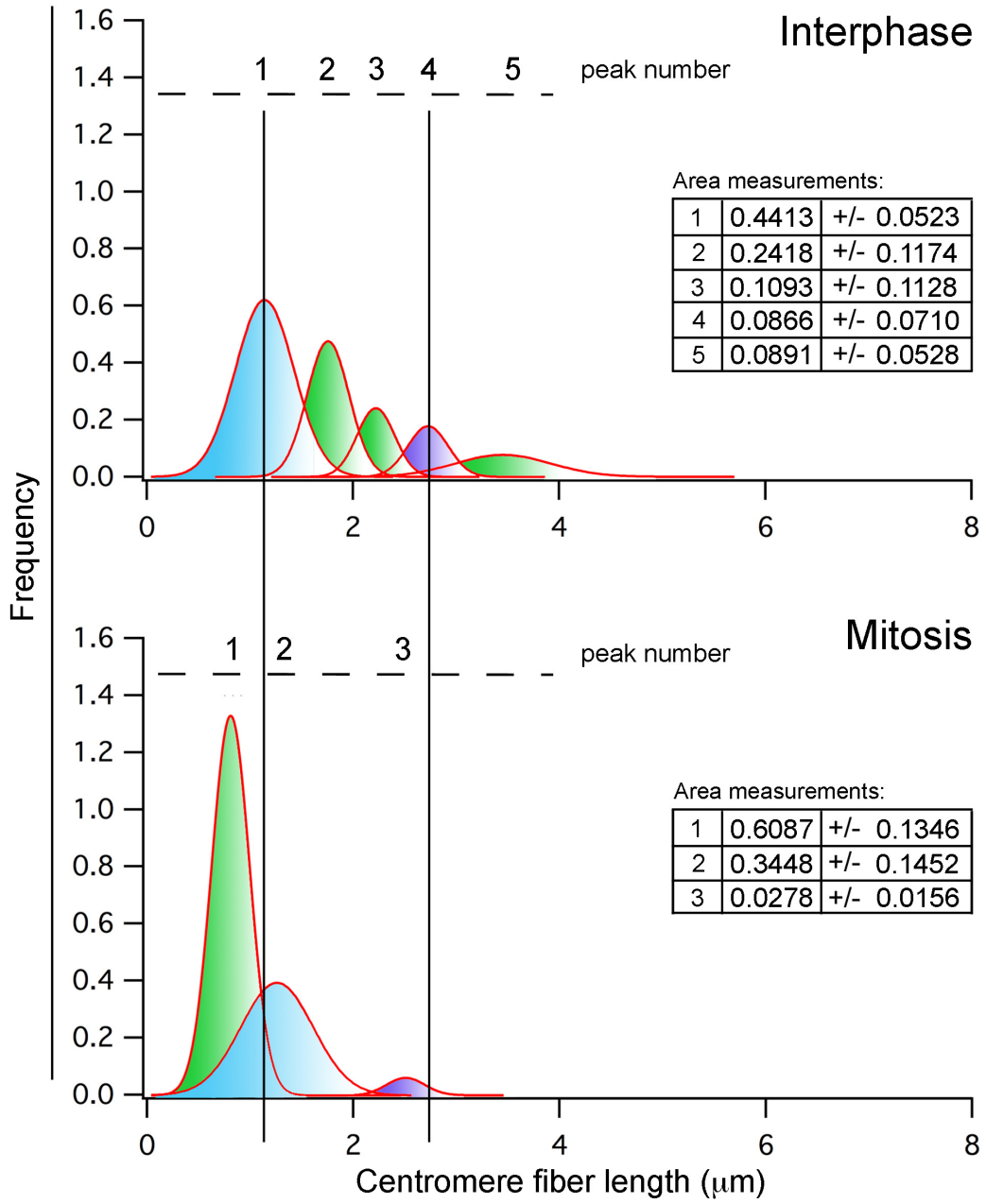

Figure 4.8. Changes in compaction of centromere chromatin layers at the transition of interphase with mitosis. Individual peaks obtained from the multi-peak analysis were aligned along the x axes and straight lines were drawn from peaks in interphase down in the mitotic peaks crossing shared peaks between interphase and mitosis. The values for the area of each peak are shown in tables. Looking at the area values it was possible to highlight with different colours putative common fiber populations between the two data sets.

4.2.3 Generation and characterization of conditional knockout (KO) and deletion (Δ) cell lines stably expressing GFP:CENP-A

Following the identification of structural differences in kinetochore chromatin between interphase and mitosis, cell lines allowing the depletion of CENPs were used to perform centromere unfolding analysis with the aim of identifying novel contributors to kinetochore structure.

The original conditional knockout (KO) and deletion (Δ) cell lines (donated to our laboratory by Prof. Fukagawa) did not express a fluorescent centromere marker, therefore it was necessary to generate new cell lines expressing GFP:CENP-A. Stable lines made included: CENP-H KO GFP:CENP-A; CENP-I KO GFP:CENP-A; CENP-O Δ GFP:CENP-A; CENP-S Δ GFP:CENP-A; CENP-C KO GFP:CENP-A. A comprehensive list of conditions used to make these cell lines is present in the Materials and Methods of this thesis (section **2.4.4**). After antibiotic selection, growing colonies were expanded and screened for GFP expression by flow cytometry (FL1-H profiles for green fluorescence shown in **2.4.4**) and further characterised by immunofluorescence. The final clones chosen showed the correct localization of GFP:CENP-A, as showed by the co-staining with anti CENP-T antibody, in every stage of mitosis and interphase **(Figure 4.9 A)**. To test that the presence of doxycycline (and therefore depletion of target proteins) did not affect GFP:CENP-A expression/localization cells were next treated with doxycycline, fixed, and probed with anti CENP-T antibody. GFP:CENP-A signal co-localized with CENP-T immuno-staining at kinetochores in both mitosis and interphase **(Figure 4.10)**. The expression of exogenous CENP-A tagged with GFP did not affect the levels of endogenous CENP-A as demonstrated by western blotting analysis **(Figure 4.9 B)**.

To test that genetic engineering of the KO and Δ cell lines, for the additional expression of GFP:CENP-A, had not interrupted the tetracycline conditional depletion mechanism, growth curves were performed. To test cell viability in presence or absence of doxycycline cell vitality was monitored using Trypan Blue (**2.4.5**). It had been previously published that depletion of these proteins would cause

Figure 4.9. Characterization of CENP conditional knockout (KO) and deletion (Δ) cell lines stably expressing GFP:CENP-A. A. Indirect immunofluorescence analysis of CENP KO and Δ cell lines stably expressing GFP:CENP-A was performed in all the selected clones. Fixed cells were probed with anti CENP-T antibody. Signals were detected using Alexa Fluor 594 conjugated secondary antibody (red). DNA was counterstained with DAPI (blue). The signal of GFP:CENP-A (green) correctly co-localized with CENP-T at kinetochores in all selected clones. Scale bar, 5 μm. **B.** Immunoblot analysis of whole cell extracts prepared from KO and Δ cell lines. In each lane 3.5 X 10^5 cells were loaded. The membrane was incubated with primary antibodies raised against tubulin, GFP and GgCENP-A. Signals were acquired using IRDye® 680 and 800 conjugated secondary antibodies. The Li-Cor Odyssey system was used for signal acquisition.

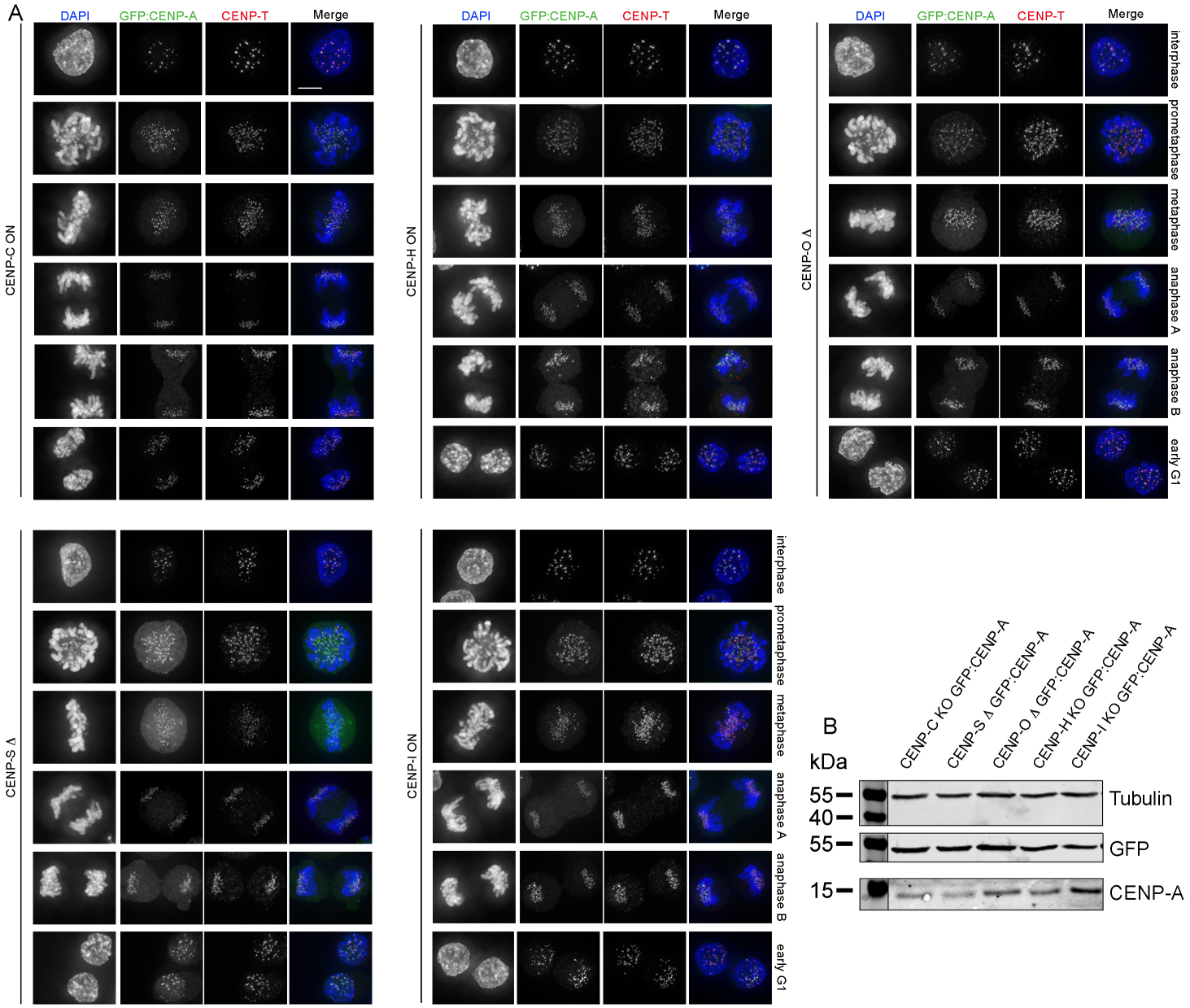
A
DAPI
GFP:CENP-A
CENP-T
Merge
CENP-C ON
CENP-H ON
CENP-O Δ
CENP-S Δ
CENP-I ON
interphase
prometaphase
metaphase
anaphase A
anaphase B
early G1
B
kDa
CENP-C KO GFP:CENP-A
CENP-S Δ GFP:CENP-A
CENP-O Δ GFP:CENP-A
CENP-H KO GFP:CENP-A
CENP-I KO GFP:CENP-A
55
40
55
15
Tubulin
GFP
CENP-A

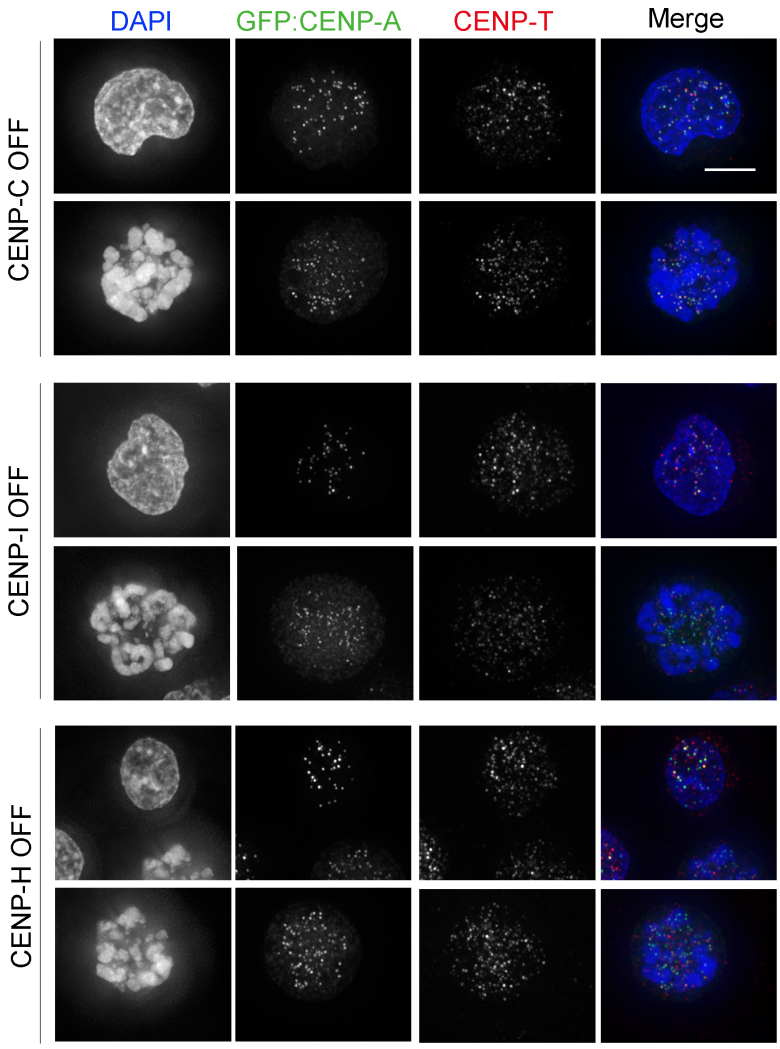

Figure 4.10. Localization of GFP:CENP-A in newly synthetized KO cell lines after doxycycline addition (CENP^{OFF}). Indirect immunofluorescence analysis of KO cell lines stably expressing GFP:CENP-A (green). Fixed cells were probed with anti CENP-T antibody. Signals were detected using Alexa Fluor 594 conjugated secondary antibody (red). DNA was counterstained with DAPI (blue). Even when each specific CENP was depleted the expressed GFP:CENP-A showed a correct co-localization with CENP-T staining at kinetochores. Scale bar, 5 μm.

an extension of the cell cycle (Amano et al., 2009; Fukagawa et al., 2001; Kwon et al., 2007; Nishihashi et al., 2002; Okada et al., 2006).

Newly generated KO and Δ cell lines (expressing GFP:CENP-A) were grown in parallel, with or without doxycycline present in the media **(Figure 4.11 A)**. Cells were counted every 24 hours. All the KO and Δ cell lines were able to divide when grown in standard media. In the presence of doxycycline, it was found that all of the KO cell lines either died or were unable to duplicate, whereas CENP-S and CENP-O Δ cell lines survived **(Figure 4.11 A**, + doxy**)**. These data suggest an unaltered response to tetracycline mediated repression of gene expression.

Following this successful functional test of CENP depletion by growth curves, I next analysed the new cell lines by western blotting. To do so, antibodies raised against chicken CENP proteins were used **(Table 2.3)**. Since antibodies raised against chicken protein are not commercially available, they had been previously generated, by rabbit inoculation, in collaborators laboratories. The Uniprot database was consulted to find out the size of the chicken centromere proteins analysed for detection **(Figure 4.11 B)**. As antibodies that are not commercialized can have low affinity for their target, and indeed CENP proteins are often in low abundance, protein samples deriving from whole cell extracts and nuclear extracts were tested.

Anti GgCENP-I antibody positively recognised a band of the right size in the KO cell line that disappeared after the addition of doxycycline **(Figure 4.11 D** yellow box, lanes 4 and 5**)**; however the same band was not present in the DT40 parental cell line (yellow box, lanes 2 and 3). This is likely due to the fact that in KO cell lines the transgene under tetracycline control inserted can be expressed at a higher level than the endogenous gene. In order to exclude any issue with the western blotting procedure itself, the membrane was additionally probed with anti GFP antibody that successfully recognised GFP:CENP-A (green box).

GgCENP-H at the predicted size of 26 kDa was not recognised with the anti GgCENP-H antibody **(Figure 4.11 E** yellow box**)**. The membrane was also incubated with anti GFP antibody and GFP:CENP-A was clearly identified (green box) in the samples. This suggested a lack of the antibody recognition rather than an unreliable performance of western blotting procedure.

Anti GgCENP-O and GgCENP-S antibodies were tested on portions of a membrane cut prior to antibody incubations **(Figure 4.11 F** and **G)**. Anti GgCENP-O antibody successfully identified one band between 35 and 40 kDa that was not present anymore in the CENP-O Δ cell line **(Figure 4.11 F** yellow box**)**. In contrast, anti GgCENP-S antibody did not highlight any band of ~ 15 kDa that was absent in the CENP-S Δ cell line **(Figure 4.11 G** yellow box**)**. In this case, incubation with anti GFP antibody was not performed as the anti CENP-O antibody clearly worked whereas anti CENP-S antibody did not.

Western blotting analysis of the CENP-C KO stably expressing GFP:CENP-A could not be tested as anti ggCENP-C antibody was not available in the laboratory.

As additional control, progenitor cell lines for each of the conditionally or stably depleted CENP were analysed in the laboratory by mass-spectrometry and an efficient decrease in levels of each of the proteins was observed (I.Samejima, data not shown).

In conclusion, new KO and Δ cell lines stably expressing GFP:CENP-A were generated. The cell lines showed an appropriate level of expression of GFP:CENP-A, which correctly localized at kinetochores, as demonstrated by co-localizing signals with CENP-T. In addition, the KO cell lines were still under tetracycline control for protein depletion as shown by growth curves and western blotting, where the antibodies worked.

Figure 4.11. Testing newly generated CENPs conditional knockout (KO) and deletion (Δ) cell lines stably expressing GFP:CENP-A. A. Representative growth curves of Δ and KO cell lines in absence and presence of doxycycline. Doxycycline was added or not at time 0 and cells were counted every 24 hours for the next five days. New KO cell lines were still under tetracycline control for CENP proteins gene repression. **B.** Schematic summarizing molecular weights of the CENP proteins analysed in chicken cells, expressed in kDa, as they appeared in the Uniprot database. **C.** Explanatory legend to apply in panels D, E, F and G. **Panels D, E, F and G.** WCE indicates whole cell extracts, NE nuclear extracts and PS protein standard. In each lane 6 X 10^5 cells were loaded. Signals were acquired using IRDye® 680 conjugated secondary antibody. The Li-Cor Odyssey system was used for signal acquisition. **Panels D and E.** Green boxes highlighted the band of GFP:CENP-A detected using anti GFP antibody. **D.** Immunoblot detection of GgCENP-I, lane: 1) PS; 2) DT40 expressing GFP:CENP-A WCE; 3) DT40 expressing GFP:CENP-A NE; 4) CENP-I KO expressing GFP:CENP-A WCE minus doxycycline; 5) CENP-I KO expressing GFP:CENP-A after addition of doxycycline WCE. **E.** Immunoblot detection of GgCENP-H, lane: 1) PS; 2) DT40 expressing GFP:CENP-A WCE; 3) DT40 expressing GFP:CENP-A NE; 4) CENP-H KO expressing GFP:CENP-A WCE minus doxycycline; 5) CENP-H KO expressing GFP:CENP-A after addition of doxycycline WCE. **F.** Immunoblot detection of GgCENP-O, lane: 1) PS at low or high exposure; 2) DT40 expressing GFP:CENP-A WCE; 3) CENP-O Δ expressing GFP:CENP-A WCE. **G.** Immunoblot detection of GgCENP-S lane: 4) DT40 expressing GFP:CENP-A WCE; 3) CENP-S Δ expressing GFP:CENP-A WCE.

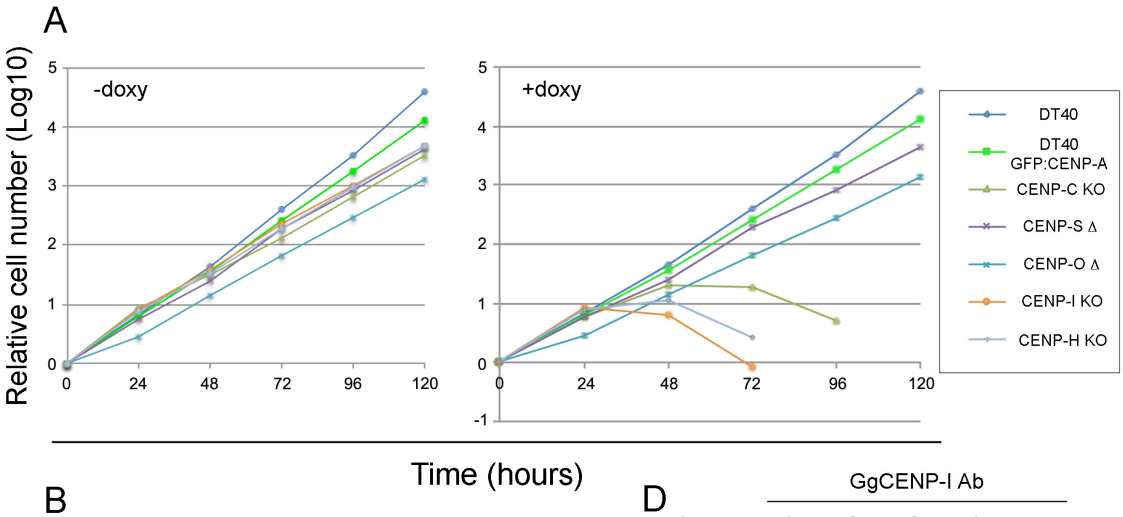

B

Protein name	Mass (kDa)
CENP-H	26
CENP-I	86
CENP-O	36.5
CENP-S	15.6

C

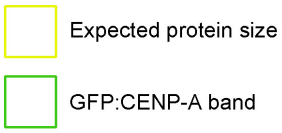

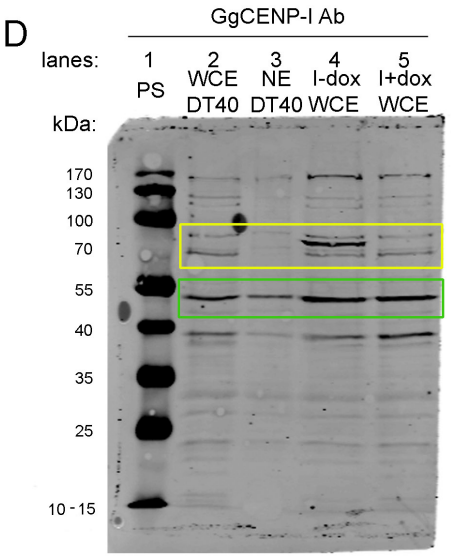

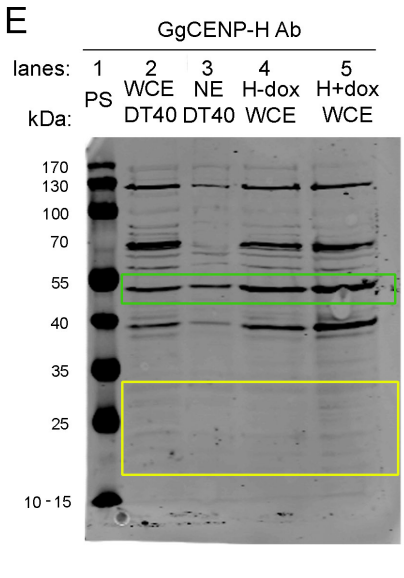

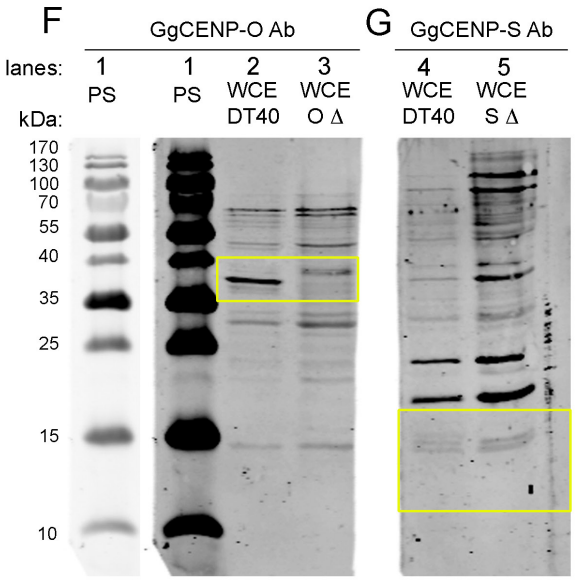

4.2.4 Depletion of CCAN components affects the structure of the kinetochore

Next, centromere stretching analysis was performed in mitotic cells, depleted of either CENP-C, -S, -H, -O and -I. These results were directly compared to the results obtained in the parental cell line. From here onwards, each sample depleted of a CCAN component will be indicated by the name of the protein followed by the word 'off' to highlight the absence of such protein. 60% confluent cultures of each cell line were treated with doxycycline for the appropriate time (**2.4.1**) and with nocodazole for 12 hours before generating fibers according to the TEEN protocol (**2.5.3**). DNA was stained with Hoechst to allow fiber visualization. Samples were subsequently imaged on a DeltaVision RT (Applied Precision) microscope. Centromere fibers were identified by the presence of the GFP signal marking CENP-A chromatin **(Figure 4.12 A)**. Fiber lengths were measured in ImageJ using the segmented line tool.

Strikingly, a large difference in the mean fiber stretching was seen between mitotic fibers of both CENP-C and CENP-S depleted samples **(Figure 4.12 B**, 2.81 μm +/- 1.97 and 2.44 μm +/- 2.14 respectively**)** compared with mitotic fibers from parental DT40 cells **(Figure 4.12 B**, 1.09 μm +/- 0.65; $p<0.0001$ for both comparisons**)**. Indeed CENP-C depletion in mitosis caused a greater fiber stretching than the one seen with parental interphase fibers **(Figure 4.12 B**, 1.97 μm +/- 1.27; $p<0.0001$**)**.

To assess whether the effect observed in CENP-S^{OFF} samples was due entirely to the lack of CENP-S, or to the loss of the entire CENP-T/W/S/X complex at kinetochores, an immunofluorescence experiment was performed in the CENP-S Δ cell line and fixed cells were incubated with anti CENP-T antibody **(Figure 4.13)**. CENP-T was still detected at kinetochores suggesting that CENP-S might a have a role in kinetochore structure in mitosis, which is CENP-T independent.

Figure 4.12. Unfolding of centromere chromatin in CCAN components depleted cell lines. A. Representative fluorescence images of fibers for each cell line. 60% confluent coverslips with KO and Δ cell lines stably expressing GFP:CENP-A were processed for chromatin unfolding with TEEN buffer (**2.5.3**). DNA was counterstained using Hoechst (blue). The centromere region was identified by the fluorescence of GFP:CENP-A (green). Scale bar, 1 μm. **B.** Boxplot displaying the spread of the data sets of fiber length measured in each cell line after a treatment with nocodazole of 12 hours to block cells in mitosis. The height of the box defines the interquartile range, whilst the whiskers indicate the 10^{th} and 90^{th} percentile. Each cell line was tested for significant difference in the spread of the data versus parental DT40 interphase and mitosis data. The only statistically not significant comparisons are highlighted in the graph (Mann-Whitney U test). The p values are indicated in the main text. The n number of measurements is specified in each box. **C.** Table summarizing the calculated p values for each comparison. **D.** Frequency histograms with 1 μm bin width. For each mutant (grey bars) parental DT40 interphase (blue bars) and mitosis (red bars) data were plotted in the same graph for direct comparison.

A

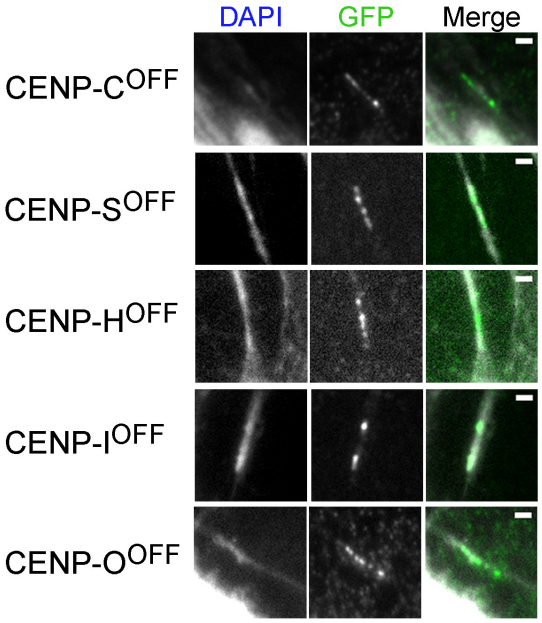

B

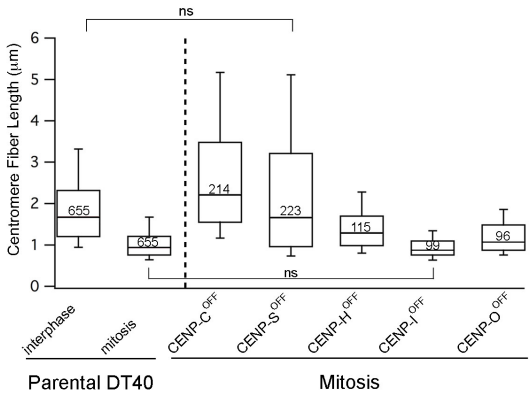

C

Obtained p values

Compare to :	Interphase parental DT40	Mitosis parental DT40
CENP-C^{OFF}	p < 0.0001	p < 0.0001
CENP-S^{OFF}	p > 0.05	p < 0.0001
CENP-H^{OFF}	p < 0.0001	p < 0.0001
CENP-O^{OFF}	p < 0.0001	p = 0.0002
CENP-I^{OFF}	p < 0.0001	p > 0.05

D

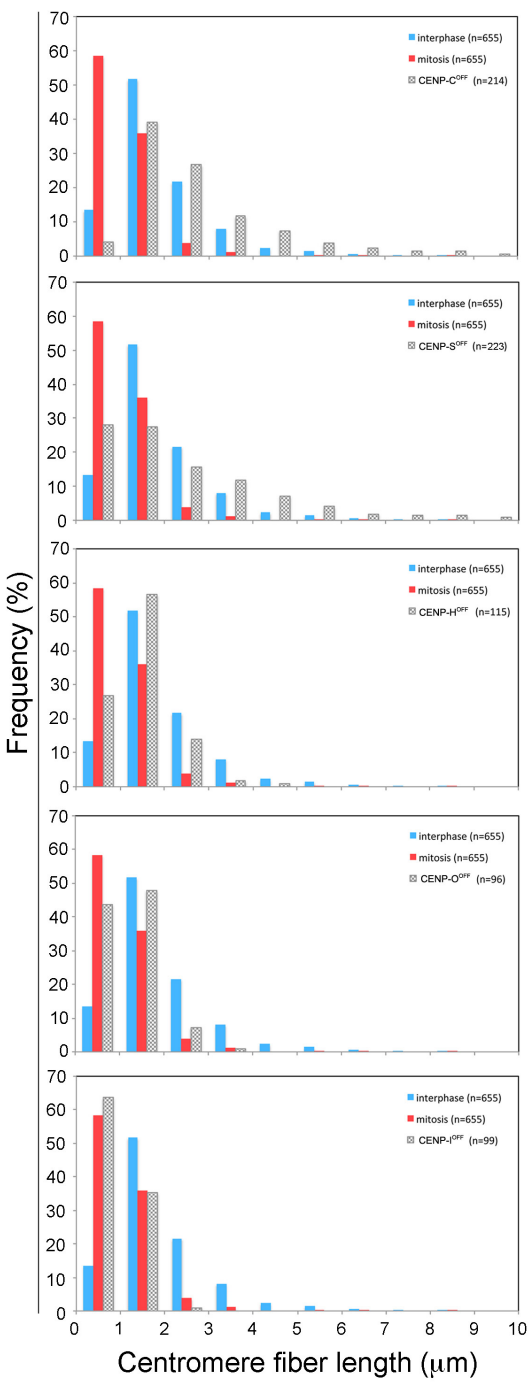

No statistically significant difference was seen between CENP-I depleted mitotic fibers and parental mitotic fiber length **(Figure 4.12 B**, 0.96 μm +/- 0.33; p>0.05**)**.

CENP-H and CENP-O depleted mitotic fibers showed a lower but still statistically significant difference from both parental interphase and mitosis fiber length **(Figure 4.12 B**, 1.43 μm +/- 0.62 and 1.21 μm +/- 0.50; Figure 4.12 C, p values table**)**.

Representing the data as frequency histograms with bin width of 1 μm **(Figure 4.12 D)** it became more apparent that CENP-C and CENP-S depleted cells blocked in mitosis behaved similarly to interphase parental cells, demonstrating an important role of CENP-C and CENP-S in creating a robust mitotic kinetochore structure; in contrast, histograms from CENP-I^{OFF} mitotic unfolded fibers better resembled the parental mitotic fibers, suggesting that the absence of CENP-I in mitotic kinetochores does not perturb the structure. CENP-H^{OFF} and CENP-O^{OFF} mitotic fibers stretched at an intermediate level between parental mitotic and interphase fibers, potentially indicating either a lesser essential role in holding mitotic kinetochore structure together or possibly effects on the targeting of CENP-C or CENP-S to kinetochores.

As previously, the number of bins used to cluster the data for further analysis was considered. The most appropriate bin width for the data acquired in the CENP depleted cell lines was 200 nm in 50 bins **(Figure 4.14)**. At 100 bins it was possible to observe an excessive increase in 'fuzziness' and breaks in the histogram continuity, particularly for CENP-C and CENP-S depleted fibers, when the measurements are spread over a large length range. In the case of CENP-H, CENP-O and CENP-I depleted fibers, although the curve profile at 100 bins was probably acceptable, for coherent and comparative purposes all the KO and Δ cell lines data was plotted in histograms with 50 bins.

A multi-peak analysis was performed using Igor Pro software (WaveMetrics) (**2.8.2**) **(Figure 4.15)**. Four peaks were identified in both CENP-C and CENP-S depleted mitotic fiber data-sets **(Figure 4.15 A)**, suggesting the existence of four subpopulations of fibers. The quality of fitting was satisfactory as indicated by

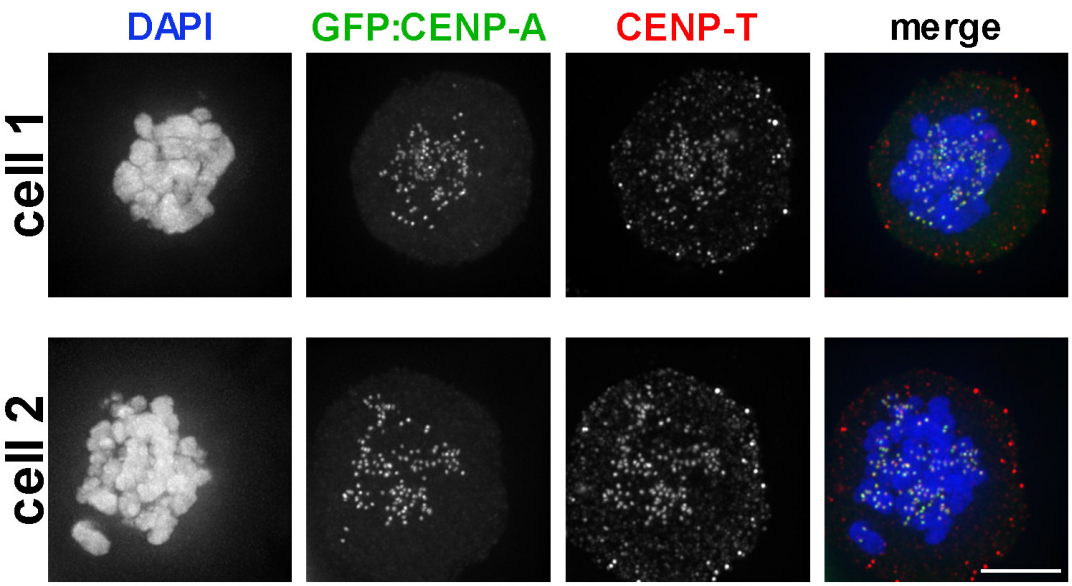

Figure 4.13. In CENP-S Δ cell line CENP-T is still present at kinetochores. Here are shown two representative images of CENP-S Δ cells stably expressing GFP:CENP-A used for measurements of unfolded fibers. Confluent coverslips were fixed and cells were probed with anti CENP-T antibody. Signals were detected using Alexa Fluor 594 conjugated secondary antibody (red). DNA was counterstained with DAPI (blue). CENP-T signal was normally detectable and showed co-localization with GFP:CENP-A (green) at kinetochores. Scale bar, 5 μm.

Figure 4.14. Testing data resolution by changing the histogram bin number in the CENP depleted data-sets. For each KO and Δ cell lines the fiber data were divided in 50 or 100 bins where the bin width was 200 or 100 nm respectively. On the y axis was represented the frequency expressed in percentages whilst on the x axis centromere length expressed in μm. Initially, the data-sets were allotted in 50 bins and successively into 100 bins. Clustering data in 100 bins seemed to better suit samples where the overall unfolding achieved was not high, however in the case of CENP-C and CENP-S depleted fibers, the histograms were often intercalated with gaps and started showing some 'fuzziness' indicating too low an n number of measurements for such a high number of bins. In order to analyse all the mutants under same conditions, 50 bins were used to represent the data in all cell lines for further analyses.

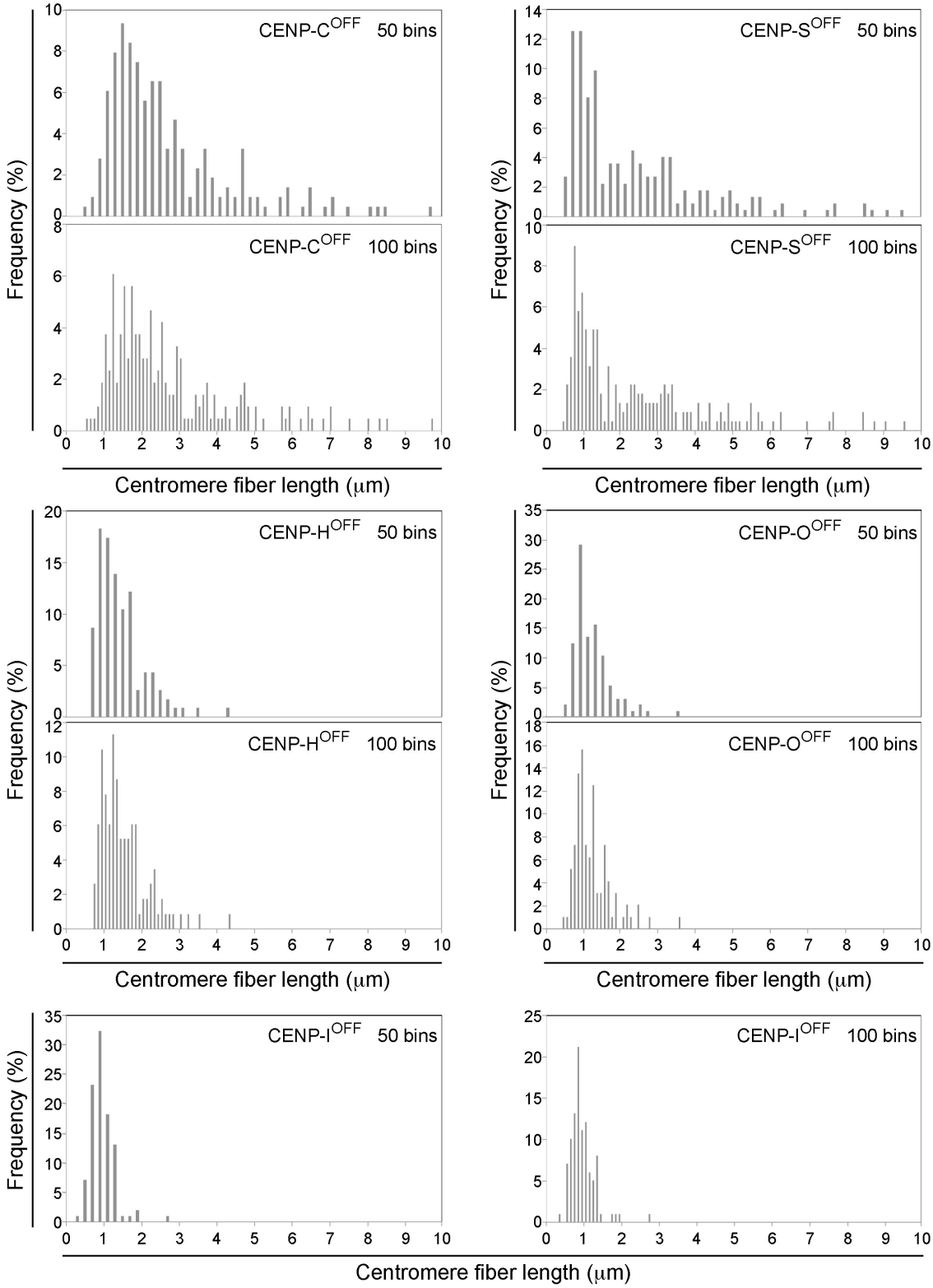
CENP-C^OFF 50 bins
CENP-C^OFF 100 bins
CENP-S^OFF 50 bins
CENP-S^OFF 100 bins
CENP-H^OFF 50 bins
CENP-H^OFF 100 bins
CENP-O^OFF 50 bins
CENP-O^OFF 100 bins
CENP-I^OFF 50 bins
CENP-I^OFF 100 bins
Frequency (%)
Centromere fiber length (μm)

the chi-square values and the residuals **(Figure 4.15 C)**. CENP-C^{OFF} mitotic fibers exhibited intervals between two adjacent peaks of 0.93, 1.38 and 0.97 μm. Interestingly, these are broadly all multiples of the step of unfolding of 0.5 μm measured in the parental cell line **(Figure 4.6 C)**. A similar pattern of unfolding was seen in CENP-S^{OFF} mitotic fibers **(Figure 4.16**, intervals = 1.22, 1.09 and 1.24 μm**)**.

In contrast, only two peaks were identified in CENP-H^{OFF}, CENP-O^{OFF} and CENP-I^{OFF} mitotic fibers **(Figure 4.15 B)** compared with three peaks in the parental mitotic sample **(Figure 4.6)**. The intervals for these samples were consistently close to 0.5 μm **(Figure 4.16)**. This suggested a possible hyper-constriction of the structure when those proteins were not present. Considering the interval values obtained from the multi-peak analysis of CENP depleted fibers, a mean unfolding step was calculated equal to 0.45 μm, where distance values close to 1 μm were counted twice and distance values close to 1.5 μm were counted three times.

In conclusion, a role of CENP-C and CENP-S in the maintenance of kinetochore structure was demonstrated. CENP-C and CENP-S depletion caused a major loosening of kinetochore structure, suggesting a function in bridging separated layers of chromatin. Decreased levels of CENP-H, CENP-O and CENP-I did not disrupt the structure of mitotic kinetochore although it is possible that the structure contracted instead. The mean step of unfolding in CENP depleted cell lines was calculated, supporting the hypothesis that multiple 500 nm layers of chromatin comprise the core component of kinetochore architecture.

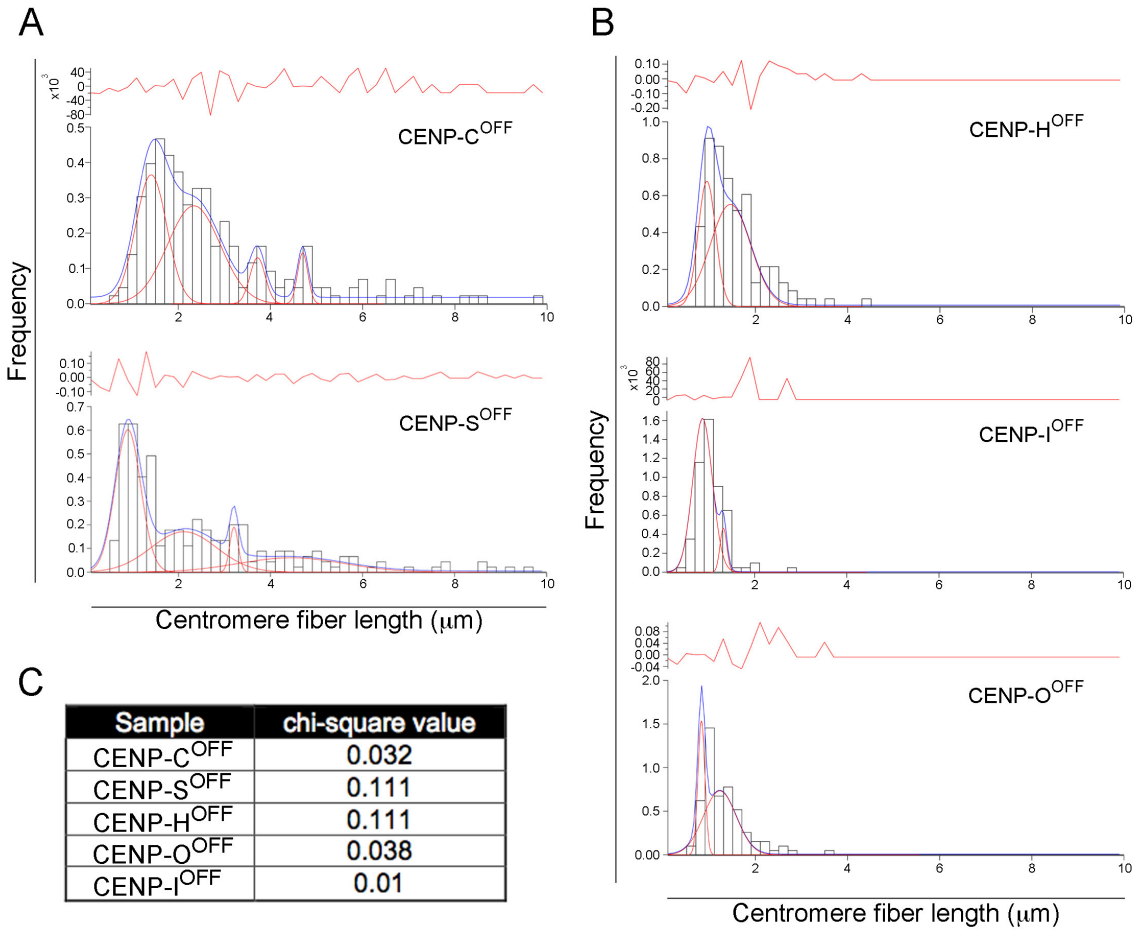

C

Sample	chi-square value
CENP-C^{OFF}	0.032
CENP-S^{OFF}	0.111
CENP-H^{OFF}	0.111
CENP-O^{OFF}	0.038
CENP-I^{OFF}	0.01

Figure 4.15. Multi-peak analysis of the unfolding data-sets in CENP depleted cell lines. Data from KO and Δ cell lines was plotted as frequency histograms and analysed with a multi-peak fitting algorithm using the Igor Pro software. The cell lines were separated in two columns depending on whether their unfolding pattern resembled the parental DT40 interphase (A) or mitosis (B). **A.** and **B.** show probability density histograms. X and y axes express respectively centromere fiber length (μm) and frequency; the data-sets were divided into 50 bins with a resolution of 200 nm per bin. The histograms showed putative subpopulations of fiber length within the data-sets recognised by discrete peaks (red curves). In addition, the best fitting curve was shown (blue) for all the samples. The upper diagram for each sample highlighted the amount of residuals. The bottom panel shows the best fitting curve, histograms representing the data and peaks identified. The scale on the y axis was kept different for the different mutants to allow a better visualization of the peaks in each sample. **C.** Schematic summarising the chi-square values for each of the fitting proposed calculated by Igor Pro software. In this case the degrees of freedom are 49 (DF = 50 – 1 = 49).

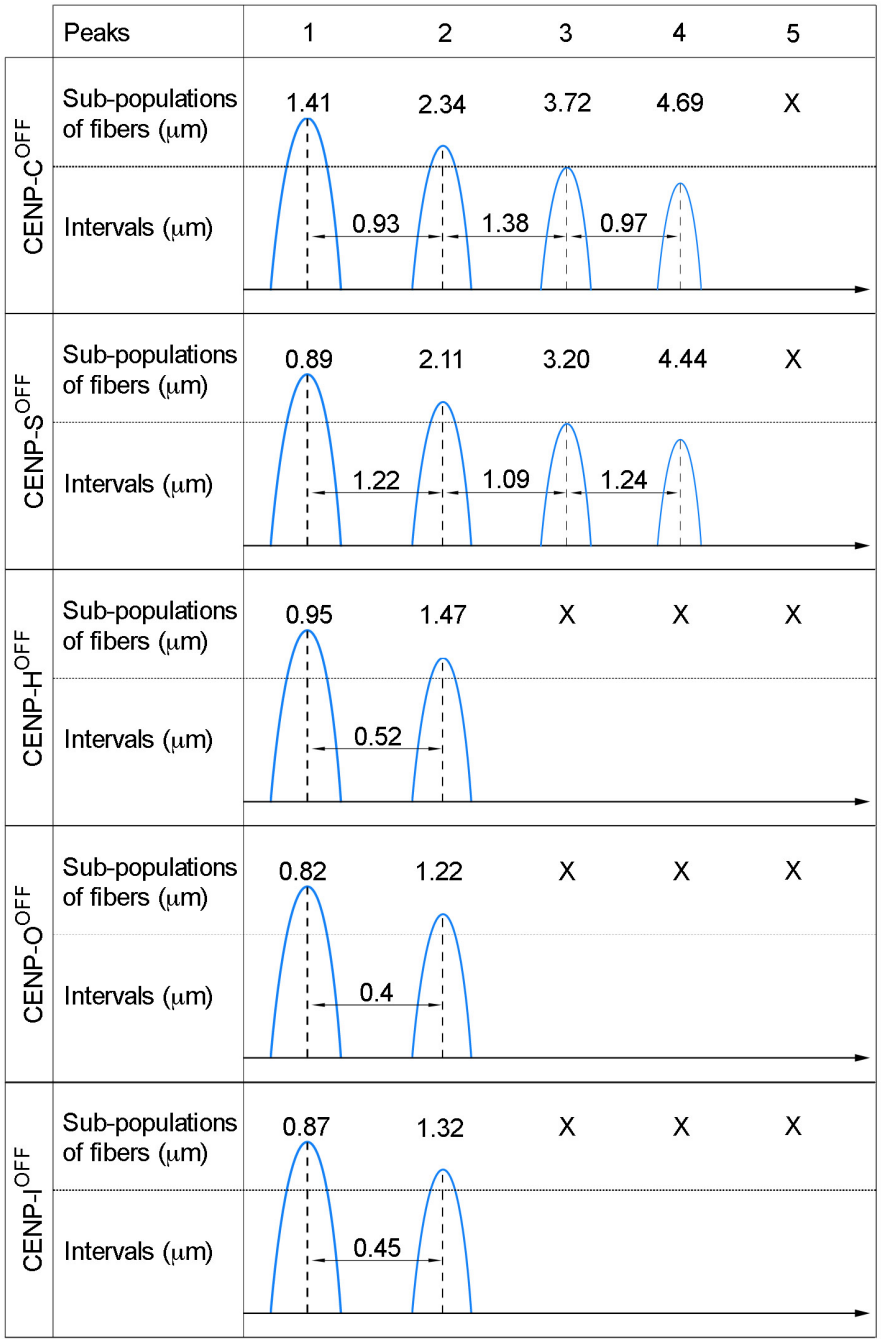

Figure 4.16. Quantifying the step of unfolding in the CENP depleted cell lines tested. Schematic showing the location of each peak (μm) and the length of the intervals between two adjacent peaks (μm). These numbers derived from the multi-peak analysis performed on the related data sets with the data allotted in 50 bins. The average step of unfolding across all the cell lines is 0.45 μm. This value was calculated by performing a mean of all the interval values, where values close to 1 μm were counted twice and values near 1.5 μm were counted three times.

4.2.5 Mapping the distribution of kinetochore components in unfolded fibers by PALM

Given that the depletion of CENP-C and CENP-S led to extended kinetochore fiber stretching by conventional light microscopy, I next considered whether super resolution microscopy of samples might provide additional insights into mapping kinetochore proteins onto chromatin fibers. Therefore, with the following experiments I aimed to observe differences in the localization of various CCAN components relative to CENP-A.

PALM is a single-molecule based microscopy technique that exploits the properties of 'blinking' or photo-switchable fluorescent molecules (Shcherbakova et al., 2014). Therefore DT40 cells stably expressing Dronpa:CENP-A were generated in order to perform the experiments. Parental DT40 cells were electroporated with a Dronpa:CENP-A expressing vector and plated with geneticin as a selective agent for one week (**2.4.4**). Growing colonies were expanded and screened for Dronpa expression by flow cytometry (FL1-H profiles for green fluorescence shown in **2.4.4**) and further characterised by immunofluorescence.

Since the use of highly specific primary antibodies is essential while performing PALM experiments, antibodies raised against chicken CENP-O, CENP-R and CENP-S proteins were first tested by immunofluorescence in DT40 cells stably expressing GFP:CENP-A using wide-field microscopy. The specificity of the antibodies was tested in both intact cells and stretched centromere fibers **(Figure 4.17 A** and **B)**. The three antibodies tested showed high specificity for kinetochores in intact cells and on chromatin, with the exception of GgCENP-S antibody, which in intact cells also seemed to stain nucleoli. Validated anti GgCENP-R antibody was chosen as the most reliable kinetochore marker and employed for the following PALM studies.

CENP-C KO and CENP-S Δ cell lines stably expressing Dronpa:CENP-A were seeded on conA coated coverslips (thickness 1.5, **2.7**). Samples were processed for chromatin fiber generation using TEEN buffer (**2.5.3**). After fixation,

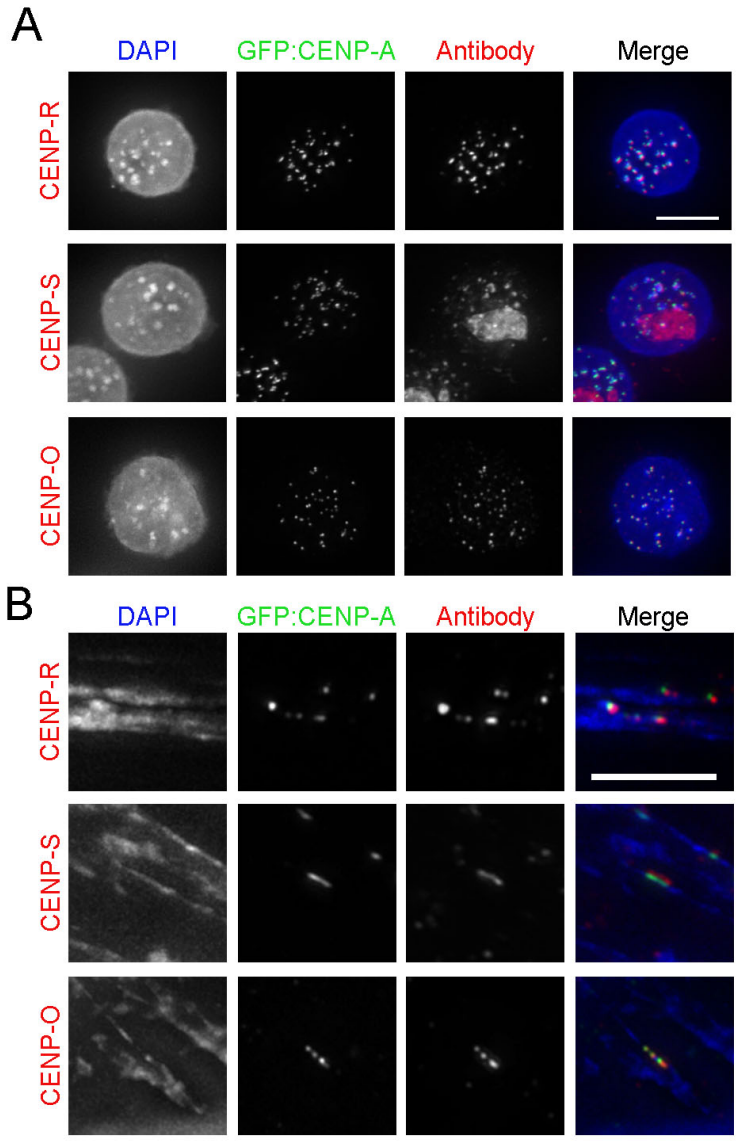

Figure 4.17. GgCENP antibody screening for PALM. A. GgCENP-R, GgCENP-S and GgCENP-O antibodies were tested in intact DT40 parental cells stably expressing GFP:CENP-A. Confluent coverslips were fixed in methanol (**2.5.2**) and probed with the antibodies separately. Signals were detected using Alexa Fluor 594 conjugated secondary antibody (red). DNA was counterstained by DAPI (blue). The centromere region was identified by the fluorescence of GFP:CENP-A (green). Scale bar, 5 μm. **B.** GgCENP-R, GgCENP-S and GgCENP-O antibodies were tested in stretched fibers of DT40 parental cells stably expressing GFP:CENP-A. 60% confluent coverslips were processed for fiber preparation using TEEN buffer (**2.5.3**). Antibody labelling was performed as explained in A. DNA was counterstained with Hoechst (blue). Scale bar, 5 μm.

samples were probed with anti CENP-R antibody, followed by incubation with Alexa Fluor 647 'blinking' secondary antibody. On the day of data acquisition, imaging chambers were mounted where samples were in direct contact with switching buffer (**2.7**); imaging was performed using an oil immersion 60X TIRF objective mounted on an inverted Nikon Eclipse TE2000 microscope. Following steps of analysis (**2.8.2**), results showed that CENP-A and CENP-R co-localized in control conditions with a frequency of 100% **(Figure 4.18**, CENP-C^{ON}, n=12 fibers**)**. However, when CENP-C or CENP-S were depleted the number of fibers in which co-localization between CENP-A and CENP-R was observed decreased to 66% and 63% respectively **(Figure 4.18**, CENP-C^{OFF} and CENP-S^{OFF}, n=9 and n=11 respectively**)**.

These findings, confirm our other data, suggesting that when CENP-C and CENP-S are depleted, ultra-structural changes in the kinetochore occur allowing the structure to lose compaction, such that CENP-A and CENP-R no longer co-localise in some cells.

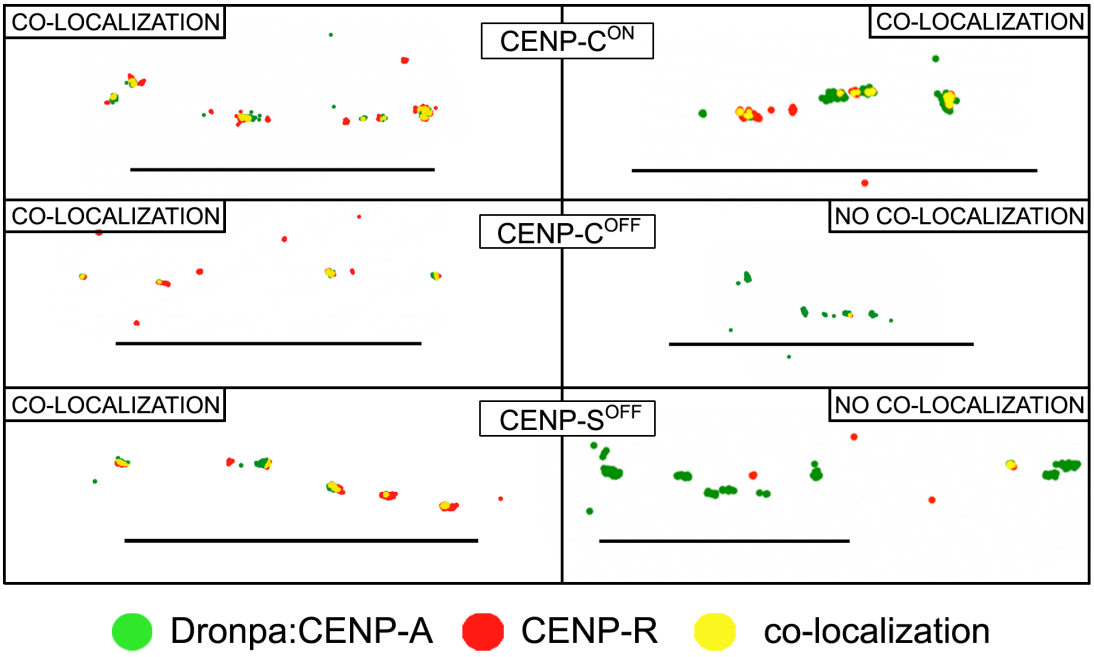

Figure 4.18. Analysis of kinetochore architecture by PALM. Reconstructed images of DT40 centromere fibers. DT40 cell lines stably expressing Dronpa:CENP-A were processed for generating chromatin fibers (**2.5.3**) and probed with anti CENP-R antibody. The signal was detected using Alexa Fluor 647 conjugated secondary antibody. Dronpa and Alexa Fluor 647 blinking properties were optimal into a switching buffer, which catalysed molecule blinking during laser irradiation. For each fiber, 500 frames were acquired in both channels and the movies were later processed through Igor Pro for particle recognition and coordinate assignment. Coordinates were imported in GraphPad where correction for photo-chromatic shift was applied and a graph generated. Green dots corresponded to Dronpa:CENP-A positions whilst the red ones to GgCENP-R positions along a chromatin fiber. Regions of co-localization were false-coloured in yellow. CENP-C^{ON}, n=12 fibers; CENP-C^{OFF}, n= 9; CENP-S^{OFF}, n=11. Scale bar, 7.4 μm.

4.2.6 Model for kinetochore folding

To better test the robustness of our findings, we generated an up-to-date model of the kinetochore ultrastructure. This model combined our findings with already known and generally accepted measurements of kinetochore dimensions **(Figure 4.19 A)** using the software Anim8or 3D Modeler. The parental DT40 interphase data predicts a kinetochore structure composed of five distinct layers of chromatin, corresponding to the five peaks recognised from the multi-peak algorithm in the same data-set **(Figure 4.6 A)**. Each layer contained ~ 500 nm of chromatin **(**average step size of unfolding, **Figure 4.6 C)** comprising both H3 and CENP-A nucleosomes **(Figure 4.19 A**, represented in grey and green respectively**)**. In the model, CENP-C was integrated as a linker between adjacent chromatin layers and intra-layer too. In the outermost layer CENP-C also extends towards the outer kinetochore in order to take contact with Mis12 (Hori et al., 2013; Przewloka et al., 2011). Estimating the total length of the chromatin in each layer it was possible to predict the number of nucleosomes assembled on such a length of chromatin. Nucleosomes size is known from EM and AFM measurements to be ~ 10 nm (Olins and Olins, 1978). By combining these known sizes with data from this thesis we would predict that ~ 50 nucleosomes could be associated with 500 nm of DNA **(Figure 4.19 B)**. Multiplying the number of nucleosomes for five layers of chromatin yields a total of 250 nucleosomes per chicken kinetochore **(50 X 5, Figure 4.19 B)**. If it is considered that one nucleosome occupies ~ 147 bp (or 200 bp including DNA linker), then 250 nucleosomes X 200 bp would predict that 50 kb of chromatin are present in a chicken kinetochore.

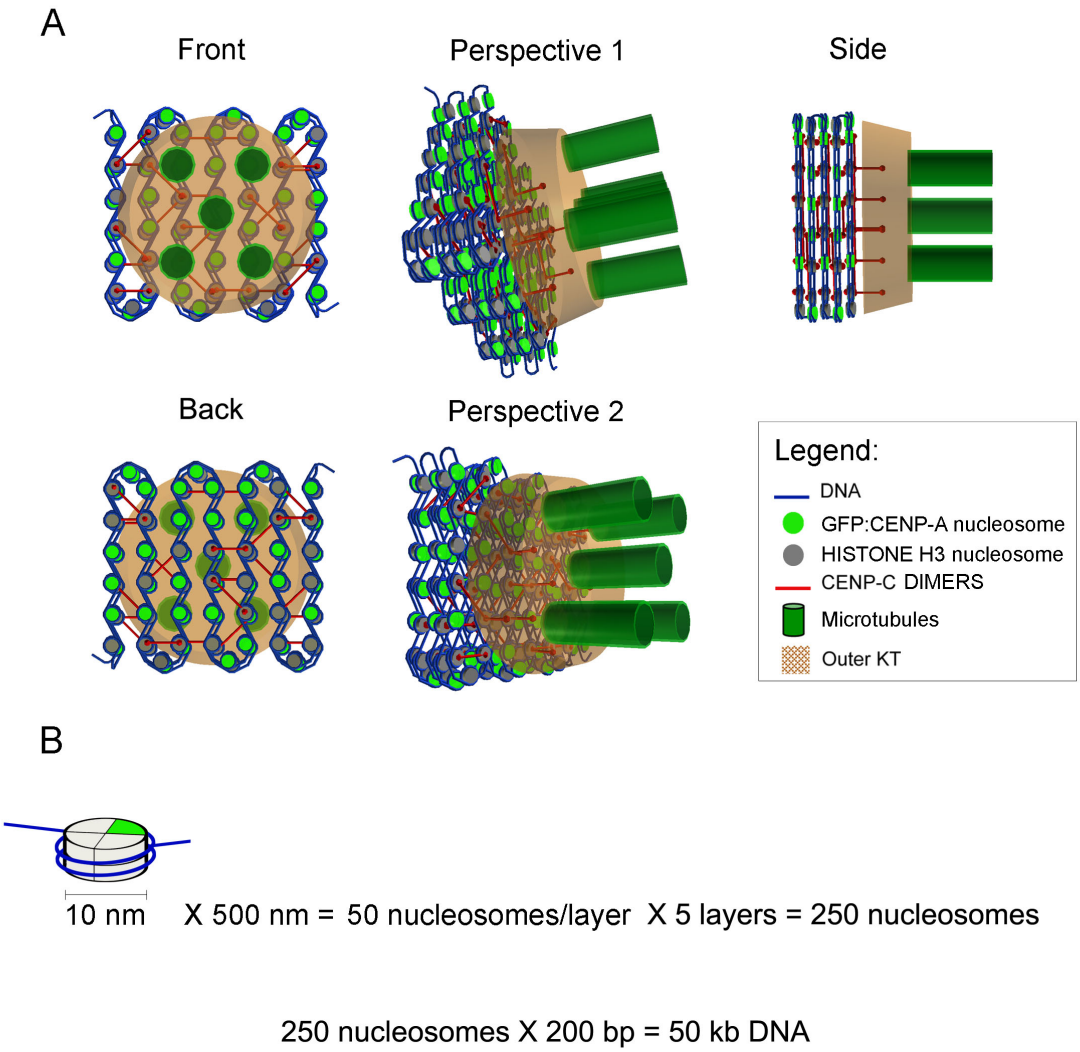

Figure 4.19. 3D model for centromere chromatin folding in a DT40 kinetochore. A. 3D model of the kinetochore chromatin designed with the free software Anim8or 3D Modeler. In the model the chromatin (blue) is wrapped around nucleosomes containing either GFP:CENP-A (green) or H3 (grey). On the basis of the data collected from parental DT40 cells in interphase, chromatin and nucleosomes are organised into repetitive units, with the shape of layers, which are composed by 500 nm of chromatin. Five layers of chromatin and nucleosomes would compose the inner kinetochore. Rod-shaped CENP-C dimers (red) can enter in contact with H3 directly and form a net of interactions between different layers and inside each layer, constituting a structural scaffold. CENP-S, not included in this model, from the data here presented clearly executes a similar function. In the outer most layers of the kinetochore, CENP-C molecules also engaged contact with Mis12, working as a bridge with the KMN network in the outer kinetochore (light brown round pattern). **B.** Schematic of the mathematics behind the calculation of the amount of DNA present in a chicken kinetochore.

4.3 Discussion and conclusion

The results presented in this chapter derived from a novel approach developed to tackle the as-yet unresolved topic of kinetochore chromatin fiber pucking. In order to answer our biological question we used stretched centromeres and measured their length looking at the fluorescence of GFP fused to CENP-A. Adopting chicken as model organism was decided on the basis of the highly reproducible unfolding procedure using TEEN buffer that did not require addition of detergents (**3.2.1**).

Initially, the study focused on highlighting differences in the structure of the kinetochore between interphase and mitosis. From chicken parental DT40 cells, it was necessary to generate a new cell line stably expressing GFP:CENP-A. It was important to confirm that the overexpression level obtained for CENP-A did not cause a spread of CENP-A in the pericentromeric region **(Figure 4.1 C)**. Once the cell line was obtained, cells were grown in absence or presence of nocodazole for the last 12 hours before fixation of interphase and mitotic samples respectively. As representative fluorescence images showed, interphase centromeres were more prone to stretch compared to mitotic ones **(Figure 4.2 A)**. For direct comparison, the entire collection of measurements for the two samples was represented in box and whiskers plots where the fibers unfolding was found to be significantly different **(Figure 4.2 B)**. This was the first time that a direct comparison between unfolded centromeres in interphase and mitosis has been quantified. Although interesting, this piece of data still did not fully reveal the internal organization of chromatin inside the kinetochore. Therefore a complex mathematical interpretation of the data was pursued.

We next aimed to test whether our large data-sets contained hidden subpopulations of fibers. This was the motivation for representing the data-sets as frequency histograms **(Figure 4.2 C)**. Achieving a high number of measurements allowed clustering of the data in bins representing 100 nm range of length **(Figure 4.4)**. It was previously suggested that chromatin at centromere could form a stack of loops (Sullivan and Karpen, 2004) or a layer of sinusoids (a boustrophedon) (Ribeiro et al., 2010). I therefore tested if it was possible to identify any repetitive units in the data-sets. Performing multi-peak analysis on the data-sets provided an insight to this

question. Five discrete populations of fibers were identified in interphase and only three in mitosis **(Figure 4.6 A** and **B)**. Each peak represented a node of accumulation of fiber lengths. One interpretation is that each peak represents unfolding of one layer of chromatin composing the kinetochore. The distance between two consecutive peaks can then be interpreted as the amount of chromatin comprising a chromatin layer **(Figure 4.6 C)**. The analysis identified a repetitive step of unfolding at the centromere of 0.5 μm. The spatial location of the peaks also suggested the presence of stronger forces holding together kinetochore chromatin along a shorter radius in mitosis compared to interphase. This could explain why, in mitosis, a lower number of peaks was detectable. Parameters used to assess whether the statistical analysis was reliable or not included residuals and chi-square values. Residuals, or fitting deviations, represent the difference between the observed values with the predicted sample mean and our best fitting curve. A positive value of residual suggests that the measured value is placed above the best fit curve whilst a negative one is referred to a value located underneath it. If the best fit curve passes through the value measured than there is no residual, therefore the residual equals zero. Comparing interphase to mitosis it was possible to observe that the fitting in interphase was probably more accurate than in mitosis as the range of the residuals was smaller **(Figure 4.7)**. The chi-square value here expressed is not on itself a p value, however it could be used to calculate the p value knowing the degrees of freedom (100 categories – 1 = 99 degrees of freedom).

Although only three peaks were detected in unfolded mitotic kinetochores, this does not necessarily imply that in mitosis there is a loss of chromatin but rather that in mitosis chromatin is more resistant to unfolding. On the basis of area measurements of the peaks it was possible to map the extra peaks present in interphase onto those detected in mitosis **(Figure 4.8)**. This tighter packaging chromatin during mitosis is probably due to the presence, at this stage of the cell cycle, of a mature kinetochore complete with the outer kinetochore proteins.

Next, we wanted to test whether the removal of specific CCAN components could affect kinetochore unfolding. The original conditional knockout and deletion cell lines were engineered to stably express GFP:CENP-A **(Figure 4.9** and **Figure**

4.10). When treated for an appropriate length of time in doxycycline, as specified in the methods section (**2.4.1**), cells were tested for protein depletion and doubling time **(Figure 4.11)**.

When TEEN experiments for chromatin stretching were performed with mitotic samples, the unfolding measurements revealed different levels of stretching depending on which member of the CCAN was depleted. Measurements of CENP depleted kinetochores were collected into box and whiskers plots. These showed that the absence of CENP-C and CENP-S in mitosis allowed an increase in the stretching of centromere fibers. In contrast, depletion of CENP-H, CENP-O and CENP-I did not profoundly change the organization of kinetochore chromatin **(Figure 4.12)**.

In parallel experiments, PALM analysis of centromere architecture in cells depleted of CENP-C or CENP-S confirmed the establishment of a less rigid and organised structure **(Figure 4.18)**.

Previous studies found CENP-C to be a fundamental component of kinetochore stability (Ribeiro et al., 2010). CENP-C is located at the inner kinetochore (Wan et al., 2009) where it can form dimers (Carroll et al., 2010) bridging nucleosomes. It was also reported, using chicken cells, that there is a direct interaction between CENP-C and H3 nucleosomes (Hori et al., 2008a). In addition, CENP-C represents a bridging point between the inner and outer kinetochore since it interacts with Mis12 (Hori et al., 2013; Przewloka et al., 2011; Screpanti et al., 2011). In agreement with this, our results confirmed a destabilisation of the structure of the kinetochore after CENP-C depletion and its effect was quantified 'in size' for the first time. We hypothesized that dimers of CENP-C can connect H3 nucleosomes present on the same or on different layers of chromatin so that, once CENP-C is depleted, more than one layer of chromatin unfolds **(Figure 4.15 A)**. This is in agreement with work recently published where the authors claim that the majority of CENP-C is restricted to the inner kinetochore and not extending into the outer kinetochore (Suzuki et al., 2014).

The CENP-S results are even more striking, as they assign to CENP-S a new role as a kinetochore structural pillar. In agreement with this finding a previous study reported that CENP-S depletion caused the formation of a longer outer plate of the

kinetochore (Amano et al., 2009). In contrast, CENP-I depletion, although not causing a statistically significant increase in kinetochore unfolding, appeared to cause an increase in the constriction between chromatin layers. CENP-I has been recently linked to the spindle checkpoint, particularly to the recruitment of Mad1 through the RZZ complex (Matson and Stukenberg, 2014). I hypothesize that CENP-I could act like a spring in the kinetochore, allowing some 'breathing' in the structure so that checkpoint components can bind in the event of microtubule detachment. CENP-H depletion does not dramatically affect the structure of the kinetochore, however the change in kinetochore structure observed in CENP-H^{OFF} samples might be related to a partial impairment in the localization of CENP-C, as previously described (Fukagawa et al., 2001). One interpretation of our data and previous observations is that when CENP-H is depleted, only a fraction of CENP-C is retained at the kinetochore, and this fraction is sufficient to hold chromatin layers together within the kinetochore. Equally to CENP-H, effects of depletion of CENP-O on kinetochore structure are only marginal, however data in *S. cerevisiae* support a structural role of COMA complex (CENP-O-P-Q-U-R complex homolog) in the looping of centromere chromatin (Anderson et al., 2009). This could explain the relatively mild effect that we were able to quantify.

After performing multi-peak analysis on the conditional knockout and deletion cell lines the mean step of unfolding was calculated and found it to be ~ 450 nm **(Figure 4.16)**. Depletion of CENP-C and CENP-S caused double or triple size steps of unfolding, supporting our model that predicts CENP-C and CENP-S to function as anchoring points between different layers of chromatin.

By combining our novel data with classical measurements of nucleosome size we generated a model, which predicts that 50 kb of DNA are included into a chicken kinetochore. This number is remarkably close to the size of chromatin domains occupied by CENP-A in chicken neocentromeres, ~ 40 kb, (Shang et al., 2013) and to the amount of DNA in chicken kinetochores measured by quantitative fluorescent microscopy, ~ 50-60 kb, (Ribeiro et al., 2014). This result is also very similar to new evidence in human cells, where the total number of CENP-A nucleosomes has been identified equal to 200 (Bodor et al., 2014), therefore roughly 40 kb of chromatin

would be the amount of DNA predicted in this study to be at the kinetochore, if one excludes the H3 nucleosome fraction.

In conclusion the present study provided, for the first time, strong evidence supporting the existence of a 500 nm repetitive chromatin unit at the base of chicken kinetochore structure, which includes a total amount of chromatin of 50 kb. A quantified difference in kinetochore organization between interphase and mitotic data-sets was also shown. Additional data on kinetochore structure in absence of members of the CCAN network highlighted a new role for CENP-S in contributing to kinetochore structure and confirmed CENP-C as an essential component for the maintenance of kinetochore architecture.

In the future, this unfolding analysis could be extended to outer kinetochore components, to evaluate their role in kinetochore structure, and to post-translational modifications. In addition, the synergistic effect of simultaneous removal of CENP-C and CENP-S on centromere stretching could be studied. To take this project onto another level, it would be interesting to continue fiber analysis using correlative light-electron microscopy (CLEM). This would potentially allow subnanometer measurements to be obtained.

5 Chapter 5: Characterisation of the novel kinetochore protein CENP-Z

5.1 Introduction

Despite the large number of publications associated with kinetochore, there is still significant information missing regarding its organization and composition. In 2010 our laboratory identified a novel group of putative kinetochore proteins by performing SILAC mass-spectrometry on isolated prometaphase chromosomes (Ohta et al., 2010). In this study, the use of several protein classifiers, combined with a 'machine learning' analysis, allowed the identification of 13 previously uncharacterised proteins. These proteins were described as kinetochore proteins from a cluster analysis and visualized at kinetochores during mitosis by microscopy. One of these *bona fide* kinetochore proteins is CENP-Z, also known as ZNF276 (NCBI gene ID: 92822). CENP-Z has two isoforms (isoform a: 67.2 kDa; isoform b: 59.8 kDa) that contain identical sequences with the exception of the first 75 aa at N-terminus of the isoform A, which are missing from isoform b. Both isoforms contain an N-terminus zinc finger associated domain (zf-AD) and a C-terminus zinc finger domain Cys_2His_2 (C2H2) fold group (Uniprot, Q8N554). Interestingly, the presence of a zinc finger domain suggests a potential role of CENP-Z in DNA binding. Moreover, analysis of putative interactors of CENP-Z using a protein-interaction database such as BioGRID (Stark et al., 2006), reported interactions in yeast two-hybrid screenings of CENP-Z with ZBTB8A and ATXN1. ZBTB8A is a zinc finger protein, which, in turn, interacts with lysine acetyltransferase 7 (KAT7). Similarly, ATXN1 is a chromatin binding factor reported to interact with the acetyltransferase 6A (KAT6A) and the histone deacetylase 4 (HDAC4) (BioGRID).

These observations suggest a role of CENP-Z in transcription regulation, making it an interesting candidate for investigating the role of transcription for kinetochore maintenance.

In this chapter, an initial characterization of the unknown CENP-Z/ZNF276 is presented. Here, CENP-Z kinetochore localization was confirmed. A more detailed

look at CENP-Z sequence conservation and secondary structure indicated the presence of a highly conserved region of the protein at the C-terminus. Using bioinformatics tools, the sequence of CENP-Z was compared with an atlas of proteins, with known structures. It was predicted that CENP-Z C-terminus could fold as a region of the histone-lysine n-methyltransferase, PRDM9, which catalyses trimethylation on H3K4. Having confirmed CENP-Z kinetochore localization in mitosis, the predicted PRDM9-like activity was tested. These results suggested a role of CENP-Z in modulating methylation states of lysine 4 of histone H3. As histone methylation profile can affect CENP-A loading (Bergmann et al., 2011; Kim et al., 2012), CENP-Z activity was tested for CENP-A recruitment at an ectopic chromosomal site. These last experiments demonstrated that CENP-Z is not necessary for CENP-A assembly. Furthermore, preliminary data showed that optimization of CENP-Z depletion by RNAi led to an accumulation of mitotic cells in prometaphase.

5.2 Results

5.2.1 Protein sequence conservation and secondary structure. Bioinformatics analyses of CENP-Z

CENP-Z is an uncharacterised protein and has no literature available. Therefore, we performed conservation and structural analyses using different on line tools, in order to predict its function.

The CENP-Z aa sequence for *Homo sapiens*, *Mus musculus*, *Gallus gallus* and *Xenopus laevis* were aligned using Jalview software (Waterhouse et al., 2009) **(Figure 5.1 A)**. Jalview showed the percentage of sequence identity across species in different shades of blue, where darker blue indicates 100% of identity and the colour progressively decrease in intensity for lower percentages of identity. The CENP-Z alignment revealed two conserved regions along the sequence of CENP-Z: the first region (81-92 aa) is comprised into a zinc finger associated domain (zf-AD, 79-153 aa) (Uniprot, Q8N554), and the second conserved region is at the C-terminus of the protein, 410-581 aa residues, containing the zinc finger domain (C2H2, 434-577) (Uniprot, Q8N554) **(Figure 5.1 A)**. This high level of conservation of these two regions suggests an essential function for the zinc finger domain of CENP-Z across vertebrates.

To acquire information regarding CENP-Z structural elements, two different tools were used: the Psi-pred platform for secondary structure prediction (Jones, 1999) and the PHYRE2 protein folding recognition server (Kelley et al., 2015). The analysis performed using Psi-pred revealed that CENP-Z presents highly unstructured N-terminus and central regions **(Figure 5.1 B)**. By using the PHYRE2 server, a predicted model for CENP-Z structure was proposed comparing its protein sequence with the sequence of proteins whose structure is known. Specifically, the region of CENP-Z that includes 480-570 aa residues was predicted to fold as the zinc finger protein ZNF297b (26% sequence identity between CENP-Z 480-570 aa and ZNF297b 4-107 aa, with 99.91% of confidence in the prediction (see section **7.2**)). Moreover, the region of CENP-Z containing aa 347-578 was predicted to fold similarly to the histone-lysine n-methyltransferase PRDM9 (8% sequence identity

Figure 5.1. Bioinformatic analysis of CENP-Z protein sequence. A. Conservation analysis of CENP-Z sequence across vertebrates expressed as percentage of identity. CENP-Z sequence of *H. sapiens* (Hs), *M .musculus* (Mm), *G. gallus* (Gg) and *X. laevis* (Xl) were aligned and conserved residues are highlighted in shades of blue, where a darker colour indicates 100% of identity, whereas a progressive lighter shades of blue indicate a lower percentage of identity. **B.** Secondary structure analysis of *H. sapiens* CENP-Z isoform a using the on-line platform for protein prediction Psi-pred. Information found in Uniprot or PHYRE2 on-line databases is also included in this diagram as follows: the protein sequence predicted to fold as a zf-AD domain is highlighted in green, as a C2H2 zinc finger domain in purple and as a PRDM9-like lysine methyltransferase in red.

A

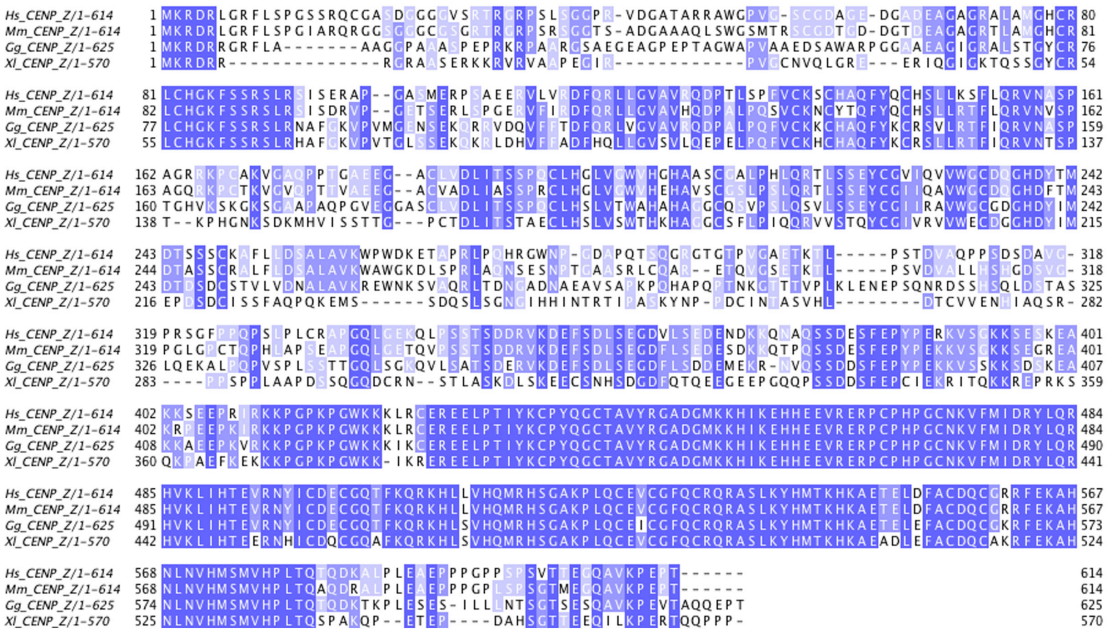
Hs_CENP_Z/1-614
Mm_CENP_Z/1-614
Gg_CENP_Z/1-625
Xl_CENP_Z/1-570

B

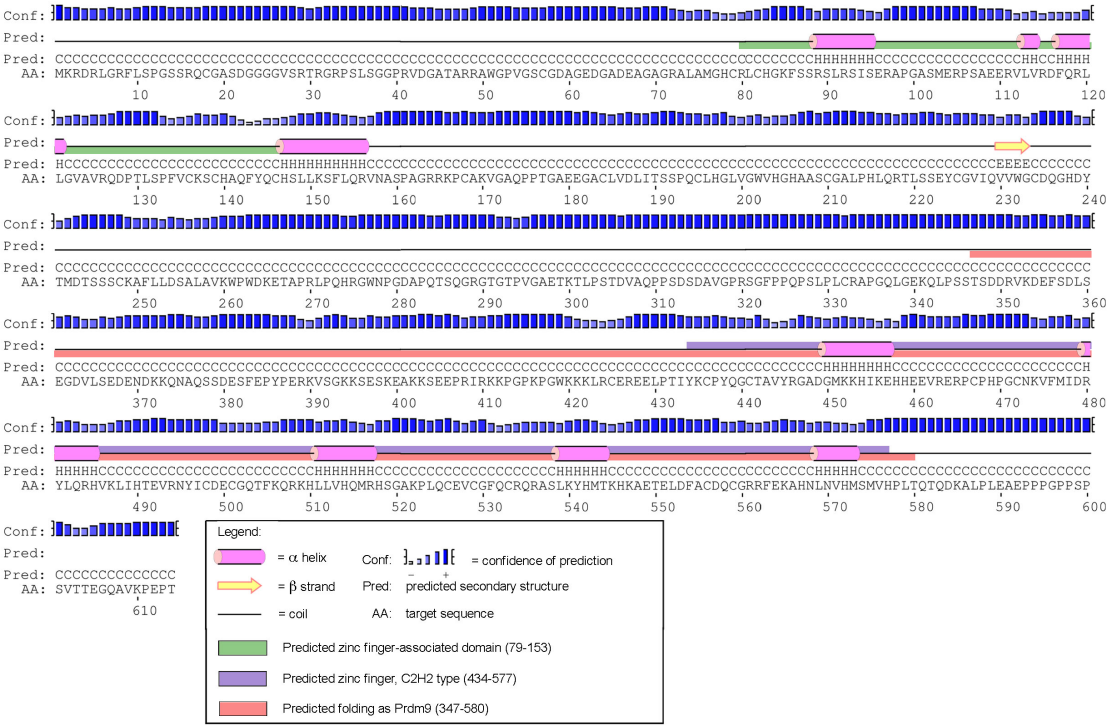
Conf:
Pred:
AA:
Legend:
= α helix
= β strand
= coil
= confidence of prediction
predicted secondary structure
target sequence
Predicted zinc finger-associated domain (79-153)
Predicted zinc finger, C2H2 type (434-577)
Predicted folding as Prdm9 (347-580)

between CENP-Z 347-578 aa and PRDM9 195-408 aa, with 99.93% of confidence in the prediction (see section **7.2**)). PRDM9 is a methyltrasferase that contains C2H2 zinc fingers and catalyses a trimethylation on H3K4. This activity has recently been linked to recombination hotspots in humans and mice meiosis (Baudat et al., 2010; Grey et al., 2011; Hayashi et al., 2005). The SET domain is the catalytic domain that confers H3K4 trimethyl transferase activity to PRDM9. This domain is found in the PRDM9 sequence comprised in 244-358 aa interval (Uniprot, Q9NQV7). Therefore, the PRDM9 SET domain (244-358) is included in the region of similarity identified by PHYRE2 between CENP-Z and PRDM9 (195-408).

These evidences suggest a possible trimethyl-transferase activity of CENP-Z on lysine 4 of histone H3, potentially activating transcription at kinetochores.

5.2.2 CENP-Z localizes at kinetochores in mitosis

Confirming the kinetochore localization of CENP-Z was necessary before proceeding with further functional studies.

Since no antibodies are available for CENP-Z, to test CENP-Z localization it was necessary to fuse it with EGFP for expression in HeLa cells (see section **2.2.5**). HeLa cells were transiently transfected with EGFP:CENP-Z isoform b (1620 bp; 540 aa) for 24 hours. Coverslips were fixed in 4% PFA, washed in 1X PBS and processed for CENP-C immuno-staining following a standardised protocol, as described in section **2.6.1**. Results showed the presence of GFP:CENP-Z at kinetochores, co-localizing with CENP-C during mitosis **(Figure 5.2)**. We also detected CENP-Z signal localising at the spindle poles **(Figure 5.2)**. Here, the presence of CENP-Z is more likely due to the overexpression in HeLa cells. This could be further clarified, in future, by using an antibody specific for endogenous CENP-Z.

The H3K4 trimethyl transferase activity predicted for CENP-Z (PHYRE2 analysis in **5.2.1**) together with CENP-Z kinetochore localization during mitosis could imply a modulation of histone methylation states as a kinetochore function for CENP-Z.

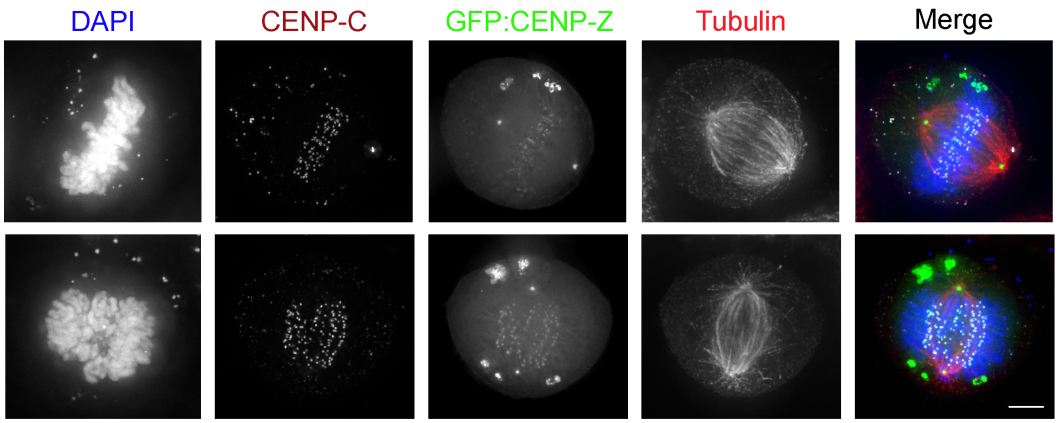

Figure 5.2. CENP-Z localises at kinetochores during mitosis. Representative fluorescence images of HeLa cells expressing GFP:CENP-Z probed with anti CENP-C and anti tubulin antibodies are present. Alexa Fluor 647 (far red, pseudo coloured in dark red) and Alexa Fluor 594 (red) conjugated secondary antibodies, respectively, were used to detect signals from the primaries. DNA was counterstained with DAPI. Scale bar, 5 μm.

5.2.3 Tethering CENP-Z to the HAC causes the removal of H3K4me2

The bioinformatics results on CENP-Z predicted that CENP-Z shares structural similarities with the histone-lysine n-methyltransferase PRDM9. Since PRDM9 catalyses methylation changes on lysine 4 of histone H3, I next tested whether CENP-Z was capable of the same catalytic activity.

H3K4me2 has been found in the centromere chromatin (Sullivan and Karpen, 2004) and it was later linked to centromeric transcription (Bergmann et al., 2011). Results from our laboratory showed that removal of H3K4me2 correlates with a decrease in centromeric transcripts at the alphoid^{tetO} HAC (Bergmann et al., 2011). As previously described, the alphoid^{tetO} HAC is constituted by an alternation of alpha satellite monomers, containing tetracycline operators (TetO), and CENP-B boxes (Kouprina et al., 2012; Nakano et al., 2008). By expressing a TetR-EYFP fusion protein, this protein is tethered to the TetO sites on the HAC and visualised through the fluorescence of EYFP **(Figure 5.3 A)**. The effects of tethered protein/chromatin modifiers to the HAC can then be assayed via fluorescence microscopy. The alphoid^{tetO} HAC contains high levels of H3K4me2 (Bergmann et al., 2011). Staining 1C7 cells for H3K4me2 showed a bright spot for this mark at the HAC, as identified by TetR-EYFP **(Figure 5.3 B**, TetR-EYFP**)**. Therefore, the alphoid^{tetO} HAC represents an optimal system to test whether CENP-Z affects H3K4me2 upon tethering. CENP-Z isoform b was fused to TetR-EYFP and expressed in 1C7 cells in the following experiments.

1C7 cells were transfected either with TetR-EYFP (control) or with TetR-EYFP:CENP-Z. 48 hours post trasfection, samples were fixed and probed with anti H3K4me2 antibody. In control cells (cells expressing TetR-EYFP only) the HAC showed a bright signal for H3K4me2; in contrast, H3K4me2 signal on the HAC decreased after tethering TetR-EYFP:CENP-Z **(Figure 5.3 B)**. The levels of H3K4me2 were quantified after tethering the TetR fusion proteins using ImageJ and results were plotted in a graph **(Figure 5.3 C)**. Results showed that tethering TetR-EYFP:CENP-Z caused a significant decrease in the fluorescence of H3K4me2 at the HAC compared to the TetR-EYFP alone (median values 0.99 and 1.83 respectively;

Figure 5.3. Reduced levels of H3K4me2 were observed at the HAC upon CENP-Z tethering. **A.** Diagram representing TetO array integrated into the HAC (yellow) in 1C7 cells. Upon transfection of TetR-EYFP fusion protein into the cells, the TetR (orange) will bind the TetO and the occurred binding can be visualized by fluorescence microscopy looking at the signal of the EYFP (green). **B.** Representative fluorescence images of 1C7 cells transfected with TetR-EYFP and TetR-EYFP:CENP-Z. In both cases, cells were fixed and probed with anti H3K4me2 antibody. The signal was detected with Alexa Fluor 594 (red) conjugated secondary antibody. The HAC was recognised by the signal of the EYFP (green). DNA was counterstained using DAPI (blue). 3 X enlargements of the HAC are shown in the insets. Scale bars, 10 μm. **C.** Quantification of H3K4me2 fluorescence intensity at the HAC from the experiment described in panel B was performed using ImageJ. Once found the best focal plane for the HAC in the EYFP channel, I moved to the H3K4me2 channel and drew a circular area of the diameter of 10 pixels around the HAC. H3K4me2 fluorescence was measured and next subtracted of the background fluorescence present outside the cell in a 10 pixels diameter area. This value obtained was then normalized for H3K4me2 fluorescence intensity present in the areas surrounding the HAC, by applying from 3 to 6 times the 10 pixel diameter area in the surroundings of the HAC and measuring H3K4me2 fluorescence intensity; a mean of these values was calculated, which was next subtracted of the same background value as before. Finally HAC fluorescence value for H3K4me2 was divided for the mean value of the surrounding areas. Compared to TetR-EYFP only, tethering TetR-EYFP:CENP-Z caused a significant decrease in H3K4me2 on the HAC (TetR-EYFP versus TetR-EYFP:CENP-Z, $p < 0.0001$; Mann-Whitney U test). Fluorescence intensities medians plus standard deviations are shown in the graph. Asterisks highlight statistical significance. For each sample 60 cells were analysed from two independent experiments.

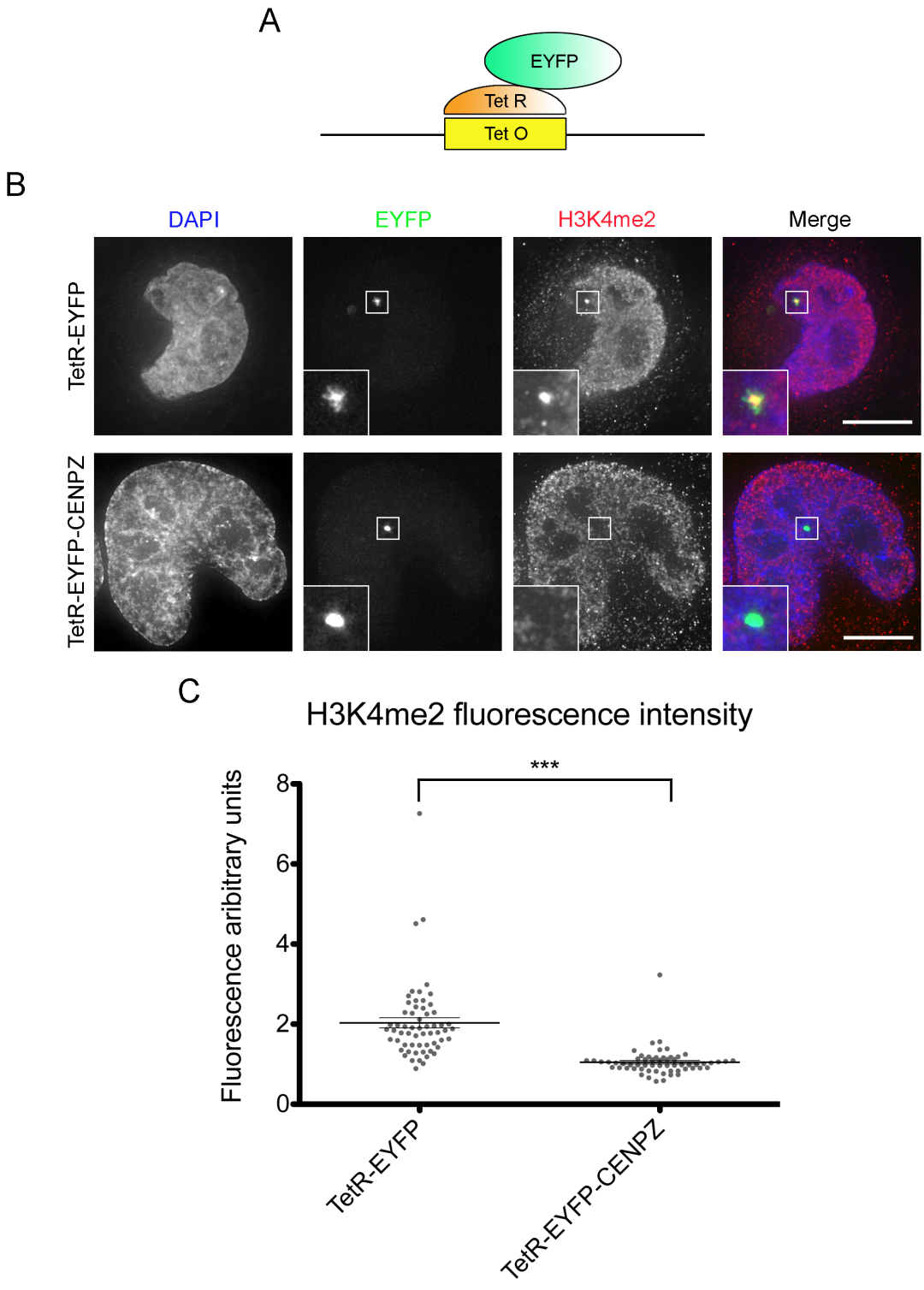
A
EYFP
Tet R
Tet O
B
DAPI
EYFP
H3K4me2
Merge
TetR-EYFP
TetR-EYFP-CENPZ
C
H3K4me2 fluorescence intensity
***
Fluorescence aribitrary units
8
6
4
2
0
TetR-EYFP
TetR-EYFP-CENPZ

$p < 0.0001$).

In conclusion, these results suggested a role for CENP-Z in the modulation of H3K4 methylation states.

5.2.4 CENP-Z is not a CENP-A assembly factor

The epigenetic environment at the centromere has been linked to CENP-A assembly and maintenance (Bergmann et al., 2011; Kim et al., 2012). Since our previous results suggested a role of CENP-Z in chromatin modulation, we aimed to assess whether CENP-Z was involved in CENP-A loading at the centromere.

For these experiments a HeLa cell line containing an alpha satellite array integrated into a chromosome arm (HeLa 3-8) (Ohzeki et al., 2012) was used. This alphoid satellite integration contains TetO as the alphoid^{tetO} HAC system described before (section **5.2.3**). As before, isoform b of CENP-Z was used in these experiments. 48 hours post transfection, the TetR-EYFP fusion proteins were tethered to the integration where TetR and TetO tightly interact. In order to highlight the possible effect of CENP-Z on CENP-A assembly, a HeLa 3-8 cell line that ovexpressed CENP-A was used. Indeed in the presence of CENP-A overexpression it is easier to observe CENP-A ectopic recruitment when it occurs. In order to assess the potential role of CENP-Z as a CENP-A loading factor, a negative control (TetR-EYFP empty vector) and a positive control for CENP-A assembly (TetR-EYFP:HJURP) were included in the analysis. HJURP is a well characterised CENP-A chaperone and it is directly involved in CENP-A loading (Dunleavy et al., 2009; Foltz et al., 2009). HeLa 3-8 cells were transfected with TetR-EYFP, TetR-EYFP:HJURP or TetR-EYFP:CENP-Z for 48 hours. After fixation with 4% PFA, cells were probed with anti CENP-A antibody. A minimum of 20 images of transfected interphase cells were acquired using a DeltaVision RT microscope (Applied Precision). Representative images of transfected cells are shown in **Figure 5.4 A**. As in previous experiments, TetR-EYFP fusion proteins were identified by the EYFP signal at the integration. Fluorescence intensity of CENP-A was measured

Figure 5.4. CENP-Z did not recruit CENP-A when tethered to a chromosome arm. A. Representative fluorescence images of HeLa 3-8 transfected with TetR-EYFP, TetR-EYFP:CENP-Z and TetR-EYFP:HJURP. In all the three cases, cells were fixed and probed with anti CENP-A antibody. The signal was detected with Alexa Fluor 647 conjugated secondary antibody (red). The integration was recognised by the signal of the EYFP (green). DNA was counterstained using DAPI (blue). Scale bar, 5 μm. **B.** Quantification of CENP-A fluorescence intensity at the integration from the experiment described in panel A. For quantification purposes, a macro in ImageJ custom modified from Bodor et al., 2014 was used (section **7.1**), which was able to identify the integration spot and measure intensity of signals in CENP-A channel. Among the samples, HJURP is the best CENP-A recruiter (TetR-EYFP:HJURP versus TetR-EYFP or TetR-EYFP:CENP-Z, $p< 0.0001$; Mann-Whitney U test). Tethering CENP-Z did not cause CENP-A loading when compared to the TetR empty vector (TetR-EYFP:CENP-Z versus TetR-EYFP, $p=0.1058$; Mann-Whitney U test). Fluorescence intensities medians plus standard deviations are shown in the graph. Asterisks highlight statistical significance. For each sample 45 cells were analysed in two independent experiments.

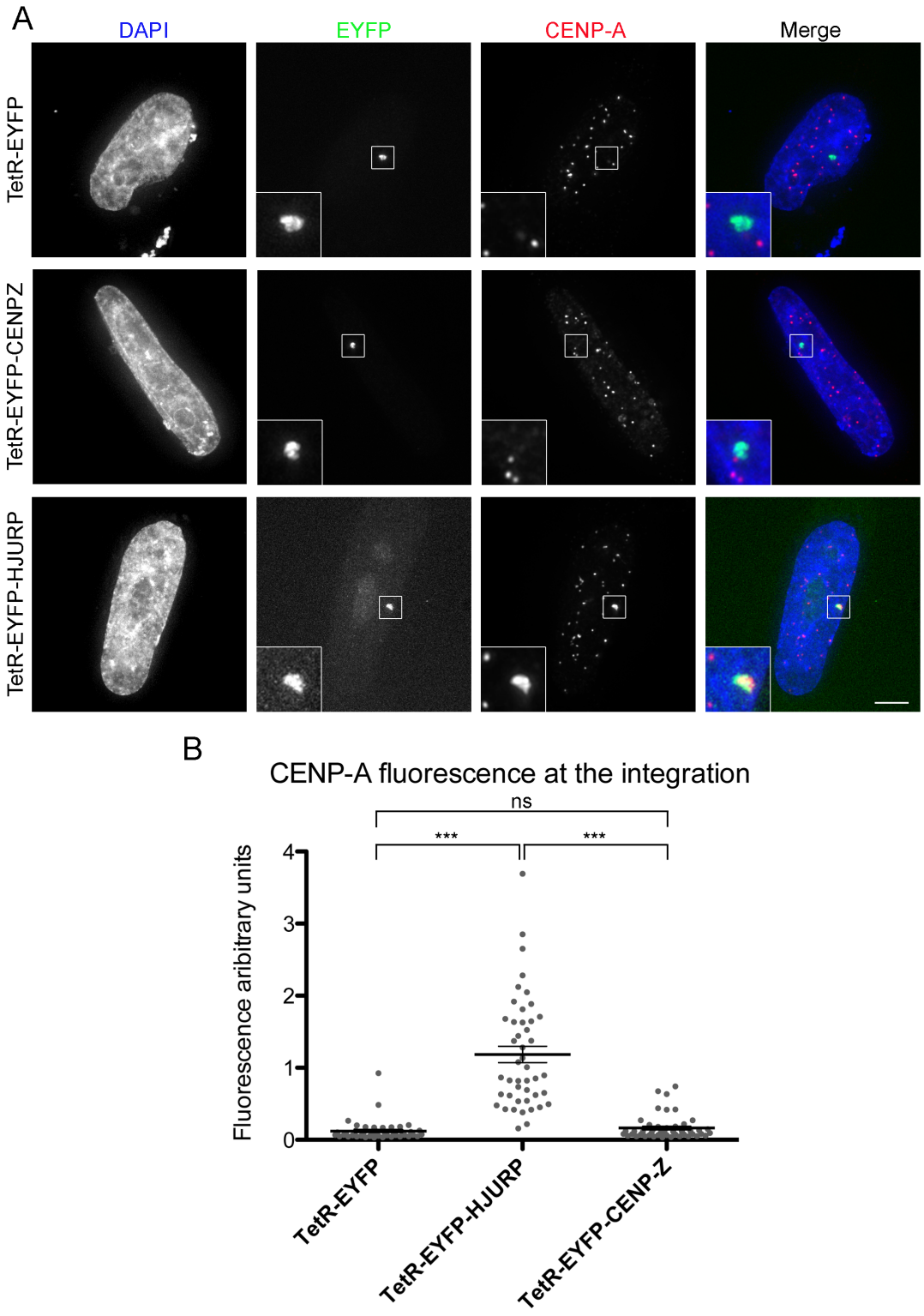
A
DAPI
EYFP
CENP-A
Merge
TetR-EYFP
TetR-EYFP-CENPZ
TetR-EYFP-HJURP
B
CENP-A fluorescence at the integration
ns
***
***
Fluorescence aribitrary units
4
3
2
1
0
TetR-EYFP
TetR-EYFP-HJURP
TetR-EYFP-CENP-Z

was measured using a custom made macro in ImageJ modified from Bodor et al., 2014 (see section **7.1**). This macro automatically identifies the area of the integration and it measures the average signal present in this area in the CENP-A channel. Results of the quantification of CENP-A signal across the three conditions tested were plotted in a graph **(Figure 5.4 B)**. Tethering of TetR-EYFP did not prompt CENP-A recruitment to the array integration. Tethering of TetR-EYFP:HJURP caused a significant increase in the signal of CENP-A at the integration, compared to the TetR-EYFP only tethering experiment **(Figure 5.4 C**, median values 0.893 and 0.079 respectively; $p<0.0001$**)**. Importantly, TetR-EYFP:CENP-Z tethering at the integration had no effects on the signal of CENP-A at the array integration compared to TetR-EYFP **(Figure 5.4 C**, median values 0.104 and 0.079 respectively; $p=0.1058$**)**.

These results demonstrated that CENP-Z is not involved in the CENP-A loading pathway. Collectively, these results suggest that CENP-Z modulate the methylation status of the centrochromatin, however this is not associated with CENP-A loading. In the future, experiments we will analyse whether this methylation control is associated with the maintenance of CENP-A.

5.2.5 Development of tools for CENP-Z detection and optimization of CENP-Z depletion

Previous results showed that CENP-Z has an activity on H3K4me2 and it was also shown to localise at kinetochores in mitosis. Therefore, we wanted to perform depletion studies in order to identify possible phenotypes related to CENP-Z knockdown, giving indications of its function. However, the lack of a specific antibody for CENP-Z makes it difficult to study this protein, as it could only be visualised by ovexpression as a GFP fusion.

To address this limitation we aimed to raise an anti CENP-Z antibody that will allow us to visualise and study endogenous CENP-Z. Anti-peptide monoclonal antibodies were synthetized by Abmart (Shanghai) Co., Ltd. CENP-Z peptides were synthesised, expressed in *E. coli*, purified and injected into mice (Abmart). Afterwards, 26 sample antibodies were received and tested, to clarify if any of them

could recognise CENP-Z by western blot. HeLa cells were transfected with GFP:CENP-Z for 24 hours after which a protein extract was prepared (see section **2.3.1**). The protein extracts were run on a SDS-PAGE gel and, following the transfer, the membrane was blotted with each of the sample antibodies received. The predicted size of CENP-Z is 67 kDa (Uniprot - Q8N554), and the expected size of GFP:CENP-Z fusion protein is approximately 100 kDa. Nitrocellulose membranes were cut into 26 strips to test each of the antibodies. The presence of GFP:CENP-Z was used as a positive control. Therefore, strips number 3, 11 and 24 were also incubated with anti GFP antibody. In addition, anti tubulin antibody was used as a control for protein loading in strips number 4, 9, 13, 17, 22 and 26. Results of the immunoblot are shown in **Figure 5.5**. Antibodies incubated with strips number 2 and 3 appeared to recognise a band of the correct size (yellow box), also confirmed by the GFP antibody. Particularly, antibody n°2 (incubated with strip 2) showed a high specificity for GFP:CENP-Z. However, no clear signal for endogenous CENP-Z (67 kDa) was observed in any of the antibodies tested. This could be due to relatively low abundance of the endogenous protein compared to the exogenous one overexpressed.

To study the localization of CENP-Z and its dynamics in different stages of cell cycle, without overexpressing the protein, Abmart antibody n°2, which gave the best signal by western blotting **(Figure 5.5)**, was subsequently tested by immunofluorescence. A range of fixation procedures **(Figure 5.6 A)** were used to prepare HeLa cell samples to perform immunofluorescences analysis where samples were incubated with n°2 CENP-Z antibody in combination with CENP-C or tubulin **(Figure 5.6 B** 1-3**)**. No co-localization was found between CENP-C and CENP-Z antibodies, even after a pre-extraction of cytosol. Indeed, anti CENP-Z antibody appeared unfocused and diffused in the cytoplasm.

With the aim of studying the role of CENP-Z at the kinetochore, several siRNA oligos were tested in order to assess the efficiency of CENP-Z depletion.

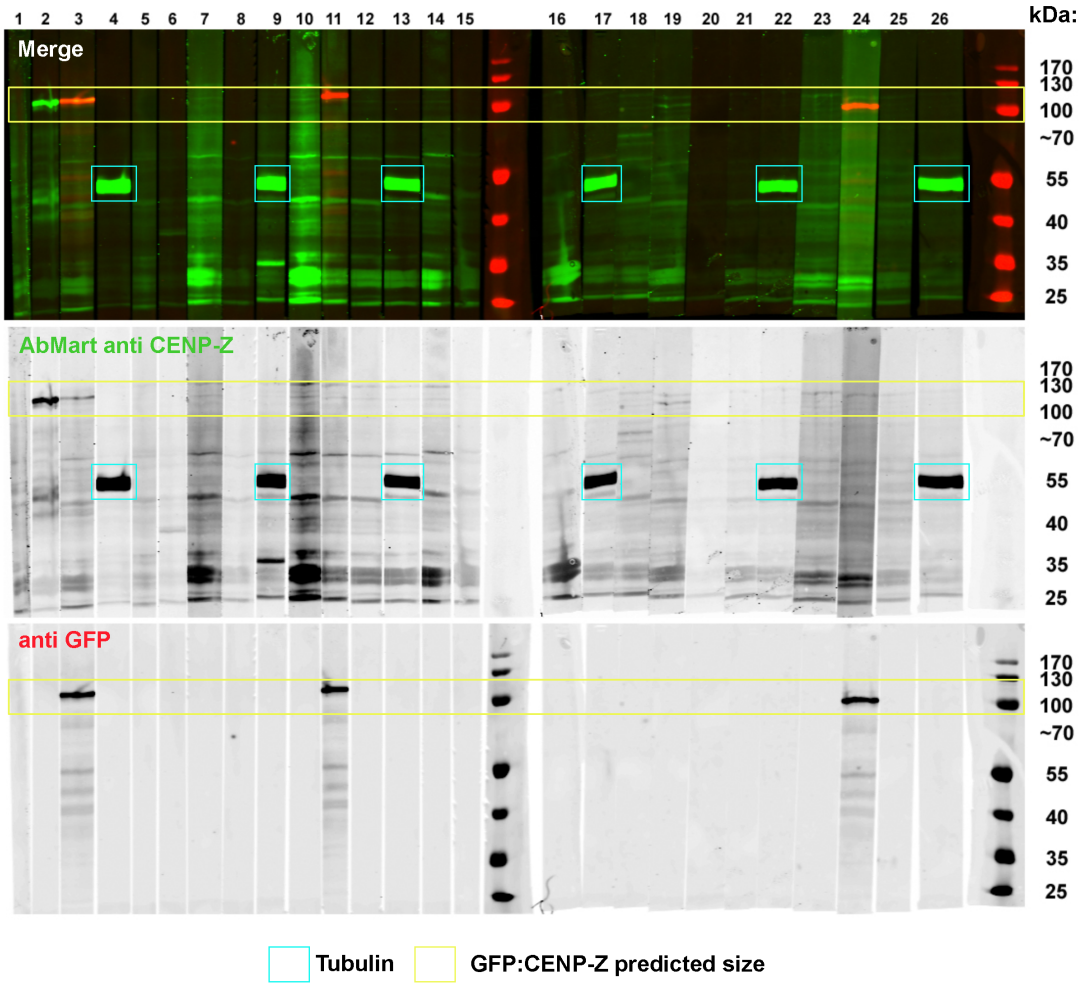

Figure 5.5. CENP-Z anti-peptide antibodies screening. HeLa cells were transfected with GFP:CENP-Z and protein extracts were prepared after 24 hours of expression. Two 10% polyacrylamide gels were loaded with 500 µg of HeLa whole cell lysate each. After transfer, nitrocellulose membranes were cut into 26 vertical strips and each of them was incubated for 2 hours at room temperature with a different antibody diluted in 1:200 in PBS-Tw20 0.05% added of 3% w/v of low fat milk. Membranes were incubated with Abmart test antibodies plus anti tubulin and anti GFP antibodies for two hours at room temperature. Signals were detected using IRDye® 680 and 800 conjugated secondary antibodies. The Li-Cor system was employed for signal acquisition. Light blue boxes highlight tubulin bands and yellow boxes were drawn at GFP:CENP-Z predicted size height.

A

	Fixation procedure
1	WASH PBS1X 37°C — 1 minute — 0.05% Tx-100 in 4% PFA diluted in PBS 1X 37°C — 10 minutes — 4% PFA diluted in PBS 1X 37°C — WASH PBS1X
2	WASH PBS1X 37°C — 10 minutes — 100% glacial MeOH -20°C — WASH PBS1X 37°C
3	WASH PBS1X 37°C — 10 minutes — 4% PFA diluted in PBS 1X 37°C — WASH PBS1X — 5 minutes — 0.15% Tx-100 in 1X PBS — WASH PBS1X

B

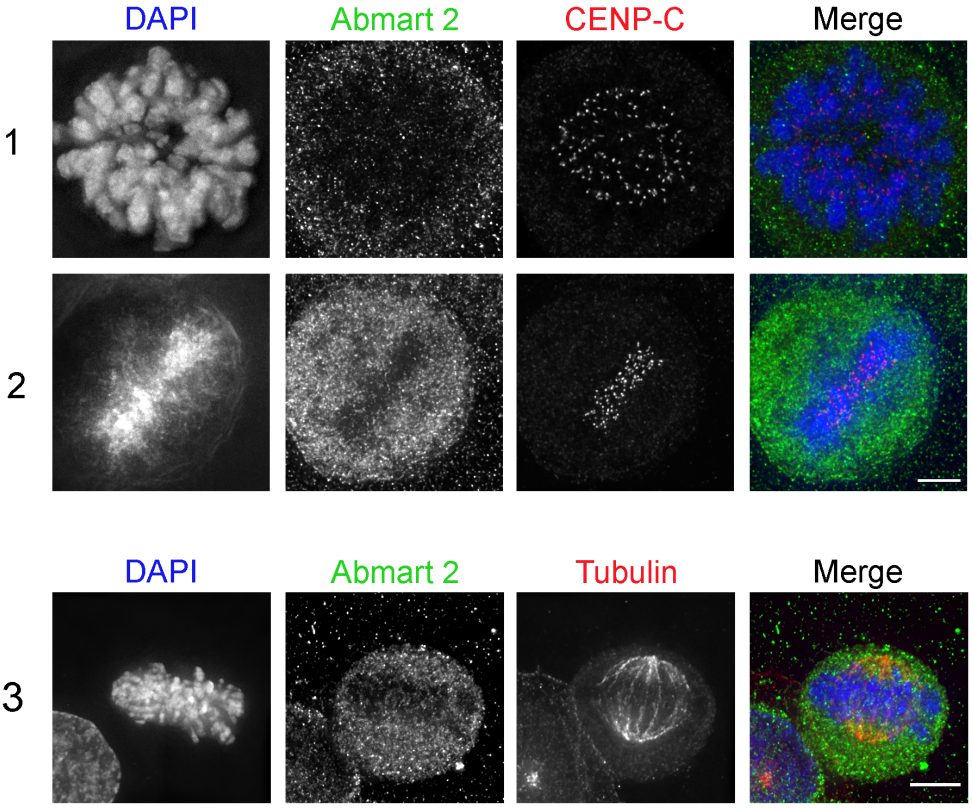

Figure 5.6. Testing Abmart antibody n°2 by immunofluorescence. Abmart antibody n°2 was tested on HeLa cells in immunofluorescence experiments. **A.** Table representing the different fixing conditions tested that were followed by antibody incubations. **B.** Representative images of HeLa cells incubated with Abmart n°2, CENP-C or tubulin primary antibodies. Signals were detected using Alexa Fluor 488 (green) and 594 (red) conjugated secondary antibodies respectively. DNA was counterstained by DAPI (blue). Scale bar, 5 µm. No kinetochore signal of Abmart n°2 antibody was observed. Rows 1, 2 and 3 in panel B are representative examples of the conditions illustrated in panel A 1, 2 and 3.

As the antibody currently available did not recognise the endogenous CENP-Z it was necessary to test RNAi oligos in cells transfected with GFP:CENP-Z. For RNAi oligo sequences against CENP-Z refer to Table **2.4**. HeLa cells were co-transfected with GFP:CENP-Z and either control siRNA or GFP:CENP-Z specific siRNAi oligos. Next, after 48 hours of knockdown, cells were pelleted and lysed. An equal amount of protein was loaded onto a polyacrylamide gel and western blotting analysis was performed to test the efficiency of CENP-Z depletion. The membrane was incubated with anti GFP antibody, to check for GFP:CENP-Z levels, and anti tubulin antibody was used, as a loading control. Results showed a good level of depletion achieved by RNAi oligo n°2 compared to the control levels in presence of scramble RNAi **(Figure 5.7**, top row**)**. RNAi oligo n°4 showed a milder effect on the levels of GFP:CENP-Z, whereas oligos n° 0, 1 and 3 did not affect GFP:CENP-Z levels. This analysis was validated by the observation of an equal sample loading as indicated by tubulin bands **(Figure 5.7**, top**)**. Rabbit anti GFP antibody gave a high number of smaller size bands. These may be degradation products of GFP:CENP-Z combined with some unspecific binding of the GFP antibody already observed **(Figure 5.5** anti GFP blot**)**, although this was not observed in the tubulin blot. This evidence suggested that CENP-Z might be an unstable protein. This correlates with the observation of unstructured regions at the N-terminus and central parts of the protein, as highlight by the Psipred analysis (section **5.2.1**). In addition, as I was interested in clarifying the reliability of the mouse Abmart antibody n°2 for western blotting analysis, a second incubation was performed. This test showed that Abmart antibody n°2 is able to detect reduced levels of GFP:CENP-Z **(Figure 5.7**, bottom row**)**, as its signal co-localise with the one of the GFP antibody (yellow bands). Furthermore, a band at the predicted size of endogenous CENP-Z (67 kDa) was recognised by this antibody (yellow box). Since the membrane was not stripped the bands corresponding to tubulin were still visible (light blue box).

Having found the appropriate conditions for knocking down CENP-Z, an RNAi experiment to analyse the effects of this depletion on mitosis progression was performed. HeLa cells were transfected with control RNAi or CENP-Z specific oligo 2 for 48 hours. Next, cells were fixed in 4% PFA and permeabilized. Samples were incubated with antibodies raised against a kinetochore marker, in this case ACA, and

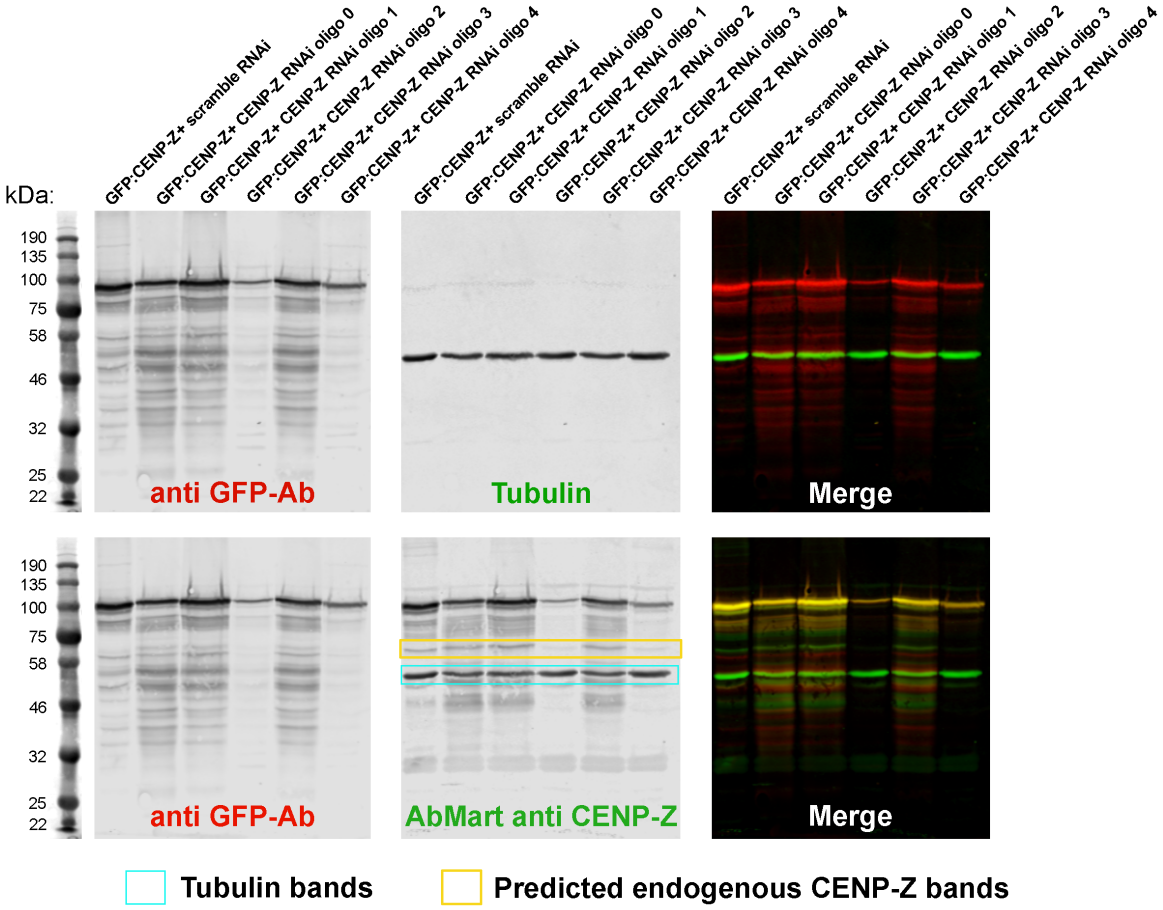

Figure 5.7. Immunoblot analysis of CENP-Z depletion. HeLa cells were transfected with GFP:CENP-Z and control RNAi or CENP-Z specific siRNA oligos. After 48 hours of transfection, cells were pelleted and lysed. Protein extracts were next loaded onto a polyacrylamide gel with, in each lane, the correspondent protein content of 4 X 10^5 cells. The membrane was incubated with primary antibodies raised against GFP and tubulin (top raw) or GFP and CENP-Z (Abmart n°2) (bottom raw, signal of the tubulin from previous hybridization is included in a light blue box). Signals were detected using IRDye® 680 and 800 conjugated secondary antibodies. The Li-Cor Odyssey system was used for signal acquisition. A yellow box includes predicted bands for endogenous CENP-Z, whilst a light blue box highlights tubulin bands across the samples.

tubulin. Microscopy analysis of 100 mitotic cells revealed the presence of a higher percentage of cells in prometaphase when CENP-Z was depleted, compared with control RNAi, as shown in **Figure 5.8 A**. Most of the chromosomes in cells transfected with CENP-Z RNAi were organised in a metaphase plate-like structure with the exception of fewer chromosomes that were not properly aligned in comparison with control RNAi treated cells. Mitotic defects needed to be quantified to reveal the effect of CENP-Z depletion in mitosis. Due to the difficulty of unambiguously categorizing a normal prometaphase and a 'delayed' one, all the prometaphase cells have been grouped together, assuming that if that particular conformation observed after 48 hour depletion was causing a delay in prometaphase, then a higher percentage of cells in prometaphase would have been observed. Counts confirmed this hypothesis showing an increase in the fraction of mitotic cells in prometaphase after 48 hours depletion, leading to a smaller number of cells in telophase/cytokinesis **(Figure 5.8 B)**.

These preliminary results, suggest that CENP-Z might have a role in chromosome alignment. To further investigate this possible role of CENP-Z more replicas of the RNAi phenotype analysis and live cell imaging will be performed.

To detect endogenous CENP-Z we attempted to generate our own antibody against CENP-Z. This work has been done in collaboration with Dr Maria Alba Abad, a post-doctoral researcher in Dr Jeyaprakash Arulanandam's laboratory. Previous experiments showed that CENP-Z full-length protein is unstable and poorly expressed in bacteria (Dr Maria Alba Abad, data not shown). Therefore, we decided to use 79-153 and 347-580 fragments of human CENP-Z as they showed higher yield of expression and, additionally, they contained the zf-AD and the zinc finger C2H2 domains **(Figure 5.1)**. 79-153 and 347-580 fragments of human CENP-Z were expressed in *E.coli* BL21 Gold competent cells. CENP-Z 79-153 fragment was purified through a glutathione *S*-transferase (GST) tag whereas 347-580 fragment had a poly-histidine (His) tag that was used for the purification **(Figure 5.9 A)** (for CENP-Z fragment purification see section **2.3.5.1** and **2.3.5.2**). Samples, acquired at

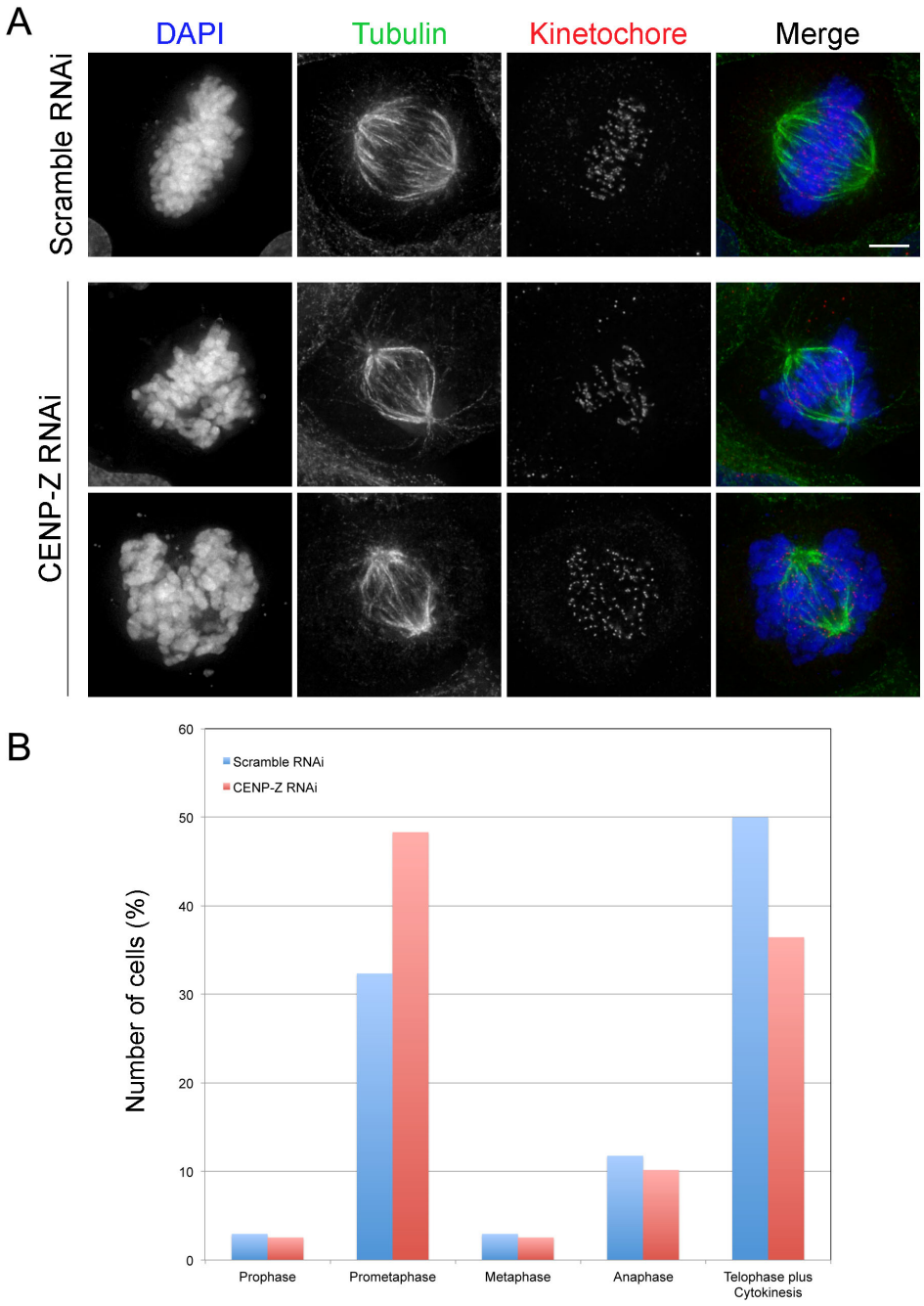

Figure 5.8. CENP-Z depletion study in mitotic human cells. A. Representative images of mitotic HeLa cells treated with control RNAi or CENP-Z RNAi oligo 2. 50% confluent coverslips with HeLa cells were transfected for 48 hours. Samples were next processed for immunofluorescence. Samples were incubated with primary antibodies raised against tubulin and kinetochore proteins, such as CENP-C and ACA. Signals were detected using Alexa Fluor 488 (green) and 594 (red) conjugated secondary antibodies. DNA was counterstained with DAPI (blue). Scale bars, 5 μm. **B.** Graph representing counts of 100 mitotic cells per samples, where cell numbers, scored for each category, are expressed in percentages.

each step of the purifications, were run on a polyacrylamide gel and the gel was stained with Comassie Blue in order to verify that each stage of the purification was successful **(Figure 5.9 C** and **D)**.

The 79-153 protein fragment was soluble, as a band can be seen in the supernatant (SP). A less intense band of the same size was observed in the flow-through (FT). As expected, an enrichment of GST-79-153 on the beads after the affinity purification step was also observed (B*). After cleavage with 3C protease the fragment was released from the beads (BA) and collected into elutions (E). The elutions contain the fragment with a size of ~ 8 kDa that corresponds to 79-153 **(Figure 5.9 C**, yellow box**)**. The 347-580 CENP-Z fragment was also soluble and, as previously, a band was observed in the supernatant (SP) and a less intense one in the flow-through (FT). The fragment has a size of ~ 26 kDa **(Figure 5.9 D**, yellow box**)** and was present in the elutions (E). After cleavage with 3C protease, a shift in the band was observed (poolE cleaved), indicating that the His tag was cleaved. In total 920 μg of 79-153 and 2.35 mg of 347-580 were purified. Next, 800 μg of both fragments were run into a 15% polyacrylamide gel and gels were stained by aqueous comassie for protein bands visualization **(Figure 5.9 E** and **F)**. Bands of the appropriate sizes (yellow box) were frozen and finely grounded for animal injection (see section **2.3.6**).

Concomitantly, pre-immune sera of 9 rabbits were tested by immunoblot on whole cell extracts of asynchronous or mitotic HeLa cells **(Figure 5.4 G)**. After this screen, rabbits n° 4, 5, 8 and 9 were chosen for the production of CENP-Z antibody as they presented the lowest levels of natural immunity (fewest number of bands) across the animals tested.

Currently, I am awaiting for rabbit bleeds to test by immunoblot and immunofluorescence experiment for CENP-Z antibody specificity.

Figure 5.9. Antigen purification and preparation for rabbit immunisation. A. Schematic representing CENP-Z where the fragment 79-153 (pink) and 347-580 (orange), used for the antibody production, are highlighted. **B.** Explanatory legend to apply in panels C, D, E and F. **C.** GST 79-153 fragment purification (see section **2.3.5.1**). Each step of the purification was checked on an polyacrylamide gel where: P indicates cell pellet, SN: supernatant, FT: flow-through, B*: beads before cleavage (although a mistake was made in here and the sample was taken few minutes after the addition of the cleavage buffer; this is why the cleaved band is already visible here), BA: beads after cleavage, E1-3: different elutions, BAelution: beads after elution. The purified fragment, when visible, is included into a yellow box. Gel was stained with Coomassie Blue to allow protein visualization. **D.** His 347-580 fragment purification (see section **2.3.5.2**). Each step of the purification was checked on a polyacrylamide gel where: P indicates cell pellet, SN: supernatant, FT: flow-through, E1-9: 9 different elutions, PoolE: pool of elutions, PoolE cleaved: pool of elutions after cleavage. The purified fragment when visible is included into a yellow box. Gel was stained with Blue Coomassie to allow protein visualization. **E.** and **F.** 800 μg of purified 79-153 (E) and 347-580 (F) CENP-Z fragments were run onto a 15% polyacrylamide gel and stained with Aqueous Blue Coomassie (see section 2.3.6). **G.** Pre-immune sera screening by immunoblotting. Pre-immune sera of 9 rabbits were incubated on membranes where whole cell protein extracts were obtained from asynchronous (left) or mitotic (right) HeLa cells. Pre-immune sera were used at the 1:100 dilution and signals were detected using an anti rabbit IRDye® 680 conjugated secondary antibody. The Li-Cor system was used for signals acquisition.

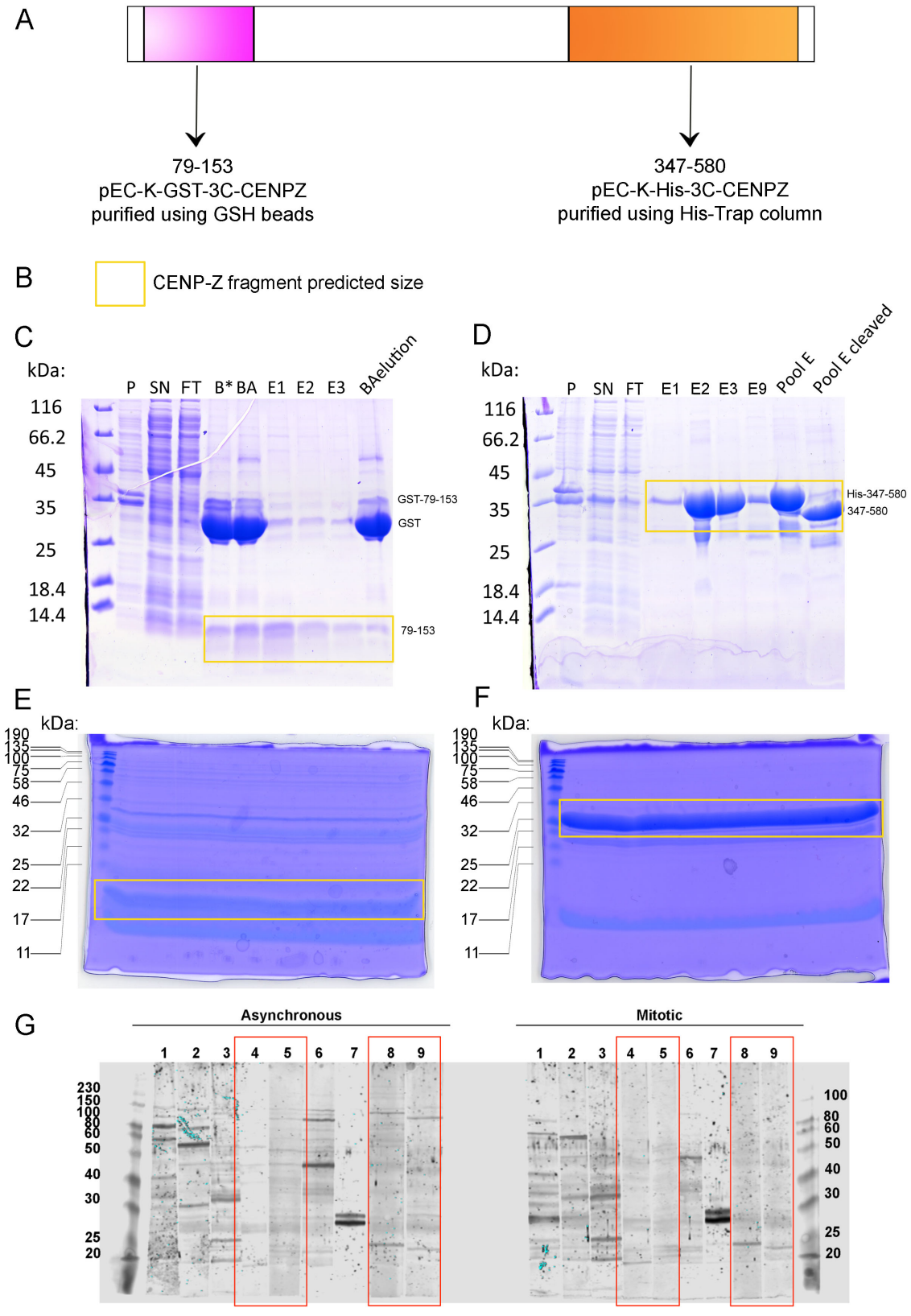
A
79-153
pEC-K-GST-3C-CENPZ
purified using GSH beads
347-580
pEC-K-His-3C-CENPZ
purified using His-Trap column
B
CENP-Z fragment predicted size
C
kDa:
P SN FT B* BA E1 E2 E3 BAelution
116
66.2
45
35
25
18.4
14.4
GST-79-153
GST
79-153
D
kDa:
P SN FT E1 E2 E3 E9 Pool E Pool E cleaved
116
66.2
45
35
25
18.4
14.4
His-347-580
347-580
E
kDa:
190
135
100
75
58
46
32
25
22
17
11
F
kDa:
190
135
100
75
58
46
32
25
22
17
11
G
Asynchronous
Mitotic
1 2 3 4 5 6 7 8 9
230
150
100
80
60
50
40
30
25
20
100
80
60
50
40
30
25
20

5.3 Discussion and conclusion

The aim of this chapter was to gain new insights on the role of CENP-Z. CENP-Z/ZNF276 was one of the proteins identified in our laboratory five years ago as a putative kinetochore protein following mass-spectrometry analysis of isolated chromosomes (Ohta et al., 2010). Despite the bioinformatic analysis applied to identify this new subset of CENP proteins, only one recent study has confirmed a genuine role in mitosis for CENP-32, which is required for normal mitotic spindle structure (Ohta et al., 2015), therefore further studies have to be performed aiming to confirm the kinetochore localization and to test the function of these novel proteins.

Despite the lack of literature and structured characterization of CENP-Z, we considered that reviewing the protein sequence would allow a prediction of possible mechanisms that CENP-Z could be involved in. Initially, information of functional domains contained in CENP-Z was found in NCBI and Uniprot databases. A predicted zinc finger domain C2H2 at the C-terminus and a predicted zf-AD at the N-terminus of CENP-Z were observed after bioinformatics analysis **(Figure 5.1 B)**. This result was interesting, as the zinc finger domains generally are associated with the binding of a protein to DNA and are common in transcription factors. Analysis of CENP-Z protein sequence conservation, in vertebrates, revealed high level of conservation in these two domains **(Figure 5.1 A)**, suggesting a conserved function for CENP-Z. Furthermore, the PHYRE2 server (Kelley et al., 2015) predicted that the C2H2 zinc finger domain region of CENP-Z folds similarly to a region of the PRDM9 methyltransferase **(Figure 5.1 B** and **7.2)**. PRDM9 catalyses the transfer of a methyl group to the di-methylated lysine 4 of histone H3 (H3K4me2), bringing H3K4 to a tri-methylated state (H3K4me3) (Hayashi et al., 2005). H3K4me2 is commonly associated with transcriptionally active euchromatin (Ernst and Kellis, 2010); in contrast, H3K4me3 is a marker enriched at active promoters. The hypothesis that CENP-Z, which was visualized at kinetochore during mitosis **(Figure 5.2)**, could activate transcription, puts forward the question: is transcription required for kinetochore function/stability? It is already known that a decrease in levels of transcription is linked to kinetochore instability (i.e. decreasing levels of kinetochore

proteins) as an effect of the tethering of the lysine-specific de-methylating enzymes (LSD1/LSD2) (Bergmann et al., 2011; Molina et al., 2015).

Therefore it was important to test the predicted methyltransferase activity of CENP-Z. The alphoid^{tetO} HAC presents high levels of H3K4me2 (Bergmann et al., 2011), and foci of enriched H3K4me2 were observed by immunofluorescence in 1C7 cells **(Figure 5.3 B)**. Therefore the alphoid^{tetO} HAC represents a good system to visualise changes in this post-translation modification. Upon tethering of CENP-Z, fluorescence intensity of H3K4me2 on the HAC decreased **(Figure 5.3 C)**. This could be due to a change of H3K4me2 into H3K4me3 for the activity of CENP-Z as a PRDM9 methyltransferase. Importantly, experiments with a catalytically dead mutant CENP-Z would ensure the specificity of this effect. Moreover, experiments where fluorescence intensity of H3K4me3 is quantified after CENP-Z tethering, should be performed to confirm H3K4 trimethyltransferase activity of CENP-Z. In addition, testing the variation, if detectable, in the amount of transcripts at the TetO in CENP-Z tethering experiments and behaviour of representative CCAN components could be the focus of future experiments. If the hypothesis of CENP-Z trimethylating H3K4 to induce transcription at kinetochores will be confirmed, that would classify CENP-Z as a novel methyltransferase able to control transcription dynamics at the centrochromatin.

As the epigenetic landscape can influence CENP-A assembly and kinetochore maintenance (Bergmann et al., 2011; Kim et al., 2012), the effects of CENP-Z tethering on a chromosome arm devoid of CENP-A were studied. However, no recruitment of CENP-A was prompted by CENP-Z activity at the alphoid^{tetO} ectopic integration **(Figure 5.4 B)**.

Finally, how does the depletion of CENP-Z affect cell division? In order to answer to this question a main technical obstacle had to be overcome. So far, CENP-Z depletion **(Figure 5.7)** was performed in cells that were also co-expressing GFP:CENP-Z as there was no specific antibody for CENP-Z. Down regulation of GFP:CENP-Z, upon treatment with a specific oligo, was visualized by using an anti GFP antibody. Detection trials of CENP-Z with an anti-peptide antibody, Abmart n°2, were performed by western blotting **(Figure 5.5** and **5.7)** and by

immunofluorescence **(Figure 5.6)**. However, although this antibody gave satisfactory results by western blotting, proper localization could not be observed by immunofluorescence microscopy. This limits the study of endogenous CENP-Z cell localization and from performing further assays such as immunoprecipitation assays to identify CENP-Z interactors. Therefore, we are currently trying to generate our own antibody against CENP-Z, specifically against 79-153 and 347-580 fragments which can be highly expressed in bacteria and correspond to the zf-AD and the C2H2 zinc finger domain **(Figure 5.9)**.

Preliminary data collected from HeLa cells depleted of CENP-Z for 48 hours, analysed by microscopy, revealed an accumulation of mitotic cells in prometaphase **(Figure 5.8 A** and **B)**. The phenotype, described as prometaphases containing a metaphase plate-like structure, is similar to the one previously observed upon CENP-E (Harborth et al., 2001) and CENP-Q (Bancroft et al., 2015) knockdown by RNAi. However, CENP-Z depletion results need to be confirmed in order to determine the statistical significance of these changes. Next, a rescue experiment will be designed to rule out the possibility of off-target effects. Also, performing live cell imaging analysis will clarify the destiny of cells depleted of CENP-Z.

Overall, in this chapter, I presented the optimisation of tools for analysing the unknown function of CENP-Z. Future experiments will be designed to clarify the role of CENP-Z on kinetochore structure and function.

6 Conclusion and final perspectives

Despite the extensive literature available on the kinetochore, key questions currently remain unanswered. As many kinetochore components (> 100 proteins) are known, it is yet to be confirmed how they assemble, relative to one another, at an ultra-structural level, to constitute a functional unit.

At present two models were proposed for the structure of the inner kinetochore, one designed as the 'amphipathic model' and the second one named the 'boustrophedon model'. The purpose of this Ph.D. was to generate data that supports one of these models.

To study the ultra-structure of the inner kinetochore chromatin I used fluorescence microscopy. Numerous sample preparations were tested and both wide-field fluorescence microscopy and super-resolution assayed while working on side projects. Unfolding centromere chromatin was the approach chosen to analyse centromere length, in several conditions, using wide-field fluorescence microscopy to acquire the data. Having optimised the 'modus operandi', analysis of chromatin fibers could begin.

The first question tackled was the identification of differences in the kinetochore structure between interphase and mitosis. In order to generate a data-set statistically representative, for each sample a large number of fibers was acquired and measured in length. Importantly, with this study, we were able to quantify differences in the structure of the centromere with a resolution of 100 nm. In addition, the data-sets generated were additionally tested for the presence of peaks, using a multi-peak algorithm. Experimental evidence suggests the presence, within the inner kinetochore, of multiple chromatin units of 500 nm in both interphase and mitosis. We next exploited conditional knockout or deletion cell lines, generated in the same model system, in order to study changes in the kinetochore ultra-structure when isolated CCAN components were depleted. A major role in the maintenance of kinetochore structure for CENP-C and CENP-S, out of a list of more CENP proteins (CENP-I, CENP-H and CENP-O), is supported by the data presented in this thesis. Strikingly, the same 500 nm long core unit was identified in the data-set of each of

the depleted CCAN components, supporting the idea of a core module repeated to form a collection of loops of chromatin or chromatin planes piled on top of each other.

Therefore which of the two models discussed here is best supported by the data presented in this thesis?

In mitotic cells the depletion of CENP-C or CENP-S suggests that these two proteins constitute two anchor points for centromere structure, and their absence caused an unfolding of chromatin, that is otherwise constricted into the typical centromere structure (control mitotic sample). This novel insight supports the boustrophedon model where CENP-C and CENP-S could create a network of connections within the chromatin layers, supplying the structural support for the maintenance of inner kinetochore structure and act as intra-layer and inter-layer linkers. In addition, CENP-C has the dual role of both contributing to the structure of the centromere and also working as a platform for the outer kinetochore components, through its interaction with the Mis12 complex. Our hypothesis is that CENP-C in the inner centromere would be involved in keeping the structure together, possibly through its dimerization, whilst in the outer chromatin layers its N-terminus would extend outwards for the interaction with Mis12. The presence of a different amount of steps of unfolding observed in different samples suggests that there could be intermediate steps of de-constructing the kinetochore, accomplished by a hierarchical system of complexity (layers containing each sinusoidal patches of chromatin), already hypothesized (Ribeiro et al., 2010). Lastly, estimating the length of chromatin included in each layer, allowed the prediction of the total number of nucleosomes residing in the kinetochore, at least in DT40 cells. The numbers obtained in our system are remarkably close to the work shown in other publications that use different approaches (Bodor et al., 2014; Ribeiro et al., 2014; Shang et al., 2013).

The loop model, or amphipathic model, does not easily adapt to the scenario just described. In terms of distribution of the proteins along the chromatin loop it would be difficult to explain how, for example CENP-C, could differentiate its function, as there would be more accessibility to the outer kinetochore components.

A further complication derives from the amount of steps of unfolding observed in the data-sets. An argument, albeit unlikely, is that with the amphipathic model you could associate a loop with a core repetitive unit, however minimal unfolding obtained in control mitosis or in mitotic cells depleted of CENP-I, CENP-H or CENP-O could not be explained. What would determine how many loops to unfold if the loops are all the same? More likely a structure with diverse levels of complexity could justify such behaviour.

In the future it will be interesting to investigate the effect exerted by histone post-translation modifications on the overall structure of the inner centromere, or by analysing the additive effect of CENP-S and CENP-C simultaneous depletion. Challenging, however exciting, would be the combination of super-resolution microscopy with electron microscopy (correlative PALM/EM) for the visualization of unfolded centromeres. Combining these two high-resolution techniques it would be possible, for example, to visualize on centromere fibers how H3 and CENP-A nucleosomes are organized relatively to each other, or where newly loaded CENP-A nucleosomes are inserted along the centromere. Difficulties will be encountered in the preparation of the EM samples as the sectioning of a thin specimen like chromatin fibers is not trivial.

The final part of this thesis attempted to characterize CENP-Z. CENP-Z was identified five years ago in the Earnshaw laboratory and visualized at kinetochores during mitosis. CENP-Z is an interesting kinetochore protein to study as it by contains a zinc finger domain and a zinc finger associated domain, which are common features of DNA interacting proteins. It was found to interact with lysine acetyl transferases (KAT) and one histone deacetylase (HDAC4), which are both involved in transcription regulation. An additional bioinformatic approach was used to analyse CENP-Z aa sequence revealing the presence of a large portion of the protein at the C-terminus, highly conserved across vertebrates, predicted to fold with 99.93% of confidence, similarly to PRDM9. PRDM9 catalyses the transfer of one methyl group to H3K4me2, generating H3K4me3, which is a mark for transcription initiation. The region of PRDM9 that was found similar to CENP-Z includes its catalitic domain, suggesting that CENP-Z could present the same methyl transferase

activity. To further investigate this aspect, tethering studies at the Human Artificial Chromosome (HAC) were performed. This system was indeed the best to studies effects on H3K4me2 upon tethering chromatin modifiers, as it presents one foci of enrichment for this mark. The results presented here showed that, upon tethering of CENP-Z, H3K4me2 fluorescence intensity at the HAC significantly decreased. Our hypothesis is that CENP-Z catalyses a change from H3K4me2 to H3K4me3. Therefore, future CENP-Z tethering experiments will be performed where levels of H3K4me3 will be measured at the HAC. This is potentially very exciting piece of data, as, if confirmed, it would imply that CENP-Z can modulate transcription initiation at kinetochore in mitosis. Additionally, CENP-Z depletion was optimised by RNAi. Preliminary analysis of the phenotypes found in mitosis revealed a block in prometaphase.

Future work will be, on the short-term, focused in the screening of rabbit sera for a specific antibody able to recognised endogenous CENP-Z and to repeating the analysis of mitotic phenotypes upon CENP-Z depletion. Also, more tethering experiments to the HAC will be performed in order to clarify whether CENP-Z is or isn't a methyl transferase specific for H3K4me2. On the long-term, provided that a specific antibody will be obtained, it would be interesting to try affinity purifications combined with mass-spectrometry in order to identify interacting partners and analyse the amount of transcripts at the HAC to confirm or deny a role in transcription. Ultimately, as CENP-Z is also present in *Gallus gallus*, it would be interesting to deplete CENP-Z in DT40 cells and perform fiber analysis to test for any effects on kinetochore ultra-structure.

In conclusion, the data presented in this thesis was the first to identify an organised array of 500 nm layers of chromatin at the inner kinetochore; the first to uncover a new role of CENP-C and CENP-S in holding together centromere structure, contributing with novel insights to the field of kinetochore structure. Finally, this thesis has also provided data suggesting that the novel kinetochore protein CENP-Z could be a PRDM9-like methyl transferase and having a potential effect on transcription at the kinetochore.

7 Appendix

7.1 ImageJ Macro

```
//####### HAC & CRaQ VERSION 1.00
//## based on CRaQ code version = "v1.06";
//####### //####### //####### //####### //####### //####### //####### //####### //####### //#######
//####### //####### //####### //####### //####### //####### //#######


run("Set Measurements...", "area mean min center feret's redirect=None decimal=3");
run("Colors...", "foreground=black background=black selection=green");


PrimaryImage=getTitle();
setTool("rectangle");
waitForUser("Select cell", "Please daw a square around a single cell to analyze.");
run("Duplicate...");
selectWindow(PrimaryImage);
close();



Dialog.create("Set Channels");
      Dialog.addMessage("\nMethod:\nProjects .dv file by Max. intensity projection.\nSelect HAC signal and draws square around it, measures it, and paints it black. \nThen detects endogenous centromeres, and performs the same.\nMeasurements are made by measuring the mean signal in the square (to account for unfolding), and subtracting the lowest signal to control for local background signal.\nOutputs the data in a log window, and leaves the PROJection image open for confirmation of detection.");
        Dialog.addChoice("Acquisition mode:", newArray("Z then wavelength(Fast Acquisition)", "Wavelength then Z"));
//            Dialog.addMessage("");
//            Dialog.addMessage("DV files:");
            Dialog.addNumber("Data channel number",2,0,0,"");
            Dialog.addNumber("Reference channel number",2,0,0,"");
            Dialog.addNumber("DAPI channel number",4,0,0,"enter 0 if no DAPI was used");
            Dialog.addNumber("Total channels",4,0,0,"");
            Dialog.addMessage("");
            Dialog.addCheckbox("Change default parameter settings?",0);
            Dialog.addCheckbox("Cropped cells?",0);
        Dialog.addChoice("Projection method", newArray("Max Intensity","Sum Slices"));
Dialog.show();
        FileType=Dialog.getChoice();
            DataCh=Dialog.getNumber();
            RefCh=Dialog.getNumber();
            DapiCh=Dialog.getNumber();
            TotCh=Dialog.getNumber();
            Change=Dialog.getCheckbox();
```

```
		CroppedCells=Dialog.getCheckbox();
	ProjectionType=Dialog.getChoice();
if (((RefCh-DapiCh)*(DataCh-DapiCh)) == 0){
		exit("Reference and Data channels should be different from DAPI channel");beep();}
if ((RefCh-DataCh) == 0){
		Dialog.create("WARNING");
			Dialog.addMessage("Reference and Data channels are the same");
		Dialog.show();
}


Dialog.create("Change parameter settings");
	Dialog.addMessage("\nMake sure that box is big enough to contain some background pixels.");
	  Dialog.addNumber("Square size",7,0,0,"pixels");
	Dialog.addMessage("\nDecreasing circularity will allow you to pick up more bright centromeres, but will also increase the chance of picking up doublets, clusters or non-centromeric regions.");
		Dialog.addNumber("Minimum Circularity",0.95,2,4,"a.u.");
	Dialog.addMessage("\nMax feret's Diam. is the longest diameter of a spot. Increasing will have similar effect to lowering Min. Circularity.");
		Dialog.addNumber("Max Feret's Diameter",6.5,1,3,"pixels");
	Dialog.addMessage("\nMin/Max Centromere size: lowering excludes more doublets, but also some brigther cents.; increasing will discard more false positives but also true positives.");
		Dialog.addNumber("Min Centromere Size",4,0,2,"pixel");
		Dialog.addNumber("Max Centromere Size",35,0,2,"pixel");
	Dialog.addMessage("\nIncreasing Threshold will improve detection of dimmer spots and decrease that of brighter ones.");
		Dialog.addNumber("Threshold Factor",1.0,2,4,"pixel intensity");
	Dialog.addMessage("\nIf known, set the chromatic aberration of the reference channel compared to the data channel, increase if Ref has signal more to top/right, or vice versa.");
		Dialog.addNumber("Chromatic aberration (horizontal): ",0,0,2,"pixels to right");
		Dialog.addNumber("Chromatic aberration (vertical): ",0,0,2,"pixels down");
if (Change == 1)
		Dialog.show();			//####################keeps defaults if "Change default" is unchecked
		SquareSize=Dialog.getNumber();
		MinCirc=Dialog.getNumber();
		MaxFeret=Dialog.getNumber();
		MinCentro=Dialog.getNumber();
		MaxCentro=Dialog.getNumber();
		OtsuUp=Dialog.getNumber();
		xCor=Dialog.getNumber();
		yCor=Dialog.getNumber();
if (MinCirc >= 1)			exit("Minimum circularity should be smaller than 1");
if (MinCentro >= MaxCentro)		exit("Minimum centromere size should be smaller than maximum centromere size");



corner=(SquareSize-1)/2;
```

```
roiManager("reset");
print("Log Reset");
print("\\Clear");
Ch=newArray(RefCh,DataCh,DapiCh);
RDM=newArray("Ref","Data","Mask");




////////////////////////FUNCTIONS////////////////////////FUNCTIONS////////////////////////FUNCTIONS////////////////////////FUNCTIONS////////////////////////


                                        TotSl=nSlices;
                                ImageFolder=getDirectory("image");
                                ImageName=getTitle();
                                        run("Properties...", "unit=pixel pixel_width=1 pixel_height=1");
                                        run("Rename...", "title=dvFile");
                                        if(nSlices>1)                   {
                                            if (FileType=="Z then wavelength(Fast Acquisition)") {Order =
'xyzct'; };
                                            else if (FileType=="Wavelength then Z") {Order = 'xyczt(default)';
}
                                            run("Stack to Hyperstack...", "order="+Order+"
channels="+TotCh+" slices="+nSlices/TotCh+" frames=1 display=Grayscale");
                                            Dialog.create("Set Z slice interval");
                                                Dialog.addNumber("First slice",1,0,0,"");
                                                    Dialog.addNumber("Last slice",nSlices/TotCh,0,0,"");
                                            Dialog.show();
                                                FirstSlice=Dialog.getNumber();
                                                    LastSlice=Dialog.getNumber();
                                            run("Z Project...", "start="+FirstSlice+" stop="+LastSlice+"
projection=["+ProjectionType+"]");
                                            run("Rename...", "title="+ImageName+"Proj.tif");
                                            saveAs("Tiff", ImageFolder+ImageName+"__PROJ.tif");
                                            }
                                        else                                run("Duplicate...", "title=PRJ");


                                run("Rename...", "title=PRJ");
                                        selectWindow("dvFile");
                                        close();
                                        for (k=0; k<Ch.length; k++){
                                                if(Ch[k]>0){
                                                        selectWindow("PRJ");
                                                        setSlice(Ch[k]);
```

```
                                        run("Duplicate...", "title="+RDM[k]);
                                        run("Brightness/Contrast...");
                                        resetMinAndMax();
                                    }
                                }

selectWindow("PRJ");
setSlice(Ch[1]);
run("Channels Tool... ");
run("Brightness/Contrast...");
resetMinAndMax();
setSlice(Ch[2]);
run("Channels Tool... ");
run("Brightness/Contrast...");
resetMinAndMax();

print (ImageName);
print ("HAC signal");


measure();



function measure(){
        count=1;

        if(DapiCh>0 && CroppedCells==0){
                selectWindow("Mask");
                run("Duplicate...", "title=blur");
                run("Gaussian Blur...", "sigma=75");
                imageCalculator("Subtract", "Mask","blur");
                selectWindow("blur");
                close();
                run("Invert");
                getStatistics(AREA,MEAN,MIN,MAX);
                for(i=0;AREA>=getWidth*getHeight;i+=10){
                        makeRectangle(0,0,0,0);
                        setThreshold(MIN,MAX-i);
                        for(j=0;j<getHeight;j+=100)     doWand(0,j);
                        getStatistics(AREA,a,b,c);
                }
                run("Convert to Mask");
                run("Fill Holes");
```

```
		run("16-bit");
		run("Multiply...", "value=257.000");
	}

	if(DapiCh>0 && CroppedCells==1){
		selectWindow("Mask");
		setAutoThreshold("Default");
		getThreshold(AAA,BBB);
		setThreshold(AAA, BBB*2/3);

		run("Convert to Mask");
		run("16-bit");
		run("Multiply...", "value=257.000");
		run("Invert");
	}


selectWindow("PRJ"); //##Shift back to the PROJ to select the HAC centromere on the Ref channel
setSlice(Ch[1]);
resetMinAndMax();
setTool("point");
waitForUser("Select HAC centromere", "Please click on the center of the HAC centromere signal");
//##Select HAC centromere.

	//#selects the signal area and adds it to ROI manager, on the Data image
	getSelectionCoordinates(x, y);
	x=round(x[0]);
	y=round(y[0]);
	cx=x-xCor;cy=y-yCor; //##This is the chromatic aberration correction
	selectWindow("Data");
	makeRectangle(x-corner, y-corner, SquareSize, SquareSize);
	getStatistics(area, no, no, no);
	makeRectangle(cx-corner, cy-corner, SquareSize, SquareSize);
	roiManager("Add");
	getStatistics(no, mean, min, max);
	if (min>0 && max<65000 && area==(SquareSize*SquareSize)){
	if (max>0)	print (round(mean-min));
	else			print ("ND");
	    fillRect(cx-corner, cy-corner, SquareSize, SquareSize);  //########## puts black box over spots, these are then disregarded in the next cycle due to "if(min>0)"
	    makeRectangle(cx-corner, cy-corner, SquareSize, SquareSize);
	print ("Endogenous centromeres");
```

```
//##Select Ref image to detect endogenous centromeres
	selectWindow("Ref");
	run("Bandpass Filter...", "filter_large=10 filter_small=1 suppress=None tolerance=5 autoscale");
	if(DapiCh>0)		imageCalculator("AND", "Ref","Mask");
	run("Invert");
	if(is("Inverting LUT"))		run("Invert LUT");
	run("MultiThresholder", "otsu");
	getThreshold(lower, upper);
	setThreshold(lower, upper*OtsuUp);
	run("Analyze Particles...", "size="+MinCentro+"-"+MaxCentro+" circularity="+MinCirc+"-1.00 show=Nothing
exclude clear");


//##Change to the Data image and go through the analyzed particles and draw rectangles around them, and measure them
	selectWindow("Data");
	for (l=0;l<nResults;l++) {
		if (getResult("Feret", l)<MaxFeret){
			x=round(getResult("XM", l));
			y=round(getResult("YM", l));
			cx=x-xCor;cy=y-yCor; //##This is the chromatic aberration correction
			makeRectangle(x-corner, y-corner, SquareSize, SquareSize);
			getStatistics(area, no, no, no);
			makeRectangle(cx-corner, cy-corner, SquareSize, SquareSize);
			getStatistics(no, mean, min, max);
			if (min>0 && max<65000 && area==(SquareSize*SquareSize)){
				if (max>0) print (round(mean-min));
				else			print ("ND");
				count++;
				fillRect(cx-corner, cy-corner, SquareSize, SquareSize); //########## puts black
box over spots, these are then disregarded in the next cycle due to "if(min>0)"
				makeRectangle(cx-corner, cy-corner, SquareSize, SquareSize);
				roiManager("Add");
			}
		}
	}
	selectWindow("Data");
	close();
	selectWindow("Ref");
	close();
	if(DapiCh>0){
		selectWindow("Mask");
		close();
	}
}
```

7.2 CENP-Z fragment predicted folding using PHYRE2 server

Phyre2

Email	giulia.vargiu@gmail.com
Description	cenpz_isoform_A
Date	Thu Apr 23 10:59:47 BST 2015
Unique Job ID	67b0e5c8a3d70364

Detailed template information

#	Template	Alignment Coverage	3D Model	Confidence	% i.d.	Template Information
1	c4ijdA_	Alignment		99.9	8	**PDB header:**transferase **Chain:** A: **PDB Molecule:**histone-lysine n-methyltransferase prdm9; **PDBTitle:** crystal structure of methyltransferase domain of human pr domain-2 containing protein 9
3	c2cshA_	Alignment	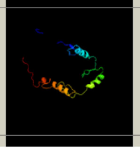	99.9	26	**PDB header:**transcription **Chain:** A: **PDB Molecule:**zinc finger protein 297b; **PDBTitle:** solution structure of tandem repeat of the zf-c2h2 domains2 of human zinc finger protein 297b

8 References

Abad, M.A., B. Medina, A. Santamaria, J. Zou, C. Plasberg-Hill, A. Madhumalar, U. Jayachandran, P.M. Redli, J. Rappsilber, E.A. Nigg, and A.A. Jeyaprakash. 2014. Structural basis for microtubule recognition by the human kinetochore Ska complex. *Nature communications*. 5:2964.

Abbe, E. 1873. Beiträge zur Theorie des Mikroskops und der mikroskopischen Wahrnehmung. *Archiv f. mikrosk. Anatomie*. 9:413-418.

Allshire, R.C., and G.H. Karpen. 2008. Epigenetic regulation of centromeric chromatin: old dogs, new tricks? *Nature reviews. Genetics*. 9:923-937.

Alonso, A., B. Fritz, D. Hasson, G. Abrusan, F. Cheung, K. Yoda, B. Radlwimmer, A.G. Ladurner, and P.E. Warburton. 2007. Co-localization of CENP-C and CENP-H to discontinuous domains of CENP-A chromatin at human neocentromeres. *Genome biology*. 8:R148.

Alushin, G.M., V.H. Ramey, S. Pasqualato, D.A. Ball, N. Grigorieff, A. Musacchio, and E. Nogales. 2010. The Ndc80 kinetochore complex forms oligomeric arrays along microtubules. *Nature*. 467:805-810.

Amano, M., A. Suzuki, T. Hori, C. Backer, K. Okawa, I.M. Cheeseman, and T. Fukagawa. 2009. The CENP-S complex is essential for the stable assembly of outer kinetochore structure. *The Journal of cell biology*. 186:173-182.

Amaro, A.C., C.P. Samora, R. Holtackers, E. Wang, I.J. Kingston, M. Alonso, M. Lampson, A.D. McAinsh, and P. Meraldi. 2010. Molecular control of kinetochore-microtubule dynamics and chromosome oscillations. *Nature cell biology*. 12:319-329.

Amor, D.J., K. Bentley, J. Ryan, J. Perry, L. Wong, H. Slater, and K.H. Choo. 2004. Human centromere repositioning "in progress". *Proceedings of the National Academy of Sciences of the United States of America*. 101:6542-6547.

Anderson, M., J. Haase, E. Yeh, and K. Bloom. 2009. Function and assembly of DNA looping, clustering, and microtubule attachment complexes within a eukaryotic kinetochore. *Mol Biol Cell*. 20:4131-4139.

Ando, R., H. Mizuno, and A. Miyawaki. 2004. Regulated fast nucleocytoplasmic shuttling observed by reversible protein highlighting. *Science*. 306:1370-1373.

Ando, S., H. Yang, N. Nozaki, T. Okazaki, and K. Yoda. 2002. CENP-A, -B, and -C chromatin complex that contains the I-type alpha-satellite array constitutes the prekinetochore in HeLa cells. *Molecular and cellular biology*. 22:2229-2241.

Andrews, P.D., Y. Ovechkina, N. Morrice, M. Wagenbach, K. Duncan, L. Wordeman, and J.R. Swedlow. 2004. Aurora B regulates MCAK at the mitotic centromere. *Dev Cell*. 6:253-268.

Asbury, C.L., D.R. Gestaut, A.F. Powers, A.D. Franck, and T.N. Davis. 2006. The Dam1 kinetochore complex harnesses microtubule dynamics to produce force and movement. *Proceedings of the National Academy of Sciences of the United States of America*. 103:9873-9878.

Ault, J.G., and C.L. Rieder. 1994. Centrosome and kinetochore movement during mitosis. *Current opinion in cell biology*. 6:41-49.

Baldin, V., J. Lukas, M.J. Marcote, M. Pagano, and G. Draetta. 1993. Cyclin D1 is a nuclear protein required for cell cycle progression in G1. *Genes Dev*. 7:812-821.

Bancroft, J., P. Auckland, C.P. Samora, and A.D. McAinsh. 2015. Chromosome congression is promoted by CENP-Q- and CENP-E-dependent pathways. *J Cell Sci*. 128:171-184.

Basilico, F., S. Maffini, J.R. Weir, D. Prumbaum, A.M. Rojas, T. Zimniak, A. De Antoni, S. Jeganathan, B. Voss, S. van Gerwen, V. Krenn, L. Massimiliano, A. Valencia, I.R. Vetter, F. Herzog, S. Raunser, S. Pasqualato, and A. Musacchio. 2014. The pseudo GTPase CENP-M drives human kinetochore assembly. *eLife*. 3:e02978.

Baudat, F., J. Buard, C. Grey, A. Fledel-Alon, C. Ober, M. Przeworski, G. Coop, and B. de Massy. 2010. PRDM9 Is a Major Determinant of Meiotic Recombination Hotspots in Humans and Mice. *Science*. 327:836-840.

Beck, D.B., A. Burton, H. Oda, C. Ziegler-Birling, M.E. Torres-Padilla, and D. Reinberg. 2012. The role of PR-Set7 in replication licensing depends on Suv4-20h. *Genes Dev*. 26:2580-2589.

Bergmann, J.H., N.M. Martins, V. Larionov, H. Masumoto, and W.C. Earnshaw. 2012. HACking the centromere chromatin code: insights from human artificial chromosomes. *Chromosome research : an international journal on the molecular, supramolecular and evolutionary aspects of chromosome biology*. 20:505-519.

Bergmann, J.H., M.G. Rodriguez, N.M. Martins, H. Kimura, D.A. Kelly, H. Masumoto, V. Larionov, L.E. Jansen, and W.C. Earnshaw. 2011. Epigenetic engineering shows H3K4me2 is required for HJURP targeting and CENP-A assembly on a synthetic human kinetochore. *The EMBO journal*. 30:328-340.

Betzig, E., G.H. Patterson, R. Sougrat, O.W. Lindwasser, S. Olenych, J.S. Bonifacino, M.W. Davidson, J. Lippincott-Schwartz, and H.F. Hess. 2006. Imaging intracellular fluorescent proteins at nanometer resolution. *Science*. 313:1642-1645.

Black, B.E., D.R. Foltz, S. Chakravarthy, K. Luger, V.L. Woods, Jr., and D.W. Cleveland. 2004. Structural determinants for generating centromeric chromatin. *Nature*. 430:578-582.

Black, B.E., L.E. Jansen, P.S. Maddox, D.R. Foltz, A.B. Desai, J.V. Shah, and D.W. Cleveland. 2007. Centromere identity maintained by nucleosomes assembled with histone H3 containing the CENP-A targeting domain. *Molecular cell*. 25:309-322.

Blower, M.D., B.A. Sullivan, and G.H. Karpen. 2002. Conserved organization of centromeric chromatin in flies and humans. *Dev Cell*. 2:319-330.

Bock, L.J., C. Pagliuca, N. Kobayashi, R.A. Grove, Y. Oku, K. Shrestha, C. Alfieri, C. Golfieri, A. Oldani, M. Dal Maschio, R. Bermejo, T.R. Hazbun, T.U. Tanaka, and P. De Wulf. 2012. Cnn1 inhibits the interactions between the KMN complexes of the yeast kinetochore. *Nature cell biology*. 14:614-624.

Bodor, D.L., J.F. Mata, M. Sergeev, A.F. David, K.J. Salimian, T. Panchenko, D.W. Cleveland, B.E. Black, J.V. Shah, and L.E. Jansen. 2014. The quantitative architecture of centromeric chromatin. *eLife*. 3:e02137.

Bornfleth, H., K. Satzler, R. Eils, and C.G. Cremer. 1998. High-precision distance measurements and volume-conserving segmentation of objects near and below the resolution limit in three-dimensional confocal fluorecsence microscopy. *Journal of microscopy*. 189:118-136.

Brenner, S., D. Pepper, M.W. Berns, E. Tan, and B.R. Brinkley. 1981. Kinetochore Structure, Duplication, and Distribution in Mammalian-Cells - Analysis by Human Autoantibodies from Scleroderma Patients. *Journal of Cell Biology*. 91:95-102.

Brinkley, B.R., and E. Stubblefield. 1966. The fine structure of the kinetochore of a mammalian cell in vitro. *Chromosoma*. 19:28-43.

Buchwitz, B.J., K. Ahmad, L.L. Moore, M.B. Roth, and S. Henikoff. 1999. A histone-H3-like protein in C. elegans. *Nature*. 401:547-548.

Caldas, G.V., K.F. DeLuca, and J.G. DeLuca. 2013. KNL1 facilitates phosphorylation of outer kinetochore proteins by promoting Aurora B kinase activity. *The Journal of cell biology*. 203:957-969.

Capalbo, L., E. Montembault, T. Takeda, Z.I. Bassi, D.M. Glover, and P.P. D'Avino. 2012. The chromosomal passenger complex controls the function of endosomal sorting complex required for transport-III Snf7 proteins during cytokinesis. *Open biology*. 2:120070.

Cardinale, S., J.H. Bergmann, D. Kelly, M. Nakano, M.M. Valdivia, H. Kimura, H. Masumoto, V. Larionov, and W.C. Earnshaw. 2009. Hierarchical inactivation of a synthetic human kinetochore by a chromatin modifier. *Mol Biol Cell*. 20:4194-4204.

Carlton, J.G., A. Caballe, M. Agromayor, M. Kloc, and J. Martin-Serrano. 2012. ESCRT-III governs the Aurora B-mediated abscission checkpoint through CHMP4C. *Science*. 336:220-225.

Carmena, M., M. Wheelock, H. Funabiki, and W.C. Earnshaw. 2012. The chromosomal passenger complex (CPC): from easy rider to the godfather of mitosis. *Nat Rev Mol Cell Bio*. 13:789-803.

Carroll, C.W., K.J. Milks, and A.F. Straight. 2010. Dual recognition of CENP-A nucleosomes is required for centromere assembly. *The Journal of cell biology*. 189:1143-1155.

Carroll, C.W., M.C. Silva, K.M. Godek, L.E. Jansen, and A.F. Straight. 2009. Centromere assembly requires the direct recognition of CENP-A nucleosomes by CENP-N. *Nature cell biology*. 11:896-902.

Cassimeris, L., C.L. Rieder, G. Rupp, and E.D. Salmon. 1990. Stability of microtubule attachment to metaphase kinetochores in PtK1 cells. *J Cell Sci*. 96 (Pt 1):9-15.

Chan, F.L., O.J. Marshall, R. Saffery, B.W. Kim, E. Earle, K.H. Choo, and L.H. Wong. 2012. Active transcription and essential role of RNA polymerase II at the centromere during mitosis. *Proceedings of the National Academy of Sciences of the United States of America*. 109:1979-1984.

Cheeseman, I.M., J.S. Chappie, E.M. Wilson-Kubalek, and A. Desai. 2006. The conserved KMN network constitutes the core microtubule-binding site of the kinetochore. *Cell*. 127:983-997.

Cheeseman, I.M., and A. Desai. 2008. Molecular architecture of the kinetochore-microtubule interface. *Nature reviews. Molecular cell biology*. 9:33-46.

Cheeseman, I.M., T. Hori, T. Fukagawa, and A. Desai. 2008. KNL1 and the CENP-H/I/K complex coordinately direct kinetochore assembly in vertebrates. *Molecular biology of the cell*. 19:587-594.

Ciferri, C., J. De Luca, S. Monzani, K.J. Ferrari, D. Ristic, C. Wyman, H. Stark, J. Kilmartin, E.D. Salmon, and A. Musacchio. 2005. Architecture of the human ndc80-hec1 complex, a critical constituent of the outer kinetochore. *The Journal of biological chemistry*. 280:29088-29095.

Ciferri, C., S. Pasqualato, E. Screpanti, G. Varetti, S. Santaguida, G. Dos Reis, A. Maiolica, J. Polka, J.G. De Luca, P. De Wulf, M. Salek, J. Rappsilber, C.A. Moores, E.D. Salmon, and A. Musacchio. 2008. Implications for kinetochore-microtubule attachment from the structure of an engineered Ndc80 complex. *Cell*. 133:427-439.

Cimini, D., and F. Degrassi. 2005. Aneuploidy: a matter of bad connections. *Trends in cell biology*. 15:442-451.

Clarke, L., and J. Carbon. 1980. Isolation of a yeast centromere and construction of functional small circular chromosomes. *Nature*. 287:504-509.

Clarke, L., and J. Carbon. 1985. The structure and function of yeast centromeres. *Annual review of genetics*. 19:29-55.

Cleveland, D.W., Y. Mao, and K.F. Sullivan. 2003. Centromeres and kinetochores: from epigenetics to mitotic checkpoint signaling. *Cell*. 112:407-421.

Coffman, V.C., P. Wu, M.R. Parthun, and J.Q. Wu. 2011. CENP-A exceeds microtubule attachment sites in centromere clusters of both budding and fission yeast. *The Journal of cell biology*. 195:563-572.

Cohen, R.L., C.W. Espelin, P. De Wulf, P.K. Sorger, S.C. Harrison, and K.T. Simons. 2008. Structural and functional dissection of Mif2p, a conserved DNA-binding kinetochore protein. *Mol Biol Cell*. 19:4480-4491.

Daum, J.R., J.D. Wren, J.J. Daniel, S. Sivakumar, J.N. McAvoy, T.A. Potapova, and G.J. Gorbsky. 2009. Ska3 is required for spindle checkpoint silencing and the maintenance of chromosome cohesion in mitosis. *Current biology : CB*. 19:1467-1472.

De Antoni, A., C.G. Pearson, D. Cimini, J.C. Canman, V. Sala, L. Nezi, M. Mapelli, L. Sironi, M. Faretta, E.D. Salmon, and A. Musacchio. 2005. The Mad1/Mad2 complex as a template for Mad2 activation in the spindle assembly checkpoint. *Current biology : CB*. 15:214-225.

DeLange, R.J., D.M. Fambrough, E.L. Smith, and J. Bonner. 1969. Calf and pea histone IV. II. The complete amino acid sequence of calf thymus histone IV; presence of epsilon-N-acetyllysine. *The Journal of biological chemistry*. 244:319-334.

DeLuca, J.G., W.E. Gall, C. Ciferri, D. Cimini, A. Musacchio, and E.D. Salmon. 2006. Kinetochore microtubule dynamics and attachment stability are regulated by Hec1. *Cell*. 127:969-982.

Desai, A., S. Rybina, T. Muller-Reichert, A. Shevchenko, A. Shevchenko, A. Hyman, and K. Oegema. 2003. KNL-1 directs assembly of the microtubule-binding interface of the kinetochore in C. elegans. *Genes Dev*. 17:2421-2435.

Dickson, R.M., A.B. Cubitt, R.Y. Tsien, and W.E. Moerner. 1997. On/off blinking and switching behaviour of single molecules of green fluorescent protein. *Nature*. 388:355-358.

Dong, Y., K.J. Vanden Beldt, X. Meng, A. Khodjakov, and B.F. McEwen. 2007. The outer plate in vertebrate kinetochores is a flexible network with multiple microtubule interactions. *Nature cell biology*. 9:516-522.

Dornblut, C., N. Quinn, S. Monajambashi, L. Prendergast, C. van Vuuren, S. Munch, W. Deng, H. Leonhardt, M.C. Cardoso, C. Hoischen, S. Diekmann, and K.F. Sullivan. 2014. A CENP-S/X complex assembles at the centromere in S and G2 phases of the human cell cycle. *Open biology*. 4:130229.

Dunleavy, E.M., D. Roche, H. Tagami, N. Lacoste, D. Ray-Gallet, Y. Nakamura, Y. Daigo, Y. Nakatani, and G. Almouzni-Pettinotti. 2009. HJURP is a cell-cycle-dependent maintenance and deposition factor of CENP-A at centromeres. *Cell*. 137:485-497.

Dyba, M., and S.W. Hell. 2002. Focal spots of size lambda/23 open up far-field fluorescence microscopy at 33 nm axial resolution. *Physical review letters*. 88:163901.

Dyba, M., S. Jakobs, and S.W. Hell. 2003. Immunofluorescence stimulated emission depletion microscopy. *Nature biotechnology*. 21:1303-1304.

Earnshaw, W.C., and C.A. Cooke. 1991. Analysis of the Distribution of the Incenps Throughout Mitosis Reveals the Existence of a Pathway of Structural-Changes in the Chromosomes during Metaphase and Early Events in Cleavage Furrow Formation. *J Cell Sci*. 98:443-461.

Earnshaw, W.C., and U.K. Laemmli. 1983. Architecture of metaphase chromosomes and chromosome scaffolds. *The Journal of cell biology*. 96:84-93.

Earnshaw, W.C., and B.R. Migeon. 1985. Three related centromere proteins are absent from the inactive centromere of a stable isodicentric chromosome. *Chromosoma*. 92:290-296.

Earnshaw, W.C., and N. Rothfield. 1985. Identification of a Family of Human Centromere Proteins Using Autoimmune Sera from Patients with Scleroderma. *Chromosoma*. 91:313-321.

Ernst, J., and M. Kellis. 2010. Discovery and characterization of chromatin states for systematic annotation of the human genome. *Nature biotechnology*. 28:817-825.

Eskat, A., W. Deng, A. Hofmeister, S. Rudolphi, S. Emmerth, D. Hellwig, T. Ulbricht, V. Doring, J.M. Bancroft, A.D. McAinsh, M.C. Cardoso, P. Meraldi, C. Hoischen, H. Leonhardt, and S. Diekmann. 2012. Step-wise assembly, maturation and dynamic behavior of the human CENP-P/O/R/Q/U kinetochore sub-complex. *PloS one*. 7:e44717.

Evans, T., E.T. Rosenthal, J. Youngblom, D. Distel, and T. Hunt. 1983. Cyclin: a protein specified by maternal mRNA in sea urchin eggs that is destroyed at each cleavage division. *Cell*. 33:389-396.

Fang, J., Y. Liu, Y. Wei, W. Deng, Z. Yu, L. Huang, Y. Teng, T. Yao, Q. You, H. Ruan, P. Chen, R.M. Xu, and G. Li. 2015. Structural transitions of centromeric chromatin regulate the cell cycle-dependent recruitment of CENP-N. *Genes Dev*. 29:1058-1073.

Field, C., R. Li, and K. Oegema. 1999. Cytokinesis in eukaryotes: a mechanistic comparison. *Current opinion in cell biology*. 11:68-80.

Flors, C., and W.C. Earnshaw. 2011. Super-resolution fluorescence microscopy as a tool to study the nanoscale organization of chromosomes. *Current opinion in chemical biology*. 15:838-844.

Foley, E.A., and T.M. Kapoor. 2013. Microtubule attachment and spindle assembly checkpoint signalling at the kinetochore. *Nature reviews. Molecular cell biology*. 14:25-37.

Foltz, D.R., L.E. Jansen, A.O. Bailey, J.R. Yates, 3rd, E.A. Bassett, S. Wood, B.E. Black, and D.W. Cleveland. 2009. Centromere-specific assembly of CENP-a nucleosomes is mediated by HJURP. *Cell*. 137:472-484.

Foltz, D.R., L.E. Jansen, B.E. Black, A.O. Bailey, J.R. Yates, 3rd, and D.W. Cleveland. 2006. The human CENP-A centromeric nucleosome-associated complex. *Nature cell biology*. 8:458-469.

Fradet-Turcotte, A., M.D. Canny, C. Escribano-Diaz, A. Orthwein, C.C. Leung, H. Huang, M.C. Landry, J. Kitevski-LeBlanc, S.M. Noordermeer, F. Sicheri, and D. Durocher. 2013. 53BP1 is a reader of the DNA-damage-induced H2A Lys 15 ubiquitin mark. *Nature*. 499:50-54.

Fujita, Y., T. Hayashi, T. Kiyomitsu, Y. Toyoda, A. Kokubu, C. Obuse, and M. Yanagida. 2007. Priming of centromere for CENP-A recruitment by human hMis18alpha, hMis18beta, and M18BP1. *Dev Cell*. 12:17-30.

Fukagawa, T., and W.C. Earnshaw. 2014. The centromere: chromatin foundation for the kinetochore machinery. *Dev Cell*. 30:496-508.

Fukagawa, T., Y. Mikami, A. Nishihashi, V. Regnier, T. Haraguchi, Y. Hiraoka, N. Sugata, K. Todokoro, W. Brown, and T. Ikemura. 2001. CENP-H, a constitutive centromere component, is required for centromere targeting of CENP-C in vertebrate cells. *The EMBO journal*. 20:4603-4617.

Gaitanos, T.N., A. Santamaria, A.A. Jeyaprakash, B. Wang, E. Conti, and E.A. Nigg. 2009. Stable kinetochore-microtubule interactions depend on the Ska complex and its new component Ska3/C13Orf3. *The EMBO journal*. 28:1442-1452.

Gascoigne, K.E., and I.M. Cheeseman. 2013. CDK-dependent phosphorylation and nuclear exclusion coordinately control kinetochore assembly state. *The Journal of cell biology*. 201:23-32.

Gascoigne, K.E., K. Takeuchi, A. Suzuki, T. Hori, T. Fukagawa, and I.M. Cheeseman. 2011. Induced ectopic kinetochore assembly bypasses the requirement for CENP-A nucleosomes. *Cell*. 145:410-422.

Glotzer, M., A.W. Murray, and M.W. Kirschner. 1991. Cyclin is degraded by the ubiquitin pathway. *Nature*. 349:132-138.

Gonen, S., B. Akiyoshi, M.G. Iadanza, D. Shi, N. Duggan, S. Biggins, and T. Gonen. 2012. The structure of purified kinetochores reveals multiple microtubule-attachment sites. *Nature structural & molecular biology*. 19:925-929.

Goshima, G., T. Kiyomitsu, K. Yoda, and M. Yanagida. 2003. Human centromere chromatin protein hMis12, essential for equal segregation, is independent of CENP-A loading pathway. *The Journal of cell biology*. 160:25-39.

Grey, C., P. Barthes, G. Chauveau-Le Friec, F. Langa, F. Baudat, and B. de Massy. 2011. Mouse PRDM9 DNA-binding specificity determines sites of histone H3 lysine 4 trimethylation for initiation of meiotic recombination. *PLoS biology*. 9:e1001176.

Grishchuk, E.L., I.S. Spiridonov, V.A. Volkov, A. Efremov, S. Westermann, D. Drubin, G. Barnes, F.I. Ataullakhanov, and J.R. McIntosh. 2008. Different assemblies of the DAM1 complex follow shortening microtubules by distinct mechanisms. *Proceedings of the National Academy of Sciences of the United States of America*. 105:6918-6923.

Guse, A., C.W. Carroll, B. Moree, C.J. Fuller, and A.F. Straight. 2011. In vitro centromere and kinetochore assembly on defined chromatin templates. *Nature*. 477:354-358.

Gustafsson, M.G. 2000. Surpassing the lateral resolution limit by a factor of two using structured illumination microscopy. *Journal of microscopy*. 198:82-87.

Gustafsson, M.G., L. Shao, P.M. Carlton, C.J. Wang, I.N. Golubovskaya, W.Z. Cande, D.A. Agard, and J.W. Sedat. 2008. Three-dimensional resolution doubling in wide-field fluorescence microscopy by structured illumination. *Biophysical journal*. 94:4957-4970.

Haase, J., P.K. Mishra, A. Stephens, R. Haggerty, C. Quammen, R.M. Taylor, 2nd, E. Yeh, M.A. Basrai, and K. Bloom. 2013. A 3D map of the yeast kinetochore reveals the presence of core and accessory centromere-specific histone. *Current biology : CB*. 23:1939-1944.

Habuchi, S., R. Ando, P. Dedecker, W. Verheijen, H. Mizuno, A. Miyawaki, and J. Hofkens. 2005. Reversible single-molecule photoswitching in the GFP-like fluorescent protein Dronpa. *Proceedings of the National Academy of Sciences of the United States of America*. 102:9511-9516.

Hadwiger, J.A., C. Wittenberg, M.D. Mendenhall, and S.I. Reed. 1989. The Saccharomyces cerevisiae CKS1 gene, a homolog of the Schizosaccharomyces pombe suc1+ gene, encodes a subunit of the Cdc28 protein kinase complex. *Molecular and cellular biology*. 9:2034-2041.

Hanisch, A., H.H. Sillje, and E.A. Nigg. 2006. Timely anaphase onset requires a novel spindle and kinetochore complex comprising Ska1 and Ska2. *The EMBO journal*. 25:5504-5515.

Harborth, J., S.M. Elbashir, K. Bechert, T. Tuschl, and K. Weber. 2001. Identification of essential genes in cultured mammalian cells using small interfering RNAs. *J Cell Sci*. 114:4557-4565.

Harrison, C.J., E.M. Jack, T.D. Allen, and R. Harris. 1985. Light and scanning electron microscopy of the same human metaphase chromosomes. *J Cell Sci*. 77:143-153.

Hayashi, K., K. Yoshida, and Y. Matsui. 2005. A histone H3 methyltransferase controls epigenetic events required for meiotic prophase. *Nature*. 438:374-378.

Hayashi, T., Y. Fujita, O. Iwasaki, Y. Adachi, K. Takahashi, and M. Yanagida. 2004. Mis16 and Mis18 are required for CENP-A loading and histone deacetylation at centromeres. *Cell*. 118:715-729.

Heilemann, M., D.P. Herten, R. Heintzmann, C. Cremer, C. Muller, P. Tinnefeld, K.D. Weston, J. Wolfrum, and M. Sauer. 2002. High-resolution colocalization of single dye molecules by fluorescence lifetime imaging microscopy. *Analytical chemistry*. 74:3511-3517.

Heilemann, M., S. van de Linde, M. Schuttpelz, R. Kasper, B. Seefeldt, A. Mukherjee, P. Tinnefeld, and M. Sauer. 2008. Subdiffraction-resolution fluorescence imaging with conventional fluorescent probes. *Angew Chem Int Ed Engl*. 47:6172-6176.

Heintzmann, R., and C.G. Cremer. 1999. Laterally modulated excitation microscopy: improvement of resolution by using a diffraction grating. Vol. 3568. 185-196.

Hell, S.W., and J. Wichmann. 1994. Breaking the diffraction resolution limit by stimulated emission: stimulated-emission-depletion fluorescence microscopy. *Optics letters*. 19:780-782.

Hellwig, D., S. Emmerth, T. Ulbricht, V. Doring, C. Hoischen, R. Martin, C.P. Samora, A.D. McAinsh, C.W. Carroll, A.F. Straight, P. Meraldi, and S.

Diekmann. 2011. Dynamics of CENP-N kinetochore binding during the cell cycle. *J Cell Sci*. 124:3871-3883.

Henikoff, S., K. Ahmad, and H.S. Malik. 2001. The centromere paradox: stable inheritance with rapidly evolving DNA. *Science*. 293:1098-1102.

Henikoff, S., K. Ahmad, J.S. Platero, and B. van Steensel. 2000. Heterochromatic deposition of centromeric histone H3-like proteins. *Proceedings of the National Academy of Sciences of the United States of America*. 97:716-721.

Hershko, A., D. Ganoth, J. Pehrson, R.E. Palazzo, and L.H. Cohen. 1991. Methylated ubiquitin inhibits cyclin degradation in clam embryo extracts. *The Journal of biological chemistry*. 266:16376-16379.

Hess, S.T., T.P. Girirajan, and M.D. Mason. 2006. Ultra-high resolution imaging by fluorescence photoactivation localization microscopy. *Biophysical journal*. 91:4258-4272.

Heun, P., S. Erhardt, M.D. Blower, S. Weiss, A.D. Skora, and G.H. Karpen. 2006. Mislocalization of the Drosophila centromere-specific histone CID promotes formation of functional ectopic kinetochores. *Dev Cell*. 10:303-315.

Hewitt, L., A. Tighe, S. Santaguida, A.M. White, C.D. Jones, A. Musacchio, S. Green, and S.S. Taylor. 2010. Sustained Mps1 activity is required in mitosis to recruit O-Mad2 to the Mad1-C-Mad2 core complex. *The Journal of cell biology*. 190:25-34.

Hirano, T. 2005. Condensins: organizing and segregating the genome. *Current biology : CB*. 15:R265-275.

Hori, T., M. Amano, A. Suzuki, C.B. Backer, J.P. Welburn, Y. Dong, B.F. McEwen, W.H. Shang, E. Suzuki, K. Okawa, I.M. Cheeseman, and T. Fukagawa. 2008a. CCAN makes multiple contacts with centromeric DNA to provide distinct pathways to the outer kinetochore. *Cell*. 135:1039-1052.

Hori, T., M. Okada, K. Maenaka, and T. Fukagawa. 2008b. CENP-O class proteins form a stable complex and are required for proper kinetochore function. *Molecular biology of the cell*. 19:843-854.

Hori, T., W.H. Shang, K. Takeuchi, and T. Fukagawa. 2013. The CCAN recruits CENP-A to the centromere and forms the structural core for kinetochore assembly. *The Journal of cell biology*. 200:45-60.

Hori, T., W.H. Shang, A. Toyoda, S. Misu, N. Monma, K. Ikeo, O. Molina, G. Vargiu, A. Fujiyama, H. Kimura, W.C. Earnshaw, and T. Fukagawa. 2014. Histone H4 Lys 20 monomethylation of the CENP-A nucleosome is essential for kinetochore assembly. *Dev Cell*. 29:740-749.

Hornung, P., M. Maier, G.M. Alushin, G.C. Lander, E. Nogales, and S. Westermann. 2011. Molecular architecture and connectivity of the budding yeast Mtw1 kinetochore complex. *Journal of molecular biology*. 405:548-559.

Howell, B.J., B.F. McEwen, J.C. Canman, D.B. Hoffman, E.M. Farrar, C.L. Rieder, and E.D. Salmon. 2001. Cytoplasmic dynein/dynactin drives kinetochore

protein transport to the spindle poles and has a role in mitotic spindle checkpoint inactivation. *The Journal of cell biology*. 155:1159-1172.

Howman, E.V., K.J. Fowler, A.J. Newson, S. Redward, A.C. MacDonald, P. Kalitsis, and K.H. Choo. 2000. Early disruption of centromeric chromatin organization in centromere protein A (Cenpa) null mice. *Proceedings of the National Academy of Sciences of the United States of America*. 97:1148-1153.

Hsu, K.S., and T. Toda. 2011. Ndc80 internal loop interacts with Dis1/TOG to ensure proper kinetochore-spindle attachment in fission yeast. *Current biology : CB*. 21:214-220.

Huang, B., M. Bates, and X. Zhuang. 2009. Super-resolution fluorescence microscopy. *Annual review of biochemistry*. 78:993-1016.

Hudson, D.F., P. Vagnarelli, R. Gassmann, and W.C. Earnshaw. 2003. Condensin is required for nonhistone protein assembly and structural integrity of vertebrate mitotic chromosomes. *Dev Cell*. 5:323-336.

Izuta, H., M. Ikeno, N. Suzuki, T. Tomonaga, N. Nozaki, C. Obuse, Y. Kisu, N. Goshima, F. Nomura, N. Nomura, and K. Yoda. 2006. Comprehensive analysis of the ICEN (Interphase Centromere Complex) components enriched in the CENP-A chromatin of human cells. *Genes to cells : devoted to molecular & cellular mechanisms*. 11:673-684.

Jansen, L.E., B.E. Black, D.R. Foltz, and D.W. Cleveland. 2007. Propagation of centromeric chromatin requires exit from mitosis. *The Journal of cell biology*. 176:795-805.

Jeyaprakash, A.A., U.R. Klein, D. Lindner, J. Ebert, E.A. Nigg, and E. Conti. 2007. Structure of a Survivin-Borealin-INCENP core complex reveals how chromosomal passengers travel together. *Cell*. 131:271-285.

Jeyaprakash, A.A., A. Santamaria, U. Jayachandran, Y.W. Chan, C. Benda, E.A. Nigg, and E. Conti. 2012. Structural and functional organization of the Ska complex, a key component of the kinetochore-microtubule interface. *Molecular cell*. 46:274-286.

Jin, W., J.C. Lamb, W. Zhang, B. Kolano, J.A. Birchler, and J. Jiang. 2008. Histone modifications associated with both A and B chromosomes of maize. *Chromosome research : an international journal on the molecular, supramolecular and evolutionary aspects of chromosome biology*. 16:1203-1214.

Joglekar, A.P., K. Bloom, and E.D. Salmon. 2009. In vivo protein architecture of the eukaryotic kinetochore with nanometer scale accuracy. *Current biology : CB*. 19:694-699.

Joglekar, A.P., K.S. Bloom, and E.D. Salmon. 2010. Mechanisms of force generation by end-on kinetochore-microtubule attachments. *Current opinion in cell biology*. 22:57-67.

Joglekar, A.P., D. Bouck, K. Finley, X. Liu, Y. Wan, J. Berman, X. He, E.D. Salmon, and K.S. Bloom. 2008. Molecular architecture of the kinetochore-

microtubule attachment site is conserved between point and regional centromeres. *The Journal of cell biology*. 181:587-594.

Joglekar, A.P., D.C. Bouck, J.N. Molk, K.S. Bloom, and E.D. Salmon. 2006. Molecular architecture of a kinetochore-microtubule attachment site. *Nature cell biology*. 8:581-585.

Jones, D.T. 1999. Protein secondary structure prediction based on position-specific scoring matrices. *Journal of molecular biology*. 292:195-202.

Kang, Y.H., C.H. Park, T.S. Kim, N.K. Soung, J.K. Bang, B.Y. Kim, J.E. Park, and K.S. Lee. 2011. Mammalian polo-like kinase 1-dependent regulation of the PBIP1-CENP-Q complex at kinetochores. *The Journal of biological chemistry*. 286:19744-19757.

Karachentsev, D., K. Sarma, D. Reinberg, and R. Steward. 2005. PR-Set7-dependent methylation of histone H4 Lys 20 functions in repression of gene expression and is essential for mitosis. *Genes Dev*. 19:431-435.

Karpen, G.H., and R.C. Allshire. 1997. The case for epigenetic effects on centromere identity and function. *Trends in genetics : TIG*. 13:489-496.

Kelley, L.A., S. Mezulis, C.M. Yates, M.N. Wass, and M.J. Sternberg. 2015. The Phyre2 web portal for protein modeling, prediction and analysis. *Nature protocols*. 10:845-858.

Khodjakov, A., R.W. Cole, B.F. McEwen, K.F. Buttle, and C.L. Rieder. 1997. Chromosome fragments possessing only one kinetochore can congress to the spindle equator. *The Journal of cell biology*. 136:229-240.

Kim, Ik S., M. Lee, Koog C. Park, Y. Jeon, Joo H. Park, Eun J. Hwang, Tae I. Jeon, S. Ko, H. Lee, Sung H. Baek, and Keun I. Kim. 2012. Roles of Mis18α in Epigenetic Regulation of Centromeric Chromatin and CENP-A Loading. *Molecular cell*. 46:260-273.

Kim, S.M., D.D. Dubey, and J.A. Huberman. 2003. Early-replicating heterochromatin. *Genes Dev*. 17:330-335.

Kiyomitsu, T., C. Obuse, and M. Yanagida. 2007. Human Blinkin/AF15q14 is required for chromosome alignment and the mitotic checkpoint through direct interaction with Bub1 and BubR1. *Dev Cell*. 13:663-676.

Klar, T.A., S. Jakobs, M. Dyba, A. Egner, and S.W. Hell. 2000. Fluorescence microscopy with diffraction resolution barrier broken by stimulated emission. *Proceedings of the National Academy of Sciences of the United States of America*. 97:8206-8210.

Kleinig, H., H. Zentgraf, P. Comes, and J. Stadler. 1971. Nuclear membranes and plasma membranes from hen erythrocytes. II. Lipid composition. *The Journal of biological chemistry*. 246:2996-3000.

Komarnitsky, P., E.J. Cho, and S. Buratowski. 2000. Different phosphorylated forms of RNA polymerase II and associated mRNA processing factors during transcription. *Genes Dev*. 14:2452-2460.

Kops, G.J., Y. Kim, B.A. Weaver, Y. Mao, I. McLeod, J.R. Yates, 3rd, M. Tagaya, and D.W. Cleveland. 2005. ZW10 links mitotic checkpoint signaling to the structural kinetochore. *The Journal of cell biology*. 169:49-60.

Koshland, D., and A. Strunnikov. 1996. Mitotic chromosome condensation. *Annual review of cell and developmental biology*. 12:305-333.

Kouprina, N., A. Samoshkin, I. Erliandri, M. Nakano, H.S. Lee, H. Fu, Y. Iida, M. Aladjem, M. Oshimura, H. Masumoto, W.C. Earnshaw, and V. Larionov. 2012. Organization of synthetic alphoid DNA array in human artificial chromosome (HAC) with a conditional centromere. *ACS synthetic biology*. 1:590-601.

Kouzarides, T. 2007. Chromatin modifications and their function. *Cell*. 128:693-705.

Kwiatkowski, N., N. Jelluma, P. Filippakopoulos, M. Soundararajan, M.S. Manak, M. Kwon, H.G. Choi, T. Sim, Q.L. Deveraux, S. Rottmann, D. Pellman, J.V. Shah, G.J. Kops, S. Knapp, and N.S. Gray. 2010. Small-molecule kinase inhibitors provide insight into Mps1 cell cycle function. *Nature chemical biology*. 6:359-368.

Kwon, M.S., T. Hori, M. Okada, and T. Fukagawa. 2007. CENP-C is involved in chromosome segregation, mitotic checkpoint function, and kinetochore assembly. *Mol Biol Cell*. 18:2155-2168.

Laemmli, U.K., S.M. Cheng, K.W. Adolph, J.R. Paulson, J.A. Brown, and W.R. Baumbach. 1978. Metaphase chromosome structure: the role of nonhistone proteins. *Cold Spring Harbor symposia on quantitative biology*. 42 Pt 1:351-360.

Lan, W., X. Zhang, S.L. Kline-Smith, S.E. Rosasco, G.A. Barrett-Wilt, J. Shabanowitz, D.F. Hunt, C.E. Walczak, and P.T. Stukenberg. 2004. Aurora B phosphorylates centromeric MCAK and regulates its localization and microtubule depolymerization activity. *Current biology : CB*. 14:273-286.

Lawrimore, J., K.S. Bloom, and E.D. Salmon. 2011. Point centromeres contain more than a single centromere-specific Cse4 (CENP-A) nucleosome. *The Journal of cell biology*. 195:573-582.

Liao, W.T., X. Wang, L.H. Xu, Q.L. Kong, C.P. Yu, M.Z. Li, L. Shi, M.S. Zeng, and L.B. Song. 2009. Centromere protein H is a novel prognostic marker for human nonsmall cell lung cancer progression and overall patient survival. *Cancer*. 115:1507-1517.

Lidke, K., B. Rieger, T. Jovin, and R. Heintzmann. 2005. Superresolution by localization of quantum dots using blinking statistics. *Optics express*. 13:7052-7062.

Lippincott-Schwartz, J., and G.H. Patterson. 2003. Development and use of fluorescent protein markers in living cells. *Science*. 300:87-91.

Lippincott-Schwartz, J., and G.H. Patterson. 2009. Photoactivatable fluorescent proteins for diffraction-limited and super-resolution imaging. *Trends in cell biology*. 19:555-565.

Liu, D., G. Vader, M.J. Vromans, M.A. Lampson, and S.M. Lens. 2009. Sensing chromosome bi-orientation by spatial separation of aurora B kinase from kinetochore substrates. *Science*. 323:1350-1353.

Liu, S.T., J.C. Hittle, S.A. Jablonski, M.S. Campbell, K. Yoda, and T.J. Yen. 2003. Human CENP-I specifies localization of CENP-F, MAD1 and MAD2 to kinetochores and is essential for mitosis. *Nature cell biology*. 5:341-345.

Lohka, M.J., M.K. Hayes, and J.L. Maller. 1988. Purification of maturation-promoting factor, an intracellular regulator of early mitotic events. *Proceedings of the National Academy of Sciences of the United States of America*. 85:3009-3013.

London, N., S. Ceto, J.A. Ranish, and S. Biggins. 2012. Phosphoregulation of Spc105 by Mps1 and PP1 regulates Bub1 localization to kinetochores. *Current biology : CB*. 22:900-906.

Luger, K., A.W. Mader, R.K. Richmond, D.F. Sargent, and T.J. Richmond. 1997. Crystal structure of the nucleosome core particle at 2.8 A resolution. *Nature*. 389:251-260.

Luo, X., G. Fang, M. Coldiron, Y. Lin, H. Yu, M.W. Kirschner, and G. Wagner. 2000. Structure of the Mad2 spindle assembly checkpoint protein and its interaction with Cdc20. *Nature structural biology*. 7:224-229.

Luo, X., Z. Tang, J. Rizo, and H. Yu. 2002. The Mad2 spindle checkpoint protein undergoes similar major conformational changes upon binding to either Mad1 or Cdc20. *Molecular cell*. 9:59-71.

Luo, X., Z. Tang, G. Xia, K. Wassmann, T. Matsumoto, J. Rizo, and H. Yu. 2004. The Mad2 spindle checkpoint protein has two distinct natively folded states. *Nature structural & molecular biology*. 11:338-345.

Luo, X., and H. Yu. 2008. Protein metamorphosis: the two-state behavior of Mad2. *Structure*. 16:1616-1625.

Maciejowski, J., K.A. George, M.E. Terret, C. Zhang, K.M. Shokat, and P.V. Jallepalli. 2010. Mps1 directs the assembly of Cdc20 inhibitory complexes during interphase and mitosis to control M phase timing and spindle checkpoint signaling. *The Journal of cell biology*. 190:89-100.

Maddox, P.S., F. Hyndman, J. Monen, K. Oegema, and A. Desai. 2007. Functional genomics identifies a Myb domain-containing protein family required for assembly of CENP-A chromatin. *The Journal of cell biology*. 176:757-763.

Maddox, P.S., K. Oegema, A. Desai, and I.M. Cheeseman. 2004. "Holo"er than thou: chromosome segregation and kinetochore function in C. elegans. *Chromosome research : an international journal on the molecular, supramolecular and evolutionary aspects of chromosome biology*. 12:641-653.

Maiato, H., J. DeLuca, E.D. Salmon, and W.C. Earnshaw. 2004. The dynamic kinetochore-microtubule interface. *J Cell Sci*. 117:5461-5477.

Maiato, H., P.J. Hergert, S. Moutinho-Pereira, Y. Dong, K.J. Vandenbeldt, C.L. Rieder, and B.F. McEwen. 2006. The ultrastructure of the kinetochore and kinetochore fiber in Drosophila somatic cells. *Chromosoma*. 115:469-480.

Mapelli, M., L. Massimiliano, S. Santaguida, and A. Musacchio. 2007. The Mad2 conformational dimer: structure and implications for the spindle assembly checkpoint. *Cell*. 131:730-743.

Mapelli, M., and A. Musacchio. 2007. MAD contortions: conformational dimerization boosts spindle checkpoint signaling. *Current opinion in structural biology*. 17:716-725.

Maskell, D.P., X.W. Hu, and M.R. Singleton. 2010. Molecular architecture and assembly of the yeast kinetochore MIND complex. *The Journal of cell biology*. 190:823-834.

Mastronarde, D.N., K.L. McDonald, R. Ding, and J.R. McIntosh. 1993. Interpolar spindle microtubules in PTK cells. *The Journal of cell biology*. 123:1475-1489.

Matson, D.R., and P.T. Stukenberg. 2014. CENP-I and Aurora B act as a molecular switch that ties RZZ/Mad1 recruitment to kinetochore attachment status. *The Journal of cell biology*. 205:541-554.

McAinsh, A.D., and P. Meraldi. 2011. The CCAN complex: linking centromere specification to control of kinetochore-microtubule dynamics. *Seminars in cell & developmental biology*. 22:946-952.

McAinsh, A.D., P. Meraldi, V.M. Draviam, A. Toso, and P.K. Sorger. 2006. The human kinetochore proteins Nnf1R and Mcm21R are required for accurate chromosome segregation. *The EMBO journal*. 25:4033-4049.

McAinsh, A.D., J.D. Tytell, and P.K. Sorger. 2003. Structure, function, and regulation of budding yeast kinetochores. *Annual review of cell and developmental biology*. 19:519-539.

McClelland, S.E., S. Borusu, A.C. Amaro, J.R. Winter, M. Belwal, A.D. McAinsh, and P. Meraldi. 2007. The CENP-A NAC/CAD kinetochore complex controls chromosome congression and spindle bipolarity. *The EMBO journal*. 26:5033-5047.

McEwen, B.F., C.E. Hsieh, A.L. Mattheyses, and C.L. Rieder. 1998. A new look at kinetochore structure in vertebrate somatic cells using high-pressure freezing and freeze substitution. *Chromosoma*. 107:366-375.

McIntosh, J.R., E. O'Toole, K. Zhudenkov, M. Morphew, C. Schwartz, F.I. Ataullakhanov, and E.L. Grishchuk. 2013. Conserved and divergent features of kinetochores and spindle microtubule ends from five species. *The Journal of cell biology*. 200:459-474.

McKinley, K.L., and I.M. Cheeseman. 2014. Polo-like kinase 1 licenses CENP-A deposition at centromeres. *Cell*. 158:397-411.

Meluh, P.B., P. Yang, L. Glowczewski, D. Koshland, and M.M. Smith. 1998. Cse4p is a component of the core centromere of Saccharomyces cerevisiae. *Cell*. 94:607-613.

Molina, O., G. Vargiu, M.A. Abad, H. Masumoto, N. Kouprina, V. Larionov, and W.C. Earnshaw. 2015. H4K4me2 is necessary to promote RNA polymerase II transcription at centromeres for CENP-A loading. *Currently under review at the Journal of Cell Biology*.

Morris, D.P., G.A. Michelotti, and D.A. Schwinn. 2005. Evidence that phosphorylation of the RNA polymerase II carboxyl-terminal repeats is similar in yeast and humans. *The Journal of biological chemistry*. 280:31368-31377.

Nakano, M., S. Cardinale, V.N. Noskov, R. Gassmann, P. Vagnarelli, S. Kandels-Lewis, V. Larionov, W.C. Earnshaw, and H. Masumoto. 2008. Inactivation of a human kinetochore by specific targeting of chromatin modifiers. *Dev Cell*. 14:507-522.

Nakayama, K.I., S. Hatakeyama, and K. Nakayama. 2001. Regulation of the cell cycle at the G1-S transition by proteolysis of cyclin E and p27Kip1. *Biochemical and biophysical research communications*. 282:853-860.

Nash, R., G. Tokiwa, S. Anand, K. Erickson, and A.B. Futcher. 1988. The WHI1+ gene of Saccharomyces cerevisiae tethers cell division to cell size and is a cyclin homolog. *The EMBO journal*. 7:4335-4346.

Nasmyth, K., J.M. Peters, and F. Uhlmann. 2000. Splitting the chromosome: cutting the ties that bind sister chromatids. *Science*. 288:1379-1385.

Nishihashi, A., T. Haraguchi, Y. Hiraoka, T. Ikemura, V. Regnier, H. Dodson, W.C. Earnshaw, and T. Fukagawa. 2002. CENP-I is essential for centromere function in vertebrate cells. *Dev Cell*. 2:463-476.

Nishino, T., F. Rago, T. Hori, K. Tomii, I.M. Cheeseman, and T. Fukagawa. 2013. CENP-T provides a structural platform for outer kinetochore assembly. *The EMBO journal*. 32:424-436.

Nishino, T., K. Takeuchi, K.E. Gascoigne, A. Suzuki, T. Hori, T. Oyama, K. Morikawa, I.M. Cheeseman, and T. Fukagawa. 2012. CENP-T-W-S-X forms a unique centromeric chromatin structure with a histone-like fold. *Cell*. 148:487-501.

Norbury, C., and P. Nurse. 1992. Animal cell cycles and their control. *Annual review of biochemistry*. 61:441-470.

Oda, H., I. Okamoto, N. Murphy, J. Chu, S.M. Price, M.M. Shen, M.E. Torres-Padilla, E. Heard, and D. Reinberg. 2009. Monomethylation of histone H4-lysine 20 is involved in chromosome structure and stability and is essential for mouse development. *Molecular and cellular biology*. 29:2278-2295.

Oegema, K., A. Desai, S. Rybina, M. Kirkham, and A.A. Hyman. 2001. Functional analysis of kinetochore assembly in Caenorhabditis elegans. *The Journal of cell biology*. 153:1209-1226.

Ohi, R., T. Sapra, J. Howard, and T.J. Mitchison. 2004. Differentiation of cytoplasmic and meiotic spindle assembly MCAK functions by Aurora B-dependent phosphorylation. *Mol Biol Cell*. 15:2895-2906.

Ohta, S., J.C. Bukowski-Wills, L. Sanchez-Pulido, L. Alves Fde, L. Wood, Z.A. Chen, M. Platani, L. Fischer, D.F. Hudson, C.P. Ponting, T. Fukagawa, W.C. Earnshaw, and J. Rappsilber. 2010. The protein composition of mitotic chromosomes determined using multiclassifier combinatorial proteomics. *Cell*. 142:810-821.

Ohta, S., L. Wood, I. Toramoto, K. Yagyu, T. Fukagawa, and W.C. Earnshaw. 2015. CENP-32 is required to maintain centrosomal dominance in bipolar spindle assembly. *Mol Biol Cell*. 26:1225-1237.

Ohzeki, J., J.H. Bergmann, N. Kouprina, V.N. Noskov, M. Nakano, H. Kimura, W.C. Earnshaw, V. Larionov, and H. Masumoto. 2012. Breaking the HAC Barrier: histone H3K9 acetyl/methyl balance regulates CENP-A assembly. *The EMBO journal*. 31:2391-2402.

Okada, M., I.M. Cheeseman, T. Hori, K. Okawa, I.X. McLeod, J.R. Yates, 3rd, A. Desai, and T. Fukagawa. 2006. The CENP-H-I complex is required for the efficient incorporation of newly synthesized CENP-A into centromeres. *Nature cell biology*. 8:446-457.

Olins, D.E., and A.L. Olins. 1978. Nucleosomes: the structural quantum in chromosomes. *American scientist*. 66:704-711.

Painter, R.B., and B.R. Young. 1980. Radiosensitivity in ataxia-telangiectasia: a new explanation. *Proceedings of the National Academy of Sciences of the United States of America*. 77:7315-7317.

Palmer, D.K., K. O'Day, H.L. Trong, H. Charbonneau, and R.L. Margolis. 1991. Purification of the centromere-specific protein CENP-A and demonstration that it is a distinctive histone. *Proceedings of the National Academy of Sciences of the United States of America*. 88:3734-3738.

Palmer, D.K., K. Oday, M.H. Wener, B.S. Andrews, and R.L. Margolis. 1987. A 17-Kd Centromere Protein (Cenp-a) Copurifies with Nucleosome Core Particles and with Histones. *Journal of Cell Biology*. 104:805-815.

Pearson, C.G., E. Yeh, M. Gardner, D. Odde, E.D. Salmon, and K. Bloom. 2004. Stable kinetochore-microtubule attachment constrains centromere positioning in metaphase. *Current biology : CB*. 14:1962-1967.

Pei, H., L. Zhang, K. Luo, Y. Qin, M. Chesi, F. Fei, P.L. Bergsagel, L. Wang, Z. You, and Z. Lou. 2011. MMSET regulates histone H4K20 methylation and 53BP1 accumulation at DNA damage sites. *Nature*. 470:124-128.

Perpelescu, M., and T. Fukagawa. 2011. The ABCs of CENPs. *Chromosoma*. 120:425-446.

Peters, J.M. 2002. The anaphase-promoting complex: proteolysis in mitosis and beyond. *Molecular cell*. 9:931-943.

Petrovic, A., S. Pasqualato, P. Dube, V. Krenn, S. Santaguida, D. Cittaro, S. Monzani, L. Massimiliano, J. Keller, A. Tarricone, A. Maiolica, H. Stark, and A. Musacchio. 2010. The MIS12 complex is a protein interaction hub for outer kinetochore assembly. *The Journal of cell biology*. 190:835-852.

Pietrasanta, L.I., D. Thrower, W. Hsieh, S. Rao, O. Stemmann, J. Lechner, J. Carbon, and H. Hansma. 1999. Probing the Saccharomyces cerevisiae centromeric DNA (CEN DNA)-binding factor 3 (CBF3) kinetochore complex by using atomic force microscopy. *Proceedings of the National Academy of Sciences of the United States of America*. 96:3757-3762.

Pines, J. 1999. Four-dimensional control of the cell cycle. *Nature cell biology*. 1:E73-79.

Pinsky, B.A., C.R. Nelson, and S. Biggins. 2009. Protein phosphatase 1 regulates exit from the spindle checkpoint in budding yeast. *Current biology : CB*. 19:1182-1187.

Pluta, A.F., A.M. Mackay, A.M. Ainsztein, I.G. Goldberg, and W.C. Earnshaw. 1995. The centromere: hub of chromosomal activities. *Science*. 270:1591-1594.

Przewloka, M.R., Z. Venkei, V.M. Bolanos-Garcia, J. Debski, M. Dadlez, and D.M. Glover. 2011. CENP-C is a structural platform for kinetochore assembly. *Current biology : CB*. 21:399-405.

Przewloka, M.R., W. Zhang, P. Costa, V. Archambault, P.P. D'Avino, K.S. Lilley, E.D. Laue, A.D. McAinsh, and D.M. Glover. 2007. Molecular analysis of core kinetochore composition and assembly in Drosophila melanogaster. *PloS one*. 2:e478.

Quenet, D., and Y. Dalal. 2014. A long non-coding RNA is required for targeting centromeric protein A to the human centromere. *eLife*. 3:e03254.

Raaijmakers, J.A., M.E. Tanenbaum, A.F. Maia, and R.H. Medema. 2009. RAMA1 is a novel kinetochore protein involved in kinetochore-microtubule attachment. *J Cell Sci*. 122:2436-2445.

Regnier, V., P. Vagnarelli, T. Fukagawa, T. Zerjal, E. Burns, D. Trouche, W. Earnshaw, and W. Brown. 2005. CENP-A is required for accurate chromosome segregation and sustained kinetochore association of BubR1. *Molecular and cellular biology*. 25:3967-3981.

Ribeiro, S.A., P. Vagnarelli, Y. Dong, T. Hori, B.F. McEwen, T. Fukagawa, C. Flors, and W.C. Earnshaw. 2010. A super-resolution map of the vertebrate kinetochore. *Proceedings of the National Academy of Sciences of the United States of America*. 107:10484-10489.

Ribeiro, S.A., P. Vagnarelli, and W.C. Earnshaw. 2014. DNA content of a functioning chicken kinetochore. *Chromosome research : an international journal on the molecular, supramolecular and evolutionary aspects of chromosome biology*. 22:7-13.

Richmond, T.J., J.T. Finch, B. Rushton, D. Rhodes, and A. Klug. 1984. Structure of the nucleosome core particle at 7 A resolution. *Nature*. 311:532-537.

Rieder, C.L. 1982. The formation, structure, and composition of the mammalian kinetochore and kinetochore fiber. *Int Rev Cytol.* . 79:1-58.

Rieder, C.L., and S.P. Alexander. 1990. Kinetochores are transported poleward along a single astral microtubule during chromosome attachment to the spindle in newt lung cells. *The Journal of cell biology*. 110:81-95.

Rieder, C.L., R.W. Cole, A. Khodjakov, and G. Sluder. 1995. The checkpoint delaying anaphase in response to chromosome monoorientation is mediated by an inhibitory signal produced by unattached kinetochores. *The Journal of cell biology*. 130:941-948.

Rieder, C.L., and A. Khodjakov. 1997. Mitosis and checkpoints that control progression through mitosis in vertebrate somatic cells. *Progress in cell cycle research*. 3:301-312.

Rust, M.J., M. Bates, and X. Zhuang. 2006. Sub-diffraction-limit imaging by stochastic optical reconstruction microscopy (STORM). *Nature methods*. 3:793-795.

Ruthenburg, A.J., H. Li, D.J. Patel, and C.D. Allis. 2007. Multivalent engagement of chromatin modifications by linked binding modules. *Nature reviews. Molecular cell biology*. 8:983-994.

Saffery, R., D.V. Irvine, B. Griffiths, P. Kalitsis, L. Wordeman, and K.H. Choo. 2000. Human centromeres and neocentromeres show identical distribution patterns of >20 functionally important kinetochore-associated proteins. *Human molecular genetics*. 9:175-185.

Saitoh, H., J. Tomkiel, C.A. Cooke, H. Ratrie, 3rd, M. Maurer, N.F. Rothfield, and W.C. Earnshaw. 1992. CENP-C, an autoantigen in scleroderma, is a component of the human inner kinetochore plate. *Cell*. 70:115-125.

Salmon, E.D. 1989. Cytokinesis in animal cells. *Current opinion in cell biology*. 1:541-547.

Salmon, E.D., and S.M. Wolniak. 1990. Role of microtubules in stimulating cytokinesis in animal cells. *Annals of the New York Academy of Sciences*. 582:88-98.

Santaguida, S., A. Tighe, A.M. D'Alise, S.S. Taylor, and A. Musacchio. 2010. Dissecting the role of MPS1 in chromosome biorientation and the spindle checkpoint through the small molecule inhibitor reversine. *The Journal of cell biology*. 190:73-87.

Schermelleh, L., P.M. Carlton, S. Haase, L. Shao, L. Winoto, P. Kner, B. Burke, M.C. Cardoso, D.A. Agard, M.G. Gustafsson, H. Leonhardt, and J.W. Sedat. 2008. Subdiffraction multicolor imaging of the nuclear periphery with 3D structured illumination microscopy. *Science*. 320:1332-1336.

Schermelleh, L., R. Heintzmann, and H. Leonhardt. 2010. A guide to super-resolution fluorescence microscopy. *The Journal of cell biology*. 190:165-175.

Schleiffer, A., M. Maier, G. Litos, F. Lampert, P. Hornung, K. Mechtler, and S. Westermann. 2012. CENP-T proteins are conserved centromere receptors of the Ndc80 complex. *Nature cell biology*. 14:604-613.

Schmidt, J.C., H. Arthanari, A. Boeszoermenyi, N.M. Dashkevich, E.M. Wilson-Kubalek, N. Monnier, M. Markus, M. Oberer, R.A. Milligan, M. Bathe, G. Wagner, E.L. Grishchuk, and I.M. Cheeseman. 2012. The kinetochore-bound Ska1 complex tracks depolymerizing microtubules and binds to curved protofilaments. *Dev Cell*. 23:968-980.

Scholey, J.M., I. Brust-Mascher, and A. Mogilner. 2003. Cell division. *Nature*. 422:746-752.

Schwann, T. 2013. Mikroskopische Untersuchungen über die Übereinstimmung in der Struktur und dem Wachstum der Tiere und Pflanzen. Salzwasser-Verlag GmbH.

Screpanti, E., A. De Antoni, G.M. Alushin, A. Petrovic, T. Melis, E. Nogales, and A. Musacchio. 2011. Direct binding of Cenp-C to the Mis12 complex joins the inner and outer kinetochore. *Current biology : CB*. 21:391-398.

Sengupta, P., S. Van Engelenburg, and J. Lippincott-Schwartz. 2012. Visualizing cell structure and function with point-localization superresolution imaging. *Dev Cell*. 23:1092-1102.

Shang, W.H., T. Hori, N.M. Martins, A. Toyoda, S. Misu, N. Monma, I. Hiratani, K. Maeshima, K. Ikeo, A. Fujiyama, H. Kimura, W.C. Earnshaw, and T. Fukagawa. 2013. Chromosome engineering allows the efficient isolation of vertebrate neocentromeres. *Dev Cell*. 24:635-648.

Shcherbakova, D.M., P. Sengupta, J. Lippincott-Schwartz, and V.V. Verkhusha. 2014. Photocontrollable fluorescent proteins for superresolution imaging. *Annual review of biophysics*. 43:303-329.

Shelby, R.D., K. Monier, and K.F. Sullivan. 2000. Chromatin assembly at kinetochores is uncoupled from DNA replication. *The Journal of cell biology*. 151:1113-1118.

Shelby, R.D., O. Vafa, and K.F. Sullivan. 1997. Assembly of CENP-A into centromeric chromatin requires a cooperative array of nucleosomal DNA contact sites. *The Journal of cell biology*. 136:501-513.

Shepperd, L.A., J.C. Meadows, A.M. Sochaj, T.C. Lancaster, J. Zou, G.J. Buttrick, J. Rappsilber, K.G. Hardwick, and J.B. Millar. 2012. Phosphodependent recruitment of Bub1 and Bub3 to Spc7/KNL1 by Mph1 kinase maintains the spindle checkpoint. *Current biology : CB*. 22:891-899.

Shigeishi, H., K. Higashikawa, S. Ono, K. Mizuta, Y. Ninomiya, S. Yoneda, M. Taki, and N. Kamata. 2006. Increased expression of CENP-H gene in human oral squamous cell carcinomas harboring high-proliferative activity. *Oncology reports*. 16:1071-1075.

Silva, M.C., D.L. Bodor, M.E. Stellfox, N.M. Martins, H. Hochegger, D.R. Foltz, and L.E. Jansen. 2012. Cdk activity couples epigenetic centromere inheritance to cell cycle progression. *Dev Cell*. 22:52-63.

Sluder, G. 1979. Role of spindle microtubules in the control of cell cycle timing. *The Journal of cell biology*. 80:674-691.

Sluder, G., and D.A. Begg. 1983. Control mechanisms of the cell cycle: role of the spatial arrangement of spindle components in the timing of mitotic events. *The Journal of cell biology*. 97:877-886.

Stark, C., B.J. Breitkreutz, T. Reguly, L. Boucher, A. Breitkreutz, and M. Tyers. 2006. BioGRID: a general repository for interaction datasets. *Nucleic acids research*. 34:D535-539.

Stoler, S., K.C. Keith, K.E. Curnick, and M. Fitzgerald-Hayes. 1995. A mutation in CSE4, an essential gene encoding a novel chromatin-associated protein in yeast, causes chromosome nondisjunction and cell cycle arrest at mitosis. *Genes Dev*. 9:573-586.

Sudakin, V., G.K. Chan, and T.J. Yen. 2001. Checkpoint inhibition of the APC/C in HeLa cells is mediated by a complex of BUBR1, BUB3, CDC20, and MAD2. *The Journal of cell biology*. 154:925-936.

Sullivan, B., and G. Karpen. 2001. Centromere identity in Drosophila is not determined in vivo by replication timing. *The Journal of cell biology*. 154:683-690.

Sullivan, B.A., M.D. Blower, and G.H. Karpen. 2001. Determining centromere identity: cyclical stories and forking paths. *Nature reviews. Genetics*. 2:584-596.

Sullivan, B.A., and G.H. Karpen. 2004. Centromeric chromatin exhibits a histone modification pattern that is distinct from both euchromatin and heterochromatin. *Nature structural & molecular biology*. 11:1076-1083.

Sullivan, B.A., and H.F. Willard. 1998. Stable dicentric X chromosomes with two functional centromeres. *Nature genetics*. 20:227-228.

Suzuki, A., B.L. Badger, X. Wan, J.G. DeLuca, and E.D. Salmon. 2014. The architecture of CCAN proteins creates a structural integrity to resist spindle forces and achieve proper Intrakinetochore stretch. *Dev Cell*. 30:717-730.

Takahashi, K., E.S. Chen, and M. Yanagida. 2000. Requirement of Mis6 centromere connector for localizing a CENP-A-like protein in fission yeast. *Science*. 288:2215-2219.

Takata, M., M.S. Sasaki, E. Sonoda, C. Morrison, M. Hashimoto, H. Utsumi, Y. Yamaguchi-Iwai, A. Shinohara, and S. Takeda. 1998. Homologous recombination and non-homologous end-joining pathways of DNA double-strand break repair have overlapping roles in the maintenance of chromosomal integrity in vertebrate cells. *The EMBO journal*. 17:5497-5508.

Takeuchi, K., and T. Fukagawa. 2012. Molecular architecture of vertebrate kinetochores. *Experimental cell research*. 318:1367-1374.

Takeuchi, K., T. Nishino, K. Mayanagi, N. Horikoshi, A. Osakabe, H. Tachiwana, T. Hori, H. Kurumizaka, and T. Fukagawa. 2014. The centromeric nucleosome-

like CENP-T-W-S-X complex induces positive supercoils into DNA. *Nucleic acids research*. 42:1644-1655.

Tanaka, K. 2013. Regulatory mechanisms of kinetochore-microtubule interaction in mitosis. *Cellular and molecular life sciences : CMLS*. 70:559-579.

Tanaka, T.U., N. Rachidi, C. Janke, G. Pereira, M. Galova, E. Schiebel, M.J. Stark, and K. Nasmyth. 2002. Evidence that the Ipl1-Sli15 (Aurora kinase-INCENP) complex promotes chromosome bi-orientation by altering kinetochore-spindle pole connections. *Cell*. 108:317-329.

Tang, J., N.W. Cho, G. Cui, E.M. Manion, N.M. Shanbhag, M.V. Botuyan, G. Mer, and R.A. Greenberg. 2013. Acetylation limits 53BP1 association with damaged chromatin to promote homologous recombination. *Nature structural & molecular biology*. 20:317-325.

Tardat, M., J. Brustel, O. Kirsh, C. Lefevbre, M. Callanan, C. Sardet, and E. Julien. 2010. The histone H4 Lys 20 methyltransferase PR-Set7 regulates replication origins in mammalian cells. *Nature cell biology*. 12:1086-1093.

Theis, M., M. Slabicki, M. Junqueira, M. Paszkowski-Rogacz, J. Sontheimer, R. Kittler, A.K. Heninger, T. Glatter, K. Kruusmaa, I. Poser, A.A. Hyman, M.T. Pisabarro, M. Gstaiger, R. Aebersold, A. Shevchenko, and F. Buchholz. 2009. Comparative profiling identifies C13orf3 as a component of the Ska complex required for mammalian cell division. *The EMBO journal*. 28:1453-1465.

Tsien, R.Y. 1998. The green fluorescent protein. *Annual review of biochemistry*. 67:509-544.

Van Hooser, A.A., Ouspenski, II, H.C. Gregson, D.A. Starr, T.J. Yen, M.L. Goldberg, K. Yokomori, W.C. Earnshaw, K.F. Sullivan, and B.R. Brinkley. 2001. Specification of kinetochore-forming chromatin by the histone H3 variant CENP-A. *J Cell Sci*. 114:3529-3542.

van Meer, G., and A.I. de Kroon. 2011. Lipid map of the mammalian cell. *J Cell Sci*. 124:5-8.

Vanoosthuyse, V., and K.G. Hardwick. 2009. A novel protein phosphatase 1-dependent spindle checkpoint silencing mechanism. *Current biology : CB*. 19:1176-1181.

Varma, D., S. Chandrasekaran, L.J. Sundin, K.T. Reidy, X. Wan, D.A. Chasse, K.R. Nevis, J.G. DeLuca, E.D. Salmon, and J.G. Cook. 2012. Recruitment of the human Cdt1 replication licensing protein by the loop domain of Hec1 is required for stable kinetochore-microtubule attachment. *Nature cell biology*. 14:593-603.

Varma, D., X. Wan, D. Cheerambathur, R. Gassmann, A. Suzuki, J. Lawrimore, A. Desai, and E.D. Salmon. 2013. Spindle assembly checkpoint proteins are positioned close to core microtubule attachment sites at kinetochores. *The Journal of cell biology*. 202:735-746.

Verdaasdonk, J.S., A.D. Stephens, J. Haase, and K. Bloom. 2014. Bending the rules: widefield microscopy and the Abbe limit of resolution. *Journal of cellular physiology*. 229:132-138.

Wan, X., R.P. O'Quinn, H.L. Pierce, A.P. Joglekar, W.E. Gall, J.G. DeLuca, C.W. Carroll, S.T. Liu, T.J. Yen, B.F. McEwen, P.T. Stukenberg, A. Desai, and E.D. Salmon. 2009. Protein architecture of the human kinetochore microtubule attachment site. *Cell*. 137:672-684.

Warburton, P.E., C.A. Cooke, S. Bourassa, O. Vafa, B.A. Sullivan, G. Stetten, G. Gimelli, D. Warburton, C. Tyler-Smith, K.F. Sullivan, G.G. Poirier, and W.C. Earnshaw. 1997. Immunolocalization of CENP-A suggests a distinct nucleosome structure at the inner kinetochore plate of active centromeres. *Current biology : CB*. 7:901-904.

Waterhouse, A.M., J.B. Procter, D.M. Martin, M. Clamp, and G.J. Barton. 2009. Jalview Version 2--a multiple sequence alignment editor and analysis workbench. *Bioinformatics*. 25:1189-1191.

Waye, J.S., and H.F. Willard. 1989. Human beta satellite DNA: genomic organization and sequence definition of a class of highly repetitive tandem DNA. *Proceedings of the National Academy of Sciences of the United States of America*. 86:6250-6254.

Wei, R.R., J. Al-Bassam, and S.C. Harrison. 2007. The Ndc80/HEC1 complex is a contact point for kinetochore-microtubule attachment. *Nature structural & molecular biology*. 14:54-59.

Wei, R.R., P.K. Sorger, and S.C. Harrison. 2005. Molecular organization of the Ndc80 complex, an essential kinetochore component. *Proceedings of the National Academy of Sciences of the United States of America*. 102:5363-5367.

Weier, H.U. 2001. DNA fiber mapping techniques for the assembly of high-resolution physical maps. *The journal of histochemistry and cytochemistry : official journal of the Histochemistry Society*. 49:939-948.

Weinert, T.A., and L.H. Hartwell. 1988. The RAD9 gene controls the cell cycle response to DNA damage in Saccharomyces cerevisiae. *Science*. 241:317-322.

Welburn, J.P., E.L. Grishchuk, C.B. Backer, E.M. Wilson-Kubalek, J.R. Yates, 3rd, and I.M. Cheeseman. 2009. The human kinetochore Ska1 complex facilitates microtubule depolymerization-coupled motility. *Dev Cell*. 16:374-385.

Westermann, S., D.G. Drubin, and G. Barnes. 2007. Structures and functions of yeast kinetochore complexes. *Annual review of biochemistry*. 76:563-591.

Westermann, S., H.W. Wang, A. Avila-Sakar, D.G. Drubin, E. Nogales, and G. Barnes. 2006. The Dam1 kinetochore ring complex moves processively on depolymerizing microtubule ends. *Nature*. 440:565-569.

Willard, H.F. 1985. Chromosome-specific organization of human alpha satellite DNA. *American journal of human genetics*. 37:524-532.

Willard, H.F. 1990. Centromeres of mammalian chromosomes. *Trends in genetics : TIG*. 6:410-416.

Yamagishi, Y., T. Honda, Y. Tanno, and Y. Watanabe. 2010. Two Histone Marks Establish the Inner Centromere and Chromosome Bi-Orientation. *Science*. 330:239-243.

Yamagishi, Y., C.H. Yang, Y. Tanno, and Y. Watanabe. 2012. MPS1/Mph1 phosphorylates the kinetochore protein KNL1/Spc7 to recruit SAC components. *Nature cell biology*. 14:746-752.

Yan, H., W. Jin, K. Nagaki, S. Tian, S. Ouyang, C.R. Buell, P.B. Talbert, S. Henikoff, and J. Jiang. 2005. Transcription and histone modifications in the recombination-free region spanning a rice centromere. *The Plant cell*. 17:3227-3238.

Yang, C.H., J. Tomkiel, H. Saitoh, D.H. Johnson, and W.C. Earnshaw. 1996. Identification of overlapping DNA-binding and centromere-targeting domains in the human kinetochore protein CENP-C. *Molecular and cellular biology*. 16:3576-3586.